

Technische Universität München  
Institut für Energietechnik

Lehrstuhl für Thermodynamik

# **Numerical Simulation of the Dynamics of Turbulent Swirling Flames**

**Luis Roberto Tay Wo Chong Hilaes**

Vollständiger Abdruck der von der Fakultät für Maschinenwesen der Technischen Universität München zur Erlangung des akademischen Grades eines

DOKTOR – INGENIEURS

genehmigten Dissertation.

Vorsitzender:

Univ.-Prof. Rafael Macián-Juan, Ph.D.

Prüfer der Dissertation:

1. Univ.-Prof. Wolfgang Polifke, Ph.D. (CCNY)

2. Assoc. Prof. Thierry Schuller, Ph.D.

École Centrale Paris / Frankreich

Die Dissertation wurde am 06.12.2011 bei der Technischen Universität München eingereicht und durch die Fakultät für Maschinenwesen am 23.01.2012 angenommen.



---

## Acknowledgments

The present work was accomplished at the Lehrstuhl für Thermodynamik at the Technische Universität München from October 2006 to December 2011. The work was financially supported by my scholarship from the Deutscher Akademischer Austauschdienst (DAAD) from October 2006 to March 2010, and by the Lehrstuhl für Thermodynamik and the Loschge-Studienstiftung from April 2010.

First of all, I would like to express my special gratitude to my advisor Prof. Wolfgang Polifke for giving me the opportunity to work at the Lehrstuhl für Thermodynamik, for his continuous support since my scholarship application, and for his trust and advices on my work. I would like to thank Prof. Thierry Schuller for being the co-examiner of the thesis and for his support in reviewing my work; and to Prof. Rafael Macián-Juan for organizing and being the chairman of the thesis committee.

I am indebted to my colleagues Thomas Komarek, Stephan Föllner, Dr. Andreas Huber, Dr. Roland Kaess, Martin Hauser, Mathieu Zellhuber, Robert Leandro, Sebastian Bomberg and Ahtsham Ulhaq who supported me during this project. A special thanks to Thomas for providing the experimental data for this work. Also, I would like to thank Mathieu Zellhuber, Anja Marosky, Florian Ettner, Ralf Blumental and Marek Czapp for their support in the translations into German of the required documentations to submit this thesis; to my office colleagues Karin Stehlik, Anton Winkler, Florian Ettner, Klaus Vollmer, Ahtsham Ulhaq and Stephan Föllner for the very nice work atmosphere; to Mrs. Helga Bassett and Mrs. Sigrid Schulz-Reichwald for their support on administrative issues; to Dr. Joao Carneiro for the nice time during our lunch breaks and his support on the cluster; to CERFACS for making available the code AVBP for my simulations; to the Leibniz-Rechenzentrum (LRZ) with the project PR32FO for letting me use their computational resources; and finally to all my colleagues at the Lehrstuhl für Thermodynamik for the great time and support.

Finally, I wish to thank Dr. Holger Lübcke, who introduced me on the field of

---

gas turbine combustion during my internship in ALSTOM Power Switzerland; to Octavian Stinga and Maria Dumitrescu, with whom I lived during my stay in Munich, for all their support during this time; to Melanie Portz for all the nice time and your support, pio; and to my family, who helped me in all sense to reach this goal. Gracias Totales!

Munich, in February 2012

Luis Tay Wo Chong Hilares

---

## **Abstract**

The flame dynamics of a perfectly premixed axial swirl burner is investigated. The study is based on large eddy simulations (LES) of compressible reacting flow in combination with system identification (SI). The unit impulse response and the transfer function of turbulent swirling flames at various operating conditions are determined. The LES/SI approach is validated against experiment, showing the capability of detecting the impact of variations in thermal boundary conditions, power rating, combustor confinement and swirler position on flame dynamics. Stability limits are analyzed with a low-order thermoacoustic network model. Results indicate that the flame transfer function obtained from single burner combustors should only be used for stability analysis of multi-burner gas turbines provided that boundary conditions and combustor geometries are equivalent.

---

## **Zusammenfassung**

Die Dynamik von perfekt vorgemischten Flammen in einem axialen Drallbrenner wurde untersucht. Die Studie erfolgte anhand von Grobstruktursimulation (LES) kompressibler reaktiver Strömungen in Kombination mit Systemidentifikationsmethoden (SI). Einheitsimpulsantworten und Flammentransferfunktion von turbulenten Drallflammen konnten damit bei unterschiedlichen Betriebsbedingungen bestimmt werden. Der LES/SI Ansatz wurde experimentell validiert und eignet sich somit für die Untersuchung der Auswirkungen von unterschiedlichen thermischen Randbedingungen, Leistung, Brennkammergröße und Drallerzeuger-Position auf die Flammendynamik. Stabilitätsgrenzen wurden mit einem Netzwerk-Modell ermittelt. Die Ergebnisse zeigen, dass Flammentransferfunktionen, die an Einzelbrennern gewonnen wurden, zur Stabilitätsanalyse in Mehrbrenner-Brennkammern nur dann verwendet werden sollten, wenn die Randbedingungen und Brennkammerabmessungen gleichwertig sind.

# Contents

<b>1</b>	<b>Introduction</b>	<b>1</b>
1.1	Combustion Instabilities . . . . .	3
1.2	Overview of the Thesis . . . . .	7
<b>2</b>	<b>Turbulent Reacting Flows</b>	<b>9</b>
2.1	Turbulence . . . . .	9
2.2	The Energy Spectrum and Turbulent Length Scales . . . . .	11
2.2.1	Turbulence Modelling Approaches . . . . .	14
2.3	Turbulent Premixed Combustion . . . . .	17
2.3.1	Combustion Regimes in Turbulent Premixed Combustion	19
2.4	Turbulent Premixed Combustion Modeling using LES . . . . .	21
2.4.1	LES Filtering . . . . .	23
2.4.2	Fundamental Transport Equations for LES Reacting Flows	24
2.4.2.1	Modeling of Subgrid Terms . . . . .	26
2.4.2.1.1	SGS Turbulent Viscosity Models . . . . .	27
2.4.2.2	Source Terms . . . . .	29
2.4.3	LES Premixed Combustion Models . . . . .	29
2.4.3.1	Thickened Flame Combustion Model . . . . .	30
2.4.3.2	Dynamically Thickened Flame Combustion Model	32
<b>3</b>	<b>Response of Premixed Flames to Velocity Disturbances</b>	<b>34</b>
3.1	The Flame Transfer Function . . . . .	35
3.2	Determination of the Flame Transfer Function . . . . .	37
3.3	Additional Parameters Influencing the Flame Response in Pre- mixed Flames . . . . .	41
3.3.1	Influence of Combustor Thermal Boundary Conditions .	43
3.3.2	Influence of Confinement Ratio . . . . .	45

---

3.3.3	Influence of Swirler Position . . . . .	46
3.4	Model of Impulse and Frequency Responses to Axial Velocity and Swirl Fluctuations . . . . .	48
<b>4</b>	<b>System Identification</b>	<b>51</b>
4.1	Background . . . . .	51
4.2	The Wiener Filter . . . . .	56
4.3	The LES/SI Method . . . . .	60
<b>5</b>	<b>Identification of Flame Transfer Functions using LES/SI</b>	<b>63</b>
5.1	Experimental Set-up of the BRS Burner . . . . .	63
5.2	Reference Case with 30 kW of Power Rating . . . . .	65
5.2.1	Numerical Set-up and Boundary Conditions . . . . .	65
5.2.2	Comparison of Mean Flame Heat Release from LES and Experiments . . . . .	67
5.2.3	Comparison of Identified and Experimental Flame Trans- fer Function with 30 kW . . . . .	68
5.2.4	Comparison of Different Excitation Amplitude on Flame Transfer Function Identification . . . . .	73
5.3	Influence of Variation in Power Rating on the Flame Transfer Function . . . . .	75
5.3.1	Comparison of Mean Flow Field and Flame Heat Release from LES and Experiments at 50 kW . . . . .	75
5.3.2	Comparison of Identified and Experimental Flame Trans- fer Function with 50 kW . . . . .	81
5.4	Influence of Thermal Boundary Conditions at the Combustor Wall on the Flame Transfer Function . . . . .	89
5.4.1	Instantaneous Reaction Rate, Temperature and Axial Ve- locity . . . . .	89
5.4.2	Mean Heat Release, Flow Field and Temperature . . . . .	91
5.4.3	Comparison of Identified Flame Transfer Functions . . . . .	93
5.5	Influence of Swirler Position on the Flame Transfer Function . . . . .	94
5.5.1	Mean Flow Field and Heat Release . . . . .	97
5.5.2	Comparison of Identified and Experimental Flame Trans- fer Function with Varied Swirler Position . . . . .	98

5.6	Influence of Combustor Confinement on the Flame Transfer Function . . . . .	105
5.6.1	Mean Flow Field and Heat Release . . . . .	106
5.6.2	Comparison of Flame Transfer Functions . . . . .	109
5.7	Flame Transfer Function Model . . . . .	111
5.7.1	Dependence of Unit Impulse Responses on Thermal Conditions, Combustor Confinement and Power Rating . . .	112
5.7.2	Comparison of Unit Impulse Responses with Swirler at Varied Positions . . . . .	114
<b>6</b>	<b>Stability Analysis with Low-Order Network Models</b>	<b>122</b>
6.1	Linear Acoustic 1D Equations . . . . .	122
6.2	Low-order Network Models . . . . .	125
6.2.1	Flame Transfer Matrix of a Compact Flame . . . . .	126
6.2.2	Use of Experimental Data in Eigenfrequency Analysis (The UIR Method) . . . . .	127
6.3	Stability Analysis of the System . . . . .	128
6.3.1	Network Model of the System . . . . .	128
6.4	Results of the Stability Analysis . . . . .	130
<b>7</b>	<b>Summary and Conclusions</b>	<b>135</b>
<b>8</b>	<b>Outlook</b>	<b>139</b>
<b>A</b>	<b>Appendices</b>	<b>165</b>
A.1	The Rayleigh Criterion . . . . .	165
A.2	Laminar Flame Reaction Kinetics . . . . .	166
A.3	One Step Reaction Mechanism for Methane-air Mixtures . . . . .	168
A.4	Derivation of the Turbulent Kinetic Energy Spectrum . . . . .	169
A.5	Generation of Signals for LES/SI . . . . .	170
A.6	Derivation of the Linearized Acoustic Equations . . . . .	173
A.7	Description of Elements in the Network Model . . . . .	175
A.7.1	Constant Section Duct . . . . .	175
A.7.2	Flame Transfer Matrix of a Compact Flame with a Different Reference Location . . . . .	176
A.7.3	Area change . . . . .	178

---

A.7.4	Inlet . . . . .	180
A.7.5	Outlet . . . . .	180
A.7.6	Swirler . . . . .	181
A.8	FTF at Different Velocity Reference Position with 30 kW and 9.5% of Excitation Amplitude . . . . .	181
A.9	Confidence Analysis of Flame Transfer Function . . . . .	183
A.10	Post-processing Tool for Line-of-sight Heat Release Integration in Tecplot . . . . .	184
A.10.1	Steps before running the Macro . . . . .	185
A.10.2	Macro . . . . .	186

# List of Figures

1.1	Left: Worldwide Gas Turbine Production. Right: Gas turbine production by sector. From [113]. Data: Bill Schmalzer, Forecast Int'l.	2
1.2	Additions to electricity generation capacity (in GW) in USA for 1985-2035. From [1]. . . . .	2
1.3	Influence of temperature on $\text{NO}_x$ and CO emissions. From [118].	3
1.4	Illustration of the feedback process responsible for combustion instability in fully premixed conditions. Adapted from [223]. . .	4
1.5	Left: Damaged combustor liner [70], Right: Combustor damage caused by high-frequency dynamics [185] . . . . .	4
2.1	Measurement of axial velocity on the center line of a turbulent jet. In [164] from the experiment of Tong and Warhaft [203]. . . .	10
2.2	Flow passing a sphere. $\text{Re}=\text{uD}/\nu=20000$ . Modified figure from [172]. Photograph by H. Werle. . . . .	12
2.3	Turbulent jets at different Reynolds numbers: (a) Low Reynolds number, (b) High Reynolds number. Illustration from [201]. . . .	13
2.4	Turbulent kinetic energy spectrum vs. Wave number. The level of computed and modeled scales in RANS, DNS and LES. Adapted from [172]. . . . .	15
2.5	Structure of a laminar premixed flame. . . . .	19
2.6	Turbulent premixed combustion diagram. Adapted from [143] .	22
2.7	(a) Wrinkled flamelet regime, (b) Corrugated flamelet regime, (c) Thin reaction zone. From [115]. . . . .	22
3.1	Overview of interaction mechanisms between heat release and acoustic waves in a fully premixed flame. Adapted from [153] . .	35

3.2	Scheme of determination of the flame transfer function with harmonic excitation. . . . .	38
4.1	Different types of systems. a)SISO, b)MIMO, c)SIMO and d)MISO. Adapted from [80]. . . . .	53
4.2	Unit Impulse Response of a FIR system. . . . .	54
4.3	System for the Identification of the Flame Transfer Function . .	58
4.4	LES/System Identification process . . . . .	61
5.1	Scheme of the BRS burner test rig. The sinter metal plate is installed <b>only</b> for stability analysis. . . . .	64
5.2	Scheme of the numerical set-up of the BRS burner . . . . .	66
5.3	Normalized spatial heat release distribution: (a) OH chemiluminescence from experiments, (b) Averaged LES at nonadiabatic conditions, and (c) at adiabatic conditions. Line-of-sight integrated heat release for simulations. Dump plane of combustor at axial position = 0 m. . . . .	69
5.4	Area normalized axial heat release distribution. . . . .	70
5.5	Flame transfer functions from experiments and LES/SI for case with 30 kW. Excitation=6.5%. . . . .	72
5.6	Heat release ( $\dot{Q}'$ ) and acoustic velocity ( $u_r'$ ) fluctuations at 0 and 70 mm upstream of the burner exit (Dump plane of combustor at $z=0$ mm) normalized by their mean values without filtering for case with 30 kW. . . . .	73
5.7	Power spectrum of acoustic velocity ( $u_r'$ ) fluctuations at 0 and 70 mm upstream of the burner exit and of heat release ( $\dot{Q}'$ ) normalized by their mean values without filtering for case with 30 kW. . . . .	74
5.8	Flame transfer functions from experiments and LES/SI for case with 30 kW with different excitation amplitude. Harmonic excitation at 100 Hz for 6.5% ( $\square$ ) and 9.5% ( $\triangle$ ) of amplitude. . . . .	76
5.9	Amplitudes from the pure-tone Fourier Transform for the normalized heat release and velocity fluctuations for 6.5% and 9.5% of excitation amplitude. . . . .	77

5.10 Mean axial velocity profiles with non-reacting flow (top) and with reacting flow (bottom) at the middle cross plane shown in Fig. 5.2 for 50 kW. o Experiments, - LES. Grey line to indicate zero-axial velocity. . . . .	78
5.11 Contours of mean axial velocity (left) and velocity vectors (right) for non-reacting (top) and reacting (bottom) flow from simulations. Zero-axial velocity isolines in black (left) and yellow (right)	79
5.12 Turbulent kinetic energy profiles with non-reacting flow and reacting flow from simulations at the middle cross plane shown in Fig. 5.2 for 50 kW. . . . .	79
5.13 Normalized spatial heat release distribution for 50 kW: (a) OH chemiluminescence from experiments, (b) Averaged LES at nonadiabatic conditions, and (c) at adiabatic conditions. Line-of-sight integrated heat release for simulations. Dump plane of combustor at axial position = 0 m. . . . .	80
5.14 Area normalized axial heat release distribution for 50 kW. . . . .	81
5.15 Transversal mode on combustion chamber for 50 kW. Contours of rms pressure at cross plane 10mm downstream the burner exit	81
5.16 Flame transfer function from experiments, LES/SI with a single time series (STS), multiple time series (MTS) and single joint time series (SJTS) for 50 KW and different excitation amplitudes. (□): Harmonic excitation at 160 Hz and 6.5% of amplitude. . . . .	83
5.17 Heat release ( $\dot{Q}'$ ) and acoustic velocity ( $u_r'$ ) fluctuations at 70 mm upstream of the burner exit (Dump plane of combustor at $z=0$ mm) normalized by their mean values without filtering for case with 50 kW. . . . .	84
5.18 Snap shot of instantaneous absolute pressure and reaction rate at combustor middle cross plane during excitation with 50 kW. The time of the snap shot is indicated in Fig. 5.17. . . . .	85
5.19 Illustration of single joint time series (SJTS) method . . . . .	86
5.20 Sequence of excitation signals in the single joint time series (SJTS) method for 50 kW and excitation=9.5% amplitude of the mean inlet velocity. . . . .	87

5.21	Instantaneous reaction rate, temperature and axial velocity with adiabatic (top) and nonadiabatic (bottom) combustor walls at 50 kW of power rating, $\phi=0.77$ . Velocity vectors are included on the temperature contours . . . . .	90
5.22	Contours of mean axial velocity (left) and mean temperature with velocity vectors (right) for the 30 kW case. Zero-axial velocity isolines in black. . . . .	92
5.23	Mean axial velocity profiles of reacting flow at various axial positions of the middle cross plane for adiabatic and nonadiabatic wall boundary conditions. 30 kW case. . . . .	92
5.24	Flame transfer functions from LES/SI using adiabatic and nonadiabatic combustor walls with 30 kW. Harmonic excitation at 100 Hz for adiabatic ( $\square$ ) and nonadiabatic ( $\triangle$ ) conditions are also shown. Excitation=9.5%. . . . .	93
5.25	Instantaneous reaction rate for one cycle of a harmonic excitation at 100 Hz using adiabatic and nonadiabatic combustor walls with 30 kW. Excitation=9.5% $\bar{U}$ . . . . .	95
5.26	Scheme of the numerical set-up of the burner with different swirler positions. . . . .	96
5.27	Contours of mean axial velocity at combustor middle cross plane and at position $z=-5$ mm with varied swirler positions. Zero-axial velocity isolines in black. . . . .	97
5.28	Normalized spatial (left) and axial (right) heat release distribution with varied swirler positions . . . . .	98
5.29	Flame transfer functions from LES/SI with the swirler at position 1 and 2 from Fig. 5.26 with 30kW. Harmonic excitation at 100 ( $\square$ ) and 160 Hz ( $\triangle$ ) are also shown. Excitation=9.5%. Experiments with the swirler at position 2 in (o). . . . .	100
5.30	BRS burner with axial swirler at position 2 without combustion chamber . . . . .	101
5.31	Normalized area averaged axial and tangential velocity fluctuations on a cross-section at $z=-10$ mm and $z=-110$ mm with harmonic excitation at 100 Hz. . . . .	103

LIST OF FIGURES

---

5.32 Area averaged tangential velocity on a cross-section at various positions with harmonic excitation at 100 Hz. . . . .	103
5.33 Area averaged axial and tangential velocity fluctuations on a cross-section at at z=-10 mm and z=-110 mm with harmonic excitation at 100 Hz. . . . .	104
5.34 Area averaged swirl number fluctuations on a cross-section at z=-10 mm and z=-110 mm with harmonic excitation at 100 Hz. .	104
5.35 Contours of mean axial velocity (left) and velocity vectors (right): Combustor chamber with 160 x 160 mm of cross section (top), Combustor chamber with 90 x 90 mm of cross section (bottom). Zero-axial velocity isolines in black (left) and yellow (right) . . .	107
5.36 Mean axial velocity profiles with low and high confinement combustors at various positions of the middle cross plane shown in Fig. 5.2. Grey line to indicate zero-axial velocity. . . . .	108
5.37 Mean tangential velocity profiles with low and high confinement combustors at various positions of the middle cross plane shown in Fig. 5.2. . . . .	108
5.38 Turbulent kinetic energy profiles with low and high confinement combustors at various positions of the middle cross plane shown in Fig. 5.2. . . . .	109
5.39 Normalized spatial heat release distribution for 30 kW: (Top) Combustor chamber with 160 x 160 mm of cross section (Bottom) Combustor chamber with 90 x 90 mm of cross section . . .	110
5.40 Area normalized axial heat release distribution with different combustor cross section. . . . .	110
5.41 Flame transfer functions from LES/SI with low and high confinement combustors with 30 kW. Excitation=9.5%. . . . .	112
5.42 UIRs from time lag model. . . . .	115
5.43 Flame transfer function from time lag model. . . . .	116
5.44 UIR from modelled, experimental and identified FTF with 30 kW at varied swirler positions. . . . .	117
5.45 Flame transfer function from LES/SI and time lag model for varied swirler positions with 30kW. . . . .	118
5.46 UIR from time lag model for the experimental FTF at position 2.	120

5.47	FTFs from experiments and from the time lag model for the experimental FTF at position 2. Experiments in (o) . . . . .	120
6.1	Acoustic wave propagation in fluid with mean flow. Adapted from [48]. . . . .	124
6.2	Scheme of a Low-order model. . . . .	125
6.3	UIR Method . . . . .	128
6.4	Low-order model of premix burner test rig. . . . .	129
6.5	Downstream reflection coefficient used in network model . . . .	130
6.6	Eigenfrequencies and cycle increments using experimental and identified FTF in the network model at various combustor lengths with 50 kW. ( $\Delta$ ) Unstable eigenfrequency in experiments.	132
6.7	Low-order model of premix burner test rig with swirler at position 2. . . . .	134
A.1	Evaluation of Rayleigh Criterion with different absolute phase between pressure and heat fluctuations. . . . .	166
A.2	DRBS Input signals in time with different frequency limit. Range: 1 to 20000 iterations . . . . .	172
A.3	DRBS Input signals in time with different frequency limit. Range: 1 to 2000 iterations . . . . .	172
A.4	Power spectrum of DRBS Input signals with different frequency limit. . . . .	173
A.5	Autocorrelation matrix of DRBS Input signals with different frequency limit. . . . .	173
A.6	Scheme for flame transfer matrix with a different velocity reference position for the FTF. Adapted from [83]. . . . .	178
A.7	Scattering Matrix of the swirler including length correction. . . .	182
A.8	Flame transfer functions for case with 30 kW with acoustic velocity ( $u'_r$ ) fluctuations measured at 0 and 70 mm upstream of the burner exit (Dump plane of combustor at $z=0$ mm). Excitation amplitude=9.5%. Experiments for $u_r$ at 70 mm upstream of the burner exit in circles. . . . .	183

LIST OF FIGURES

---

A.9 Flame Transfer Function from experiments and LES/SI for 30 kW. Top: Confidence analysis including a histogram of amplitudes from LES/SI at 100 Hz for 1000 sequences . . . . . 185

# List of Tables

2.1	LES Combustion Models . . . . .	30
5.1	Boundary Conditions . . . . .	67
5.2	Time lag model . . . . .	113
5.3	Time lag model for experimental FTF at position 2 . . . . .	119
6.1	Network Model. . . . .	129
6.2	Stability behavior from experiments and using Network Model (NM) with experimental FTF . . . . .	131
6.3	Stability analysis using Network Model (NM) with identified FTFs	132
6.4	Stability analysis using Network Model (NM) with identified FTFs	133
6.5	Amplitude and phase at the unstable eigenfrequency with dif- ferent conditions at 30 kW . . . . .	133
A.1	One Step Reaction Mechanism . . . . .	168
A.2	Schmid Number . . . . .	169

# Nomenclature

## Latin Characters

$A$	Pre-exponential factor of Arrhenius reaction rate [1/s], Amplitude [-]
$a$	Speed of sound [m/s], coefficient in UIR model [-]
$\langle a_T \rangle$	Effective strain rate [1/s]
$c$	Crosscorrelation [-]
$c_p$	Specific heat capacity at constant pressure [J/(Kg.K)]
$c_v$	Specific heat capacity at constant volume [J/(Kg.K)]
$D_{th}$	Thermal diffusivity [m <sup>2</sup> /s]
$E$	Total energy [J/kg]
$E_a$	Activation Energy [cal/kg]
$E(\kappa)$	Turbulent kinetic energy spectrum [m <sup>3</sup> /s <sup>2</sup> ]
$f$	Frequency [Hz]
$F$	Thickening factor [-]
$G_{\bar{\Delta}_e}$	LES filter [1/m <sup>3</sup> ]
$h_{s,k}$	Sensible enthalpy of species k [J/kg]
$\Delta h_{f,k}^0$	Enthalpy of formation of species k at temperature $T_0 = 0$ K [J/kg]
$k$	Turbulent kinetic energy [m <sup>2</sup> /s <sup>2</sup> ]
$k_x$	Acoustic wave number [1/m]
$l$	Length [m]
$L$	Maximum index of the UIR coefficients [-]
$n$	Interaction Index [-]
$Q$	Heat release [W]
$r$	Radius [m], Response [-]
$R$	Universal gas constant [ J/(mol.K) ]

---

$R_{ij}$	Two-point velocity correlation [ $\text{m}^2/\text{s}^2$ ]
$s$	Signal [-]
$s_L$	Laminar flame speed [ $\text{m}/\text{s}$ ]
$s_L^0$	Unstretched laminar flame speed [ $\text{m}/\text{s}$ ]
$S$	Entropy [ $\text{J}/\text{K}$ ]
$t$	Time [ $\text{s}$ ]
$\mathcal{T}$	Time interval [ $\text{s}$ ]
$T$	Temperature [ $\text{K}$ ]
$u$	Velocity [ $\text{m}/\text{s}$ ]
$V_i^c$	Correction velocity in species equation [ $\text{m}/\text{s}$ ]
$W$	Molecular weight [ $\text{mol}/\text{g}$ ]
$Y$	Mass fraction [-]
$\mathcal{Y}_k$	Symbol for species k [-]

### Greek Characters

$\alpha$	Model constant in the TFM [-]
$\beta$	Model constant in the DTFM [-]
$\delta_L$	Laminar flame thickness [ $\text{m}$ ]
$\delta_{ij}$	Kronecker delta [-]
$\Delta_e$	Scale characteristic of the mesh [ $\text{m}$ ]
$\epsilon$	Turbulent dissipation rate [ $\text{m}^2/\text{s}^3$ ]
$\Gamma$	Autocorrelation [-]
$\gamma$	Ratio of specific heats ( $c_p/c_v$ ) [-]
$\kappa$	Wave number [ $1/\text{m}$ ]
$\lambda$	Thermal conductivity [ $\text{J}/\text{kg}\cdot\text{K}$ ]
$\nu$	Kinematic viscosity [ $\text{m}^2/\text{s}$ ]
$\eta$	Kolgomorov length scale [ $\text{m}$ ]
$\omega$	Angular Frequency= $2\pi f$ [ $\text{rad}/\text{s}$ ]
$\Omega$	Modified reaction rate sensor [-]
$\phi$	Equivalence ratio [-]
$\Phi$	Velocity potential [ $\text{m}^2/\text{s}$ ]
$\rho$	Density [ $\text{kg}/\text{m}^3$ ]

## Nomenclature

---

$\psi$	Model constant of the DTFM [-]
$\nu$	Molar stoichiometric coefficient[-]
$\varepsilon$	Efficiency function [-]
$\Xi$	Wrinkling factor [-]
$\zeta$	Loss coefficient [-]

## Superscripts

'	Fluctuation
-	LES filtering
^	Complex number
~	Mass-weighted Favre filtering
0	Unthickened flame
1	Thickened flame
'	Fluctuation
$t$	Subgrid term

## Indices

ax	Axial
bexit	Burner exit
cc	Combustion chamber
chem	Chemical
cut	Cut-off wave number
$d$	Burnt conditions
ext	External
int	Internal
$F$	Fuel
$f$	Flame
$K$	Kolgomorov
$L$	Laminar

<i>M</i>	Mixture
<i>MF</i>	Mass Flow
<i>O</i>	Oxidizer
prop	Propagation
<i>r</i>	Reference
stoich	Stoichiometric
<i>S</i>	Swirl
<i>t</i>	Turbulent
tan	Tangential
<i>u</i>	Unburnt conditions
$\lambda$	Wave length

### **Abbreviations**

<i>CSCF</i>	Collection of Small Conical Flames
<i>CFL</i>	Courant–Friedrichs–Lewy
<i>DNS</i>	Direct Numerical Simulation
<i>DTFM</i>	Dynamically Thickened Flame Model
<i>FAR</i>	Fuel–air ratio
<i>FDF</i>	Flame Describing Function
<i>FEM</i>	Finite Element Method
<i>FIR</i>	Finite Impulse Response
<i>FVM</i>	Finite Volume Method
<i>FTF</i>	Flame Transfer Function
<i>HC</i>	High Confinement
<i>IC</i>	Initial Condition
<i>LES</i>	Large Eddy Simulation
<i>LC</i>	Low Confinement
<i>LOS</i>	Line-of-Sight
<i>MIMO</i>	Multiple-Input Multiple-Output
<i>MISO</i>	Multiple-Input Single-Output
<i>PT</i>	Pure tone
<i>P1</i>	Position 1

<i>P2</i>	Position 2
<i>RANS</i>	Reynolds Averaged Navier-Stokes
<i>SGS</i>	Sub-Grid Scale
<i>SI</i>	System Identification
<i>SISO</i>	Single-Input Single-Output
<i>TFM</i>	Thickened Flame Model
<i>UIR</i>	Unit Impulse Response

### **Non-dimensional Numbers**

Da	Damhkohler Number
Ka	Karlovitz Number
M	Mach Number
$P_r$	Prandtl Number
Re	Reynolds Number
$S_c$	Schmid Number

### **Scalar-vectors-tensors**

<i>u</i>	Scalar
<b>u</b>	Vector
$u_i$	Component i of the vector <b>u</b>

### **Operators**

$\langle \rangle$	Reynolds averaging
$\cdot$	Scalar product
sign	Sign function



# 1 Introduction

Gas turbines have been used for energy production and jet propulsion for decades. During this time, significant technological developments have been achieved as the increase in efficiency<sup>1</sup> [16], power output, thrust, etc. Even under the high prices of fuel, and the strong focus on renewable energy nowadays, the gas turbine market has a strong projection as shown in Fig. 1.1.

In the energy production sector, combined cycle power plants present some advantages [16] to other kind of generation systems based on nuclear, wind or solar energy. They have low construction costs<sup>2</sup>, load flexibility, can be built quickly, and are very efficient [16,92]. Fossil-fuel (especially natural gas) power plants are expected to continue as one of the major generators of electricity into the next decades (e.g., see Fig. 1.2 for the additions to electricity generation capacity in USA by sources).

In the combustion process in gas turbines, combustion products such as carbon dioxide ( $\text{CO}_2$ ) and pollutants (as carbon monoxide ( $\text{CO}$ ), oxides of nitrogen ( $\text{NO}_x$ )) are created due to the chemical reactions inside the combustor.  $\text{CO}_2$  and  $\text{CH}_4$  are greenhouse gases that contribute to the global warming, which can be reduced by improving the efficiency of the machine [120]. For the pollutants,  $\text{NO}_x$  is mainly created due to the high combustion temperatures and contributes to the production of smog and acid rain;  $\text{CO}$  is created from incomplete combustion (for example, by improper fuel/air ratios or mixing [220], insufficient residence time [118], etc.) or by dissociation of  $\text{CO}_2$  at very high temperatures [118], and has consequences on human health [118] as the reduction of the capacity of the blood to absorb oxygen, production of asphyxiation, etc. To reduce the environmental impact from the pollutants,

---

<sup>1</sup>For example, the first electrical gas turbine power plant produced by Brown Boveri in 1939 produced 4 MW of output with a thermal efficiency of 18% [112], while nowadays the Siemens SGT5-8000H can produce 375 MW with an efficiency of 40% in simple cycle and 60% in combined cycle operation

<sup>2</sup>A good comparison of the production prices can be found in the report by S. Kaplan [92]

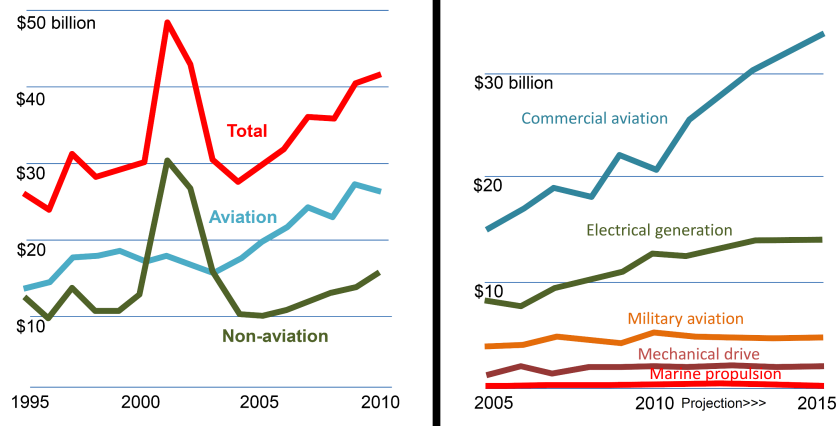


**Figure 1.1:** Left: Worldwide Gas Turbine Production. Right: Gas turbine production by sector. From [113]. Data: Bill Schmalzer, Forecast Int'l.

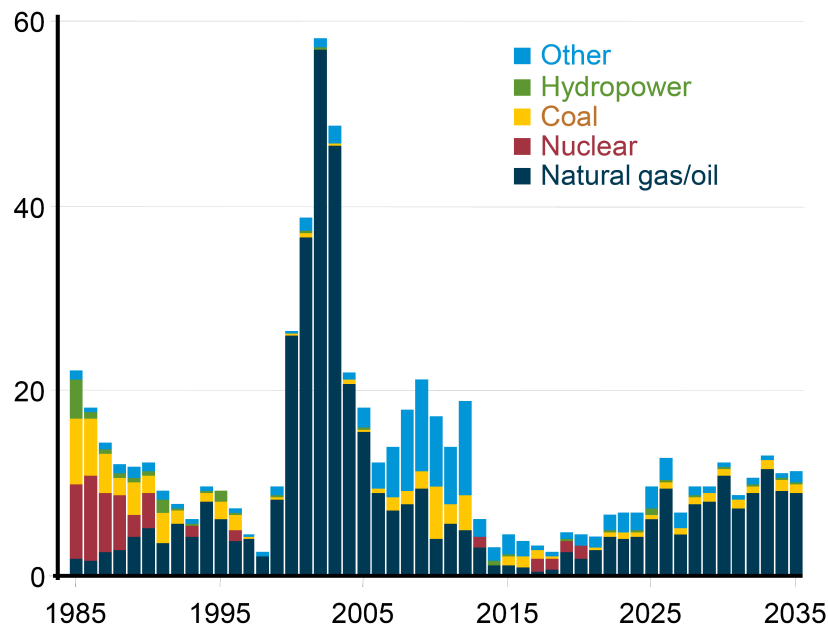


**Figure 1.2:** Additions to electricity generation capacity (in GW) in USA for 1985-2035. From [1].

stringent emission regulations have been established for gas turbines. In order to comply with these regulations, lean premixed combustion technology (see section 2.3 for more details about premixed combustion), which offers

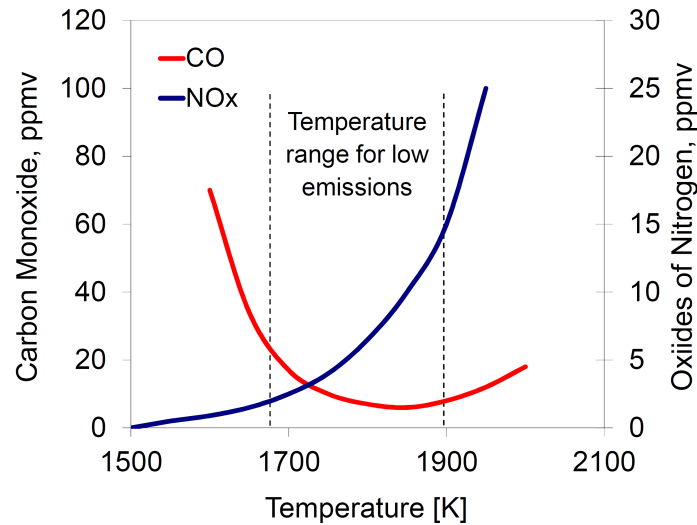


**Figure 1.3:** Influence of temperature on  $\text{NO}_x$  and CO emissions. From [118].

a number of advantages in controlling emission levels, has been introduced. Using this technology, the combustors operate with excess air to reduce the combustion temperature and the production of  $\text{NO}_x$  as shown in Fig. 1.3. Nevertheless at low combustion temperatures, the level of CO increases due to the slow rates of oxidation [118]. Thus, there is a range of operating temperatures where the levels of emissions are according to the regulations.

However, this mode of operation makes the combustor prone to blow-out, flashback and in particular to combustion instabilities [37, 95].

## 1.1 Combustion Instabilities

Considering fully premixed conditions (without mixture inhomogeneities) as in this study, combustion instabilities would appear due to a feedback loop between flow perturbations, heat release and acoustic oscillations [223] (see Fig. 1.4). So, if the energy from the driving mechanisms of oscillations (e.g., the flame adds energy to acoustic field when the Rayleigh criterion is fulfilled (see Appendix A.1)) exceeds the energy losses from the damping mechanisms (e.g., from viscosity, heat transfer, sound radiation through boundaries, etc.),

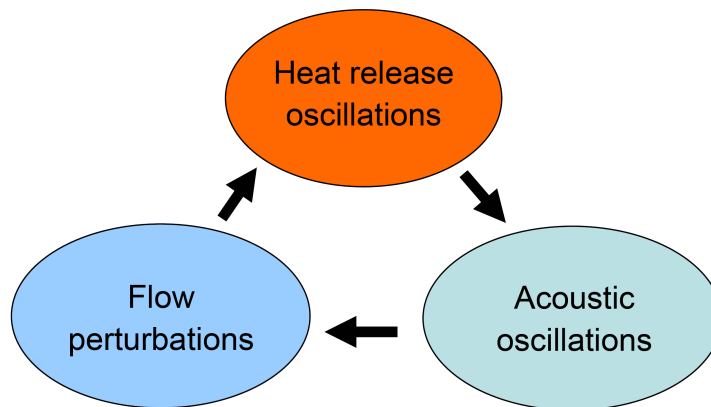


**Figure 1.4:** Illustration of the feedback process responsible for combustion instability in fully premixed conditions. Adapted from [223].

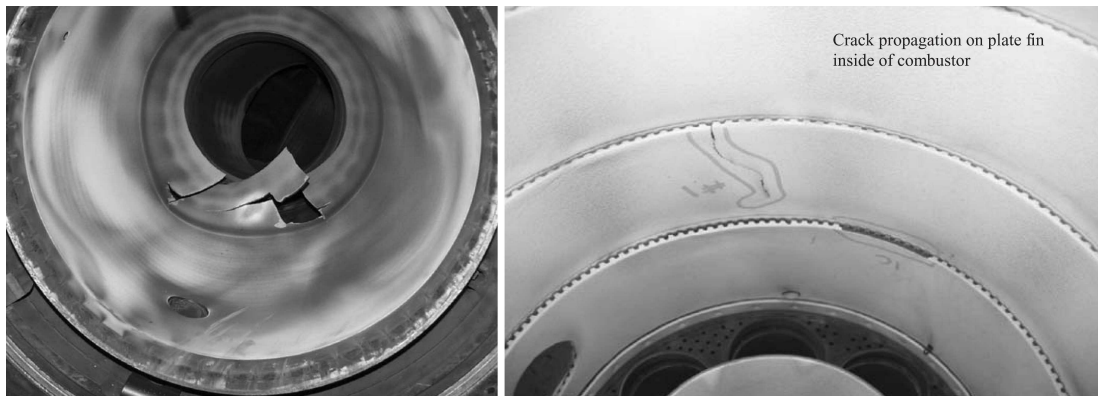


**Figure 1.5:** Left: Damaged combustor liner [70], Right: Combustor damage caused by high-frequency dynamics [185]

an instability can appear. A good review of the different driving and damping mechanisms of oscillations is presented in [223]. This process would lead to a unstable feedback cycle, resulting on large amplitude pressure and velocity oscillations, structural damage (see Fig. 1.5), etc.

To prevent the appearance of combustion instabilities, it is desirable to carry out a stability analysis of the combustion system early in the design process. Different tools (e.g., Computational Fluid Dynamics (CFD) [126, 184], solution of the Linearized Euler Equations with finite element (FEM) or finite volume (FVM) [216] methods, acoustic network models [116, 117, 152, 156], etc.) may

be used for this task. The idea is to see if the small perturbations that can appear in our system would grow in time, leading to an unstable point of the combustion system. In the case of CFD simulations, Large Eddy Simulation (LES) is now established as a powerful, albeit computationally expensive, tool for the study of turbulent (reacting) flows. LES has shown its potential for laboratory and industry scale configurations [31, 66, 152, 171, 175, 184, 199]. LES makes possible a more accurate description of the turbulence-flame interaction than conventional Reynolds-Averaged Navier-Stokes simulations (RANS, or URANS for “unsteady” or transient cases), as the large turbulent scales are resolved. Despite the possibility to get a good reproduction of the flame dynamics, the use of only LES for stability analysis presents some limitations as [106, 154]:

- Only the dominant unstable mode can be detected. Unstable modes with smaller growth rates or stable modes cannot be identified.
- Huge computational times and resources are needed due to the small time steps and mesh sizes.
- The use of appropriate boundary conditions with the correct acoustic impedance (reflection coefficient) to acoustic waves is very difficult. A way to overcome this problem is proposed by Roux et. al [171] by modeling also the surroundings of the combustion chamber, pushing the outlet boundary conditions as far away as possible. In this way, the acoustic waves are properly transmitted and reflected at the outlet of the combustion chamber without specifying an impedance, because this part is not a boundary condition but part of the computational domain. Nevertheless, the computational demands are increased using this approach. If the impedance is known, impedance acoustic boundary conditions as the ones in [86, 89, 179] can be applied.

Other methods for stability analysis (e.g. in network models) require information as input of how the flame responds to the perturbations. This information may be provided by the flame transfer function (FTF). The flame transfer function relates in the frequency domain the fluctuations upstream of the flame to

fluctuations of the heat release . Flame transfer functions may be obtained experimentally, using velocity or pressure sensors in combination with chemiluminescence as an indicator of heat release in the flame (see e.g. [9, 78, 96, 137]). Unfortunately, the experimental determination of FTFs for configurations of technical interest is very difficult and costly. (Semi-)analytical models for the FTF have been also proposed (see e.g. [78, 85, 116, 181]). However, it is in general difficult to predict flame responses from first principles. Alternatively, it is possible to determine the FTF with CFD: First an unsteady CFD simulation is performed to generate time series of fluctuating velocity and heat release rate. Then the FTF is reconstructed from the data using methods from system identification (SI) [66, 85, 158, 160, 199]. These methods should provide information about the flame dynamics with a reasonable accuracy to proceed to the stability analysis. Having an incorrect description of the flame dynamics can lead to a wrong prediction of the stability behavior [198]. Thus, it is important to validate the modeling approaches used to obtain the flame transfer function.

A strategy of “*Divide and Conquer*” [106, 154, 156] is applied in this work, using a hybrid methodology for the stability analysis. The methodology is based on the description of the different elements of the system in an acoustic network model, providing the information about the flame response from LES or experiments. In this way, the system and boundary conditions are described in a suitable way, including an appropriate description of the flame dynamics, and reducing the demand of resources for the analysis.

Furthermore, as experimental investigations on multi-burner industrial gas turbines at operating conditions are very costly, they are often carried out in a single burner configuration. However, for annular combustors, single burner experiments are in general not representative of machine conditions due to variations in combustor wall temperatures, combustor cross section size, operating pressure, flame-flame interaction between adjacent burners, etc. Such variations in general influence both flow field and flame shape, changing the flame dynamics, and under certain conditions the stability behavior of the system.

## 1.2 Overview of the Thesis

In this study, the flame dynamics in a perfectly premixed axial swirl burner is investigated. LES in combination with system identification methods is applied to obtain the flame transfer function. The validation of the method with experimental data is carried out in a first step. Then the potential of the LES/SI approach to detect the impact of different conditions interacting with the flame on the FTF is investigated and compared with the reference case. The influence of the differences in the flame transfer functions on stability limits is analyzed with a low-order thermoacoustic model.

In *Chapter 2*, an overview of concepts in turbulent combustion, as the energy spectrum and combustion regimes, is presented. This is followed by the fundamental governing equations for reacting flow LES used in the code AVBP. Finally, the Thickened Flame and Dynamically Thickened Flame combustion models used in this study are presented.

In *Chapter 3*, the flame dynamics of premixed flames submitted to velocity disturbances is reviewed, presenting the definition of the flame transfer function and the different methods to obtain it. The influences of various parameters on the flame transfer function are shown. At the end of the chapter, the model of the flame transfer function produced by axial velocity and swirl fluctuations from Komarek and Polifke [103] is shown to describe the flame dynamics by the unit impulse responses of the different perturbations.

In *Chapter 4*, background about system identification for linear-time invariant systems is presented, followed by the description and derivation of the Wiener Filter. Finally, the LES/SI method for the identification of the flame transfer function is described.

In *Chapter 5*, results from the identification of the flame transfer functions obtained using the LES/SI method for different conditions are presented. First, the experimental set-up developed by Komarek [103] is introduced; followed by the validation of the method with experiments. After that, the geometrical and operating conditions in the combustor and burner are varied by changing the level of heat transfer in thermal boundary conditions at the combus-

tor walls, increasing of combustor cross section area, changing the position of the swirler and increasing the power rating, to study the impact of these variations on the flame dynamics. Then, the observed differences in flow field and flame shape are discussed in relation to the unit impulse response of the flame and a FTF model.

In *Chapter 6*, background about 1D acoustics and network models is presented. The stability analysis of the combustion system with the different conditions investigated on Chapter 5 was carried out using a network model tool to evaluate and compare their eigenfrequencies and cycle increments for different combustor lengths. Results of the stability analysis for the reference case are validated with experiments.

The summary and conclusions of the work are presented in *Chapter 7*, followed by the outlook of the work in *Chapter 8*.

All the experimental data was carried out at the Lehrstuhl für Thermodynamik in TU München by T. Komarek [104].

## 2 Turbulent Reacting Flows

In turbulent reacting flows, the interaction of different complex phenomena as turbulence and chemical reactions is present in combination with mass, momentum and heat transfer. The fundamental concepts in turbulent combustion are reviewed in sections 2.1 and 2.3, followed by the fundamental governing equations in a LES context. Finally, an overview of turbulent premixed combustion modeling using LES is presented in section 2.4.

### 2.1 Turbulence

Most flows in engineering applications are turbulent. Turbulence is still one of the most challenging and unsolved problems in physics, and its complexity increases under the presence of chemical reactions [115]. Turbulent flows are unsteady by nature with the presence of continuous fluctuations of velocity, which can produce fluctuations in other scalars as temperature, density and mixture composition [214]. These fluctuations are generated by the presence of vortices (called also eddies) with different scales (sizes) in the flow. These eddies are originated by the development of an instability (e.g., hydrodynamic instabilities associated with sheared flows [208]). If the instability is damped (e.g., by viscous effects), the fluctuations produced by the instability would decay to a steady condition of a laminar flow.

An indicator of the tendency for a flow to become turbulent [115] is the Reynolds number (Re) [169]. It is defined by the ratio of the inertial forces (which are related to convective effects) to the viscous forces in the flow:

$$\text{Re} = \frac{ul}{\nu}, \quad (2.1)$$

where  $\nu$ ,  $u$  and  $l$  are the kinematic viscosity, the characteristic velocity and

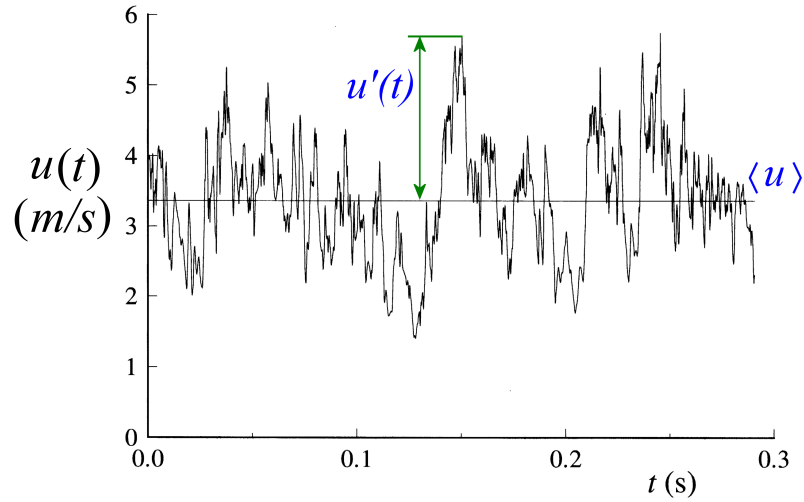


**Figure 2.1:** Measurement of axial velocity on the center line of a turbulent jet. In [164] from the experiment of Tong and Warhaft [203].

the characteristic length scale of the flow (which depends of the geometry), respectively. When the Reynolds number exceeds a certain value (called critical Reynolds number), the flow starts a transition process and the fluctuations produced by the instability would grow in a chaotic manner leading to the development of a fully turbulent flow. The inertial forces from convection have a “destabilization” effect, while the viscous forces try to “stabilize” the flow from the instability [214]. As illustration, a typical measurement velocity in a turbulent flow is shown in Fig. 2.1.

The turbulent flow field can be characterized by the Reynolds decomposition in its steady mean velocity  $\langle u \rangle$  obtained from a statistical average, and a fluctuating contribution  $u'$  superimposed on it [208]:

$$u(t) = \langle u \rangle + u'(t), \quad (2.2)$$

$$\langle u \rangle = \frac{1}{\mathcal{T}} \int_t^{t+\mathcal{T}} u(t) dt, \quad (2.3)$$

$$\langle u'(t) \rangle = 0. \quad (2.4)$$

where  $\mathcal{T}$  is a time interval much longer than all the time scales of the turbulent flow [145].

The kinetic energy (per unit mass) produced by the instantaneous velocity turbulent fluctuations is defined by:

$$k \equiv \frac{1}{2} u'_i u'_i = \frac{1}{2} (u'^2_x + u'^2_y + u'^2_z). \quad (2.5)$$

The mean value of the instantaneous kinetic energy of the turbulent fluctuations is called the turbulent kinetic energy [164] and defined by:

$$\langle k \rangle \equiv \frac{1}{2} \langle u'_i u'_i \rangle = \frac{1}{2} (\langle u'^2_x \rangle + \langle u'^2_y \rangle + \langle u'^2_z \rangle). \quad (2.6)$$

## 2.2 The Energy Spectrum and Turbulent Length Scales

Eddies with various length scales are present in turbulent flows producing different amounts of kinetic energy. An example to illustrate the variation of scales in a turbulent flow is shown in Figs. 2.2 and 2.3. Inside the flow, the eddies are mixed and continually forming and breaking down. In this process, the largest scale eddies interact with and extract energy from the mean flow mainly by vortex stretching (due to mean velocity gradients) [201, 208] and transfer it to the smaller scales. The large eddies break down into smaller ones, which break down into yet smaller eddies, until they become small enough that viscous dissipation effects dominate and simply dissipate into internal energy [130]. This concept, known also as the energy cascade, was introduced by Richardson in 1922 [170]. He summarized this process with the following verse:

*Big whorls have little whorls,  
Which feed on their velocity,  
And little whorls have lesser whorls,  
And so on to viscosity.*

From the concept of energy cascade, the turbulent kinetic energy (Eq. (2.6)) depends on the energy produced by the different eddies. The contribution of the different scales on the turbulent kinetic energy can be defined by its spectrum in wave number space  $E(\kappa)$ . Then the turbulent kinetic energy is

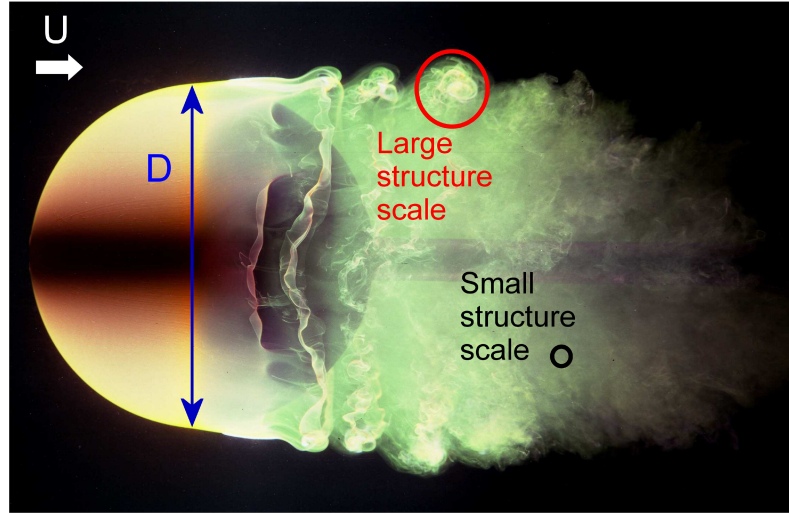


**Figure 2.2:** Flow passing a sphere.  $Re=uD/\nu=20000$ . Modified figure from [172]. Photograph by H. Werle.

obtained by:

$$\langle k \rangle = \frac{1}{2} \langle u'^2 \rangle = \int_0^\infty E(\kappa) d\kappa. \quad (2.7)$$

The derivation of Eq. (2.7) is presented in Appendix A.4.

An illustration of the turbulent kinetic energy spectrum is shown in Fig. 2.4. Different subranges are defined according of how the energy is provided and dissipated:

- The *energy containing range*, which contains the largest eddy scales and concentrations of turbulent kinetic energy. In this range, mean flow effects are dominant with an exchange of energy from the mean flow to the turbulence. This range is not universal and usually modeled by a spectrum taken to be proportional to  $\kappa^{-4}$  [172]. A characteristic scale called the integral length scale ( $l_t$ ) is in this range. It is considered as the size of the eddies containing most of the turbulent kinetic energy [143]. From the two point velocity correlation:

$$R_{ij}(\mathbf{x}, t) = \left\langle u'_i(\mathbf{x}_0, t) u'_j(\mathbf{x}_0 + \mathbf{x}, t) \right\rangle, \quad (2.8)$$

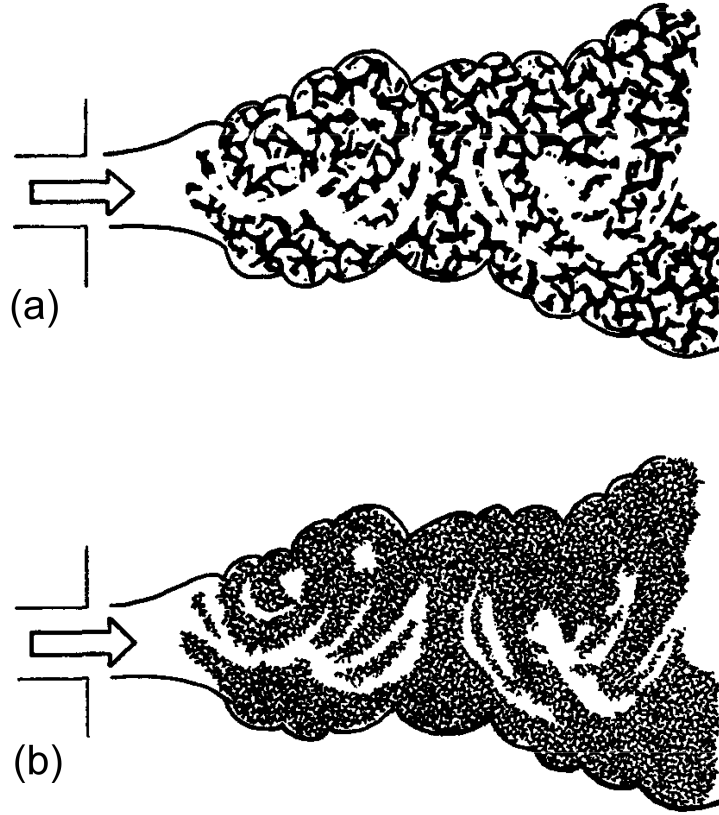


**Figure 2.3:** Turbulent jets at different Reynolds numbers: (a) Low Reynolds number, (b) High Reynolds number. Illustration from [201].

and, considering that for isotropic turbulence the position  $\mathbf{x}_0$  is arbitrary and that  $r = |\mathbf{x}|$ , the integral length scale is defined by [143]:

$$l_t = \int_0^\infty f(r, t) dr, \quad (2.9)$$

$$f(r, t) = \frac{R(r, t)}{\langle u'^2(t) \rangle}. \quad (2.10)$$

- The *inertial subrange*, which is the largest range of the turbulence spectrum. In this range, based on the Kolgomorov hypothesis [101], at sufficient high Reynolds number the small-scale turbulent motions are statistically isotropic [164] with the energy transfer rate independent of the molecular viscosity [115] and equal to the dissipation rate ( $\epsilon$ ). The dissipation rate is proportional to the turbulent kinetic energy divided by its

time scale [174]:

$$\epsilon \sim \frac{u'(l)^2}{l/u'(l)} = \frac{u'(l)^3}{l}, \quad (2.11)$$

where  $u'(l)$  and  $l$  are the velocity and length scale of an eddy, respectively. The dissipation rate is constant in this range and the energy spectrum  $E(\kappa)$  decreases following the  $\kappa^{-5/3}$  relation (derived by Kolgomorov [101] from dimensional analysis) and defined by:

$$E(\kappa) \sim C\kappa^{-5/3}\epsilon^{2/3}. \quad (2.12)$$

- The *dissipation range* corresponds to the domain where the turbulent kinetic energy per unit wave number exhibits a strong decrement. In this range, the turbulent kinetic energy is transferred to the mean flow by viscous effects [42]. With the increase of wave number, the Reynolds number decreases (due to the smaller scales) until a point that the turbulent kinetic energy is dissipated into heat. This occurs in the smallest turbulent scale called the Kolgomorov length scale ( $\eta_K$ ) and defined by:

$$\eta_K = (\nu^3/\epsilon)^{1/4}. \quad (2.13)$$

The Reynolds number produced by such an eddy with a velocity fluctuation  $u'_K$  is equal to one:

$$\text{Re}_K = \frac{u'_K \eta_K}{\nu} = 1. \quad (2.14)$$

In Fig. 2.4, other scales are also defined (see [164]). The length scale  $l_{EI}$  is defined as the length scale that separates the *energy containing range* with the *inertial subrange*. It has dimensions close to  $l_t/6$ . The length scale  $l_{DI}$  (with  $l_{DI} \approx 60\eta_K$  [164]) divides the inertial subrange and the dissipation range inside the universal equilibrium range.

### 2.2.1 Turbulence Modelling Approaches

To simulate turbulent flows with CFD, the different length scales need to be resolved or modeled. An eddy can be resolved if the mesh size used for the

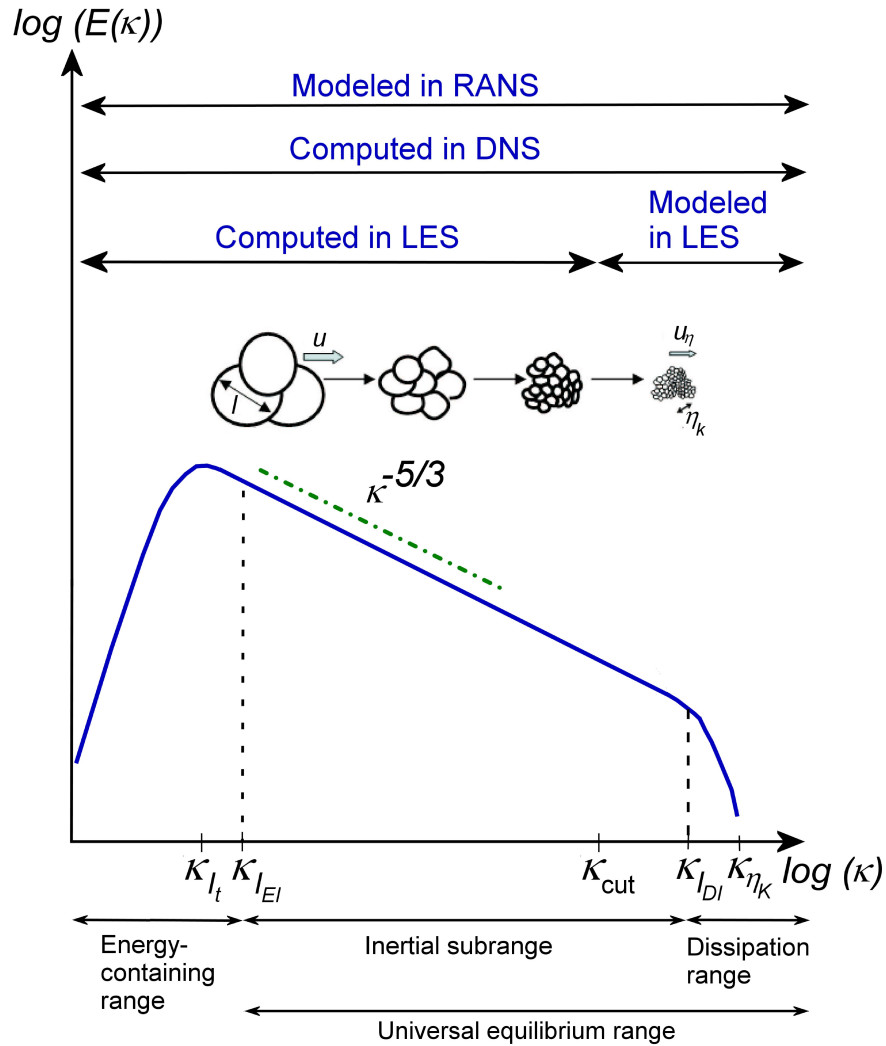


**Figure 2.4:** Turbulent kinetic energy spectrum vs. Wave number. The level of computed and modeled scales in RANS, DNS and LES. Adapted from [172].

simulation is smaller than the size of the eddy. If not, a model needs to be applied to describe the turbulence. Three different approaches for turbulence modeling are distinguished, according to the level of resolution of the turbulent scales as shown in Fig. 2.4:

- Direct Numerical Simulation (DNS): In DNS, all the scales involved in the turbulent spectrum are resolved. This implies the solution of the full

instantaneous Navier-Stokes equations without any turbulence model [152]. The problem of using this approach is the requirement of high computational resources. As the smallest scales (the Kolmogorov scales) should be resolved considering at least 2 cells [164], the mesh size for these eddies is much smaller than the geometrical lengths of practical applications. Considering the integral length scale as a reference measure, the number of nodes required for a DNS simulation in a flow in  $D$  dimensions is [115]:

$$N_{nodes} = \left( \frac{l_t}{\eta_K} \right)^D = \text{Re}_t^{\frac{3}{4}D}, \quad (2.15)$$

where:

$$\text{Re}_t = \frac{u' l_t}{\nu}. \quad (2.16)$$

is the turbulent Reynolds number. Considering the high Reynolds numbers in technical applications, its use is still limited to flows with low Reynolds numbers.

- **Reynolds Averaged Navier-Stokes (RANS) Simulations:** RANS simulations are based on the statistical description of the flow. In RANS, the instantaneous balance equations are Reynolds-averaged to describe the evolution of the mean quantities, which are of most interest in technical applications. From the averaging procedure, some terms involving the turbulent fluctuations appear (e.g., the Reynolds stress term, scalar turbulent fluxes, etc.). The effect of turbulent fluctuations must be modeled to close the system. This implies that the various scales on the turbulent kinetic energy spectrum are modeled as shown in Fig. 2.4. Various turbulence models for the Reynolds stresses have been derived and used frequently in different applications. Examples of these models are the two-equation models (e.g.  $k-\epsilon$  [88],  $k-\omega$  [218], SST [128], etc.), the Reynolds Stress closures [114, 190], etc. In RANS it is possible to use meshes with a size much bigger than in DNS, being computationally affordable to simulate applications with high turbulent flows. However, since only statistical information is extracted from the simulations, the intermittency of the turbulence is not captured, not allowing an accurate description of highly unsteady flows [172].

- **Large Eddy Simulations (LES):** LES is a technique intermediate between DNS and RANS. In LES, the large turbulent scales (which are affected by the flow geometry and are not universal [164]) are calculated explicitly, whereas the effects of smaller ones (which are nearly isotropic and universal) are modeled using subgrid closures. To separate the large from the small scales, LES is based on a filtering operation considering a filter width. The filter function determines the size and structure of the small scales [145]. In Fig. 2.4, the spectrum of resolved and modeled scales is separated by a cut-off wave number defined by:

$$\kappa_{\text{cut}} = \frac{\pi}{\bar{\Delta}_e}. \quad (2.17)$$

where  $\bar{\Delta}_e$  is a scale characteristic of the mesh. It is usually defined based on the cell volume ( $V_{\text{cell}}$ ) by:

$$\bar{\Delta}_e = V_{\text{cell}}^{1/3}. \quad (2.18)$$

Details about the filtering procedure are shown in section 2.4.1. As the large scales are the ones resolved, and usually of most interest in industrial applications, it allows the use of a mesh with a smaller size than one for DNS, reducing the computational effort.

## 2.3 Turbulent Premixed Combustion

Turbulent combustion results from the interaction between chemical reactions and turbulence [152]. The different turbulent eddies interact with a flame produced by an exothermic chemical reaction between a fuel and an oxidizer. The flame can be categorized depending on their mixing process before ignition as follows:

- **Non-premixed Flames:** In this kind of flames, also called diffusion flames, fuel and oxidizer are introduced separately before combustion and brought together, creating a zone where mixing between them takes place by convective and diffusion effects during the combustion process [115]. The physical process was described by Warnatz et al. [214]

as the process where fuel and oxidizer diffuse to the flame zone where chemical kinetics converts them into products. The energy released and the combustion products diffuse away from the flame zone into the fuel and the oxidizer.

- **Premixed Flames:** In premixed Flames, the mixture is well mixed before combustion. The flame is present in a thin reaction zone separating reactants and products, and it can be described as a reaction zone that moves with respect to the fuel mixture supporting it [46]. The structure of a laminar premix flame is illustrated in Fig. 2.5. Under the presence of turbulence, the different zones on the flame are affected, changing the flame structure depending of the turbulence level and mixture characteristics. The different regimes of turbulent premixed flames are detailed in section 2.3.1. Depending on the equivalence ratio ( $\phi$ ) of the mixtures of fuel and air, combustion in premixed flames is defined in rich ( $\phi > 1$ ), stoichiometric ( $\phi = 1$ ) and lean ( $\phi < 1$ ) combustion. The equivalence ratio ( $\phi$ ) is defined by the ratio of fuel–air ratio (FAR) of the mixture with the stoichiometric fuel–air ratio:

$$\phi = \frac{FAR}{FAR_{\text{stoich}}}, \quad (2.19)$$

$$FAR = \frac{\text{mass of fuel}}{\text{mass of air}}. \quad (2.20)$$

- **Partially-Premixed Flames:** In partially-premixed flames, the fuel and oxidizer are introduced separately as in non-premixed Flames, but the mixing process starts before combustion. The mixing is not perfect as in premixed flames and the flame is in an inhomogeneous fuel mixture. This kind of flame is usually present in technical applications as in aircraft gas turbines, direct injection gasoline engines, etc. [143].

As this work is focused only in turbulent premixed flames, only this kind of flame will be discussed in the following. An extended information about turbulent non-premixed and partially-premixed combustion theory and modeling is shown in [115, 143, 148, 152, 214].

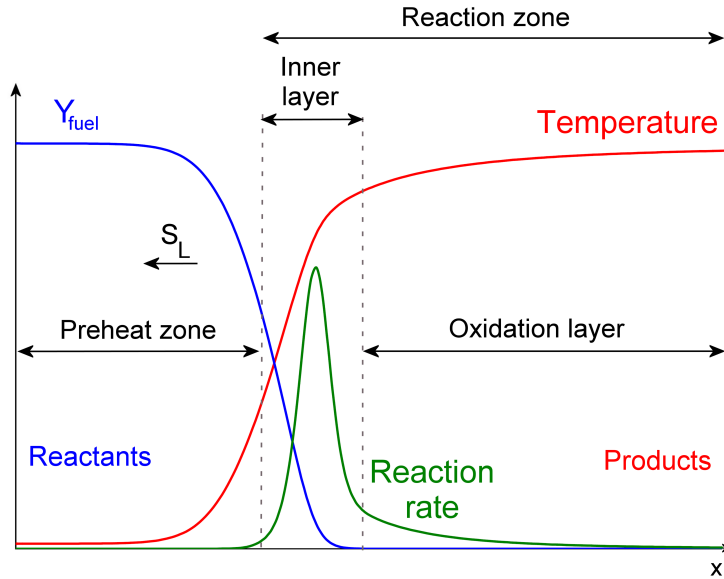


**Figure 2.5:** Structure of a laminar premixed flame.

### 2.3.1 Combustion Regimes in Turbulent Premixed Combustion

As indicated before, under the presence of turbulence, the flame structure is modified compared to a laminar flame. The main effect from turbulence is to deform the flame (mainly by the large scales), increasing its area. This is called the *wrinkling* of the flame. This results in an increase of the reaction rate and heat release compared to a laminar flame. To characterize the interaction between flame and turbulence in premixed turbulent combustion, regime diagrams are commonly used. These diagrams take into account the level of turbulence and scales in the flow and the thermo-chemical characteristics of the mixture to characterize the behavior of the flame. These diagrams are defined by different non-dimensional numbers as the turbulent Reynolds, Damkohler and Karlovitz numbers. The turbulent Reynolds number was defined previously in Eq. (2.16). The turbulent Damkohler number is defined as the ratio of the turbulent time produced by the large eddies to the chemical time of a laminar flame, and expressed by:

$$\text{Da}_t = \frac{t_t}{t_{chem}} = \frac{l_t / u'}{\delta_L / s_L}. \quad (2.21)$$

where  $s_L$  and  $\delta_L$  are the laminar flame speed and flame thickness, respectively.  $\delta_L$  is usually considered as the diffusion flame thickness defined by [152]:

$$\delta_L = \frac{D_{th_u}}{s_L}, \quad (2.22)$$

where  $D_{th_u}$  is the thermal diffusivity at unburnt conditions. The turbulent Damkohler number is an indicator if the chemical reaction rate is faster or smaller than the mixing rates from turbulence [204]. The turbulent Karlovitz number is defined as the ratio of the chemical time to the Kolmogorov time and defined by [152]:

$$\text{Ka}_t = \frac{\delta_L/s_L}{\eta/u'_K} = \frac{\delta_L^2}{\eta^2}. \quad (2.23)$$

It is an indicator if the smallest eddies have any influence on the flame front [42]. It also relates the flame thickness ( $\delta_L$ ) to the Kolmogorov length scale ( $\eta$ ). Another Karlovitz number based on the inner layer thickness  $\delta_r$  can be defined by:

$$\text{Ka}_r = \frac{\delta_r/s_L}{\eta/u'_K} = \frac{\delta_r^2}{\eta^2} \approx 100\text{Ka}_t. \quad (2.24)$$

Based on Eqs. (2.16), (2.21) and (2.23), the following relation is established:

$$\text{Re}_t = \text{Da}_t^2 \text{Ka}_t^2. \quad (2.25)$$

An example of a turbulent premixed combustion diagram is the modified Borghi diagram by Peters [143] shown in Fig. 2.6. The following regimes can be identified [20, 143]:

- **Laminar flame regime:** Laminar flames are present for  $\text{Re}_t \leq 1$ , indicating a laminar flow field.
- **Wrinkled flamelet regime:** It is defined for  $\text{Re}_t > 1$ ,  $\text{Da}_t > 1$ ,  $\text{Ka}_t < 1$  and  $u'/s_L < 1$ . In this regime,  $u'$  is lower than the laminar flame speed, therefore, laminar flame propagation dominates over turbulence effects [143]. The flame front is slightly wrinkled (see Fig. 2.7 (a)).
- **Corrugated flamelet regime:** It is defined for  $\text{Re}_t > 1$ ,  $\text{Da}_t > 1$ ,  $\text{Ka}_t < 1$  and  $u'/s_L > 1$ . The flame thickness is thinner than the Kolmogorov scales.

Then, the flame structure is not internally modified by turbulent structures as they do not penetrate in the flame. The turbulent eddies can only wrinkle or distort the thin laminar flame zone (see Fig. 2.7 (b)).

- Thin reaction zone: In the thin reaction zone,  $Re_t > 1$ ,  $Da_t > 1$ ,  $Ka_t > 1$  and  $Ka_r < 1$ . In this regime, the small eddies with Kolmogorov size can enter into the pre-heat zone, broadening the flame and enhancing the heat and mass transfer rates (see Fig. 2.7 (c)). The Kolmogorov eddies are still bigger than the inner layer and do not penetrate into this layer. Then, this layer is only wrinkled without affecting its structure [115].
- Well stirred reactor: It is defined for  $Re_t > 1$ ,  $Da_t < 1$ ,  $Ka_t > 1$  and  $Ka_r < 1$ . In this regime the chemical time scale is higher than the turbulent time scale, then the reaction rate is limited by chemistry. The Kolmogorov scales are not fast enough to disturb the inner layer of the flame front [42].
- Broken reaction zone: It is defined for  $Re_t > 1$ ,  $Da_t < 1$  and  $Ka_r > 1$ . In this regime, the Kolmogorov scales are smaller than the pre-heat zone and the inner layer thickness and can penetrate in both layers, being strongly affected. A thin flame structure can not be identified.

## 2.4 Turbulent Premixed Combustion Modeling using LES

A detailed resolution of a combustion process is quite complicated as it requires the solution of multi-dimensional transport equations of multiple species which present non-linear reaction terms following an Arrhenius law. Furthermore, different steep gradients are on the flame front, which should be resolved. If turbulence is also involved, the level of complexity increases. Then it is necessary to reduce the complexity by combustion modeling. In section 2.2.1, different turbulence modeling approaches were discussed. The combustion models are derived or extended (e.g., from RANS to LES) according to the turbulence modeling approach. From the turbulence modeling approaches discussed in section 2.2.1, DNS is still unaffordable for technical

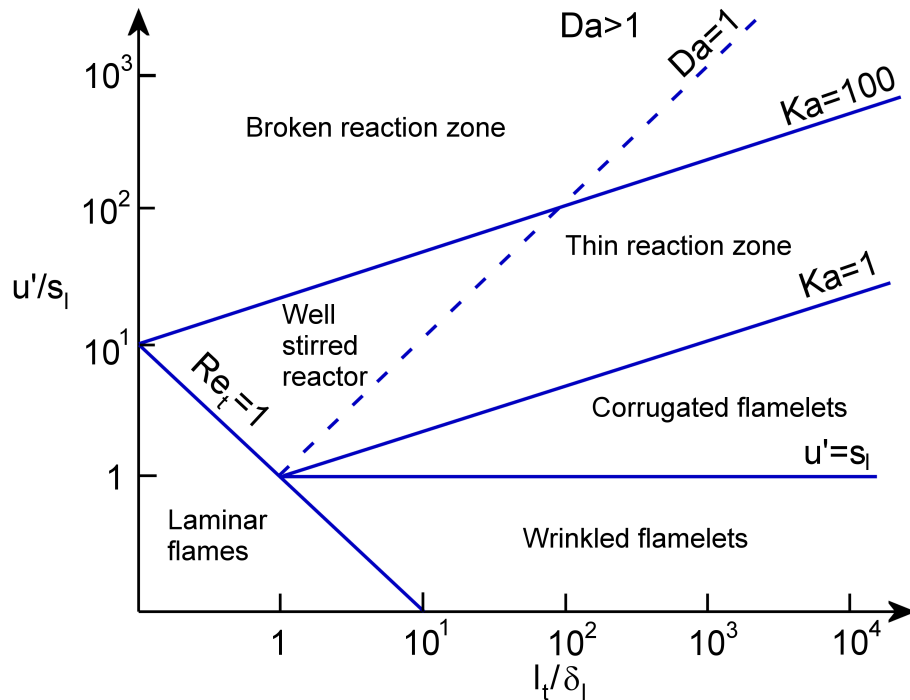


**Figure 2.6:** Turbulent premixed combustion diagram. Adapted from [143]

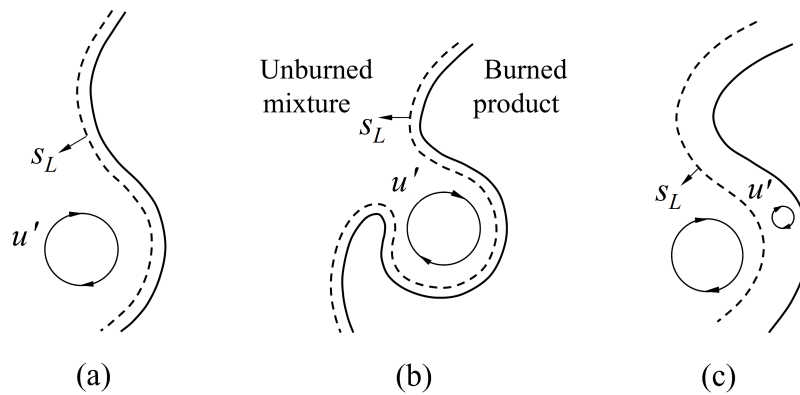


**Figure 2.7:** (a) Wrinkled flamelet regime, (b) Corrugated flamelet regime, (c) Thin reaction zone. From [115].

applications and limited to low turbulence levels. Some recent DNS applications in reacting flows are shown in [24, 144]. RANS models have limitations on describing flame/turbulence interaction and intermittency between fresh

and burnt gases [152], which are important for analyzing the flame dynamics. LES has the advantage that intermittency is taken into account as at a given time the flame position is known at the resolved scale level [152]. In the following, the governing equations and modeling approaches will be shown only in the LES context.

### 2.4.1 LES Filtering

In LES, the filtering procedure is applied to the variables and their transport equations in spatial (weighted average over a given volume) or a spectral space (components greater than a given cut-off frequency are suppressed) [152]. The filtered resolved part ( $\overline{\phi}$ ) of the variable  $\phi$  results from the convolution of the variable with the applied filter and defined by:

$$\overline{\phi(\mathbf{x})} = \iiint_{-\infty}^{\infty} \phi(\xi) G_{\bar{\Delta}_e}(\mathbf{x} - \xi) d\xi, \quad (2.26)$$

where  $\mathbf{x}$  is defined by the spatial coordinates  $(x_1, x_2, x_3)$ , and  $G_{\bar{\Delta}_e}$  is the filter function. The filter is normalized by:

$$\iiint_{-\infty}^{\infty} G_{\bar{\Delta}_e} d\xi = 1. \quad (2.27)$$

The small unresolved subgrid part of the variable is defined by:

$$\phi'(\mathbf{x}) = \phi(\mathbf{x}) - \overline{\phi(\mathbf{x})}, \quad (2.28)$$

$$\overline{\phi'(\mathbf{x})} = 0. \quad (2.29)$$

For reacting flows, a mass-weighted Favre filtering ( $\widetilde{\phantom{\phi}}$ ) is applied to the variable [210] by:

$$\widetilde{\phi(\mathbf{x})} = \frac{1}{\bar{\rho}} \iiint_{-\infty}^{\infty} \rho \phi(\xi) G_{\bar{\Delta}_e}(\mathbf{x} - \xi) d\xi. \quad (2.30)$$

The most common filter is the box-top hat filter in physical space defined by [152]:

$$G_{\bar{\Delta}_e}(\mathbf{x}) = \begin{cases} 1/\bar{\Delta}_e^3, & \text{if } |x_i| \leq \bar{\Delta}_e/2, i = 1, 2, 3; \\ 0, & \text{Otherwise} \end{cases} \quad (2.31)$$

A review of different filter definitions for  $G_{\bar{\Delta}_e}$  can be found in [63, 152, 211].

## 2.4.2 Fundamental Transport Equations for LES Reacting Flows

The transport equations for LES are obtained by filtering the instantaneous transport equations of conservation of mass, momentum, energy and species. A detailed description of the instantaneous transport equations for reacting flow is shown in [115, 152, 214, 219]. The filtered transport equations are [22, 152]:

- Conservation of mass

$$\frac{\partial \bar{\rho}}{\partial t} + \frac{\partial \bar{\rho} \tilde{u}_i}{\partial x_i} = 0, \quad (2.32)$$

- Conservation of momentum

$$\frac{\partial \bar{\rho} \tilde{u}_i}{\partial t} + \frac{\partial \bar{\rho} \tilde{u}_i \tilde{u}_j}{\partial x_j} = -\frac{\partial \bar{p} \delta_{ij}}{\partial x_j} + \frac{\partial \bar{\tau}_{ij}}{\partial x_j} + \frac{\partial \bar{\tau}_{ij}^t}{\partial x_j}, \quad (2.33)$$

- Conservation of energy

$$\frac{\partial \bar{\rho} \tilde{E}}{\partial t} + \frac{\partial \bar{\rho} \tilde{u}_j \tilde{E}}{\partial x_j} = -\frac{\partial [u_i (p \delta_{ij} - \tau_{ij}) + \bar{q}_j + \bar{q}_j^t]}{\partial x_j} + \bar{\dot{\omega}}_T, \quad (2.34)$$

- Species mass fraction

$$\frac{\partial \bar{\rho} \tilde{Y}_k}{\partial t} + \frac{\partial \bar{\rho} \tilde{u}_j \tilde{Y}_k}{\partial x_j} = \frac{\partial [\bar{J}_{j,k} + \bar{J}_{j,k}^t]}{\partial x_j} + \bar{\dot{\omega}}_k. \quad (2.35)$$

where  $\tau_{ij}$ ,  $q_j$ ,  $J_{j,k}$ ,  $\dot{\omega}_T$  and  $\dot{\omega}_k$  are the viscous stress tensor, the heat flux, the diffusive species flux, the heat release and the reaction rate of the  $k^{th}$  species. The superscript  $t$  indicates subgrid turbulent terms which are modeled.

Additionally, the equation of state for an ideal gas mixture is defined by:

$$p = \bar{\rho} \bar{R} T, \quad (2.36)$$

$$\bar{R} = \frac{R}{W_{\text{mix}}}, \quad (2.37)$$

where  $R$  is the universal gas constant and  $W_{\text{mix}}$  is the molecular weight of the mixture.

The transport equations presented before are for conventional LES simulations of reacting and non-reacting flows. Nevertheless, a specific implementation is necessary for the Dynamically Thickened Flame (DTFM) combustion model as the model introduces some modifications on the energy and species transport equations as shown in section 2.4.3.2. The filtered viscous stress tensor, heat flux and diffusive species flux are defined as:

- The filtered viscous stress tensor [22]:

$$\overline{\tau_{ij}} = \overline{2\mu \left( S_{ij} - \frac{1}{3} S_{ll} \delta_{ij} \right)}, \quad (2.38)$$

$$\approx 2\overline{\mu} \left( \tilde{S}_{ij} - \frac{1}{3} \delta_{ij} \tilde{S}_{kk} \right). \quad (2.39)$$

where:

$$\tilde{S}_{ij} = \frac{1}{2} \left( \frac{\partial \tilde{u}_j}{\partial x_i} + \frac{\partial \tilde{u}_i}{\partial x_j} \right), \quad (2.40)$$

$$\tilde{S}_{kk} = \frac{\partial \tilde{u}_k}{\partial x_k}. \quad (2.41)$$

- The filtered diffusive species flux [22]:

$$\overline{J_{j,k}} = -\overline{\rho \left( D_k \frac{\partial Y_k}{\partial x_j} - Y_k V_i^c \right)}, \quad (2.42)$$

$$\approx -\overline{\rho} \left( \overline{D_k} \frac{\partial \tilde{Y}_k}{\partial x_j} - \tilde{Y}_k \tilde{V}_i^c \right). \quad (2.43)$$

where  $V_i^c$  is a correction velocity added to the convection velocity in the species equations to ensure global mass conservation [152] and defined by:

$$\tilde{V}_i^c = \sum_{k=1}^N D_k \frac{\partial \tilde{Y}_k}{\partial x_j}. \quad (2.44)$$

- The filtered heat flux [22]:

$$\overline{q_j} = -\overline{\lambda \frac{\partial T}{\partial x_j}} + \sum_{k=1}^N \overline{J_{j,k} h_{s,k}}, \quad (2.45)$$

$$\approx -\overline{\lambda} \frac{\partial \tilde{T}}{\partial x_j} + \sum_{k=1}^N \overline{J_{j,k} \tilde{h}_{s,k}} \quad (2.46)$$

### 2.4.2.1 Modeling of Subgrid Terms

The subgrid turbulent terms in the transport equations need to be modeled. Most subgrid models are based on the eddy-viscosity assumption (Boussinesq's hypothesis). The subgrid stress tensor  $\overline{\tau}_{ij}^t$  is modeled by:

$$\overline{\tau}_{ij}^t = -\bar{\rho} (\overline{u_i u_j} - \tilde{u}_i \tilde{u}_j), \quad (2.47)$$

$$= 2\bar{\rho} \nu_t \left( \tilde{S}_{ij} - \frac{1}{3} \tilde{S}_{kk} \delta_{ij} \right). \quad (2.48)$$

where  $\nu_t$  is the SGS turbulent viscosity. Some models proposed for  $\nu_t$  are shown in the next section.

The other terms as the subgrid diffusive and heat flux are modeled by:

- The Subgrid scale diffusive species flux:

$$\overline{J_{j,k}}^t = \bar{\rho} (\overline{u_i Y_k} - \tilde{u}_i \tilde{Y}_k), \quad (2.49)$$

$$= -\bar{\rho} \left( D_k^t \frac{\partial \tilde{Y}_k}{\partial x_j} - \tilde{Y}_k \tilde{V}_i^{c,t} \right). \quad (2.50)$$

where,

$$D_k^t = \frac{\nu_t}{S_{c,k}^t}, \quad (2.51)$$

$$\tilde{V}_i^{c,t} = \sum_{k=1}^N \frac{\mu_t}{\bar{\rho} S_{c,k}^t} \frac{\partial \tilde{Y}_k}{\partial x_j}. \quad (2.52)$$

$S_{c,k}^t$  is the turbulent Schmidt number equal to 0.6 for all species [22].

- The Subgrid heat flux:

$$\overline{q_j}^t = \bar{\rho} (\overline{u_i E} - \tilde{u}_i \tilde{E}), \quad (2.53)$$

$$= -\lambda_t \frac{\partial \tilde{T}}{\partial x_j} + \sum_{k=1}^N \overline{J_{j,k}}^t \tilde{h}_{s,k}. \quad (2.54)$$

where,

$$\lambda_t = \frac{\mu_t C_p}{P_r^t} \quad (2.55)$$

The turbulent Prandtl number  $P_r^t$  is equal to 0.6 [22].

### 2.4.2.1.1 SGS Turbulent Viscosity Models

In Eq. (2.48), the SGS turbulent viscosity  $\nu_t$  was introduced to model the subgrid stress tensor. Two models available in the code AVBP are detailed:

- The Smagorinsky Model:

The Smagorinsky model [186] is probably the most popular and the oldest LES sub-grid model. It is obtained from dimensional analysis and based on the mixing-length hypothesis [164, 211]. Considering that:

$$\nu_t \propto \frac{l_0^2}{t_0}, \quad (2.56)$$

and assuming that the cut-off length scale  $\bar{\Delta}_e$  is representative of the sub-grid modes [211], then

$$l_0 = C_s \bar{\Delta}_e, \quad (2.57)$$

where  $C_s$  is a model constant. A theoretical value of  $C_s=0.18$  is estimated using the local equilibrium hypothesis and the Kolgomorov spectrum [63, 164, 211]. The characteristic time scale  $t_0$  is considered to be equal to the turnover time of the resolved scales [211]:

$$t_0 = \frac{1}{\sqrt{2\tilde{S}_{ij}\tilde{S}_{ij}}}. \quad (2.58)$$

Then,

$$\nu_t = (C_s \bar{\Delta}_e)^2 \sqrt{2\tilde{S}_{ij}\tilde{S}_{ij}}. \quad (2.59)$$

The model has some drawbacks:

- (a) The constant  $C_s$  has to be “tuned” for different turbulent fields (e.g., in rotating or sheared flows, near solid walls, etc.).
- (b) The model is over-dissipative in region of large mean strain [63]. It is limited to predict transition from laminar to turbulent flows.
- (c) The model gives a non-zero value of the turbulent viscosity near the wall. Turbulent fluctuations are damped at the wall, so that the turbulent viscosity should be zero [133].

Some of these drawbacks can be overcome using a dynamic formulation of the constant  $C_s$  at each point and at each time step [63, 65] (but it can become computationally unstable [63, 211]), or using a damping function (as the Van Driest function [133, 205]) to recover the correct behavior at the wall.

- The WALE Model:

The Wall-Adapting Local Eddy-viscosity (WALE) model from Nicoud and Ducros [133] is based on the square of the velocity gradient tensor  $\bar{g}_{ij}$

$$\bar{g}_{ij} = \frac{\partial \bar{u}_i}{\partial x_j}, \quad (2.60)$$

and developed for wall bounded flows in an attempt to reproduce the proper scaling at the wall ( $\nu_t = O(y^3)$ ).

The SGS turbulent viscosity is defined as:

$$\nu_t = (C_w \bar{\Delta}_e)^2 \frac{(S_{ij}^d S_{ij}^d)^{3/2}}{(\bar{S}_{ij} \bar{S}_{ij})^{5/2} + (S_{ij}^d S_{ij}^d)^{5/4}} \quad (2.61)$$

where,

$$S_{ij}^d = \frac{1}{2} (\bar{g}_{ij}^2 + \bar{g}_{ji}^2) - \frac{1}{3} \delta_{ij} \bar{g}_{kk}^2, \quad (2.62)$$

$$= \bar{S}_{ik} \bar{S}_{kj} + \bar{\Omega}_{ik} \bar{\Omega}_{kj} - \frac{1}{3} \delta_{ij} (\bar{S}_{mn} \bar{S}_{mn} - \bar{\Omega}_{mn} \bar{\Omega}_{mn}), \quad (2.63)$$

where  $\bar{\Omega}$  the anti-symmetric part of  $\bar{g}$ :

$$\bar{\Omega}_{ij} = \frac{1}{2} \left( \frac{\partial \bar{u}_i}{\partial x_j} - \frac{\partial \bar{u}_j}{\partial x_i} \right). \quad (2.64)$$

The model constant  $C_w = 0.4929$  is set in AVBP. The WALE model is used in the present study because [133]:

- (a) the spatial operator consists of a mixing of the local strain and rotation rates. All the turbulence structures relevant for the kinetic energy dissipation are detected by the model.

- (b) the eddy-viscosity goes to zero in the vicinity of a wall so that a (dynamic) constant adjustment or a damping function are not needed for wall bounded flows.
- (c) in case of a pure shear, the model produces zero eddy viscosity, being able to reproduce the laminar to turbulent transition process.

### 2.4.2.2 Source Terms

In Eqs. (2.34) and (2.35), the filtered heat release ( $\overline{\dot{\omega}_T}$ ) and the reaction rate ( $\overline{\dot{\omega}_k}$ ) are introduced in the transport equations as source terms. As these terms can not be resolved on an LES mesh, modeling is necessary to be applied. This is detailed in the next section.

### 2.4.3 LES Premixed Combustion Models

Different combustion models for LES have been developed in recent years. Most of them are an extension of RANS combustion models to the LES context, and based on different approaches to model the flame propagation and reaction rate. Some LES combustion models are shown in Table 2.1 indicating their modeling approach.

In this investigation, the LES program AVBP [21, 22] from CERFACS was used due to its good performance and results on highly parallel compressible reacting flow simulations (see [3, 175, 184, 188, 191]). The Thickened Flame Model (TFM) from Colin et al. [27] and the Dynamically Thickened Flame Model (DTFM) from Legier et al. [119], which is an extension of the TFM, are available in the code. These models are based on laminar flame reaction kinetics theory. An overview of reaction kinetics for laminar flames is included in Appendix A.2. The TFM and DTFM models have the capabilities to predict ignition and flame extinction from heat losses (which is important in order to obtain the correct flame stabilization [175, 199, 200]) due to their Arrhenius formulation. Most of the other combustion models indicated in Table 2.1 do not include the influence of heat losses in their formulations, and their use

**Table 2.1:** LES Combustion Models

Based on:	Models
Solution of transport equations of species mass fractions and modeling of the reaction rate.	(Dynamically-) Thickened Flame Model. [27, 119], Eddy-Break up model [62, 152].
Solution of transport equations of reaction progress variable (a normalized temperature or reaction product mass fraction [148]) and modeling of the reaction rate by a Turbulent Flame Speed closure.	TFC model [42, 54, 222].
Solution of transport equations of reaction progress variable and modeling of the Flame Surface Density (FSD).	Modeling of FSD [12, 197], Transport Equation of the FSD [76], Transport Equation of the Flame Surface Wrinkling [196].
Flame front tracking describing the flame front propagation of a iso-surface $G$ .	G-equation [99, 146, 147].
Probabilistic approach using Filtered Density Functions (FDF).	Transported FDF [28, 69, 163].

would have an influence in the analysis of flame dynamics due to the incorrect flame stabilization.

#### 2.4.3.1 Thickened Flame Combustion Model

For simulating reacting flows, the thickness of a premixed flame is typically smaller than the mesh size. Due to this, the reaction source term of the species transport equations needs to be modeled. Based on laminar flame theory, the flame speed  $s_L^0$  and the flame thickness  $\delta_L^0$  can be expressed as

$$s_L^0 \propto \sqrt{D_{th}A}, \quad (2.65)$$

$$\delta_L^0 \propto \frac{D_{th}}{s_L^0} = \sqrt{\frac{D_{th}}{A}} \quad (2.66)$$

where  $D_{th}$  represents the thermal diffusivity and  $A$  the pre-exponential factor of the reaction rate based on Arrhenius expressions. If the thermal diffusivity is increased by a factor  $F$  (called the *thickening factor*) and at the same

time the pre-exponential factor is reduced by the same factor, the laminar flame speed is preserved and the thickness is increased by this factor. This procedure affects the ratio between turbulent and chemical time scale, the Damköhler Number (Da); and hence, the reaction of the flame to turbulence. This implies that the flame is less sensitive to turbulent motions. The reaction on eddies smaller than the thickened flame thickness vanishes and the reaction on eddies bigger than that may be modified. An efficiency function  $\varepsilon$  is introduced in order to compensate this effect [27]. This function is based on the ratio of wrinkling factors of an unthickened ( $^0$ ) and a thickened ( $^1$ ) flame. The wrinkling factor is estimated by:

$$\Xi = 1 + \alpha \frac{\Delta_e}{s_L^0} \langle a_T \rangle, \quad (2.67)$$

$$\langle a_T \rangle = \Gamma_e \frac{u'_{\Delta_e}}{\bar{\Delta}_e}, \quad (2.68)$$

where  $\langle a_T \rangle$  is the effective strain rate defined by the subgrid scale turbulent velocity, the filter size  $\bar{\Delta}_e$  and a function  $\Gamma_e$  which represents the integration of the effective strain rate induced by all scales affected by the artificial thickening.  $\Gamma_e$  is defined by:

$$\Gamma_e \left( \frac{\bar{\Delta}_e}{\delta_L^1}, \frac{u'_{\Delta_e}}{s_L^0} \right) \approx 0.75 \exp \left[ -\frac{1.2}{(u'_{\Delta_e}/s_L^0)^{0.3}} \right] \left( \frac{\bar{\Delta}_e}{\delta_L^1} \right)^{2/3}. \quad (2.69)$$

$\alpha$  denotes a model constant, which can be estimated by:

$$\alpha = \frac{2 \ln(2)}{3 c_{ms} (\text{Re}_t^{1/2} - 1)}, \quad (2.70)$$

where  $c_{ms} = 0.28$  [27]. Finally, the efficiency function  $\varepsilon$  is defined by:

$$\varepsilon = \frac{\Xi(\delta_L^0)}{\Xi(\delta_L^1)} = \frac{1 + \alpha \frac{u'_{\Delta_e}}{s_L^0} \Gamma_e \left( \frac{\bar{\Delta}_e}{\delta_L^0}, \frac{u'_{\Delta_e}}{s_L^0} \right)}{1 + \alpha \frac{u'_{\Delta_e}}{s_L^0} \Gamma_e \left( \frac{\bar{\Delta}_e}{\delta_L^1}, \frac{u'_{\Delta_e}}{s_L^0} \right)}. \quad (2.71)$$

Then, the diffusivity and reaction rate in the species and energy filtered trans-

port equations have to be modified according to [152]:

$$\text{Diffusivity: } D_{th} \xrightarrow{\text{Thickening+wrinkling}} \varepsilon F D_{th}, \quad (2.72)$$

$$\text{Pre-exponential factor: } A \xrightarrow{\text{Thickening+wrinkling}} \varepsilon \frac{A}{F}, \quad (2.73)$$

while the mass and momentum filtered equations are unmodified.

The transport equations for energy and species for the Thickened Flame Model are [22]:

- Energy

$$\begin{aligned} \frac{\partial \bar{\rho} \tilde{E}}{\partial t} + \frac{\partial \bar{\rho} \tilde{u}_j \tilde{E}}{\partial x_j} = & - \frac{\partial}{\partial x_j} \left\{ \tilde{u}_i \left[ \bar{\rho} \delta_{ij} - 2\bar{\mu} \left( \tilde{S}_{ij} - \frac{1}{3} \tilde{S}_{kk} \delta_{ij} \right) \right] \right\} \\ & + \frac{\partial}{\partial x_j} \left\{ C_p \varepsilon F \frac{\bar{\mu}}{P_r} \frac{\partial \tilde{T}}{\partial x_j} \right\} \\ & + \frac{\partial}{\partial x_j} \left\{ \sum_{k=1}^N \left[ \left( \varepsilon F \frac{\bar{\mu}}{S_{c,k}} \right) \frac{\partial \tilde{Y}_k}{\partial x_j} \right. \right. \\ & \left. \left. - \bar{\rho} \tilde{Y}_k \left( \tilde{V}_j^c + \tilde{V}_j^{c,t} \right) \right] \overline{h_{s,k}} \right\} + \frac{\varepsilon \dot{\omega}_T}{F}, \end{aligned} \quad (2.74)$$

- Species mass fraction

$$\begin{aligned} \frac{\partial \bar{\rho} \tilde{Y}_k}{\partial t} + \frac{\partial \bar{\rho} \tilde{u}_j \tilde{Y}_k}{\partial x_j} = & \frac{\partial}{\partial x_j} \left[ \varepsilon F \frac{\bar{\mu}}{S_{c,k}} \frac{\partial \tilde{Y}_k}{\partial x_j} - \bar{\rho} \tilde{Y}_k \left( \tilde{V}_j^c + \tilde{V}_j^{c,t} \right) \right] \\ & + \frac{\varepsilon \dot{\omega}_k}{F}. \end{aligned} \quad (2.75)$$

#### 2.4.3.2 Dynamically Thickened Flame Combustion Model

The Thickened Flame Model applies the thickening in the complete domain. With this, the diffusion in non-reactive zones will be overestimated by a factor  $F$ . Legier [119] proposed the Dynamically Thickened Flame Model (DTFM) based on the Thickened Flame Model to overcome this deficiency. In the

DTFM, the thickening factor  $F$  is not constant, but approaches a maximum value ( $F_{max}$ ) inside the reaction zone and unity in non-reactive zones. A “sensor” ( $S$ ) of the reactive zone is used to indicate if the thickening should be applied ( $S=1$ ) or not ( $S=0$ ). It is defined by:

$$S = \tanh\left(\beta_F \frac{\Omega}{\Omega_{max}}\right), \quad (2.76)$$

$$\Omega = Y_F^{v_F} Y_O^{v_O} e^{-\Psi \frac{T_a}{T}}. \quad (2.77)$$

where  $\Psi$  and  $\beta_F$  are model constants equal to 0.5 and 500, respectively [22].  $\Psi$  is lower than 1 to activate the sensor  $S$  before reaction.  $\Omega$  is a modified reaction rate used to activate the sensor  $S$  [174].  $\Omega_{max}$  is the maximum of  $\Omega$  and it can be obtained using 1D laminar flame calculations. Finally, the sensor controls the value of the thickening  $F$  by [22]:

$$F = 1 + (F_{max} - 1)S \quad (2.78)$$

The transport equations for energy and species for the Dynamically Thickened Flame model are [22]:

- Energy

$$\begin{aligned} \frac{\partial \bar{\rho} \tilde{E}}{\partial t} + \frac{\partial \bar{\rho} \tilde{u}_j \tilde{E}}{\partial x_j} = & - \frac{\partial}{\partial x_j} \left\{ \tilde{u}_i \left[ \bar{p} \delta_{ij} - 2\bar{\mu} \left( \tilde{S}_{ij} - \frac{1}{3} \tilde{S}_{kk} \delta_{ij} \right) \right] \right\} \\ & + \frac{\partial}{\partial x_j} \left\{ C_p \left[ \varepsilon F \frac{\bar{\mu}}{P_r} + (1-S) \frac{\mu_t}{P_r^t} \right] \frac{\partial \tilde{T}}{\partial x_j} \right\} \\ & + \frac{\partial}{\partial x_j} \left\{ \sum_{k=1}^N \left[ \left[ \varepsilon F \frac{\bar{\mu}}{S_{c,k}} + (1-S) \frac{\mu_t}{S_{c,k}^t} \right] \frac{\partial \tilde{Y}_k}{\partial x_j} \right. \right. \\ & \left. \left. - \bar{\rho} \tilde{Y}_k \left( \tilde{V}_j^c + \tilde{V}_j^{c,t} \right) \right] \bar{h}_{s,k} \right\} + \frac{\varepsilon \bar{\dot{\omega}}_T}{F}, \end{aligned} \quad (2.79)$$

- Species mass fraction

$$\begin{aligned} \frac{\partial \bar{\rho} \tilde{Y}_k}{\partial t} + \frac{\partial \bar{\rho} \tilde{u}_j \tilde{Y}_k}{\partial x_j} = & \frac{\partial}{\partial x_j} \left\{ \left[ \varepsilon F \frac{\bar{\mu}}{S_{c,k}} + (1-S) \frac{\mu_t}{S_{c,k}^t} \right] \frac{\partial \tilde{Y}_k}{\partial x_j} - \bar{\rho} \tilde{Y}_k \left( \tilde{V}_j^c + \tilde{V}_j^{c,t} \right) \right\} \\ & + \frac{\varepsilon \bar{\dot{\omega}}_k}{F}. \end{aligned} \quad (2.80)$$

### 3 Response of Premixed Flames to Velocity Disturbances

As mention in the introduction, premix enclosed flames are prone to develop instabilities. The instabilities can develop from the appearance of hydrodynamic or acoustic perturbations inside the system. The flame has a dynamic response to these perturbations acting as a source or as a damper of this perturbations. Various mechanisms are related to the fluctuations of heat release ( $\dot{Q}'$ ) produced by the acoustic velocity fluctuations ( $u'$ ). These mechanisms are described in Fig. 3.1 for fully premixed conditions. The flame dynamics have also a strong influence by equivalence ratio fluctuations [83,85,121,173], which is not investigated in the present study.

From these mechanisms, the fluctuation of heat release is mainly produced by the variations in flame surface area. When the perturbation reaches the flame, a kinematic response is produced, creating modulations in flame surface area which are convected along the flame [83,153,181] and finally producing fluctuations in the heat release. With the presence of a swirler, fluctuations in the swirl number at the burner exit are induced by the appearance of fluctuations in the tangential velocity (more details in section 3.3.3). The variation of the swirl number produces modulations in the flame angle, which creates variations of flame surface area. Additionally, the turbulence intensity in the shear layers can be modified by turbulent fluctuations induced by the perturbation, producing fluctuations in the turbulent flame speed. External turbulent eddies generated by the environment and not induced by the velocity perturbation can interact also with the flame, producing fluctuations in the heat release. Coherent structures can develop by hydrodynamic instabilities [150] or at high amplitudes of the velocity perturbation [111], inducing deformation on the flame surface area [153] by vortex roll-up.

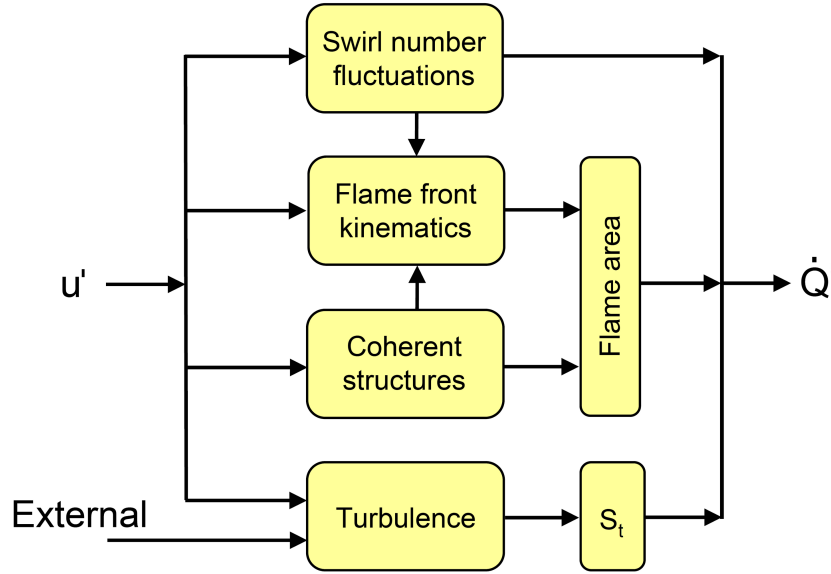


**Figure 3.1:** Overview of interaction mechanisms between heat release and acoustic waves in a fully premixed flame. Adapted from [153]

To characterize a global response of the flame to a perturbation, the concept of the Flame Transfer Function is introduced.

### 3.1 The Flame Transfer Function

The dynamic response of a flame to a perturbation can be represented in the frequency domain by its flame transfer function  $FTF(\omega)$  (also “frequency response”). It relates fluctuations of mass flow rate or velocity  $u'_r$  at a reference position  $r$  upstream of the flame to fluctuations of the flame heat release  $\dot{Q}'$ :

$$FTF(\omega) = \frac{\dot{Q}'(\omega)/\bar{\dot{Q}}}{u'_r(\omega)/\bar{u}_r} = A(\omega) e^{i\theta(\omega)}. \quad (3.1)$$

Here fluctuations  $\dot{Q}'$  and  $u'_r$  are normalized with the respective mean values of heat release  $\bar{\dot{Q}}$  and velocity  $\bar{u}_r$ . The heat release is obtained by a volume integration of the heat release in the domain.  $A(\omega)$  and  $\theta(\omega)$  are the amplitude and the phase of flame transfer function. Considering that  $\dot{Q}'$  and  $u'_r$  have an

harmonic behavior [59, 75]:

$$\dot{Q}'(\omega) = \hat{Q}(\omega) e^{i(\omega t + \theta_{\dot{Q}})}, \quad (3.2)$$

$$\dot{u}'_r(\omega) = \hat{u}_r(\omega) e^{i(\omega t + \theta_{u_r})}, \quad (3.3)$$

the amplitude of FTF is defined by:

$$A(\omega) = \frac{\hat{Q}(\omega) / \bar{Q}}{\hat{u}_r(\omega) / \bar{u}_r}, \quad (3.4)$$

and the phase by:

$$\theta(\omega) = \theta_{\dot{Q}}(\omega) - \theta_{u_r}(\omega). \quad (3.5)$$

In the right side of Fig. 3.2, an experimental flame transfer function is shown. In the low frequency limit, the amplitude and phase approach 1 and 0, respectively. This is due to the quasi-steady response of the flame [159]. The amplitude indicates how the relative fluctuation of heat release from the flame response is with respect to the relative fluctuation of velocity at the reference position [66]. Taking as example the FTF in Fig. 3.2 with an amplitude equal to 1.8 at 100 Hz: If a velocity fluctuation at 100 Hz and with an amplitude of 5% of its mean value is measured at the reference position, the heat release fluctuation of the flame will be 9% of its mean value. The variations in amplitude in the FTF (in some cases with values higher than one as in the example) are produced by a constructive or destructive interaction of different mechanisms induced by the perturbation [17, 75, 78, 87, 103, 137, 165] (e.g., the interaction between acoustic and swirl number fluctuations [75, 78, 103, 137, 139, 140]). The phase of the FTF indicates a *global* time lag between the velocity fluctuation and the flame response. The response is *global* because in Eq. (3.1) the heat release is obtained by the volume integration of the heat release in all the domain. In this way, the flame is considered as a discontinuity. It has been seen that the flame response is a distribution of time lags [53, 103, 173, 178] from different contributions. The determination of distributed FTFs as in [98] was not carried out in the present work. Moreover, the flame transfer function can be extended to be in function of the amplitude of the excitation, becoming the *flame describing function* [134, 137]. The flame describing function is investigated for the analysis of non-linear flame dynamics, which is not covered in the present study.

## 3.2 Determination of the Flame Transfer Function

Crocco [29] introduced in 1951 the concept of time lag as the time delay between the moment that the fluctuation (in his case, fluctuations in fuel produced by pressure oscillations) is created and the moment when the flame reaction is produced. Some years later, Merk [129] in 1956 proposed the definition of flame transfer function by the relation between heat release and velocity fluctuations. Since then, extended work has been carried out to obtain the flame transfer function.

Flame transfer functions may be obtained by different methods. Most of the investigations in the determination of the FTF have been carried out experimentally. By introducing harmonic excitation with a loudspeaker or siren at the inlet, the flame transfer function  $FTF(\omega)$  is obtained from time series of velocity ( $u'_r$ ) and heat release ( $\dot{Q}'$ ) fluctuations with spectral analysis. The velocity fluctuations may be measured using a Constant Temperature Anemometry or by the multi-microphone method, while the heat release of the flame is deduced from chemiluminescence intensity measured with a photomultiplier. After this, a Fast Fourier Transform (FFT) is applied to obtain the response for a single frequency in amplitude and phase. A scheme of this procedure is shown in Fig. 3.2.

Extended experimental work has been carried out in premixed laminar flames to obtain the flame transfer functions in fundamental flame geometries as Bunsen flames [41, 108], using a bluff body [11, 43, 44, 180] or perforated plates [107, 134]. The influence of the configuration and the flame geometry in the flame response [44] was observed. In experimental investigations in turbulent swirling flames, a strong dependence of the burner swirl number was observed. Fischer [50] investigated a radial swirl burner, observing that with the increase of swirl number, the amplitude of the FTF increases, while the phase exhibits a decrease. He investigated also the influence of the change in the flame transfer function by variations in the equivalence ratio of the mixture. The FTF shows some small variations, with a decrease in the amplitude and in the phase, for higher equivalence ratios. With the increase in equivalence ratio, the flame speed and reaction rate are increased, creating a shorter

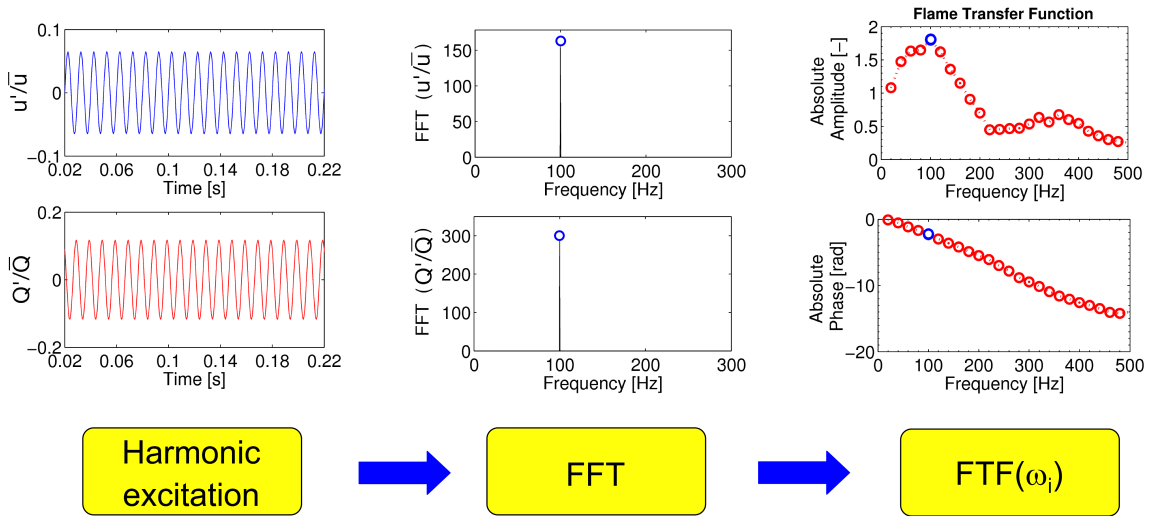


**Figure 3.2:** Scheme of determination of the flame transfer function with harmonic excitation.

flame. Similar behavior with the variation of burner swirl number was found by Kulsheimer and Buchner in another swirl burner [111], and for the variation of equivalence ratio by Jones et al. [87] and Lohrman et al. [124]. Also, it was observed that with the increase of inlet pre-heating temperature [124] and power rating [97, 111, 137], the amplitudes of flame transfer function move to higher frequencies with a decrease in the phase. For both cases, the FTF shows a good scaling with the Strouhal number. Kim et al. [97] investigated an axial swirl burner and observed that with the enrichment of hydrogen, the flame topology can switch from a V-flame shape to an M-flame shape, modifying the flame response. In his work, lower amplitudes were observed than in the V-flame. Due to the enrichment, the flame speed increases and has a similar behavior than with the increase of equivalence ratio in the premixed mixture. In all the previous studies with turbulent swirl burners, amplitudes higher than 1 were observed in certain range of frequencies. This is produced by a superposition mechanism between perturbations [78, 87, 103, 137]. If the interaction of perturbations is in phase (at similar time), a constructively interference is created, producing amplitudes higher than 1 [87, 137, 139, 140] in the FTF. In the same way, such perturbations can have a destructively interference when they are out of phase, decreasing the amplitude of the FTF. In

general, the experimental determination of FTFs for configurations of technical interest is very difficult and costly, but necessary for validation. In order to reduce the time and cost of experiments, analytical and numerical tools have been developed to investigate the flame response. For (Semi-)analytical models of the FTF, most of the models have been derived for laminar flames. A simple analytical model was proposed based on the time lag description by Crocco and Cheng [30] called the  $n$ - $\tau$  model, where the FTF is defined by:

$$\text{FTF}(\omega) = ne^{i\omega\tau}, \quad (3.6)$$

where  $n$  is called the interaction index and  $\tau$  is the time lag between heat release and velocity. If the value of  $n$  is considered constant, the interaction index takes the value of 1 [59] due to the low frequency limit of the FTF, where the amplitude should approach unity [159]. As it is shown by Eq. (3.6), the model does not capture variations in the amplitude of the FTF by the flame dynamics and only capture the variations in a single time lag. More advanced models have been derived based on the flame front kinematics and the propagation of a perturbation along the flame [15, 41, 51, 181], creating a deformation of flame surface area. Schuller et al. [181] extended the model of Ducruix et al. [41], which is based on the works from Fleifil et al. [51] and Boyer and Quinard [15], to introduce the effects of a disturbance convected along the flame front in a conical and a V-flame. For the V-flame, similar to most flames stabilized in swirl burners, it was observed that the FTF presents amplitudes higher than 1 from a certain value of the flame angle with respect to the center line, and that the amplitude is increased with the decrease of the flame angle. This behavior of V-flames was also confirmed with experiments [43], indicating that this kind of flame is prone to develop combustion instabilities. Additional models were extended to turbulent combustion [33, 116]. However, it is in general difficult to predict flame responses from first principles, especially for turbulent flames.

Alternatively, it is possible to determine the FTF with computational fluid dynamics (CFD). Steady state CFD simulations [52, 53, 109, 110] can be used to track the fuel particles until they are consumed to create a time lag distribution and introduce it into a model. The problem of using this method is that the amplitude of the FTF, which describes the dynamic response of the flame

to the perturbations, can not be well reproduced as some effects (e.g., flame front kinematics, swirl fluctuations, etc.) are not considered. Instead an unsteady CFD simulation can be performed to generate time series of fluctuating velocity and heat release rate. Thus, the FTF is reconstructed from the extracted data. The FTF can be obtained using harmonic excitation [5, 68, 77, 93] as in the experimental determination of the FTF, applying special signals as an impulse or white noise and doing spectral analysis [66, 206], or by using methods from system identification (SI) [64, 66, 67, 85, 158, 160, 199]. The advantage of using system identification methods is that it is possible to obtain the frequency flame response over a range of frequencies from a single CFD simulation, reducing the computational effort. Furthermore, it removes the contributions in the flame response by external “noise” by correlation analysis and that are present on the spectral analysis. Details about SI are indicated in Chapter 4. Gentemann and Polifke [64] investigated a radial swirl burner in an axisymmetric 2D simulation to identify the FTF using URANS and SI. Good qualitative agreement was obtained with experimental results. Discrepancies are argued to be due to limitations in the combustion and turbulence model to reproduce the flame and flow field. Giauque et al. [67] simulated a premixed turbulent swirl burner in a  $15^\circ$  sector of an annular combustor with LES. Harmonic and white noise excitation at the inlet were applied to identify the FTF by a FFT using the harmonic excitations and by SI methods using the white noise signal. Good agreement was obtained in amplitude and phase between the FTF identified by harmonic excitation and SI. Results were not validated with experiments. Additionally, in [66] a spectral analysis was carried out to the signals extracted using the white noise excitation. High differences were found between the results obtained by the Harmonic-FFT and White noise/SI. Borghesi et al. [13] carried out the identification of the FTF of a conical swirl burner with aerodynamic stabilization of the flame (without the use of bluff body as in [64] and in this study). The FTF is represented by the element  $T_{22}$  of the flame transfer matrix, with good agreement with experiments. Also, he indicates that the flame response is dominated by the displacement of the inner recirculation zone due to the aerodynamic stabilization of the flame.

Recently, Cuquel et al. [32] applied experimentally random velocity perturbations in combination with system identification techniques to obtain the FTF

of a laminar conical flame. With this technique, the FTF is obtained over a range of frequencies from a single experiment. For excitations in the linear regime, good agreement was achieved between the FTFs obtained with harmonic excitation and with system identification. For higher excitation amplitudes, the amplitude of the FTF is underestimated when random velocity perturbations are applied.

### **3.3 Additional Parameters Influencing the Flame Response in Premixed Flames**

As mentioned before, the FTF is influenced by different parameters. Most studies were carried out to look at its dependence by the increase of power rating or by modifying the mixture properties (temperature and equivalence ratio). Nevertheless, the change of other conditions in a combustion system can also lead to a variation on the flame response. From the practical point of view, typical investigations on the design of gas turbines are carried out using single burner test rigs. Nevertheless, when the same burner is installed on the engine, which can have similar inlet conditions (mixture, inlet flow and equivalence ratio) as in the single burner tests, other variations can appear as the change of thermal conditions at the combustor walls, variation of combustor cross section size, flame-flame interaction between adjacent burners, operating pressure, etc. Also, the position of the swirler can be changed because of design reasons. These additional variations can lead to differences on the flame shape and burner aerodynamics.

Flame shape and topology have a strong influence on the flame dynamics. Schuller et al. [180] studied the self-induced instabilities of laminar premixed flames stabilized on an unconfined annular burner. The burner included a bluff body rod for flame stabilization. It was observed that under similar operating conditions, it was possible to obtain different flame topologies (conical, V-, or M-Flame) depending on the location of the ignition point. In this study, the flame transfer function of the M-flame was measured for different equivalence ratios and incoming velocities. It was observed that there exists

a strong mutual interaction (leading to annihilation) between the flames stabilized on both shear layers, causing an amplification behavior (amplitudes higher than 1) on the flame transfer function for a frequency range. Durox et al. [44] investigated the same burner to measure the Flame Describing Functions (FDF) of the different flame geometries mentioned before. The investigation included an additional configuration consisting on a Collection of Small Conical Flames (CSCF) stabilized on a perforated plate. The compared cases were performed at slightly rich conditions ( $\phi=1.08$ ) for a methane-air mixture. Under these conditions, it was possible to obtain all flame shapes mentioned before with the same incoming flow and equivalence ratio. The flame response was different between cases, concluding that the steady-state flame geometry has a strong influence on the flame response. The CSCF, V-shape and M-shape flames showed similar behavior with amplitudes higher than 1 for low frequencies, followed by a decay in amplitude at higher frequencies. Additionally, the M-flame exhibited a broader frequency response (with amplitudes higher than 1) than the other flames. This different flame response can lead also to a varied production of combustion noise [19] and stability behavior [82, 96].

Variation of the flame shape and length in premixed cases can be obtained using the same burner by modifying operational conditions such as:

- *Fuel and mixture conditions*: Kim et al. [97] investigated the flame response in a lean-premixed axial swirl burner with various equivalence ratios and methane-hydrogen-air mixture compositions at atmospheric conditions. It was observed that for the same inlet velocity and mixture temperature, a V-flame stabilized initially at certain methane-air equivalence ratio can change to a M-flame by the increase of equivalence ratio or by hydrogen enrichment. With the increase in these parameters, the flame speed and reaction rate are increased, and flame stabilization can be achieved in both shear layers.
- *Inlet pre-heat temperature*: Huang and Yang [81] analyzed experimentally and numerically the transition of flame structure from a stable to an unstable state in a lean-premixed axial swirl burner. It was observed that with the increase of the inlet mixture temperature, a stable system with

a V-flame shape shifted to an unstable system with a M-flame. The transition appears due to the increase of flame speed by the increase of inlet temperature. Then, the flame flashes back, penetrating in the outer recirculation zone and stabilizing in the outer shear layer. Foley et al. [55] investigated also the influence of variation of equivalence ratios and inlet temperature on the flame shape, observing similar transition behavior as in the previously cited study. In their work, additional flame shapes, as a lifted flame or a flame with stabilization only in the outer shear layer, were observed.

- *Operating Pressure:* The increase of pressure has an influence on the flame length [17, 59, 60]. By increasing the operating pressure on the burner and keeping the same equivalence ratio, inlet pre-heating temperature and inlet velocity, the output power increases due to the higher total mass flow produced by the higher density at this condition. Furthermore, the chemical kinetics and reaction rate changes [115] with the increase of pressure. It was observed on references [17, 59, 60] that the flame length is reduced with the increase of operating pressure. Change of the flame topology due to the increase in pressure was not observed on the previous cited investigations.

This investigation has a special emphasis on the influence of thermal boundary conditions at the combustor wall, confinement ratio and swirler position on the flame dynamics. Previous studies related with these variations on conditions are reviewed in the following.

#### **3.3.1 Influence of Combustor Thermal Boundary Conditions**

Heat losses can modify the flame structure as the flame reaction has a strong dependence on the temperature [115]. In combustion systems, the burnt gases approach temperatures between 1500 and 2500 K, while the combustor walls have temperatures between 400 and 600 K [152] because of the cooling to protect the material. Under nonadiabatic conditions, the heat losses can lead to the extinction of the flame [35, 127, 187]. The influence of thermal

conditions on the flame has been studied in different configurations. In numerical studies of flame propagation in channels with variations of thermal conditions [34, 73, 189], it was observed that the flame structure and propagation can change due to the quenching effects on the flame from the cooled walls. Veynante and Poinso [151, 209] investigated with DNS a premixed flame stabilized on a back ward facing step and found a different flame stabilization by varying the thermal conditions of the combustor walls. The flame was anchored to the step using adiabatic wall conditions; while using nonadiabatic walls with temperatures equal to the fuel mixture, quenching effects appear close to the wall, resulting in a lifted flame. Similar effects on the flame stabilization were found by Kaess et al. [90, 91] on a DNS study of a laminar conical flame stabilized on a perforated plate with different thermal conditions at the wall. It was observed that this variation on the flame stabilization had an influence on the flame response [90, 209]. Using a very similar configuration as Kaess et al., Duchaine and Poinso [40] explored the sensitivity of premix flame FTF to changes in a variety of input parameters. With an uncertainty in the wall plate temperature of 50 K, only a small influence in the FTF was observed. Higher wall temperature variations were not investigated.

In the case of combustors with swirl burners, due to the formation of an outer recirculation zone, combustion products cooled by the combustor wall cooling are transported back and interact with the flame, affecting the flame stabilization. The flame stabilization on a premixed swirl burner with different thermal conditions was investigated using LES by Schmitt et al. [175, 176]. Using adiabatic walls, the flame showed strong stabilization in the outer shear layer; while with nonadiabatic walls, as in the experimental configuration, quenching effects appeared in the outer shear layer, having a flame stabilized mainly in the inner recirculation zone, and in good agreement with the one from experiments. Additionally, Waesle et al. [215] designed an unconfined swirl burner surrounded by co-flow gases with different temperatures and composition. A hot exhaust gas stream is generated by a porous burner surrounding the flame, and positioned at the same level of the burner exit. It was observed that different flame topologies can be obtained depending on the surrounding gas temperature and composition. Furthermore, the level of heat loss in the combustor changes with increasing pressure as shown by Frei-

tag et al. [59, 60]. In his work, it is observed a decrease on the heat losses per power rating with the increase in pressure. The variation on heat losses by pressure variation can have an influence on the flame length.

#### 3.3.2 Influence of Confinement Ratio

Strong differences on the flow field and flame structure between confined and unconfined flames have been observed [4]. The degree of confinement can have an influence in the flame dynamics. The influence of confinement ratio (CR) in non-reacting and reacting flow has been investigated by various authors. The confined ratio is defined by:

$$CR = \frac{A_{\text{bexit}}}{A_{\text{cc}}}, \quad (3.7)$$

where  $A_{\text{bexit}}$  is the area of the burner exit using the external perimeter, and  $A_{\text{cc}}$  is the area of the combustor cross section. Beltagui and Maccallum [10] studied non-reacting and reacting swirling flows in a cylindrical furnace combustor, observing variations in the flow patterns when the combustor had a different confinement ratio. In their investigations, the inner recirculation zone was longer and bigger for the case with lower confinement ratio. Similar results were found in a similar configuration by Rao et al. [167] and by Hallet and Ding [74]. Birbaud et al. [11] investigated the flame dynamics for confined and unconfined laminar flames. It was observed that for low levels of confinement ratio, where the flame did not have interaction with the walls, the response was similar to the unconfined case. For the cases with higher confinement, interaction of the flame with the wall influences the dynamics of the flame tip and the flame wrinkling, changing the flame response. Fu et al. [61] investigated the effect of combustor confinement on the flow field using a swirl burner at isothermal conditions. A strong influence of the confinement in the size and strength of the inner recirculation zone (IRZ) was found. Additionally, they found that there is a level of confinement where the flow has some hysteresis and different flow regimes can be established, changing the angle of the shear layers and the size of the IRZ. Fanaca et al. [49] investigated experimentally the flow field and flame on a single burner and an annular combustor. It is

considered that the differences on the aerodynamics and flame shape are the causes of discrepancies in the FTFs obtained in these configurations. Hauser et al. [75] investigated the influence of the confinement on the Flame Transfer Function in two combustors with different square section area, showing differences between cases in amplitude and phase. The differences in phase is attributed to the higher convection velocities in the high confinement combustor.

### 3.3.3 Influence of Swirler Position

Straub and Douglas [194] investigated the influence of the position of an axial swirler on the stability of a combustion system. The experiments were at pre-mix conditions with high pressure and mixture pre-heating. Different stability behavior was observed in the combustor, depending on the position of the axial swirler. In their work, the flame response was not investigated, but it is mentioned that due to the presence of the swirler, tangential velocity fluctuations propagating with a convective speed can reach the flame and have some effect on it.

The flame response and flow field have a strong dependence on the swirl number of the burner [50, 111], which is defined by [10, 82, 142]:

$$S_n = \frac{G_{\text{tan}}}{r_{\text{ext}} G_{\text{ax}}}, \quad (3.8)$$

where  $G_{\text{ax}}$  and  $G_{\text{tan}}$  are defined for an axisymmetric configuration by:

$$G_{\text{ax}} = \int_{r_{\text{int}}}^{r_{\text{ext}}} \rho u_{\text{ax}}^2 2\pi r dr, \quad (3.9)$$

$$G_{\text{tan}} = \int_{r_{\text{int}}}^{r_{\text{ext}}} \rho u_{\text{ax}} u_{\text{tan}} 2\pi r^2 dr, \quad (3.10)$$

indicating the fluxes of axial and angular momentum.  $r_{\text{ext}}$  and  $r_{\text{int}}$  are the external and internal radius, respectively; and  $u_{\text{ax}}$  and  $u_{\text{tan}}$  are the axial and tangential velocity, respectively. Due to the presence of tangential velocity fluctuations, swirl number fluctuations can be induced, modifying the flame response and the stability behavior of the system.

A small decay in swirl number is also produced by moving the swirler to a position more upstream to the burner exit. The axial decay in swirl number has been studied experimentally and numerically in tubes [6, 100, 192] and annular ducts [26, 36, 131]. It was found that the decay has an exponential behavior [36, 100] with respect to the distance to the swirl generator. The decay appears due to the loss of angular momentum produced by the wall friction and stresses. Additionally, Clayton and Morsi [26] have shown experimentally in an annular duct that the axial decay of swirl increases with the increase of swirl number.

The mechanism of the impact of swirl number fluctuations in the flame response was investigated in different previous studies [78, 103, 137, 139, 141]. Hirsch [78] proposed a mechanism of how the presence of swirl fluctuations can induce a secondary velocity fluctuation (created by fluctuations in vorticity) which influence the flame response. Wang and Yang [212] investigated numerically an imposed perturbation in a radial swirl burner. It was found that the swirler can induce two perturbations with different propagation speed: One is a vortical wave with convective propagation speed, and the other is an acoustic wave propagating with the speed of sound. The flame response was not analyzed by them. Komarek and Polifke [103, 104] investigated experimentally and numerically the influence on the flame response by the variation of the position of an axial swirl burner. It was observed by the use of unit impulse responses that when an acoustic perturbation is imposed at the inlet, it travels through the swirler, and an axial and a tangential velocity fluctuation are created. While the axial velocity fluctuation travels with an acoustic behavior, the tangential velocity fluctuation travels with a convective speed, which induces fluctuations of swirl number at the burner exit, thus influencing the flame response. This variation in the flame response was observed experimentally [103, 104] and numerically [104]. Furthermore, a model based on the Unit Impulse Responses of the different perturbations (see section 3.4) was developed to describe the impact of the different time lags on the flame response. Palies et al. [137, 139] carried out a fundamental investigation of this mechanism on the flame response and on the mode conversion mechanism of the tangential velocity fluctuation in the swirler. They carried out experimental measurements of the flame describing function and velocity mea-

surements at the burner exit at two different frequencies to identify the varied propagations speeds of the perturbations and the variations of swirl number produced by them. The impact of the variations of swirl number and by the phase between perturbations on the flame response was analyzed. It was observed that when the axial and tangential velocity fluctuations were almost out of phase, swirl number fluctuations were present, inducing variations on the flame angle. Under these conditions, a destructive interaction mechanism is produced, which decreases the amplitude of the flame describing function. On the other hand, when both perturbations were almost in phase, the amplitude of the swirl number fluctuation decreased, and a constructive interaction mechanism is produced, showing a peak amplitude in the flame describing function. The investigations mentioned before demonstrate that the position of the swirler has a strong impact on the flame response.

Finally, non-linearity is also an important issue on the studies of flame dynamics. It appears from a saturation response of the flame to the increase of the amplitude of the fluctuation. This topic is not investigated in the present study as it is focus on the use of tools in the linear regime as linear system identification with finite impulse response filters and network models using linearized Navier-Stokes equations. Thus the flame was excited to amplitudes in the linear regime of the flame [96]. While experimental and analytical investigations has been extensively carried out in the investigation of non-linear effects, the development of non-linear system identification tools for thermo-acoustics systems [157, 182, 183] is in its early stages, showing that a much complex process needs to be carried out for the identification compared to the linear identification tools.

### **3.4 Model of Impulse and Frequency Responses to Axial Velocity and Swirl Fluctuations**

Various models have been proposed to describe the flame response as mentioned in section 3.2. Some of these models are based on time lag distributions. A model for the flame dynamics was proposed by Komarek and Po-

lifke [103] to study the impact of fluctuations of velocity (or mass flow rate) and swirl on heat release rate. This model is based on the approaches by Lawn and Polifke [116] and Schuermans et al. [178] to model equivalence ratio fluctuations.

The responses to perturbations of mass flow rate and swirl are described in the time domain by the unit impulse responses  $h_{k,\text{MF}}$  and  $h_{k,\text{S}}$ , respectively. Detailed description of the UIR is shown in section 4.1.

The UIR  $h_{k,\text{MF}}$  to mass flow rate fluctuations is assumed to follow a Gaussian distribution of time lags with a mean  $\tau_1$  and a spread  $\sigma_1$ , corresponding roughly to the axial distribution of heat release and an overall convective velocity. An increase in the flow rate of premixture results in a corresponding increase in heat release. Thus the transfer function between fluctuations of flow rate and heat release of a perfectly premixed flame must be unity in the limit of zero frequency [159],

$$\lim_{\omega \rightarrow 0} F_{\text{MF}}(\omega) = \sum_{k=0}^L h_{k,\text{MF}} = 1 \quad \text{for } k = 0, \dots, L. \quad (3.11)$$

On the other hand, fluctuations of swirl do not supply additional premixture to the flame, therefore

$$\lim_{\omega \rightarrow 0} F_{\text{S}}(\omega) = \sum_{k=0}^L h_{k,\text{S}} = 0 \quad \text{for } k = 0, \dots, L, \quad (3.12)$$

which implies that some coefficients  $h_{k,\text{S}}$  *must* be negative.

Komarek and Polifke [103] have proposed to represent the UIR  $h_{k,\text{S}}$  to perturbations of swirl as a superposition of two Gaussian distributions of equal magnitude but with opposite signs. The distributions are defined by their mean time lags  $\tau_2, \tau_3$  and their spreads  $\sigma_2, \sigma_3$ , respectively.

The overall unit impulse response of a premix swirl flame is thus modeled as:

$$h_k = \frac{1}{\sigma_1 \sqrt{2\pi}} e^{-\frac{1}{2} \left( \frac{k\Delta t - \tau_1}{\sigma_1} \right)^2} + a \left( \frac{1}{\sigma_2 \sqrt{2\pi}} e^{-\frac{1}{2} \left( \frac{k\Delta t - \tau_2}{\sigma_2} \right)^2} - \frac{1}{\sigma_3 \sqrt{2\pi}} e^{-\frac{1}{2} \left( \frac{k\Delta t - \tau_3}{\sigma_3} \right)^2} \right). \quad (3.13)$$

The coefficient  $a$  is introduced in the present study to introduce intensity variations on the contribution of swirl fluctuations on the flame response.  $a$  is

equal to unity in the original model of Komarek and Polifke. The corresponding FTF in the frequency domain (cf [116, 178]) is written as:

$$FTF(\omega) \approx e^{-i\omega\tau_1 - \frac{1}{2}\omega^2\sigma_1^2} + a \left( e^{-i\omega\tau_2 - \frac{1}{2}\omega^2\sigma_2^2} - e^{-i\omega\tau_3 - \frac{1}{2}\omega^2\sigma_3^2} \right). \quad (3.14)$$

## 4 System Identification

The Flame Transfer Function can be determined by analytical, experimental or numerical methods as mentioned in Chapter 3. In experiments, the system is usually excited introducing harmonic excitation. In the presence of turbulent noise, fairly long time series over several hundred cycles are required to achieve good accuracy. If the flame transfer function is required over a range of frequencies, the procedure must be repeated many times, which is tedious, time consuming and costly.

The experimental approach of repeated, single-frequency spectral analysis could in principle also be used to determine the flame transfer function from CFD time series data. However, this would be compute intensive. Instead, advanced methods based on System Identification (SI) from digital signal processing have been developed for the identification of the flame transfer function and of acoustic elements [7, 85, 158, 160, 199]. In this chapter, basic background about system identification is presented in the beginning, followed by the description and derivation of the Wiener Filter. Finally, the LES/SI method is described for the identification of the flame transfer function.

### 4.1 Background

The idea of system identification is to “reconstruct” the dynamic behavior of a system, which is considered as a black box, based on input and output signals. A system can be categorized according to its number of inputs and outputs as follows:

- a) SISO: Single-Input Single-Output system (e.g., the FTF of a fully premixed turbulent flame, where the input is the velocity fluctuations; and the out-

put, the heat release fluctuations [199]).

- b) MIMO: Multiple-Input Multiple-Output system. (e.g., for the determination of the acoustic transfer or scattering matrix of a heat source [160] or of acoustic elements [57], where the system is excited by two or more sources at the same time from the inlets and the outlets).
- c) SIMO: Single-Input Multiple-Output system.
- d) MISO: Multiple-Input Single-Output system. (e.g., the FTF of a partially premixed turbulent flame, where the inputs are the velocity and equivalence ratio fluctuations; and the output, the heat release fluctuations).

A good overview of the description of these systems is presented in [80]. In Fig. 4.1, the different types of systems are shown indicating their inputs ( $s$ ) and outputs ( $r$ ). In these systems, the output  $r_l^*$  is defined by the response of the system ( $r_l = T[s_l]$ ) to the input signal  $s_l$  plus some “noise”  $e_l$ , which can be defined as an unwanted signal that interferes with the measurement of another signal [207].  $T[\ ]$  is defined as an operator performed by the system to reproduce the output signal  $r_l$  from the input signal  $s_l$ . This operator is for example the convolution of the input signal with the *Unit Impulse Response* ( $h$ ) of a *Linear, Time-Invariant* system. Then,

$$r_l^* = T[s_l] + e_l, \quad (4.1)$$

$$r_l = T[s_l]. \quad (4.2)$$

These systems can show different characteristics (linear, nonlinear, etc.). The different techniques to be applied to identify the system will depend on their characteristics [123]. For small levels of perturbation, the system’s response may be assumed to be *linear* (and *time-invariant*). A system is linear if the rules of homogeneity and additivity (called also the principle of superposition) can be applied on it [80]. For a homogeneous system, if an input signal  $s^{(1)}$  is scaled by a factor  $A$ , then its response  $r^{(1)}$  is also scaled by the same factor. A system is considered additive if the response to a sum of two signals ( $s^{(1)}$  and  $s^{(2)}$ ) is the sum of the two responses ( $r^{(1)}$  and  $r^{(2)}$ ) [80]. Furthermore, a system is considered time-invariant when the response does not depend on the

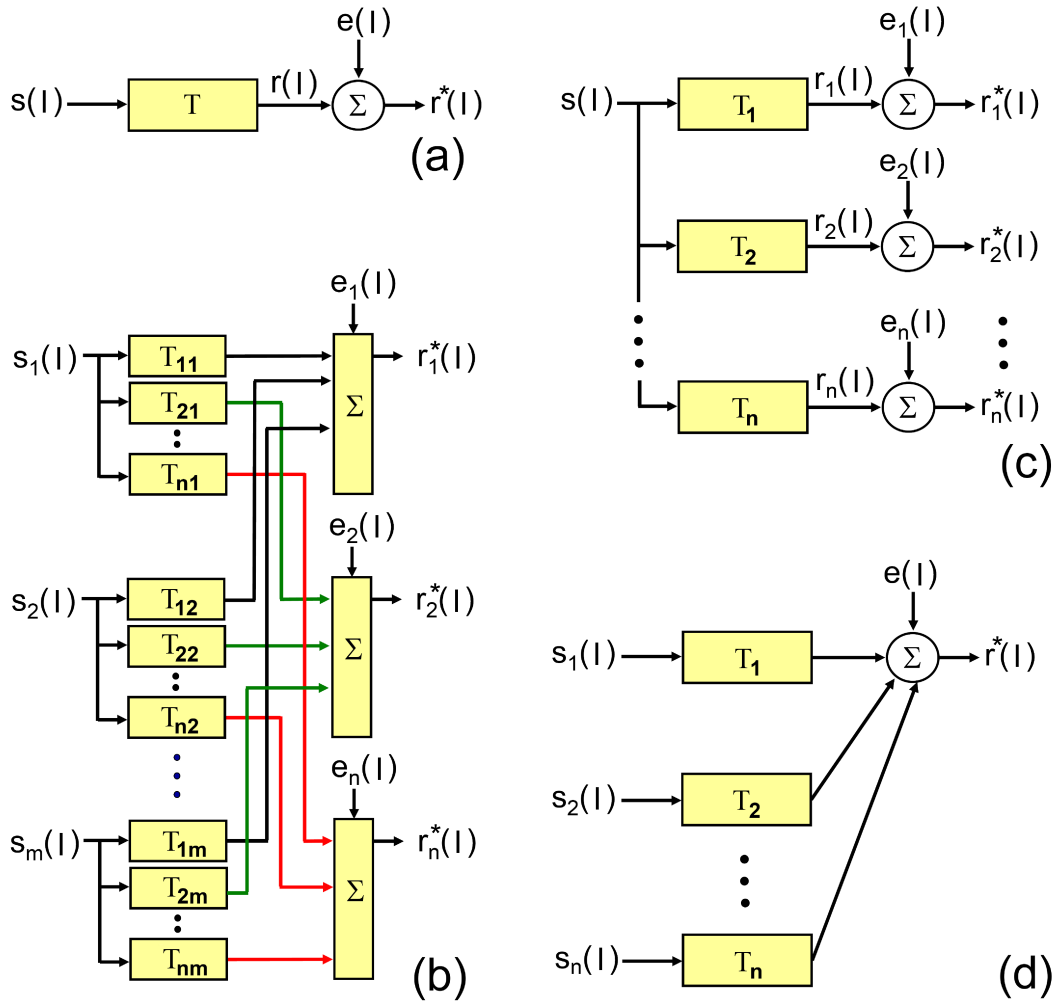


**Figure 4.1:** Different types of systems. a) SISO, b) MIMO, c) SIMO and d) MISO. Adapted from [80].

time when the input signal was applied. This means that a shift in the input signal leads to the same shift in the response (e.g., a signal  $s_l$  is applied today producing a response  $r_l$ , then if one applies the same signal but another day ( $s_{l+n}$ ), the same response ( $r_{l+n}$ ) will be produced). Then:

$$\text{Linear: } As^{(1)} + Bs^{(2)} \xrightarrow{\text{results in}} Ar^{(1)} + Br^{(2)}, \quad (4.3)$$

$$\text{Time-Invariant: } s_l = s_{l+n} \xrightarrow{\text{results in}} r_l = r_{l+n}. \quad (4.4)$$

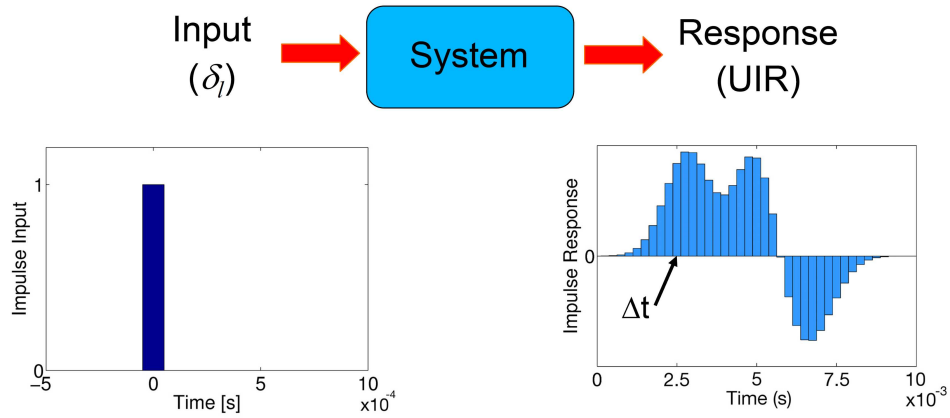


**Figure 4.2:** Unit Impulse Response of a FIR system.

A system with these characteristics is called *Linear Time-Invariant* (LTI). The advantage of using LTI systems is that they can be characterized by their *Unit Impulse Response* (UIR). The UIR is the response in time of a system to a Unit Sample (also called Unit Impulse) input signal ( $\delta_l$ ).  $\delta_l$  is defined by:

$$\delta_l = \begin{cases} 1 & \text{if } l = 0; \\ 0 & \text{if } l \neq 0. \end{cases}$$

Then,

$$\mathbf{h} = T[\delta_l], \quad (4.5)$$

where  $\mathbf{h}$  is the vector of coefficients of the UIR with a time increment  $\Delta t$ . A graphical interpretation of the UIR of a *Finite Impulse Response* (FIR) system is shown in Fig. 4.2. In a FIR system, the coefficients of the UIR are zero after a certain time, then the UIR can be defined for a certain number of coefficients. Figure 4.2 shows that after a pulse has been applied to the system at time 0, the system has a dynamic response in time to this pulse.

A system is also called *causal* if its response depends only on present and past inputs. Then, a LTI system is causal if and only if its impulse response is zero for negative  $l$  values in Eq. (4.5) (see [166]).

Taking into account the definition of the Unit Sample sequence  $\delta_l$ , an input signal  $s_l$  can be decomposed into a sum of weighted shifted Unit Sample se-

quences by [166]:

$$s_l = \sum_{k=-\infty}^{\infty} \delta_{l-k} s_k. \quad (4.6)$$

then the response of the system to  $s_l$  is the corresponding sum of weighted outputs [166]:

$$r_l = T[s_l] = T \left[ \sum_{k=-\infty}^{\infty} \delta_{l-k} s_k \right], \quad (4.7)$$

$$= \sum_{k=-\infty}^{\infty} T[\delta_{l-k}] s_k, \quad (4.8)$$

$$= \sum_{k=-\infty}^{\infty} h_{l-k} s_k. \quad (4.9)$$

Equation 4.9 is called the *convolution* operation. The convolution is commutative in the sense that any of the sequences can be shifted while the other is unaltered [166]. Then:

$$r_l = \sum_{k=-\infty}^{\infty} h_{l-k} s_k = \sum_{k=-\infty}^{\infty} h_k s_{l-k}. \quad (4.10)$$

For a LTI system, the output signal  $r_l$  is the *convolution* (Eq. (4.10)) of the input signal and its UIR. The goal for system identification of a LTI system is to “reconstruct” the UIR of the system.

The convolution of a causal LTI discrete system described by a FIR unit impulse response is defined by:

$$r_l = \sum_{k=0}^L h_k s_{l-k}, \text{ for } k = 0, \dots, L, \quad (4.11)$$

$$h_k \neq 0, \text{ for } 0 \leq k \leq L, \quad (4.12)$$

$$h_k = 0, \text{ everywhere else.} \quad (4.13)$$

$h_k(k = 0, \dots, L)$  is the  $k$ -th coefficient of the UIR  $\mathbf{h}$ .

## 4.2 The Wiener Filter

The Wiener filter was proposed by Norbert Wiener [217] to reduce the amount of noise present in a signal based on the Least Mean Square error estimation [122, 166, 207]. For our study, the Wiener filter is used to identify the different  $h_k$  coefficients of the UIR, which describe the flame response in time domain. The filter allows at the same time to reduce the influence of noise in the identification process. Different system identification methods exist in the literature (see [122, 123]), nevertheless the Wiener filter presents the advantage of being a robust system identification method which is very straight forward to implement. Furthermore, it requires only modest computational resources and time for the identification process. This makes it attractive to use for practical applications. Before the filter is described, some statistical terms are defined which are important for correlation analysis in discrete random processes:

- The mean value: For a sequence  $X_k$  with  $k=0, \dots, N$ ; its mean value is defined by:

$$\hat{\mu}_X = \frac{1}{N+1} \sum_{k=0}^N X(k). \quad (4.14)$$

- The cross-correlation: For two sequences  $X_k$  and  $Y_k$ , the cross correlation is a measure of similarity between the two sequences [166] and defined by:

$$c_i = \lim_{N \rightarrow +\infty} \frac{1}{2N+1} \sum_{k=-N}^N X_k Y_{k-i} \quad \text{for } i = 0, \pm 1, \pm 2, \dots, N. \quad (4.15)$$

For a sequence with a finite number of  $N+1$  samples in a causal FIR system, the cross-correlation is estimated as:

$$\hat{c}_i = \frac{1}{N+1} \sum_{k=0}^N X_k Y_{k-i} \quad \text{for } i = 0, \dots, L. \quad (4.16)$$

The index  $i$  is called the *lag* and indicates the (time) shift between the sequences.

- The auto-correlation: The autocorrelation is the cross-correlation of a signal with itself. It would sound strange to compare a signal with itself, but with the lag  $i$ , the signal is actually being compared at different times [193]. For a sequence with a finite number of  $N+1$  samples in a causal FIR system, the autocorrelation is estimated as:

$$\hat{\Gamma}_i = \frac{1}{N+1} \sum_{k=0}^N X_k X_{k-i} \text{ for } i = 0, \dots, L. \quad (4.17)$$

In the following, the Wiener filter is derived in the context of the identification of the Flame Transfer Function.

Consider the flame as the SISO system shown in Fig. 4.3, where the input signal is  $s_l = u'_{r,l} / \bar{u}$  and the output signal is  $r_l^* = \dot{Q}'^* / \bar{Q}$ .  $u'_{r,l} / \bar{u}$  represents the acoustic velocity fluctuation  $u'$  captured at a reference position and normalized by the mean velocity.  $\dot{Q}'^* / \bar{Q}$  is the heat release fluctuation from the flame including the influence of “noise” and normalized by its mean value. The “noise” in the output signal is produced by some response of the flame to some external perturbations (e.g., from turbulent fluctuations inside the combustor) which are not correlated to our input signal. It is assumed that the input signal and the “noise” are uncorrelated. The noise  $e_l$  is defined by:

$$e_l = r_l^* - r_l, \quad (4.18)$$

where  $r_l = \dot{Q}' / \bar{Q}$  is the system’s output without influence of noise.  $r_l$  is obtained from the convolution of the input signal  $s_l$  and the UIR of the flame:

$$e_l = r_l^* - \sum_{k=0}^L h_k s_{l-k}. \quad (4.19)$$

In the Least Mean Square error estimation, the idea is to minimize the error between a signal and a desired signal. In our case, the error consists of the estimation error plus the noise. The mean square error is computed and mi-

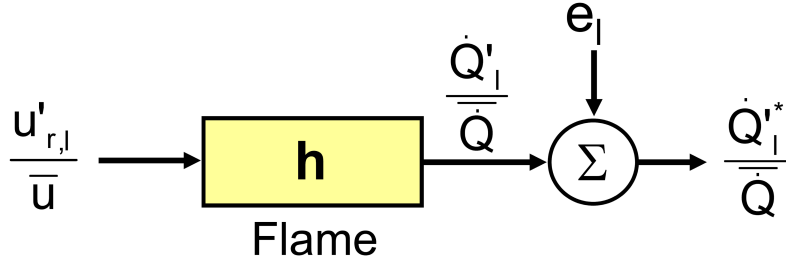


**Figure 4.3:** System for the Identification of the Flame Transfer Function

nimized with respect to the filter coefficients:

$$\hat{\mu}_{e_l^2} = \frac{1}{N+1} \sum_{l=0}^N \left( r_l^* - \sum_{k=0}^L h_k s_{l-k} \right)^2, \quad (4.20)$$

$$\hat{\mu}_{e_l^2} = \frac{1}{N+1} \sum_{l=0}^N \left[ (r_l^*)^2 - 2r_l^* \sum_{k=0}^L h_k s_{l-k} + \left( \sum_{k=0}^L h_k s_{l-k} \right)^2 \right]. \quad (4.21)$$

The Least Mean Square error is obtained by setting the derivative of Eq. (4.21) with respect to  $h_k$  equal to zero:

$$\frac{\partial \hat{\mu}_{e_l^2}}{\partial h_k} = \frac{-2}{N+1} \sum_{l=0}^N (r_l^* s_{l-k}) + \frac{2}{N+1} \sum_{l=0}^N \left( \sum_{j=0}^L h_j s_{l-j} \right) s_{l-k}, \text{ for } k = 0, \dots, L \quad (4.22)$$

$$0 = \frac{-2}{N+1} \sum_{l=0}^N (r_l^* s_{l-k}) + \frac{2}{N+1} \sum_{j=0}^L h_j \sum_{l=0}^N (s_{l-j} s_{l-k}) \quad (4.23)$$

$$\underbrace{\frac{1}{N+1} \sum_{l=0}^N (r_l^* s_{l-k})}_{\hat{c}_k} = \sum_{j=0}^L h_j \underbrace{\left[ \frac{1}{N+1} \sum_{l=0}^N (s_{l-k} s_{l-j}) \right]}_{\hat{\Gamma}_{k,j}}, \quad (4.24)$$

$$\hat{c}_k = \sum_{j=0}^L h_j \hat{\Gamma}_{k,j}. \quad (4.25)$$

where:

$$\sum_{l=0}^N s_{l-k} s_{l-j} = \sum_{l=0}^N s_{l-j} s_{l-k}. \quad (4.26)$$

Considering that  $N \gg L$ , the cross- and auto-correlation can be approximated as:

$$\hat{c}_k \approx \frac{1}{N-L+1} \sum_{l=L}^N r_l^* s_{l-k}, \text{ for } k = 0, \dots, L, \quad (4.27)$$

$$\hat{\Gamma}_{k,j} \approx \frac{1}{N-L+1} \sum_{l=L}^N s_{l-k} s_{l-j}, \text{ for } j, k = 0, \dots, L. \quad (4.28)$$

Equation (4.25) is defined in matrix form as:

$$\begin{pmatrix} c_0 \\ c_1 \\ c_2 \\ \vdots \\ c_L \end{pmatrix} = \begin{pmatrix} \Gamma_{00} & \Gamma_{01} & \Gamma_{02} & \cdots & \Gamma_{0(L)} \\ \Gamma_{10} & \Gamma_{11} & \Gamma_{12} & \cdots & \Gamma_{1(L)} \\ \Gamma_{20} & \Gamma_{21} & \Gamma_{22} & \cdots & \Gamma_{2(L)} \\ \vdots & \vdots & \vdots & \ddots & \vdots \\ \Gamma_{(L)0} & \Gamma_{(L)1} & \Gamma_{(L)2} & \cdots & \Gamma_{(L)(L)} \end{pmatrix} \begin{pmatrix} h_0 \\ h_1 \\ h_2 \\ \vdots \\ h_L \end{pmatrix} \quad (4.29)$$

$$\mathbf{c} = \mathbf{\Gamma} \mathbf{h}. \quad (4.30)$$

Equation (4.30) is called the Wiener-Hopf equation. By the inversion of the Wiener-Hopf equation, the vector of UIR coefficients ( $\mathbf{h}$ ) is obtained:

$$\mathbf{\Gamma}^{-1} \mathbf{c} = \mathbf{h}. \quad (4.31)$$

The auto-correlation matrix  $\mathbf{\Gamma}$  must be inverted to obtain the UIR coefficients  $\mathbf{h}$ . If the matrix is ill-conditioned, the accuracy of the solution will suffer for the solution of the linear system [80]. A system of equations is considered to be ill-conditioned if a small change in the coefficient matrix ( $\mathbf{\Gamma}$ ) or a small change in the right hand side of the system ( $\mathbf{c}$ ) results in a large change in the solution vector ( $\mathbf{h}$ ) [94]. In the case of ill-conditioned matrices, it is recommended to use appropriate numerical methods for the solution of the system, such as the LSQR method (an algorithm for sparse linear equations and sparse least squares) from Paige and Saunders [135]. Additionally, if the input signal is “white noise” (defined as an uncorrelated random process with equal power for all frequencies [207]), then the auto-correlation matrix reduces to the unit matrix and the UIR is equal to the cross-correlation [158].

### 4.3 The LES/SI Method

To perform the identification of the FTF, a LES simulation of the system under consideration is set up first. The use of non-reflective boundary conditions (NRBC) should be considered to avoid the development of resonance modes, which can degenerate the identification process due to an ill-conditioned auto-correlation matrix [221]. After obtaining a statistically stabilized solution, the system is excited with a broadband perturbation superimposed on the mean flow at the inlet. As the method is based on correlation analysis, having an input signal that is highly decorrelated with itself with “white noise” characteristics allows a faster decorrelation between the input signal and noise. Nevertheless, FTF investigations are usually limited to low frequencies (usually lower than 1000 Hz) as the flame response of most flames is quite low at high frequencies. Considering the small time steps used in compressible LES (in the range of  $10^{-6}$  and  $10^{-7}$  s), the level of decorrelation with itself (shown by the Autocorrelation) of the input signal is deteriorated as shown in the analysis of Appendix A.5. To generate a signal with high decorrelation characteristics for a limited frequency range more advanced methods should be applied as in [58], which is not investigated in this study.

Huber [83, 84] investigated various types of broadband excitation signals (overlaid multi-frequency, broadband white noise (WN) and discrete random binary signals (DRBS)) and their influence on identification quality. From these three types of excitation signals, the discrete random binary signal (which is created by a random process taking only values of  $\pm u_{\text{amp}}$  at any time) showed the best results as this kind of signal has the lowest crest factor and the highest power spectral density with respect to the other ones [83]. Then, this kind of signal is recommended for the excitation. A detailed description of the DRBS signal is shown in Appendix A.5.

During the excitation process, the perturbations will propagate to the flame front and create a response in the heat release of the flame. A plane is defined upstream of the flame at a reference position, and area-averaged instantaneous axial velocity values are exported at each time step (or in short intervals) from this plane. The global heat release is obtained by a volume

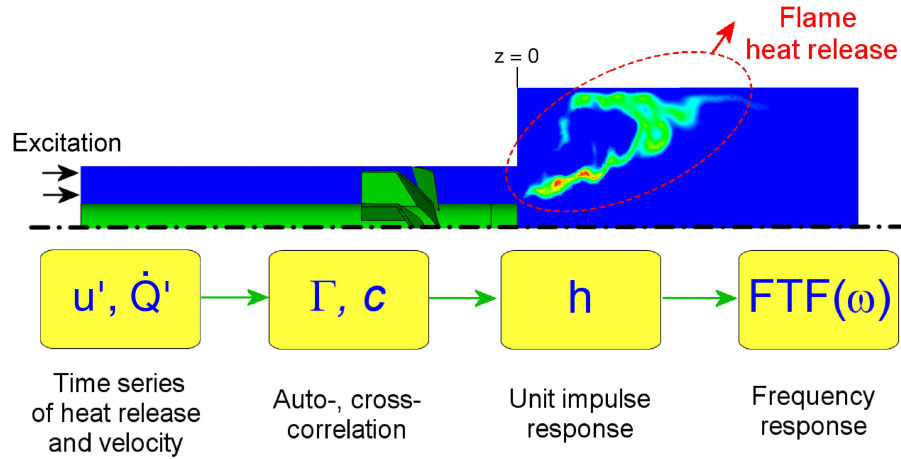


**Figure 4.4:** LES/System Identification process

integration of the heat release over the computational domain and also exported at each time step (or interval). These time series will be imported into a post-processor. The mean values (computed as the mean value of the extracted time series) of axial velocity  $\bar{u}$  and heat release  $\bar{Q}$  are subtracted from the exported time series to obtain their fluctuations ( $u'$ ,  $\dot{Q}'$ ). These values are normalized with the mean values of velocity and heat release. To obtain the acoustic velocity at the reference plane, the characteristics based filter (CBF) [105] has been used to identify the acoustic plane wave component. After this procedure, the auto-correlation matrix  $\Gamma$  and cross-correlation vector  $\mathbf{c}$  of the signals are calculated (see Eqs. (4.27) and (4.28)). Then, the Wiener-Hopf equation is inverted (Eq. (4.31)) to obtain the unit impulse response  $\mathbf{h}$  of the signals. The sum of all coefficients in the UIR is equal to unity, in agreement with the zero frequency limit for the amplitude of the FTF [159]. To obtain this, the number of coefficients should be selected to cover all the responses during a period of time equal to  $L\Delta t$ .  $\Delta t$  is the time increment of the UIR coefficients. Finally, the UIR is transformed from the time domain to the frequency domain using the z-transform defined by:

$$\text{FTF}(\omega) = \sum_{k=0}^L h_k e^{-i\omega\Delta tk} = A(\omega) e^{i\theta(\omega)}. \quad (4.32)$$

Here  $h_k$  ( $k = 0, \dots, L$ ) is the  $k$ -th coefficient of the UIR  $\mathbf{h}$ , with time increment  $\Delta t$ .  $L$  is the maximum index of the UIR coefficients.

A flow chart of the LES/SI method is given in Fig. 4.4 [199]. The advantage of using the LES/SI method is that it is possible to obtain the frequency flame response over a range of frequencies from a single CFD simulation, reducing the computational effort (“You can shoot all the birds that you want with only one shot”).

## 5 Identification of Flame Transfer Functions using LES/SI

In this chapter, the flame dynamics of an axial swirl burner is investigated by the determination of its Flame Transfer Function with the LES/SI method. The experimental set-up is introduced at the beginning, followed by the validation of the method with experiments. The case of a nonadiabatic combustor with 30 kW is used as reference for the validation. After that, the geometrical and operating conditions in the combustor and burner are varied by changing the thermal conditions at the combustor walls, increasing combustor cross section area, changing the position of the swirler and increasing the power rating, to study the impact of these variations on the flame dynamics. All experimental data was carried out and provided by T. Komarek [104].

### 5.1 Experimental Set-up of the BRS Burner

The BRS (Beschäufelter RingSpalt) burner is a swirl-stabilized burner with an axial swirl generator developed by Komarek and Polifke [103] in the framework of the KW 21 project GV 6 Premixed Flame Dynamics. A scheme of the experimental set-up is shown in Fig. 5.1. The burner is operated in “perfectly premixed” mode with a completely homogeneous mixture of natural gas and air to eliminate any equivalence ratio fluctuations. The experimental set-up consists of a cylindrical plenum followed by the burner with the axial swirl generator of 30 mm length mounted on a central bluff body. The burner exit has an annular section with an inner and outer diameter of 16 and 40 mm, respectively. A combustor of quadratic cross section of 90×90 mm and a length of 300 mm follows the burner. With this combustor length, the test conditions were stable to perform OH chemiluminescence, flow field and FTF measure-

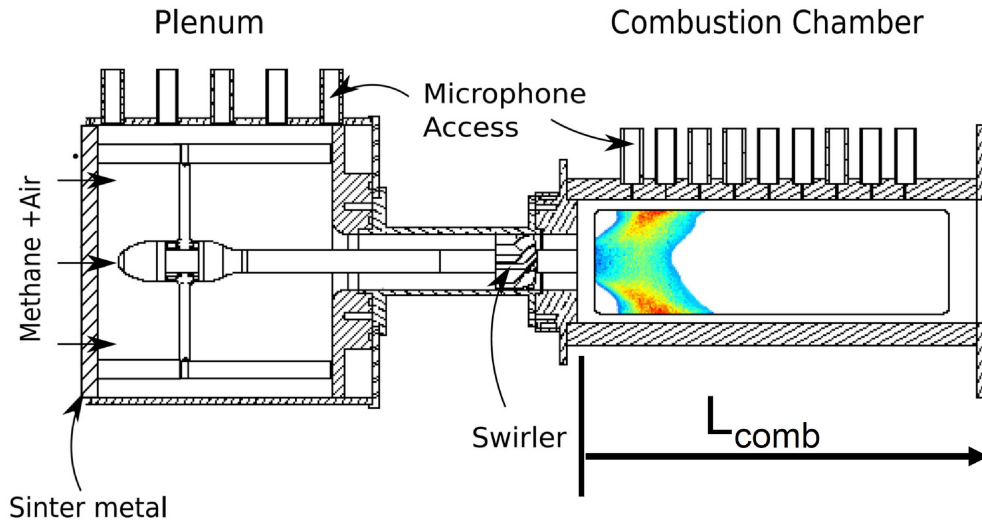


**Figure 5.1:** Scheme of the BRS burner test rig. The sinter metal plate is installed **only** for stability analysis.

ments. The combustor can be also increased to a length of 700 mm. The end of the combustion chamber is equipped with a perforated plate with 6 holes of 20 mm of diameter in order to create a low reflective acoustic boundary condition. The position of the swirler is variable. For the reference case (section 5.2), the swirler position is 30 mm upstream of the burner exit. A different swirler position at 130 mm was investigated also experimentally by Komarek [103] to identify the impact of swirler position in the flame transfer function.

To obtain the flame transfer function, the velocity signal is obtained by Constant Temperature Anemometry (CTA) measurements. The CTA was initially positioned between swirler and burner exit, however the signal obtained at that position was strongly affected by turbulent noise, making it not optimal for the measurement [102]. It should be taken into account that a CTA measures the velocity at only one reference point, and that the measured velocity includes turbulent and acoustic fluctuations. Thus, strong turbulent fluctuations, as the ones created after the swirler, can have an impact on the accuracy of the measurements. As mentioned by Kim et al. [96], the axial swirler can be considered *acoustically transparent*, meaning that the amplitude and phase of the acoustic waves are not significantly affected by the swirler. Thus, the CTA

probe would be positioned upstream of the swirl generator. Nevertheless it should be taken into account the compactness between the reference position and the burner exit. The acoustic compactness is evaluated by a Helmholtz number (He) defined by:

$$\text{He} = \frac{l_d}{l_\lambda}, \quad (5.1)$$

where  $l_\lambda$  is the acoustic wave length defined by:

$$l_\lambda = \frac{a}{f}, \quad (5.2)$$

where  $a$  is the speed of sound, and  $f$  is the frequency.  $l_d$  is the distance between the reference position and the burner exit. Compactness is achieved for  $\text{He} \ll 1$ . The new position of the CTA probe is at 10 mm upstream of the swirl generator, which corresponds to a distance of 70 mm to the burner exit. Considering that the maximum excitation frequency for the identification is 500 Hz, the maximum He is equal to 0.1. Acoustic compactness is assumed for this value. To evaluate the influence of this modification on the FTF, the FTFs identified with LES/SI at two different reference positions are also compared. For the identification of the FTF using the Wiener-Hopf Inversion, an internal code developed at the Lehrstuhl für Thermodynamik in TU München [56] called WHI (Wiener-Hopf-Inverter) is used.

## 5.2 Reference Case with 30 kW of Power Rating

### 5.2.1 Numerical Set-up and Boundary Conditions

In Fig. 5.2, the geometry / computational domain of the BRS burner is shown. A full 3D unstructured mesh consisting of around 7.5 million cells was created using the program Gambit. The plenum of the combustion test rig was not included in the computational domain in order to reduce computation requirements and to impose an excitation signal without resonance peaks in the power spectral distribution. The combustor size in the simulations was set to 200 mm to reduce computational requirements, taking into account that

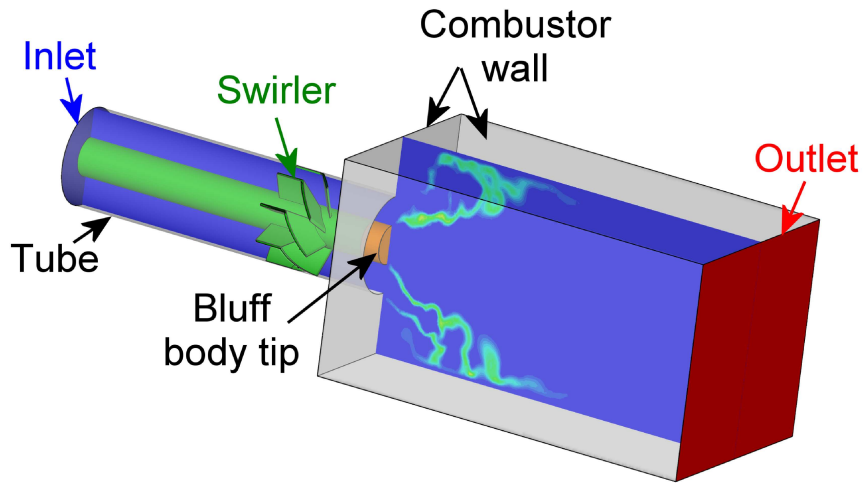


**Figure 5.2:** Scheme of the numerical set-up of the BRS burner

the size of the flame and of the recirculation zone were around the half of this value and far from the outlet.

For the reference case, the full compressible multi-species Navier-Stokes equations are solved for a methane-air mixture with an equivalence ratio ( $\phi$ ) of 0.77 at atmospheric conditions for 30 kW of power rating. The subgrid stresses are modeled using the WALE model [133]. Reacting flow calculations are carried out using the Dynamically Thickened Flame combustion model with one step kinetics and a maximum thickening factor value of 5, which is selected to match the heat release distribution. Details on the one step global reaction mechanism are specified in Appendix A.3. The Lax-Wendroff second order numerical scheme [132] is chosen as discretization scheme. The temporal integration is carried out using a single step explicit scheme. The code has a very low level of acoustic dissipation using these numerical schemes when a mesh resolution higher than 40 cells per wave length is applied [57]. The time step of the simulations is  $1.25 \times 10^{-7}$  s to ensure an acoustic CFL number lower than 0.7.

For the inlet and outlet, the non-reflective boundary conditions from Kaess et al. [89] are applied. These boundary conditions are based on the Navier-Stokes Characteristics-based Boundary Conditions (NSCBC) of Poinot and Lele [149] including the techniques of “plane wave masking” [162] and Cha-

**Table 5.1:** Boundary Conditions

B. Condition	Type	Details
Inlet (30 kW)	Non-reflective velocity inlet	$V_{\text{inlet}}=11.3$ m/s
Outlet	Non-reflective pressure outlet	$P_{\text{outlet}}=101325$ Pa
Combustor wall	Isothermal no-slip wall	$T_{\text{Wall\_isot}}=600$ K
Tube/swirler	Adiabatic no-slip wall	-
Bluff body tip	Isothermal no-slip wall	$T_{\text{Wall\_isot}}=600$ K

racteristics Based Filter [105]. The simulation is carried out considering non-adiabatic conditions on the combustor walls. The nonadiabatic combustor walls and the bluff body tip are no-slip isothermal walls with a temperature of 600 K, which is an estimated value from wall temperature measurements performed in another combustor at similar conditions [47]. The boundary conditions are indicated in Table 5.1 and shown in Fig. 5.2.

Velocity measurements were not carried out for this power rating. Experiments were performed only for the heat release using the line-of-sight integrated OH chemiluminescence as indicator. For the measurements, in order to separate the signal from other emissions, an interference filter centered on a wavelength of 307.1 nm with a half power bandwidth of  $10\pm 2$  nm and a transmission of 15% was used. The signal was recorded with an intensified CMOS camera. 200 pictures with a recording time of about 4 s were averaged in order to determine the steady state average of the OH chemiluminescence emissions.

### 5.2.2 Comparison of Mean Flame Heat Release from LES and Experiments

The averaging time in the simulations to obtain the mean heat release is 125 ms. This represents  $10^6$  iterations with a time step of  $1.25\times 10^{-7}$  s. To compare experiments with simulations, the averaged heat release from LES is integrated over the depth of the combustion chamber, in order to determine the distribution in correspondence to the line-of-sight integrated view. To perform this task, a post processing tool is developed in the program TECPLOT.

Details of this tool are found in Appendix A.10. In Fig. 5.3, the normalized (with its maximum value) spatial distribution of OH chemiluminescence and heat release from experiments and simulations, respectively, are shown. Good agreement is found between LES and experiments due to the correct flame stabilization predicted in the simulations [199]. In experiments, the combustor walls are cooled down using convective cooling, resulting in significant heat loss for the combustion products in the outer recirculation zone. Thus the flame is quenched in the outer shear layer and stabilizes predominantly in the inner shear layer with the characteristics of a “V-flame”. In simulations, isothermal nonadiabatic walls are used to take into account the effects of heat losses on flame stabilization. If the heat loss effect is not taken into account (e.g. using adiabatic walls in the combustor or using combustion models without an influence from heat loss), the flame shape can exhibit a different topology. For comparison, the line-of-sight integrated view of the flame using adiabatic walls is additionally shown in Fig. 5.3(c) and discussed in more detail in section 5.4.

In Fig. 5.4, the axial heat release distributions from experiment and simulations are shown. The values are normalized taking into account that the area of the distribution from experiments and simulations should be the same, because the same amount of fuel is burnt in both cases. Good agreement is achieved, but with a slight difference in the position of the maximum heat release.

### **5.2.3 Comparison of Identified and Experimental Flame Transfer Function with 30 kW**

To identify the flame transfer function, perturbations on the characteristic ingoing wave are imposed at the inlet using broadband excitation with a frequency-limited (1000 Hz) discrete random binary signal (see Appendix A.5). A signal with an amplitude of 6.5% of the inlet mean velocity is used initially. The amplitude of the signal is increased in subsequent simulations. The simulation is run for 250 ms in real time (2 million iterations). This simulation time gives a frequency resolution of 4 Hz, which nominally is also the

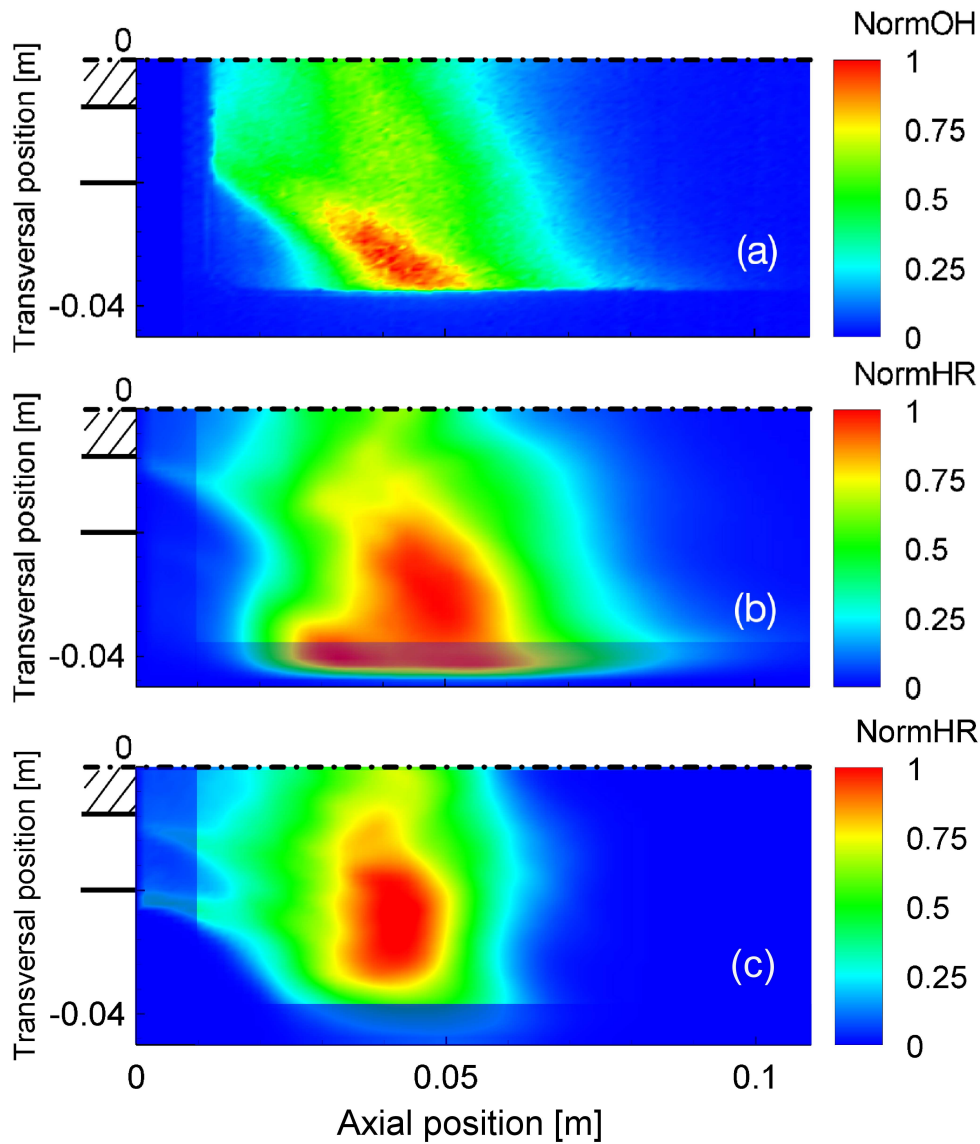


**Figure 5.3:** Normalized spatial heat release distribution: (a) OH chemiluminescence from experiments, (b) Averaged LES at nonadiabatic conditions, and (c) at adiabatic conditions. Line-of-sight integrated heat release for simulations. Dump plane of combustor at axial position = 0 m.

lowest resolved frequency. The acoustic velocity fluctuations are obtained at 70 mm upstream the burner exit as in the experiments. For the identifica-

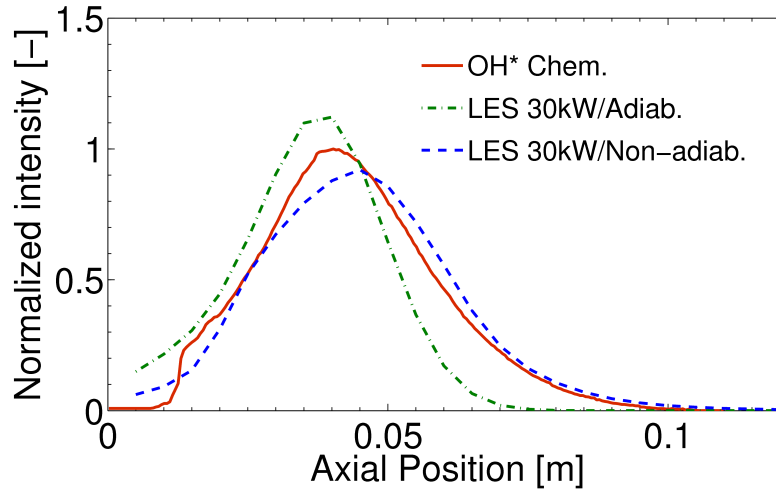


**Figure 5.4:** Area normalized axial heat release distribution.

tion process, the first 190000 iterations are considered as a transition period and not taken into account. Axial velocities and volume integrated heat release are extracted “on-the-fly” every 10 iterations during the simulations. The signals are then filtered to remove frequency content higher than 600Hz. The Wiener-Hopf inversion is then applied to obtain the UIR; and finally via  $z$ -transform, the flame transfer function is identified in amplitude and phase (see Fig. 4.4). In Fig. 5.5, the flame transfer functions from experiment and LES/SI are shown with good agreement between them. The experimental and identified FTF show amplitudes higher than 1 for frequencies below 175 Hz and a decrease at higher frequencies. The observed excess in gain of the FTF (amplitudes  $> 1$ ) is related to a constructive interaction of acoustic and swirl fluctuations [78, 103, 137] (see section 5.5.2). Moreover, instabilities are more susceptible to develop under this condition [181]. The phase of the transfer function, which is of particular importance for thermo-acoustic instability, was also well reproduced for frequencies below 260 Hz, where the amplitudes of the experimental and identified FTF have good agreement. At higher frequencies, the agreement between experiment and simulations decreases, exhibiting high deviations in the phase. These discrepancies could be produced by limitations of the combustion model to capture the response at high frequencies, or also by a low signal-to-noise ratio in the identification. In LES,

the resolved turbulent fluctuations result in a low signal-to-noise ratio for the higher frequencies, where the coherent flame response is weak as shown in Fig. 5.7. For the FTF, the signal-to-noise ratio is the ratio of the flame response which corresponds to the imposed excitation to the one produced by another perturbation which is not related to our excitation signal. The turbulent fluctuations inside of the combustor, which are broadband and considered uncorrelated to our excitation signal, can be comparable in magnitude to the acoustic perturbations (especially for systems with high Reynolds numbers). Using the Wiener Filter, the response from noise is “filtered” by correlation, but the identification process is deteriorated under low signal-to-noise ratios [83]. The signal-to-noise ratio can be increased applying a higher excitation signal, but with a signal still in the linear regime. Results are additionally plotted by the Strouhal number, defined by [137]:

$$\text{Str} = \frac{f D_{\text{ext}}}{u_{\text{bexit}}}, \quad (5.3)$$

where  $f$  is the frequency,  $D_{\text{ext}}$  is the external diameter of the burner exit, and  $u_{\text{bexit}}$  is the mean axial velocity at the burner exit. The maximum amplitude of the FTF is shown at  $\text{Str} \approx 0.35$ .

The reference position for the measurement of the velocity fluctuations is ideally at the burner exit, where the perturbations will reach the flame and the flame response begins. Nevertheless, as mentioned before, in the experiment the CTA was necessarily positioned in an upstream location to perform more accurate measurements. To look at the influence of the velocity reference position on the identification of the flame transfer function, the acoustic velocity ( $u'_r$ ) fluctuations from simulations and normalized by their mean values at positions 0 and 70 mm upstream the burner exit in time and frequency domain are shown in Figs. 5.6 and 5.7, respectively. The heat release ( $\dot{Q}'$ ) is additionally shown. For frequencies higher than 260 Hz, the flame response weakens. The acoustic velocity exhibits similar values at both positions. This confirms the observation of Kim et al. [96] that the axial swirler can be considered *acoustically transparent*. The flame transfer functions identified with LES/SI at reference planes upstream ( $z=0$  mm) and downstream ( $z=-70$  mm) of the swirler show similar amplitudes and phases. Similar behavior is observed using a different excitation amplitude (see Fig. A.8). The low impact of the axial swirler

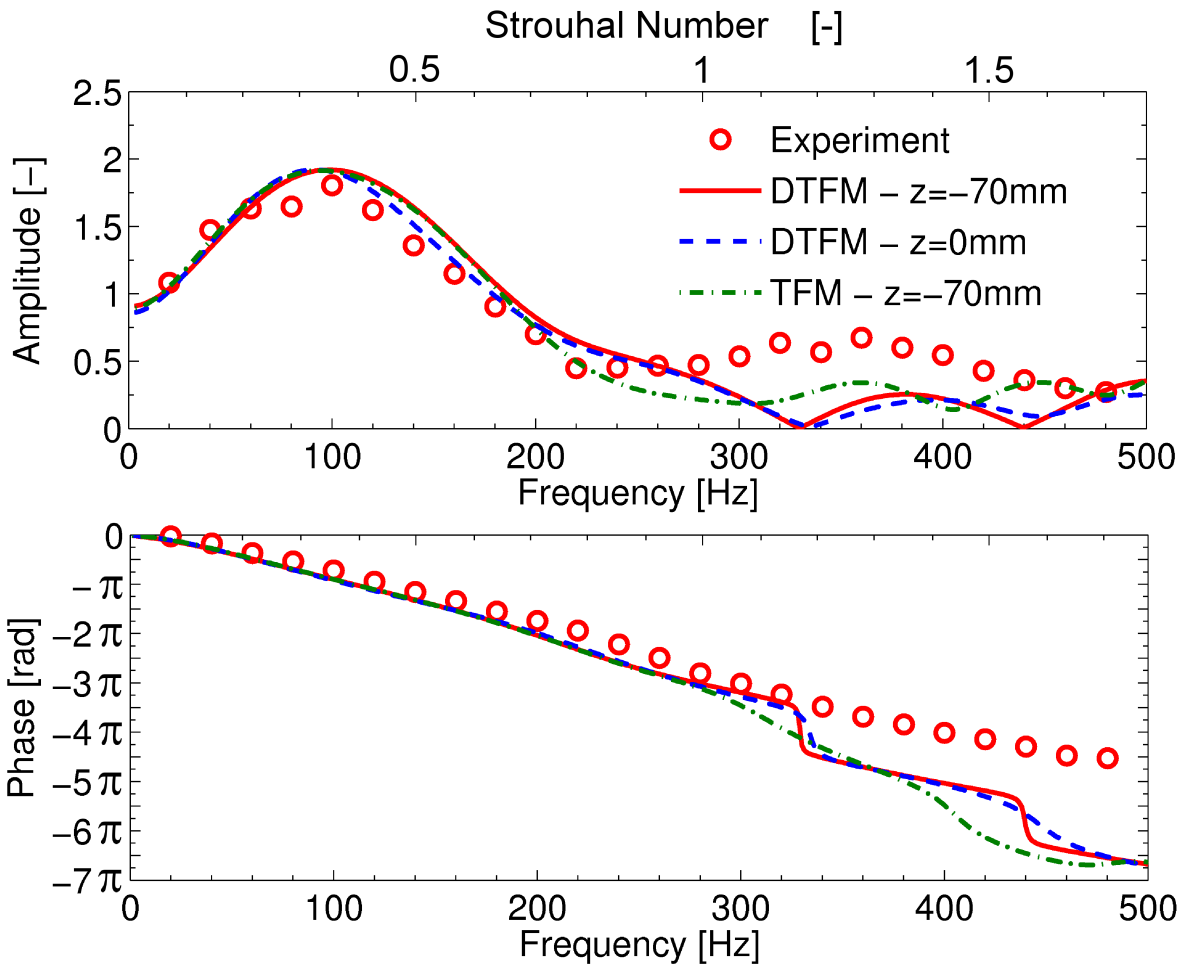


**Figure 5.5:** Flame transfer functions from experiments and LES/SI for case with 30 kW. Excitation=6.5%.

on the FTF has been observed also by Palies et al. [138]. It should be taken into account that in our work, and in the ones from Kim et al. [96] and Palies et al. [138], the excitation frequencies are below 500 Hz, which gives a  $He \approx 0.1$  at  $z=-70$  mm. At much higher frequencies, the velocity fluctuations might be affected due to the lower compactness. For example, in Fig. 5.7 it is shown that the difference in the amplitude of the power spectrum increases for frequencies higher than 300 Hz.

The flame transfer function is also identified using the Thickened Flame Model to compare with the Dynamically Thickened Flame Model. The same

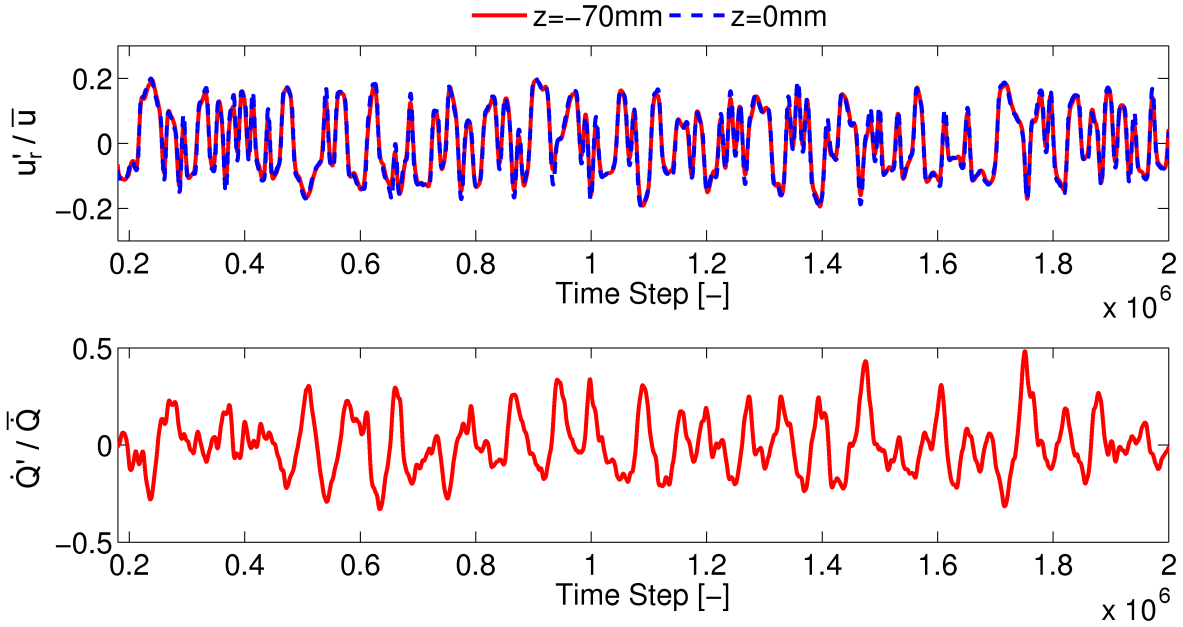


**Figure 5.6:** Heat release ( $\dot{Q}'$ ) and acoustic velocity ( $u'_r$ ) fluctuations at 0 and 70 mm upstream of the burner exit (Dump plane of combustor at  $z=0$  mm) normalized by their mean values without filtering for case with 30 kW.

excitation signal is imposed on both simulations. The flame transfer functions with both combustion models exhibit similar response in amplitude and phase for frequencies lower than 200 Hz. For higher frequencies, small variations between both models are shown. The use of the DTFM is preferable over the TFM, because it gives a better representation of the diffusion terms. As this case is under fully premixed conditions, both models show only small differences between them on the flow field and flame.

#### 5.2.4 Comparison of Different Excitation Amplitude on Flame Transfer Function Identification

In Fig. 5.8, the identification results of the case with 30 kW using an input signal with larger amplitudes (9.5% of the inlet mean velocity) is shown. The flame response is still considered linear for this increased amplitude [96].

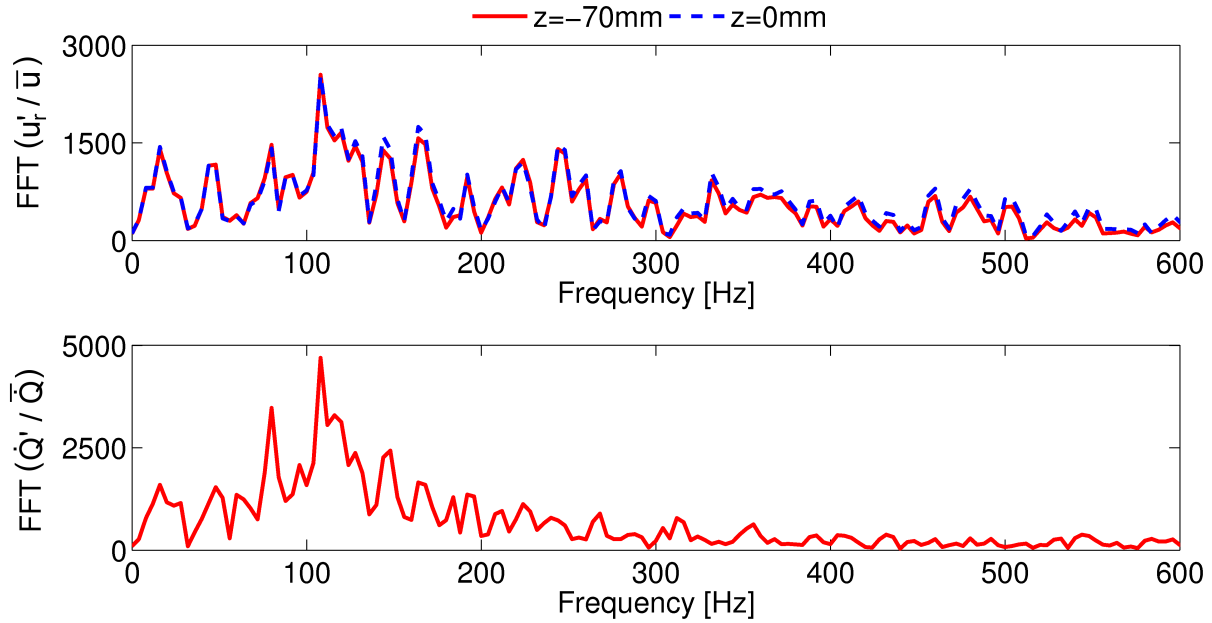


**Figure 5.7:** Power spectrum of acoustic velocity ( $u'_r$ ) fluctuations at 0 and 70 mm upstream of the burner exit and of heat release ( $\dot{Q}'$ ) normalized by their mean values without filtering for case with 30 kW.

Comparing both FTFs with experiment, the case with 9.5% shows a better agreement with the experiments and also on the low frequency limit, where the amplitude should approach unity. The case with 6.5% of excitation amplitude shows in the limit to 0 Hz an amplitude lower than 1; while in the case with 9.5%, it approaches 1. Furthermore, the discrepancies in the phase for frequencies higher than 300 Hz mentioned in section 5.2.3 are not present with the excitation of 9.5%. The increase in signal-to-noise ratio by increasing the signal amplitude can improve the identification. To evaluate linearity and possible inaccuracy in the identification, harmonic excitations at 100 Hz are run for 1040000 iterations, which represents 13 cycles with a time step of  $1.25 \times 10^{-7}$  s. The first 240000 iterations are not taken into account, as they are considered as a transition period. To determine the amplitude and phase for the harmonic excitation, a pure-tone Fourier transform defined by [177]:

$$y(\omega_{PT}) = \frac{2}{N} \sum_{n=1}^N y(n\Delta t) e^{-i\omega_{PT}n\Delta t}, \quad (5.4)$$

is applied, where  $y$  is the variable to be analyzed,  $N$  is the number of samples,  $\Delta t$  is the time step of the samples and  $\omega_{PT}$  is the angular frequency at the frequency of interest. The plots of the amplitude from the pure-tone Fourier Transform for the normalized heat release and velocity fluctuations with 6.5% and 9.5% of excitation amplitude are shown in Fig. 5.9. The ratio between the amplitudes at different excitation amplitudes is in good agreement with the ratio of 6.5/9.5. The amplitude and phases from the harmonic excitations at 100 Hz are shown in Fig. 5.8, presenting similar values with both excitation amplitudes and close to the identified FTF using 9.5%. This indicates that the flame exhibits a linear response and that the identification is improved using the higher excitation amplitude. Nevertheless, in both cases the amplitude for frequencies higher than 300 Hz is lower than in experiments.

## 5.3 Influence of Variation in Power Rating on the Flame Transfer Function

The same burner might be used with an increase of mixture mass flow to increase the power rating. Then the flow field and turbulence levels at the burner and combustor will change, affecting also the flame. To compare the influence of different power rating on the flame transfer function, the velocity at the inlet is incremented to 19 m/s, which corresponds to a power rating of 50 kW. The mean flow field and mean heat release from experiment and simulation are compared in a first step, followed by the identification of the FTF.

### 5.3.1 Comparison of Mean Flow Field and Flame Heat Release from LES and Experiments at 50 kW

The averaged flow fields from non-reacting as well as reacting flow simulations (without excitation) are compared against particle image velocimetry (PIV) data. The averaging time for the simulations is 37.5 and 57.5 ms for the non-reacting and reacting case, respectively. In Fig. 5.10, axial velocity profiles at the middle cross plane for various positions of the combustor are shown.

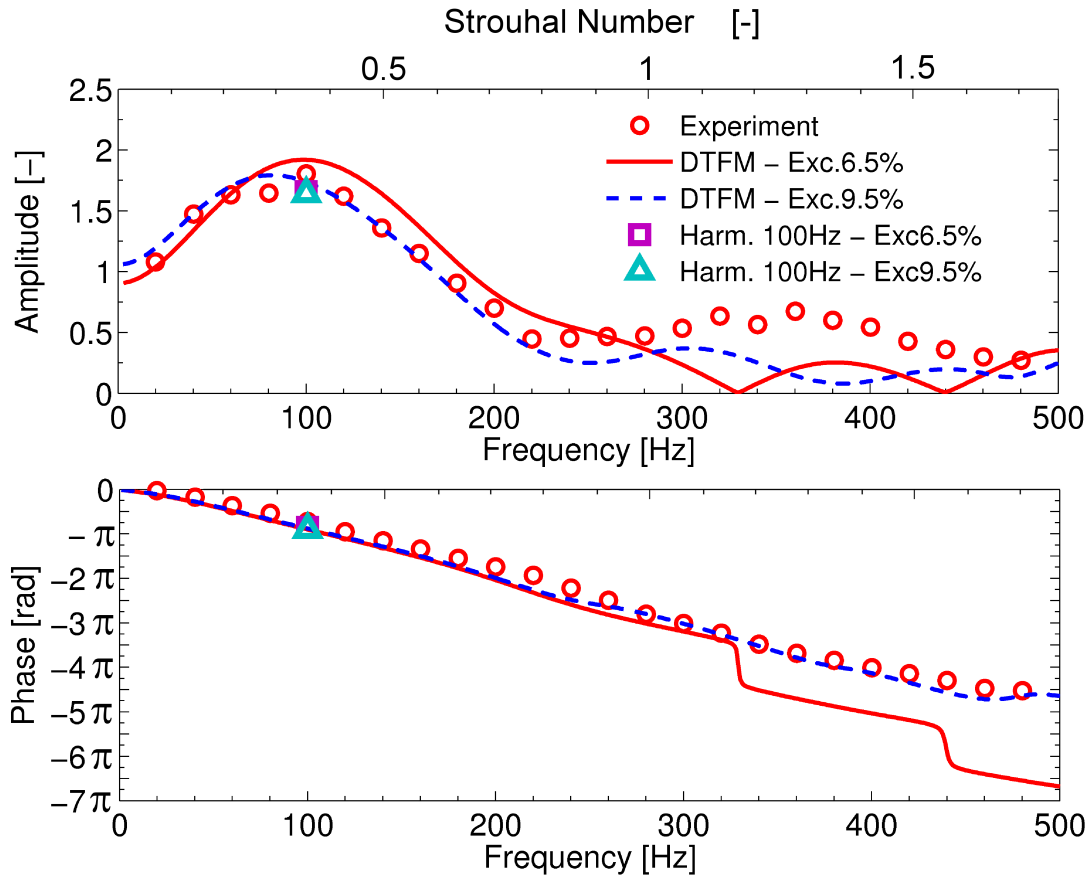


**Figure 5.8:** Flame transfer functions from experiments and LES/SI for case with 30 kW with different excitation amplitude. Harmonic excitation at 100 Hz for 6.5% ( $\square$ ) and 9.5% ( $\triangle$ ) of amplitude.

A grey line at zero axial velocity is introduced to indicate the position of the recirculation zone. The agreement with experiment for non-reacting flow is very good. The size of the recirculation zone and velocity magnitudes are well reproduced. The presence of a precessing vortex core was observed. For the reacting case, the agreement is satisfactory, although the velocities inside the recirculation zone are not well reproduced. In both cases, inner and outer recirculation zones are created due to the strong swirl and the confinement created by the combustion chamber. A comparison of the axial velocity contours between the non-reacting and the reacting case is shown in Fig. 5.11. The reacting case shows a shorter and broader recirculation zone than the

### 5.3 Influence of Variation in Power Rating on the Flame Transfer Function

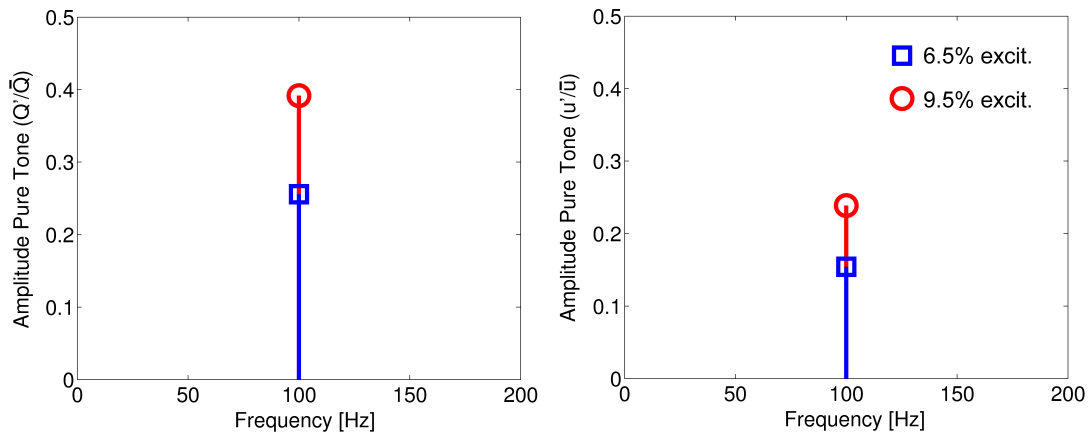


**Figure 5.9:** Amplitudes from the pure-tone Fourier Transform for the normalized heat release and velocity fluctuations for 6.5% and 9.5% of excitation amplitude.

non-reacting case. Furthermore, the zones of maximum negative velocity in the inner recirculation zone for the reacting case are more downstream from the burner exit than in the non-reacting case. Higher velocities on the shear layer are produced by the flow expansion from the heat release of the flame. Additionally, the angle of the jet from the burner exit increases with combustion [4]. In Fig. 5.12, the profiles of turbulent kinetic energy calculated using Eq. (2.6) with the rms values of the velocity fluctuations for non-reacting and reacting flow are shown. The values with combustion are much higher due to the higher fluctuations induced in the flow by the flame. Strong differences on flow field and turbulence between non-reacting and reacting simulations are shown. This indicates that using non-reacting simulations or experiments to estimate other variables or parameters for cases involving combustion can produce inaccuracies due to the mismatches shown before.

In Figs. 5.13 and 5.14, the spatial and axial distributions of OH chemiluminescence from experiments and the heat release from simulations are shown, exhibiting good agreement between them. The flame is longer than the one in the 30 kW case due to the higher velocities.

During the simulations with 50 kW, a transversal eigenmode at 3920 Hz developed in the combustion chamber, which matches with the first (fundamen-

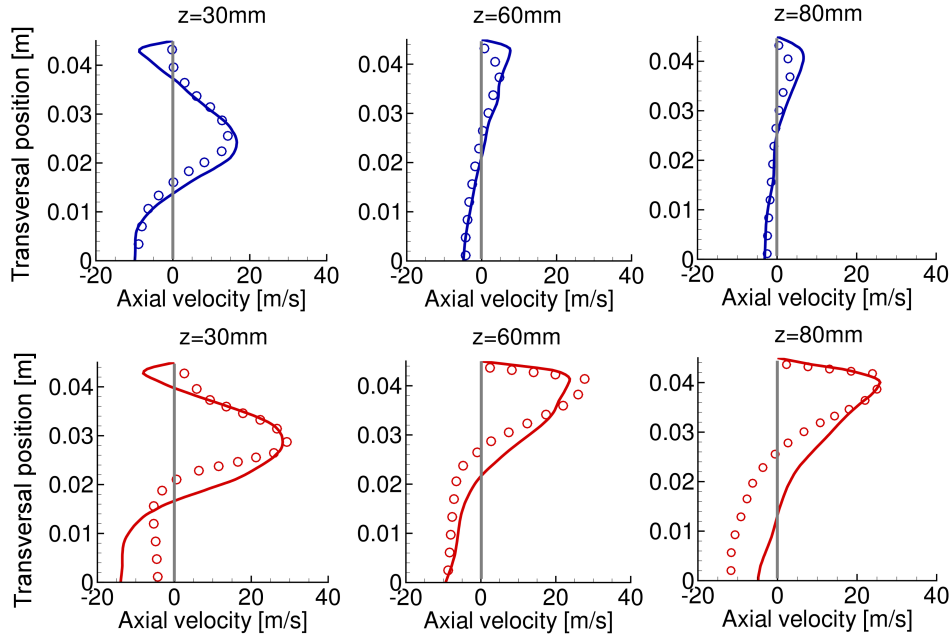


**Figure 5.10:** Mean axial velocity profiles with non-reacting flow (top) and with reacting flow (bottom) at the middle cross plane shown in Fig. 5.2 for 50 kW. o Experiments, - LES. Grey line to indicate zero-axial velocity.

tal) transversal eigenfrequency of the geometry. Similar experiences have been reported by Selle et al. [184]. The transversal mode shown in Fig. 5.15 is due to a combination of the two degenerate transversal modes. The high frequency instability did not appear in experiments. In experiments, the combustor walls have certain level of acoustic damping by vibration, which is not taken into account in numerical simulations. Some acoustic damping is created due to the wall heat losses. Nevertheless if the instability driving mechanisms are higher than the damping mechanisms in the system, as indicated by the Rayleigh criterion, an instability develops. It is argued that the damping in the simulations is lower than in experiments. In the nonadiabatic case with 30 kW, the transversal mode did not develop. The acoustic power produced by the flame increases with the increase of power rating [79]. Thus the flames in simulations with higher power rating in the same system are more susceptible to develop an acoustic instability. This was confirmed by a LES simulation at 70 kW, where the transversal mode developed in a shorter time and stronger

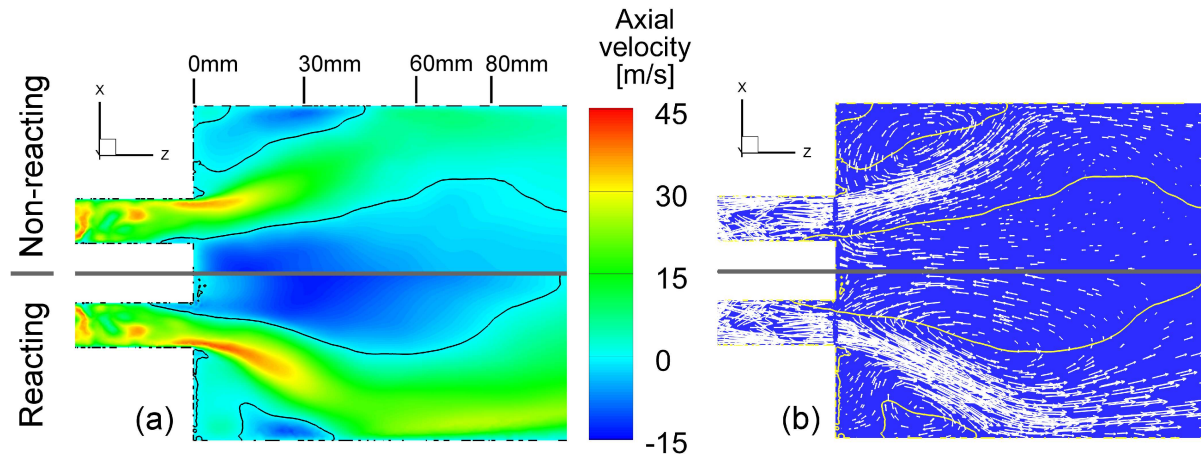


**Figure 5.11:** Contours of mean axial velocity (left) and velocity vectors (right) for non-reacting (top) and reacting (bottom) flow from simulations. Zero-axial velocity isolines in black (left) and yellow (right)

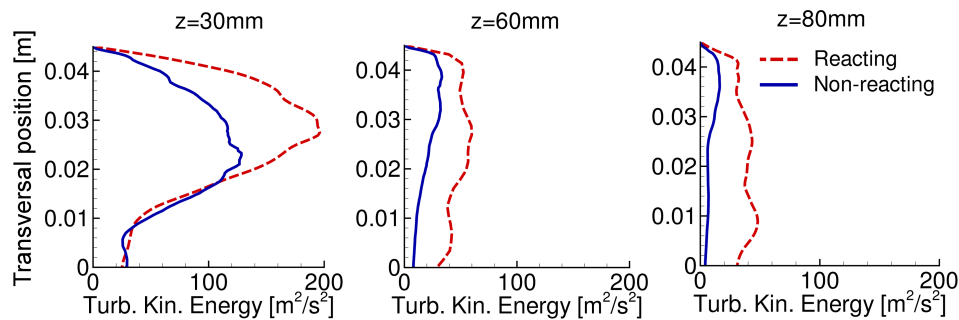


**Figure 5.12:** Turbulent kinetic energy profiles with non-reacting flow and reacting flow from simulations at the middle cross plane shown in Fig. 5.2 for 50 kW.

than in the 50 kW case. Furthermore, the boundary conditions at the inlet and outlet have a one-dimensional formulation and are non-reflective for plane waves. The transversal fluctuations created by the transversal mode are not dumped using this formulation. Boundary conditions should include additional terms to take into account three-dimensional effects on the reflection coefficient or impedance. The NSCBC of Poinot and Lele [149] has been recently extended by Granet et al. [71] to include a transversal contribution to the boundary condition in the incoming wave, which is aimed to reduce spu-

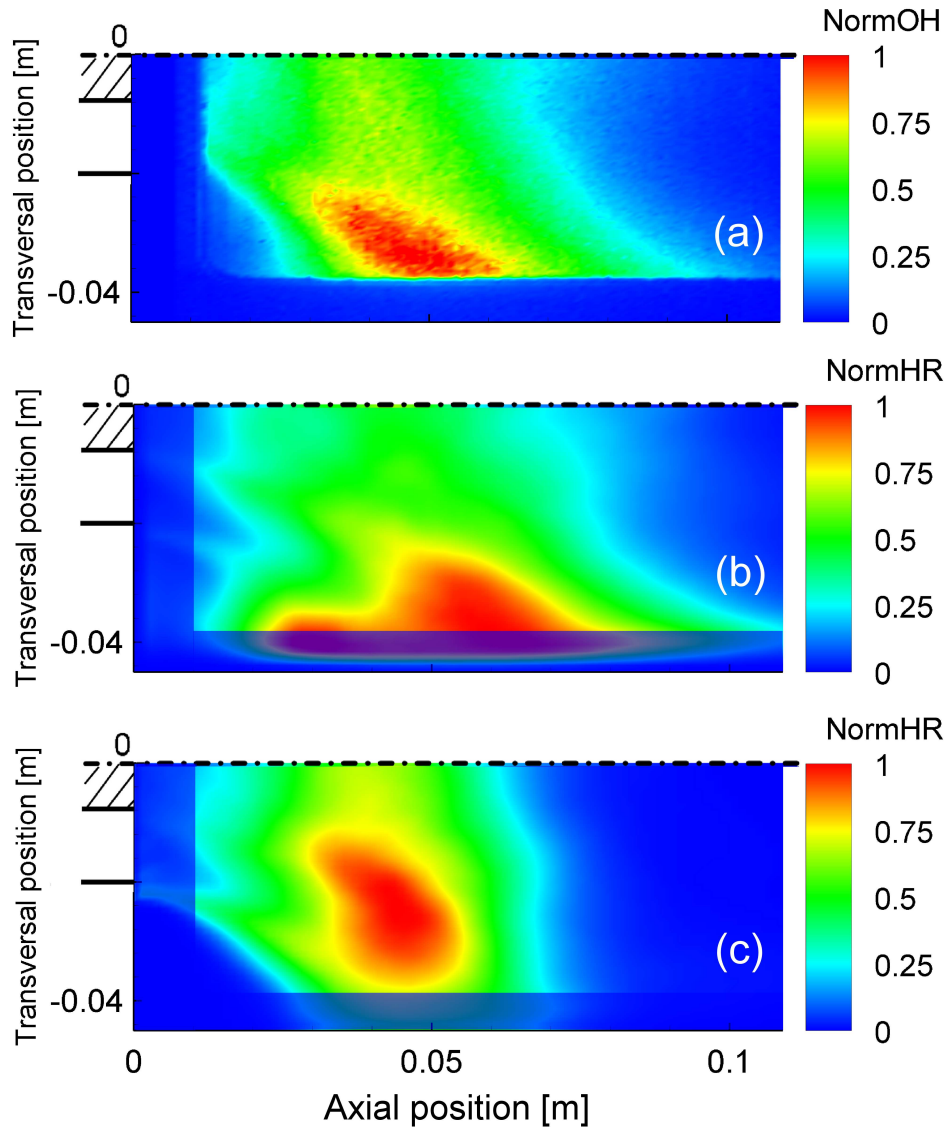


**Figure 5.13:** Normalized spatial heat release distribution for 50 kW: (a) OH chemiluminescence from experiments, (b) Averaged LES at nonadiabatic conditions, and (c) at adiabatic conditions. Line-of-sight integrated heat release for simulations. Dump plane of combustor at axial position = 0 m.

rious acoustic wave reflections [23]. This boundary condition is not applied as it is not available in the version of AVBP (6.0) used in this study.

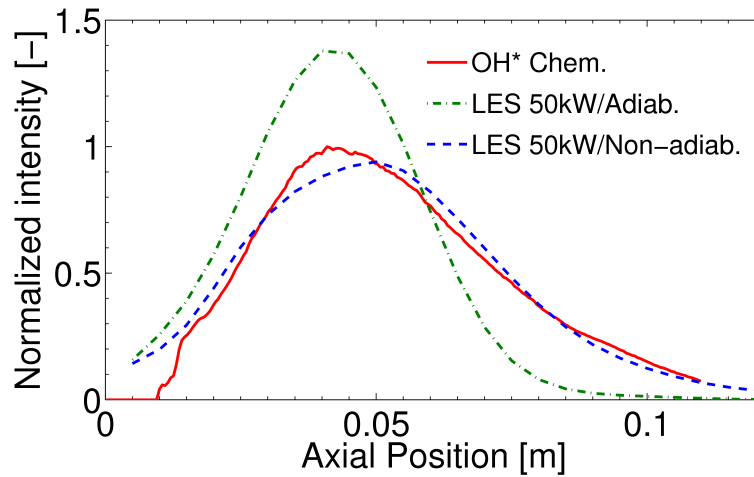


**Figure 5.14:** Area normalized axial heat release distribution for 50 kW.

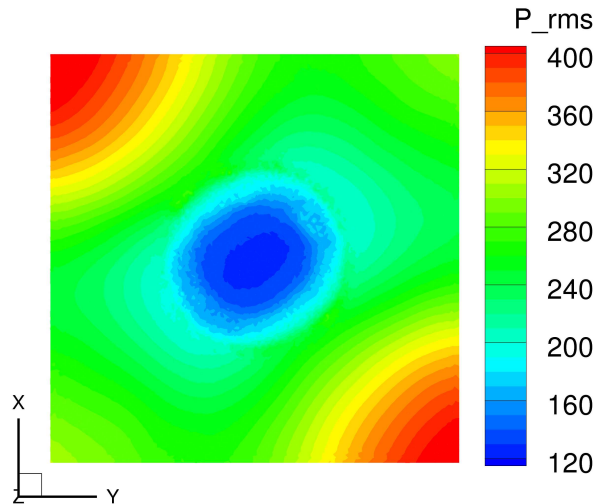


**Figure 5.15:** Transversal mode on combustion chamber for 50 kW. Contours of rms pressure at cross plane 10mm downstream the burner exit

### 5.3.2 Comparison of Identified and Experimental Flame Transfer Function with 50 kW

To perform the identification of the FTF, the excitation is initially carried out using the same signal of the 30 kW case, but scaled for 50 kW with an amplitude of 6.5% of the inlet mean velocity. The FTF identified from a single time

series of length 1800000 (STS) and filtered to 600 Hz is presented in Fig. 5.16. The level of agreement with the experimental data is not satisfactory. Strong oscillations in the amplitude and phase are present. It is expected that the significant disagreements are due to the influence of “noise”, i.e. turbulent “pseudo sound”, fluctuations of the heat release produced by resolved turbulent fluctuations, and in particular perturbations introduced by the transversal modes, which grow to significant amplitudes after about 750000 iterations, as shown in Figs. 5.17 and 5.18. These perturbations introduce spurious contributions to the auto- and cross-correlations  $\Gamma$  and  $\mathbf{c}$  of signal and response, respectively, and thus deteriorate the quality of the identification scheme. In general, the identification quality can be improved by using a longer time series [84]. This is not possible in the present case due to the unstable transversal mode, which kept growing in amplitude as the run continued.

Attempts to suppress the transversal mode were not successful, therefore a “work-around” is devised: In order to obtain a more robust identification, time series generated from several LES runs are combined. Two methodologies were developed. In the first one, called *Multiple Time Series* (MTS), the auto- and cross-correlation coefficients from various runs are combined into a multiple time series auto- and cross-correlation by an averaging procedure, thus suppressing the relative magnitude of uncorrelated noise. Each run started from the same initial condition, but used different excitation time series, generated from various seeds of the random number generator. The combined auto- and cross-correlation coefficients are approximated by:

$$\hat{\Gamma}_{k,j}|_{\text{MTS}} \approx \sum_{i=1}^{\text{MS}} \left( \frac{1}{N-L+1} \sum_{l=L}^N s_{l-k} s_{l-j} \right)_i, \text{ for } j, k = 0, \dots, L, \quad (5.5)$$

$$\hat{c}_k|_{\text{MTS}} \approx \sum_{i=1}^{\text{MS}} \left( \frac{1}{N-L+1} \sum_{l=L}^N r_l^* s_{l-k} \right)_i, \text{ for } k = 0, \dots, L. \quad (5.6)$$

where MS is the number of multiple sequences with the number of elements N. The WHI is applied using  $\hat{\Gamma}_{k,j}|_{\text{MTS}}$  and  $\hat{c}_k|_{\text{MTS}}$  as the auto- and cross-correlations. The second method is called *Single Joint Time Series* (SJTS). For creating a SJTS, first a long time series is created from the random number generator as the base excitation signal (see Fig. 5.20(a)). Similar to the MTS

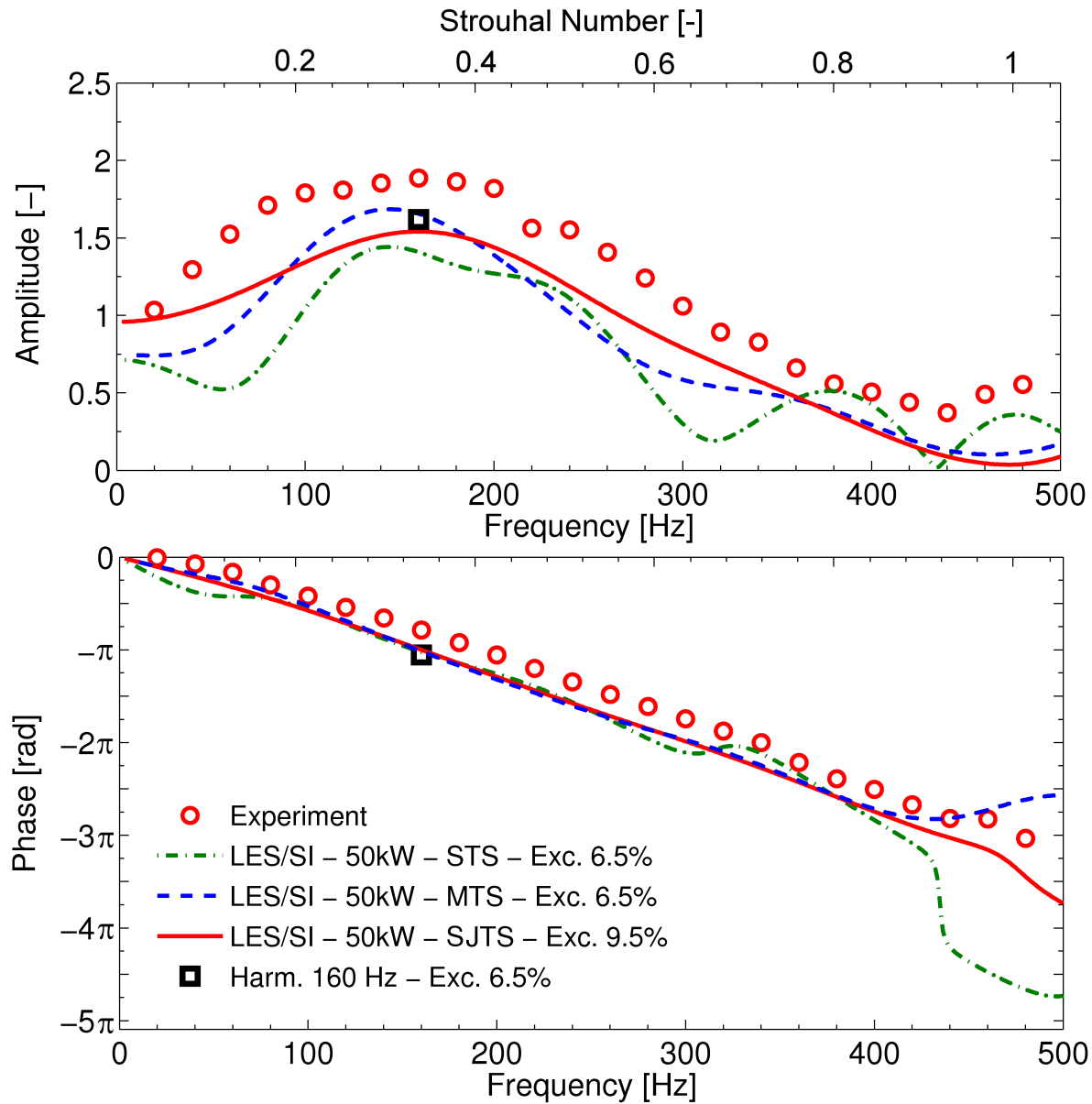


**Figure 5.16:** Flame transfer function from experiments, LES/SI with a single time series (STS), multiple time series (MTS) and single joint time series (SJTS) for 50 kW and different excitation amplitudes. (□): Harmonic excitation at 160 Hz and 6.5% of amplitude.

method, several runs of 750000 iterations are also combined, but the idea is to create a *single joint time series* from all the runs. The method is based on the

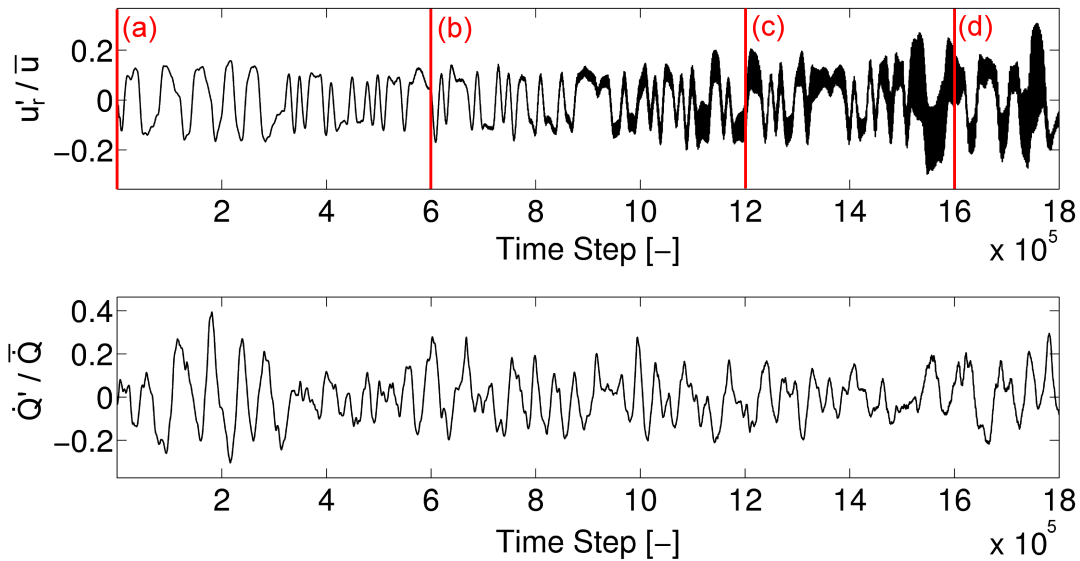


**Figure 5.17:** Heat release ( $\dot{Q}'$ ) and acoustic velocity ( $u'_r$ ) fluctuations at 70 mm upstream of the burner exit (Dump plane of combustor at  $z=0$  mm) normalized by their mean values without filtering for case with 50 kW.

concept of *linear and time-invariant* systems. If the same system is excited using two different simulations (similar to say at two “different times”) and with the same excitation signal, the response of both simulations will be similar. Thus various simulations can be used to “continue” a previous one. This is illustrated in the following example: In Fig. 5.19, two input signals (normalized velocity fluctuations) are shown with their respective responses (normalized heat release fluctuations). The system is excited first with signal 1 until 750000 iterations. After this, the same system at the same initial point of the run with signal 1 is excited with signal 2 also for 750000 iterations. The values of signal 2 in the first 250000 iterations are the same as the last 250000 values of signal 1. It is shown that after a time interval (approx. 55000 iterations), both cases exhibit the same response. At this point both signals can be joined into a *single joint time series* consisting in information from signal 1 from iterations 0 to 555000 and from signal 2 from iterations 555000 to 1250000. The joint time series can be extended with additional simulations. In this way, the influence of the transversal mode is reduced and it is possible to obtain a single long

### 5.3 Influence of Variation in Power Rating on the Flame Transfer Function

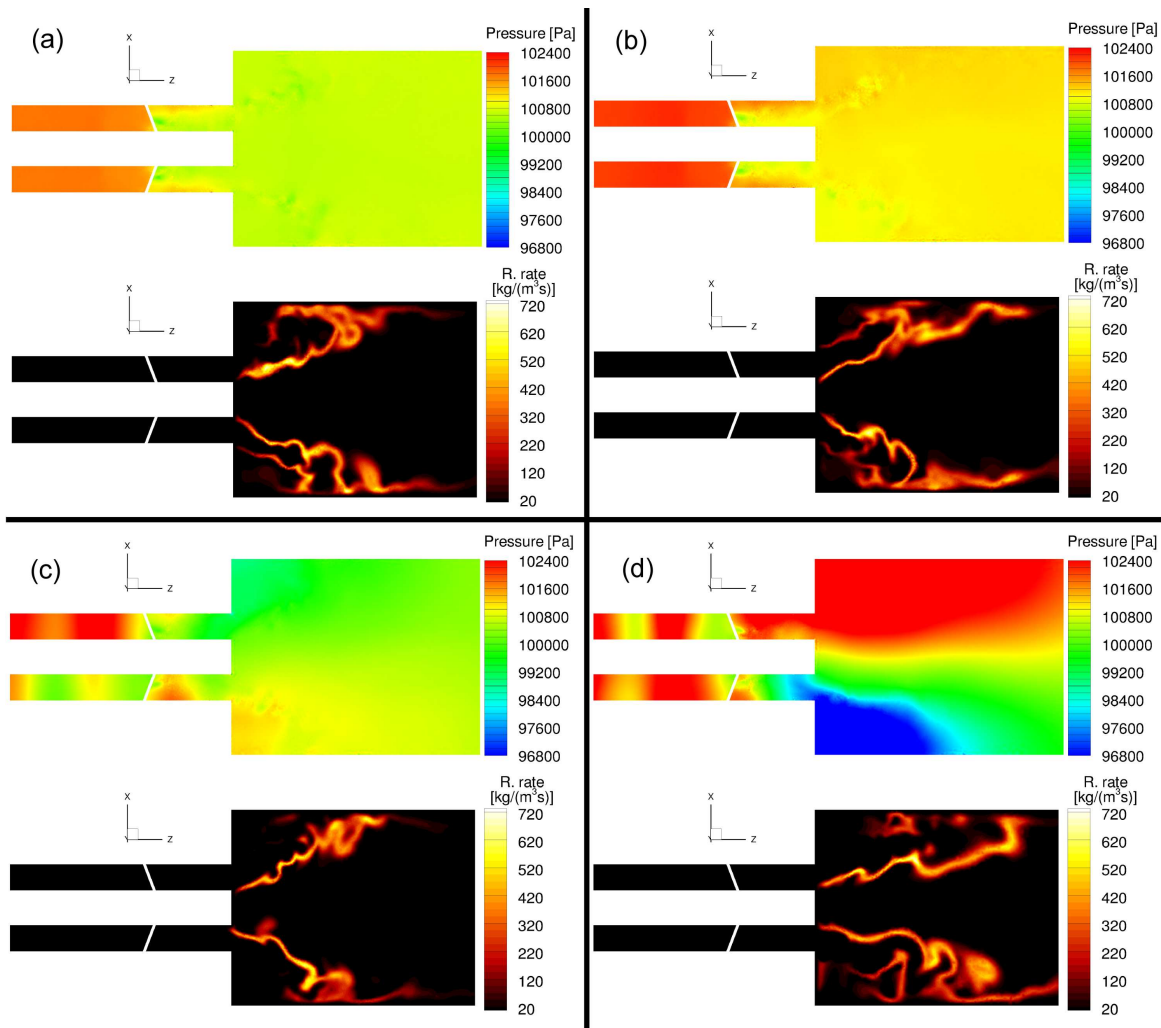


**Figure 5.18:** Snap shot of instantaneous absolute pressure and reaction rate at combustor middle cross plane during excitation with 50 kW. The time of the snap shot is indicated in Fig. 5.17.

time series of velocity and heat release fluctuations to compute their auto- and cross-correlation. In Fig. 5.20, the sequence of the excitation signals used for the identification of the FTF with the SJTS is shown.

In Fig. 5.16, results for the flame transfer function from MTS and SJTS are also shown for different excitation amplitudes. For the MTS case with 6.5% of excitation amplitude, four different excitation signals of length 750000 with the same statistical characteristics as the single signal excitation are used. The first

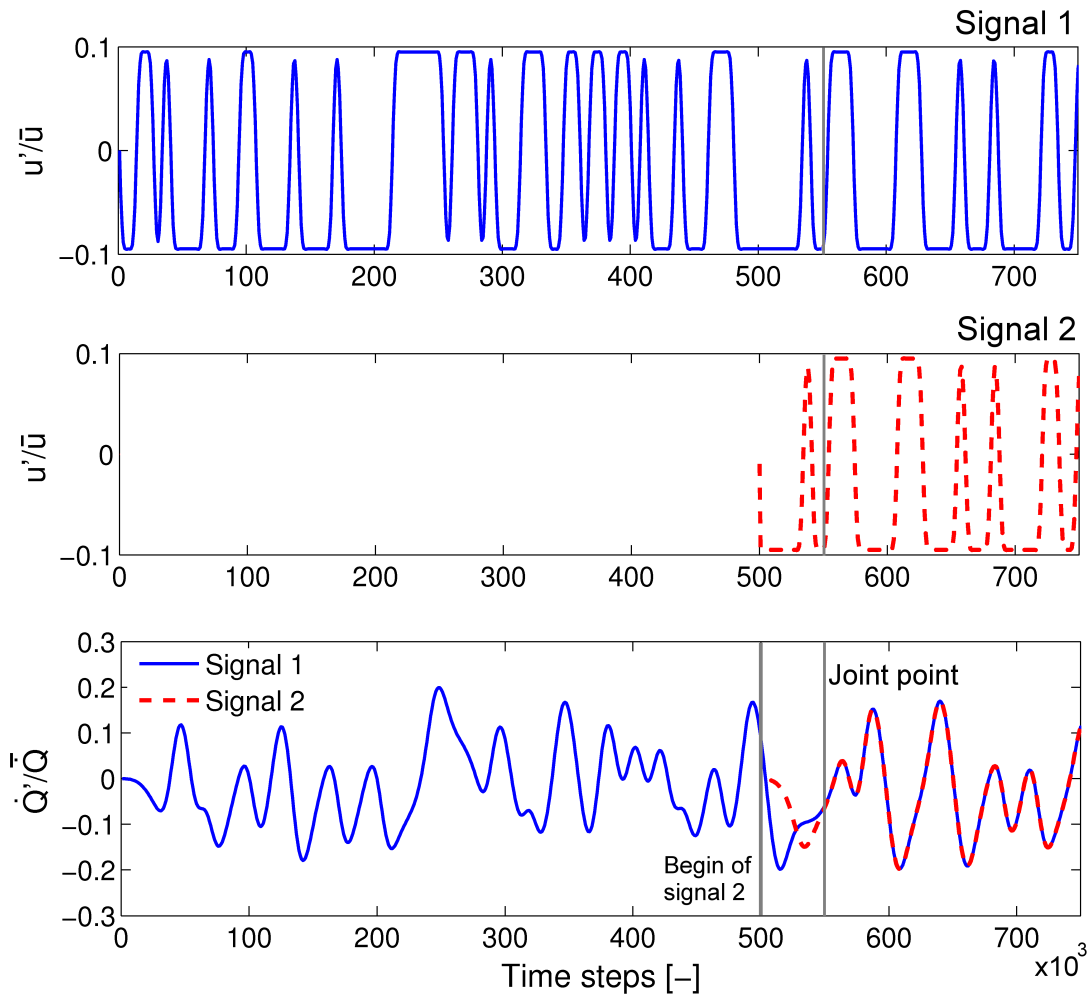


**Figure 5.19:** Illustration of single joint time series (SJTS) method

$10^5$  iterations are not considered. It can be seen that the agreement with experiment is noticeably improved, but the identified FTF exhibits an amplitude of 0.75 at the lowest frequency identified. However, the amplitude of the Flame Transfer Function should approach unity in the limit of low frequency [159]. Huber and Polifke [84] have investigated the influence of noise on the identification of the FTF and indeed observed decreased gain at low frequencies if high levels of noise are present. The transversal mode develops perturbations inside the combustion chamber, which create a certain level of response that is introduced as “noise” to the signal, not allowing for a “clean” identification process to identify the FTF. It affects not only the response, but also

### 5.3 Influence of Variation in Power Rating on the Flame Transfer Function

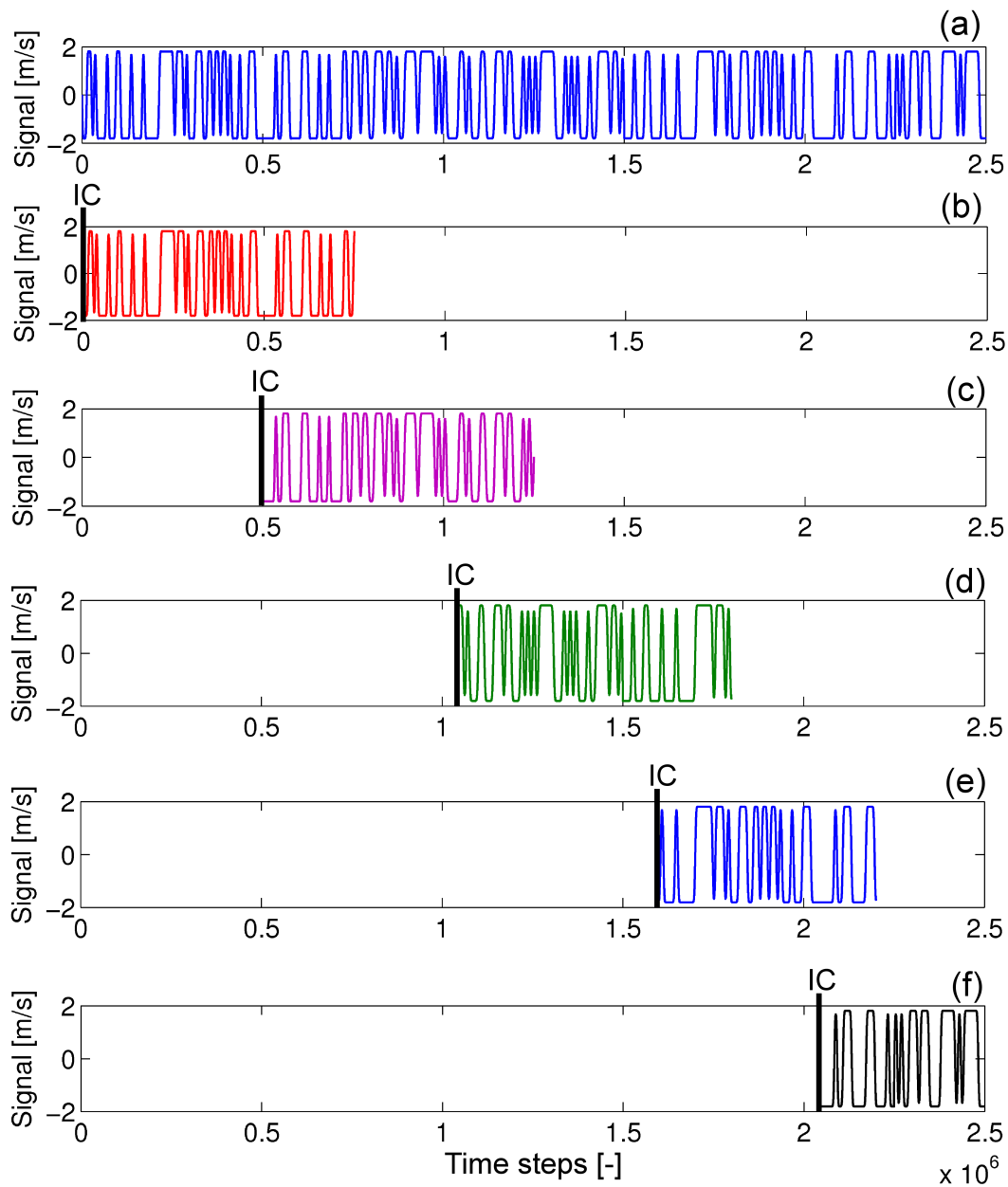


**Figure 5.20:** Sequence of excitation signals in the single joint time series (SJTS) method for 50 kW and excitation=9.5% amplitude of the mean inlet velocity.

can introduce perturbations into the burner as shown in Fig. 5.18, which can influence the identification process. The agreement in the phase is also improved, but small oscillations are still present. As a next step, the amplitude of

the signal is increased to 9.5% of the inlet mean velocity to increase the signal-to-noise ratio. For this case with higher excitation amplitude, the MTS and the SJTS methods are applied using six different simulations of length 750000 with a total length of 2.8 million iterations for the SJTS. The first 190000 iterations of the SJTS are not considered. Both methods yielded similar results and only the results from the SJTS are shown in Fig. 5.16. Results are also plotted in Strouhal number. For this new case, the amplitude of the FTF approaches unity in the low frequency limit, with good qualitative agreement in the amplitude. The experimental and identified FTFs show their maximum amplitudes at similar Strouhal numbers ( $\approx 0.34$ ), and with a good scaling with the 30 kW case. The value of the maximum amplitude of the experimental FTF is not reproduced by the identification. The phase exhibits good agreement with the experiment and the oscillations mentioned before are not present. Comparing the amplitudes in the FTF for 6.5% and 9.5%, both are qualitatively similar with small discrepancies between them. Furthermore, both cases exhibit lower amplitudes than the experiment. Harmonic excitation at 160 Hz with an excitation amplitude of 6.5% is carried out for  $5 \times 10^5$  iterations, which represents 10 cycles with a time step of  $1.25 \times 10^{-7}$  s. The first  $10^5$  iterations are not taken into account. The agreement in amplitude and phase of the harmonic excitation with the identified FTF is good. As the amplitude between the harmonic excitation and the one from the identification is in good agreement, the response at this frequency is well identified by the LES/SI method. This indicates that the lower amplitude in the identified FTF than in the experiments is not produced by limitations of the identification process, but from other reasons, e.g. inaccuracies in the measurements (no information about the accuracy of the experimental results is available), or by the lower resolution of the simulation with higher Reynolds numbers using the same mesh. In a simulation using the same mesh and increasing the Reynolds number, the cut-off wave number defined by the grid size is the same. However, the energy spectrum becomes broader [14] due to the smaller turbulent scales (see Fig. 2.3). Thus the resolved turbulent kinetic energy is decreased, and the accuracy of the sub-grid models (for turbulence and combustion) becomes more influential on the results. Moreover, the dynamical response of the flame might be reduced with the lower resolution of the turbulent scales, producing a lower

flame response. The settings (combustion model, numerical schemes, sub-grid model, etc.) in the simulations with 30 kW (which has shown good agreement with experiments) and 50 kW of power rating are the same, and were additionally cross-checked. The only variation is the velocity at the inlet as it was indicated previously. The impact of the disagreement in the amplitude between simulations and experiments on the stability analysis is analyzed in Chapter 6.

## **5.4 Influence of Thermal Boundary Conditions at the Combustor Wall on the Flame Transfer Function**

It is well known that thermal boundary conditions at the combustor wall or heat losses can influence the flame shape, even modify the flame structure, because heat release rates are very sensitive to temperature. Furthermore, most CFD simulations of swirl burner combustors do not take into account the effects of heat losses imposing adiabatic combustor walls or using combustion models that are not influenced by heat losses. To analyze the influence of thermal conditions at the combustor walls on the flame transfer function, the nonadiabatic combustor walls (Table 5.1) are modified to adiabatic conditions. The bluff body tip is kept as nonadiabatic. Experiments were not carried out at adiabatic conditions. In this study, the instantaneous and mean reaction rate, temperature and axial velocity are compared initially, followed by the comparison of the identified FTFs using the varied thermal conditions.

### **5.4.1 Instantaneous Reaction Rate, Temperature and Axial Velocity**

In Fig. 5.21, the instantaneous reaction rate, temperature and axial velocity contours for the case with 50 kW are shown for adiabatic and nonadiabatic conditions. From the contours of reaction rate and temperature, the influence of the wall heat loss on the flame stabilization is clearly seen (cf [176, 199]). In the adiabatic case, strong reaction in the outer shear layer is present, having the topology of a “M-flame”. In the nonadiabatic case, combustion cooled

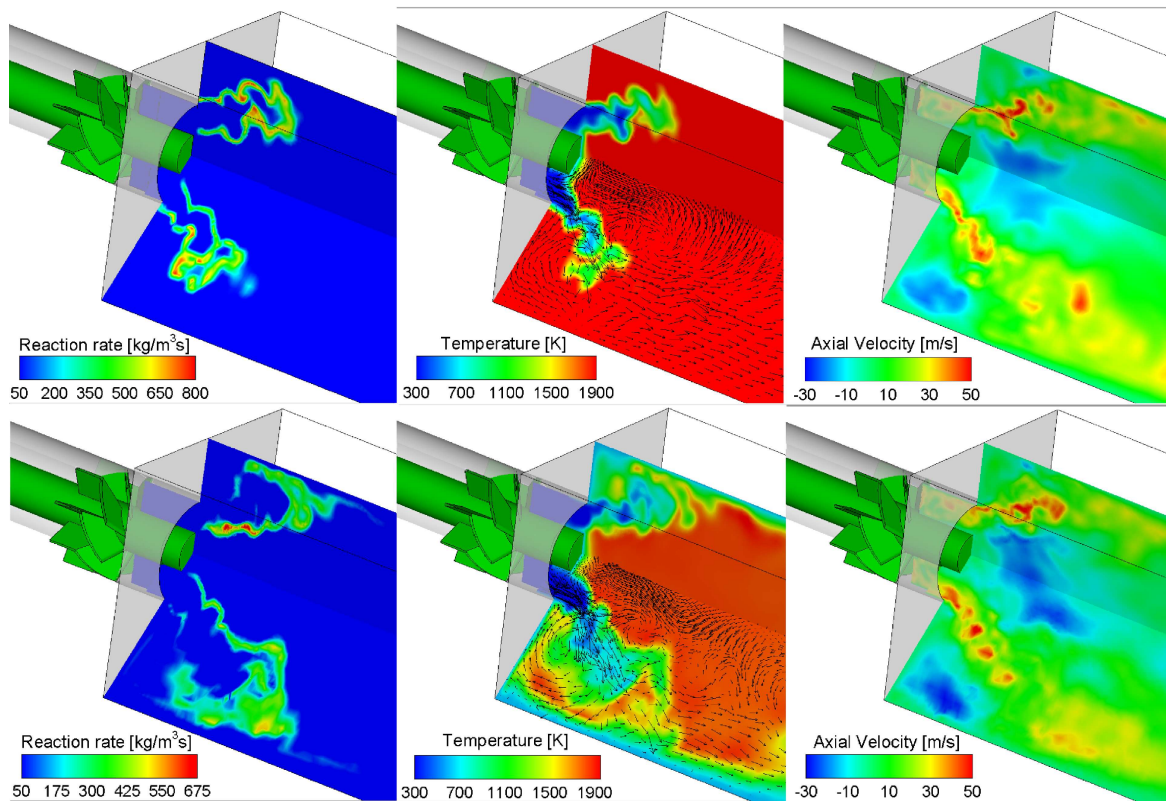


**Figure 5.21:** Instantaneous reaction rate, temperature and axial velocity with adiabatic (top) and nonadiabatic (bottom) combustor walls at 50 kW of power rating,  $\phi=0.77$ . Velocity vectors are included on the temperature contours

products are transported to the flame by the outer recirculation zone (see the velocity vectors and the axial velocity contour to identify the inner and outer recirculation zone). Due to the Arrhenius formulation of the dynamically thickened flame model, heat loss effects on the reaction rate are captured, resulting in quenching effects in the outer shear layer. The nonadiabatic case shows an elongated flame with strong interaction with the wall, while the flame in the adiabatic case does not interact with the wall. Similar behavior is observed in the 30 kW case.

### 5.4.2 Mean Heat Release, Flow Field and Temperature

To compare with experiments, the LOS integrated view of the averaged heat release is shown in Figs. 5.3 and 5.13 for the 30 and 50 kW cases, respectively. The averaging time for the adiabatic simulations are 112.5 and 62.4 ms, respectively. Different spatial heat release distributions are observed between adiabatic and nonadiabatic conditions. To look at the flame length, the axial heat release distributions for adiabatic and nonadiabatic conditions are plotted in Figs. 5.4 and 5.14 for the 30 and 50 kW cases, respectively. The cases with adiabatic walls exhibit a flame much shorter compared to experiments and simulations with nonadiabatic conditions due to the flame stabilization in both shear layers. This different flame stabilization topology between adiabatic and nonadiabatic cases can have some influence on the flame response. As mentioned by Durox et al. [44] and Kim et al. [97], the dynamic flame response depends on the flame shape. Thus, correct prediction of the flame structure and its mechanism of stabilization is important for the identification of the FTF.

For the comparison of the mean axial velocity and mean temperature between the two different thermal conditions, the 30 kW case is chosen as reference. This case is used also as reference case for the comparison of the flame transfer function. In Fig. 5.22 (a), the mean axial velocity contours for the adiabatic and nonadiabatic cases at the combustor middle cross plane are shown. The zero-axial velocity isolines are showed in black. The velocities upstream the burner exit are the same, as the same boundary conditions are applied. Comparing both thermal conditions, the adiabatic case shows a shorter and narrower recirculation zone, with the zone of maximum negative velocity closer to the burner and with higher velocities close to the walls than in the nonadiabatic case (see Fig. 5.22). The differences mentioned before are shown in more detail by plotting axial velocity profiles at different axial positions of the combustor middle cross plane in Fig. 5.23. A grey line at zero axial velocity is introduced to indicate the position of the recirculation zone. The variations between cases are due to different temperature distribution (shown in Fig. 5.22 (b)) and flame stabilization patterns, which induce variations on the flow field. Schmitt et al. [175] performed also a comparison of the influence of

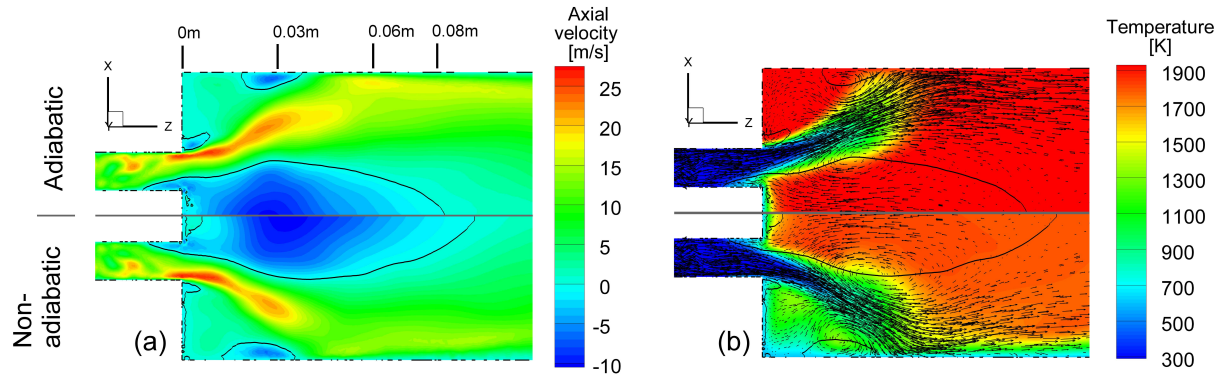


**Figure 5.22:** Contours of mean axial velocity (left) and mean temperature with velocity vectors (right) for the 30 kW case. Zero-axial velocity iso-lines in black.

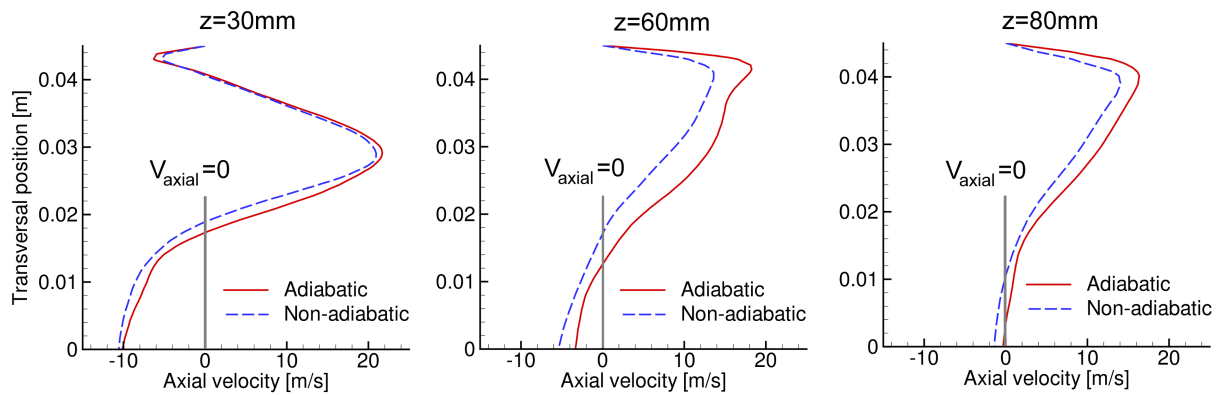


**Figure 5.23:** Mean axial velocity profiles of reacting flow at various axial positions of the middle cross plane for adiabatic and nonadiabatic wall boundary conditions. 30 kW case.

different thermal conditions at the combustor wall on the flow field and flame shape. The length of the recirculation zone is not specified, but similar variations on the flame stabilization and flow field are shown. Velocity vectors are additionally plotted in Fig. 5.22 (b).

## 5.4 Influence of Thermal Boundary Conditions at the Combustor Wall on the Flame Transfer Function

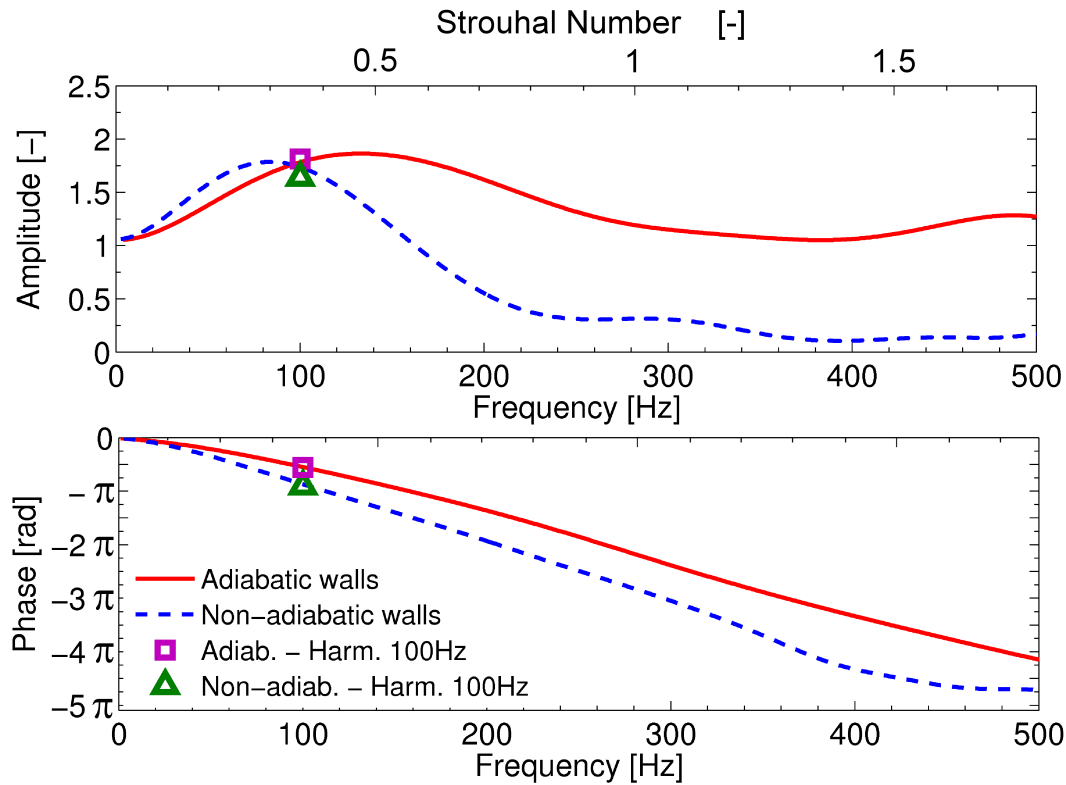


**Figure 5.24:** Flame transfer functions from LES/SI using adiabatic and nonadiabatic combustor walls with 30 kW. Harmonic excitation at 100 Hz for adiabatic ( $\square$ ) and nonadiabatic ( $\triangle$ ) conditions are also shown. Excitation=9.5%.

### 5.4.3 Comparison of Identified Flame Transfer Functions

To identify the flame transfer functions, the simulations are excited using the same signal applied in the 30 kW case with an amplitude of 9.5% of the inlet mean velocity. Results for the identified FTFs are shown in Fig. 5.24. Similar to the comparison done by Durox et al. [44] in laminar cases, the adiabatic case with the M-flame shape exhibits a broader frequency response (with amplitudes higher than 1) than in the nonadiabatic case with the V-flame shape. Also, the adiabatic case shows a less steep phase than the nonadiabatic case, which is produced by the smaller time lag associated with the shorter flame (see Fig. 5.4).

To analyze the dynamics of the flames by the different thermal conditions at the combustor wall, a harmonic excitation at 100 Hz for both thermal conditions is carried out. The flame response for the harmonic excitation is also in good agreement in amplitude and phase with the one obtained using system identification as shown in Fig. 5.24. The flame response for both cases in a complete cycle of the heat release fluctuation is illustrated in Fig. 5.25. For the V-flame, the perturbations travel along the flame and at the moment of maximum heat release (in (b)), the flame is elongated along the combustor walls, creating an increase of flame surface area. In (c), the flame tip is rolled up by the vortices produced at the burner exit [11, 44, 136], followed by a reduction on the flame surface in (d). Additionally, the flame tip in (d) falls in the outer recirculation zone due to the roll-up, inducing some reaction in the outer shear layer. Strong flame-wall interaction is observed during all the sequence. For the M-flame, the interaction with the wall is small, but strong interaction between flames in the inner and outer shear layer is observed. In (b), the flame is elongated and the flames in the inner and outer shear layer get closer to each other, creating annihilation between them. The same effect was shown in laminar flames by Schuller et al. [180] and Durox et al. [44]. In (c) and (d), the continuous reduction of flame surface is observed including annihilation between flames. Additionally, in both cases, the flame angle is also modified not only by the unsteady flapping behavior of flame, but also by the presence of swirl number fluctuations [78, 103, 137, 141]. These sequences showed the different flame dynamics between both flame topologies, leading to different flame transfer functions.

## 5.5 Influence of Swirler Position on the Flame Transfer Function

Komarek and Polifke [103, 104] carried out an experimental and RANS-based study showing the impact of swirler position on the FTF. Their investigations are extended in this work to a LES context. Investigations are carried out for two varied positions of the swirler: One with the swirler at 30 mm upstream the burner exit (position 1), and the other with the swirler at 130 mm upstream the

## 5.5 Influence of Swirler Position on the Flame Transfer Function

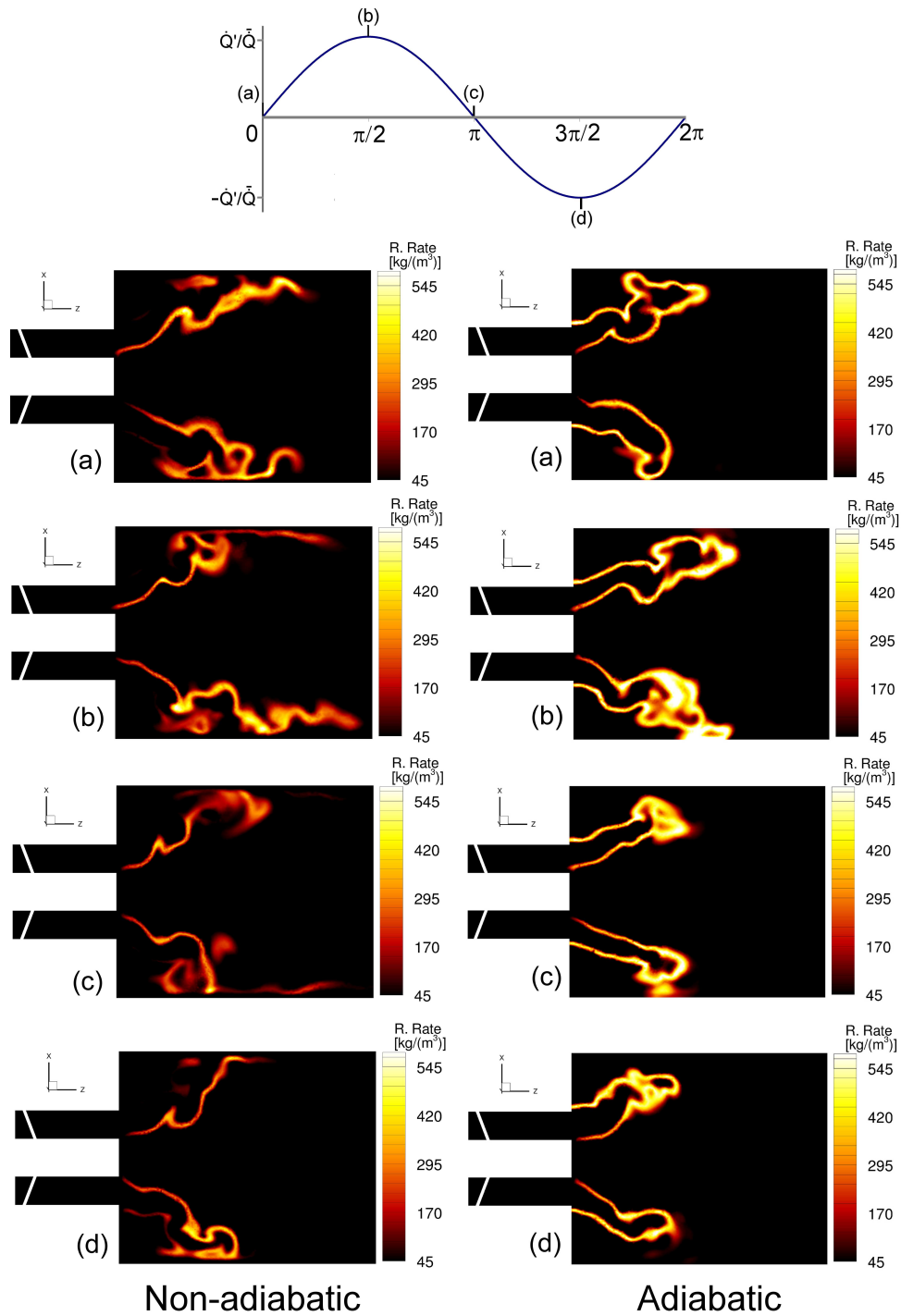


**Figure 5.25:** Instantaneous reaction rate for one cycle of a harmonic excitation at 100 Hz using adiabatic and nonadiabatic combustor walls with 30 kW. Excitation=9.5%  $\bar{U}$ .

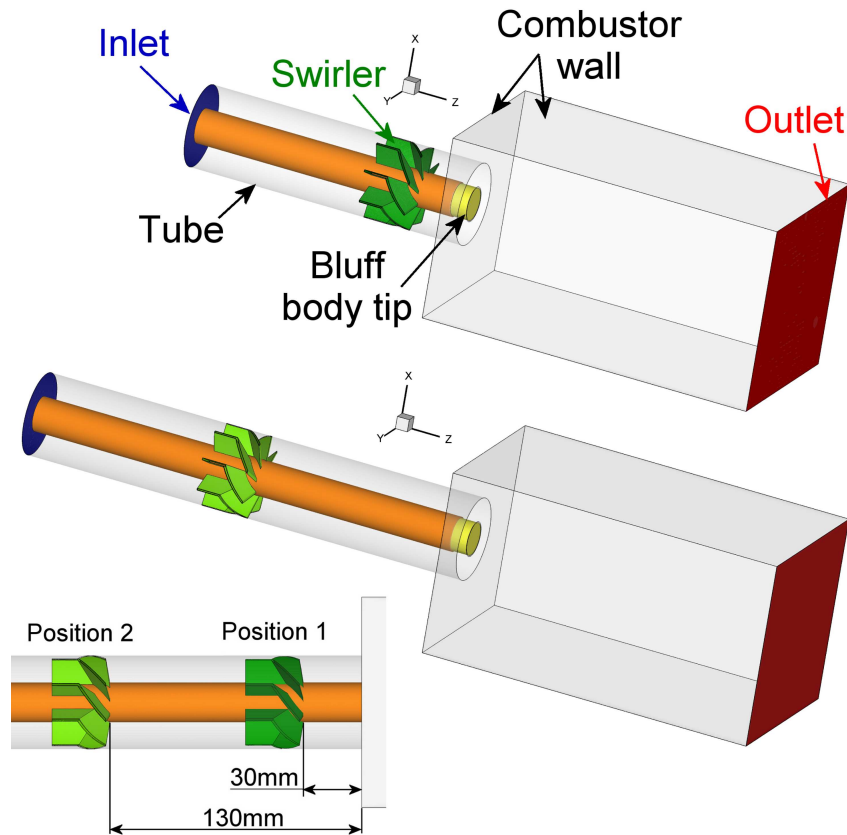


**Figure 5.26:** Scheme of the numerical set-up of the burner with different swirler positions.

burner exit (position 2) (see Fig. 5.26), to look at the influence of swirler position on the flame dynamics. In the work of Komarek and Polifke, the swirler was moved upstream keeping the same length of the tube in Fig. 5.2. Nevertheless, the swirler will be too close to the inlet for the simulations, which is not optimal for the non-reflective boundary conditions (NRBC) based on plane wave masking used in this study. For the simulations, the swirler is moved also at 130 mm upstream the burner exit as in the experiments carried out by Komarek, but the length of the tube is increased 100 mm to keep the distance of the inlet and the swirler as in the case with the swirler at 30 mm. The boundary conditions are similar for both cases and indicated in Table 5.1.

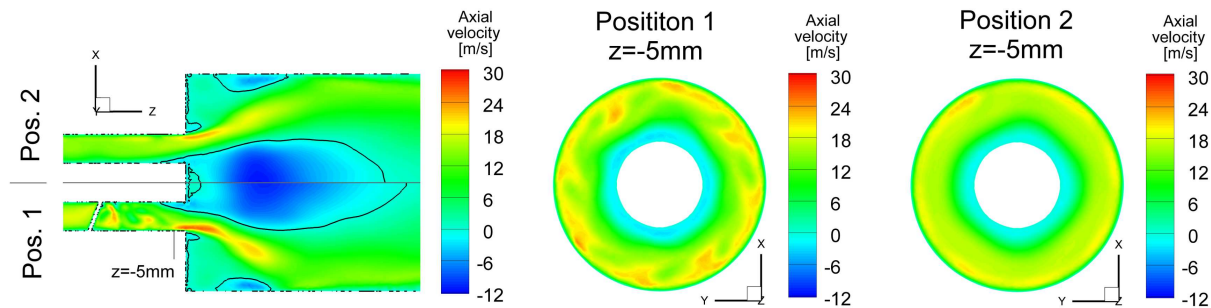


**Figure 5.27:** Contours of mean axial velocity at combustor middle cross plane and at position  $z=-5$  mm with varied swirler positions. Zero-axial velocity isolines in black.

### 5.5.1 Mean Flow Field and Heat Release

The computed mean axial velocity at the combustor middle cross plane and 5 mm upstream the burner exit are shown in Fig. 5.27. Flow field measurements were not performed at this power rating. The flow field distribution inside the combustor shows small differences between cases. The inner recirculation zone with the swirler at position 2 is slightly thinner and shorter than the one with the swirler at position 1. As the swirler at position 1 is closer to the burner exit, the axial velocity distribution at a plane 5 mm upstream the burner exit is less uniform than the one with the swirler at position 2, showing areas with higher maximum axial velocity. The mass flow rate was cross-checked between cases at this plane, obtaining same values. The swirl number, computed using Eq. (3.9), 5 mm upstream the burner exit is 0.75 and 0.68 for the swirler at position 1 and 2, respectively. As mentioned in section 3.3.3, due to the longer distance between the swirler at position 2 and the burner exit, swirl decay appears due to the no-slip wall conditions in the wall tube, which produces stresses against the rotating flow and a decrease in the angular momentum. The size of the recirculation zone is increased with the increase of swirl number [72], which is in agreement with the observations mentioned before.

The spatial and axial heat release distribution with the swirler at positions 1 and 2 are shown in Fig. 5.28. Both distributions are very similar as differences

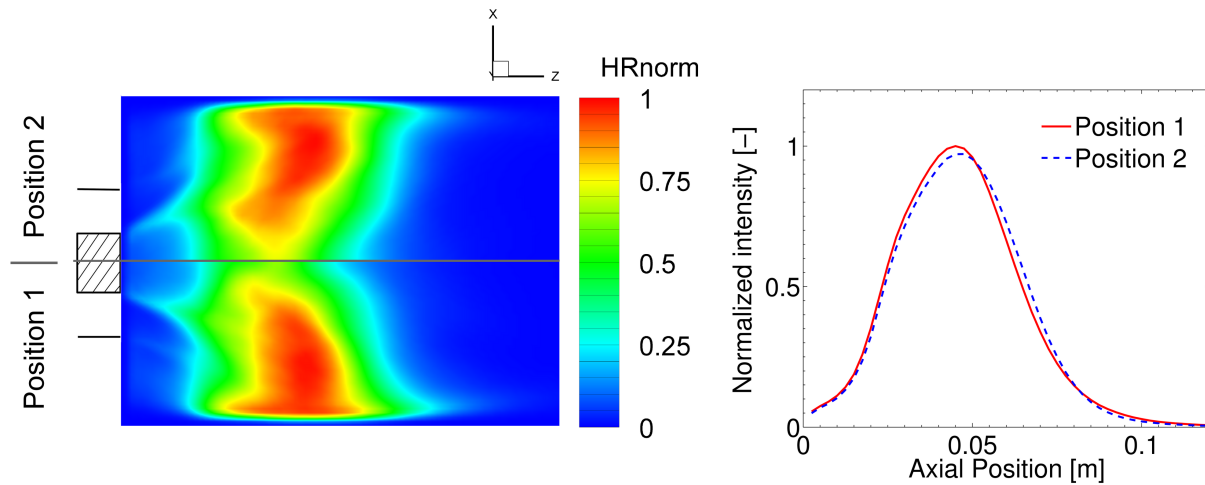


**Figure 5.28:** Normalized spatial (left) and axial (right) heat release distribution with varied swirler positions

on the flow field are small.

### 5.5.2 Comparison of Identified and Experimental Flame Transfer Function with Varied Swirler Position

Simulations with the swirler at varied positions are excited using the same signal used in section 5.4.3 with an amplitude of 9.5% of the mean inlet velocity and run for 350 ms in real time (2.8 million time steps). The acoustic velocity fluctuations are obtained 70 mm upstream of the burner exit, as in experiments. The identified and measured FTFs are shown in Fig. 5.29. Comparing the identified flame transfer functions at varied swirler positions, both show a very different flame response. While the FTF at position 1 exhibits a shape with only one peak with the maximum amplitude (higher than 1) at approx. 90 Hz, the FTF at position 2 exhibits a first peak with the maximum amplitude at a lower frequency (40 Hz), followed by a strong decrease in amplitude with a minimum value of 0.3 at 90 Hz. From 90 Hz, the gain starts to increase to form a second peak with a maximum value of 1.1 at approx. 135 Hz. For frequencies higher than 135 Hz, the gain decreases and oscillates with values lower than 0.5. The phase exhibits an increased modulation with the swirler at po-

sition 2. Comparing the identified FTF with the swirler at position 2 with the experimental one, it shows a qualitative agreement, but the magnitudes are not well captured. Additional harmonic excitations are performed at 100 Hz and 160 Hz to compare with the identified FTF. For the excitation at 100 Hz, the agreement with the amplitude is good, but not for the phase. As the flame response is quite low, the phase determination is not accurate. For the excitation at 160 Hz, good agreement is found in amplitude and phase with the identified FTF because the response of the flame is stronger.

As shown in Fig. 5.29, at 100 Hz the amplitude in the FTF at position 1 is very different from the one at position 2, showing values higher than 1 for the former case, and around 0.5 for the latter case. The phase difference between cases at this frequency is small. The mechanism of the varied flame response between cases is described in section 3.3.3, and it is related to the different propagation velocities of the axial and tangential velocity fluctuations [78, 103, 137, 139–141, 212]. Palies et al. [137, 140, 141] carried out an experimental and numerical investigation of the influence of the axial and tangential velocity fluctuations on the flame response applying harmonic excitation at two frequencies where the flame response showed high and low amplitudes in the flame describing function. The mechanism of the different response at two varied frequencies with a fixed position of the swirler is similar to the one for a single frequency, but with the swirler at varied position. To investigate this mechanism in our case, harmonic excitation at 100 Hz using only the swirler at position 2 without the combustor is carried out to analyze the axial and tangential velocity fluctuations. The geometry and reference planes are shown in Fig. 5.30. The simulation is carried out using the same mixture and inlet conditions indicated on Table 5.1 for 960000 iterations with a time step of  $1.25 \times 10^{-7}$  s. The “on-the-fly” extracting tool from AVBP used on previous simulations did not include the extraction of the tangential velocity. Thus, result files are saved every 1000 iterations and the tangential velocity is obtained by post-processing using the program TECPLOT.

In Fig. 5.31, the normalized axial and tangential velocity fluctuations are shown at two different reference planes (10 and 110 mm upstream the burner exit). The plane at 110 mm represents a plane 10 mm upstream the burner exit

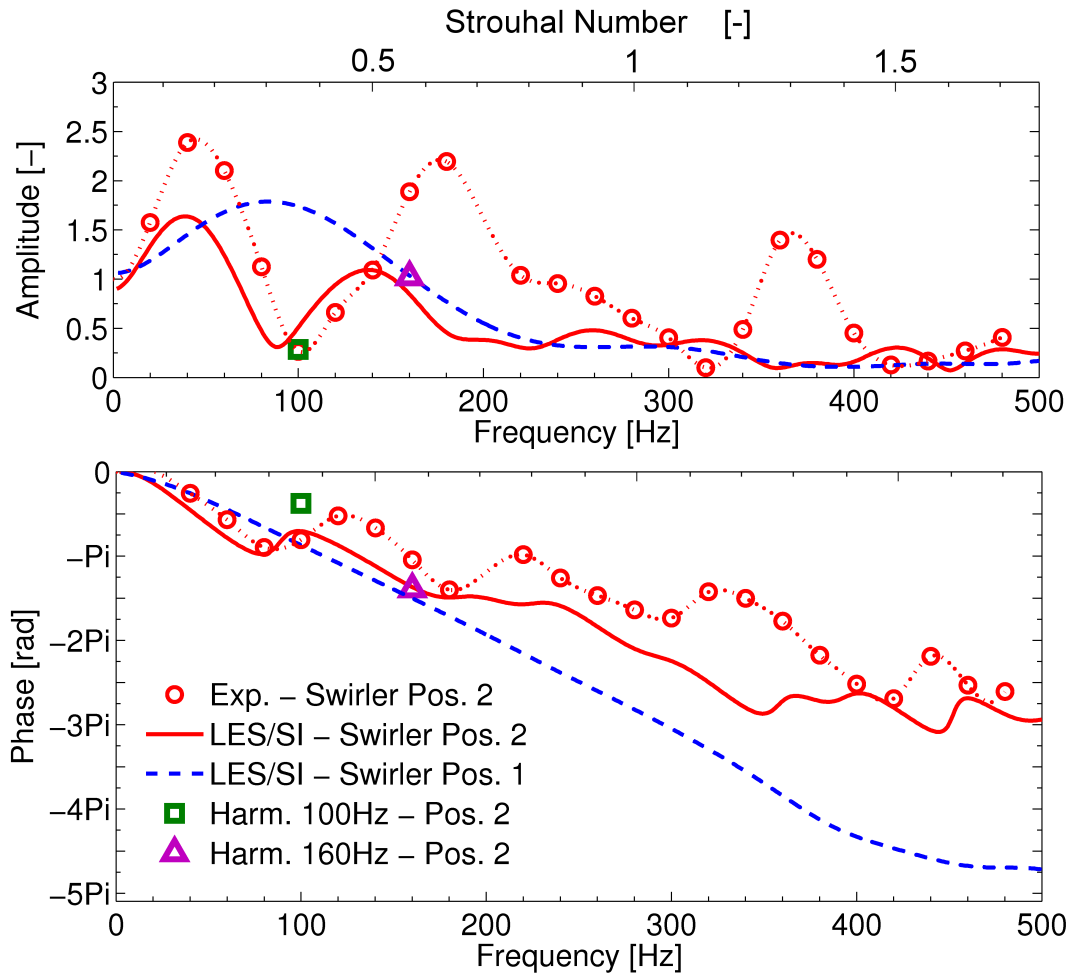


**Figure 5.29:** Flame transfer functions from LES/SI with the swirler at position 1 and 2 from Fig. 5.26 with 30kW. Harmonic excitation at 100 ( $\square$ ) and 160 Hz ( $\triangle$ ) are also shown. Excitation=9.5%. Experiments with the swirler at position 2 in (o).

at position 1. Comparing the phase between axial and tangential velocity fluctuations at both planes, at the plane 110 mm upstream the burner exit both fluctuations are almost in phase; while at 10 mm upstream the burner exit, both fluctuations are almost out of phase. Relating the phase difference between perturbations with the amplitude of the identified FTFs: when the axial and tangential velocity fluctuations are in phase, amplitudes higher than 1 are obtained due to a constructive mechanism induced by them. On the other

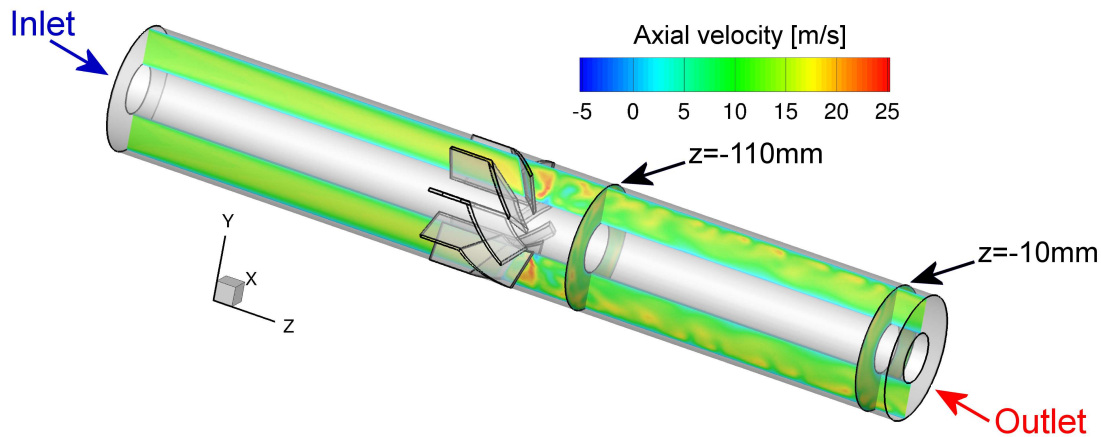


**Figure 5.30:** BRS burner with axial swirler at position 2 without combustion chamber

hand, when both perturbations are out of phase, a destructive mechanism develops and a low amplitude in the FTF is shown. This is in agreement with the experimental results from Palies et al. [137].

The propagation speed of the axial velocity fluctuations is much higher than the one of the tangential velocity fluctuations. The axial velocity fluctuation propagates with an acoustic velocity, while the tangential velocity fluctuation with a convective velocity [103, 137]. Using the phase difference of the perturbation at the two different positions, the time lag between planes and the propagation speed can be determined. The phase difference is computed using the pure-tone Fourier transform (Eq. (5.4)). For the axial velocity fluctuation, a time lag of  $2.7713 \times 10^{-4}$  s is obtained between planes, corresponding to a propagation speed of 360 m/s, which is in good agreement with the propagation speed defined by the speed of sound of the mixture (348.6 m/s) plus the axial mean flow speed. For the tangential velocity fluctuation, the time lag is  $5.137 \times 10^{-3}$  s, which corresponds to a propagation speed of 19.5 m/s. This propagation speed is around 72% higher than the mean axial velocity on the cross section, which is usually considered as the convective speed of the perturbation. The increase in the propagation speed of the tangential velocity fluctuations was observed previously by Komarek and Polifke [103] and by Palies et al. [136, 139, 140]. Komarek and Polifke [103] have shown this e-

effect in the same burner, but with a power rating of 70 kW (around 2.33 times higher than the one used in this study) using URANS. The propagation speed for the tangential velocity fluctuation for the 70 kW case was 40% higher than the mean axial velocity on the cross section. From the axial velocity contours in Fig. 5.27, it is observed that the distribution of axial velocities in the cross section and along the tube show sectors with maximum velocities around the double of the mean axial velocity of the cross section and close to the propagation speed of the tangential velocity fluctuations [136, 139, 140]. The propagation velocity of the tangential velocity fluctuation locally is not uniform and travels convectively with the local convective velocity. This effect can be observed on Fig. 5.32, where the area averaged tangential velocity on a cross-section at different positions is shown. For positions further downstream, the harmonic oscillations become less smooth, indicating some nonuniformity in the propagation. Furthermore, the mean tangential velocity (taken in this case by the tangential velocity at time 0 s) is lower at positions more downstream from the swirler. This is created due to the decay of swirl mentioned before.

In Fig. 5.33, the area averaged axial and tangential velocity fluctuations without normalization are shown. The axial velocity fluctuation did not present a decrease in amplitude, which indicates the low level of acoustic dissipation from the code. The tangential velocity fluctuation presented a decay of 16.4% in amplitude at the plane  $z=-10$  mm with respect to the one at  $z=-110$  mm, indicating that the decay in swirl affected also the tangential velocity fluctuations, which influence the flame response.

In Fig. 5.34, the area averaged swirl number fluctuations are shown. The case with swirler at position 2 presents higher swirl number fluctuations in spite of the lower tangential velocity fluctuations. This is created due to the different phase between axial and tangential velocity fluctuations at the reference planes as shown in Fig. 5.33.

The results indicate that a flame with similar heat release distribution and flow field can have a different flame response due to the varied time lag response to the perturbations. The analysis is extended in section 5.7.2 to identify the different time lags between perturbations and the discrepancies in the amplitudes between experimental and identified FTF in Fig. 5.29.

## 5.5 Influence of Swirler Position on the Flame Transfer Function

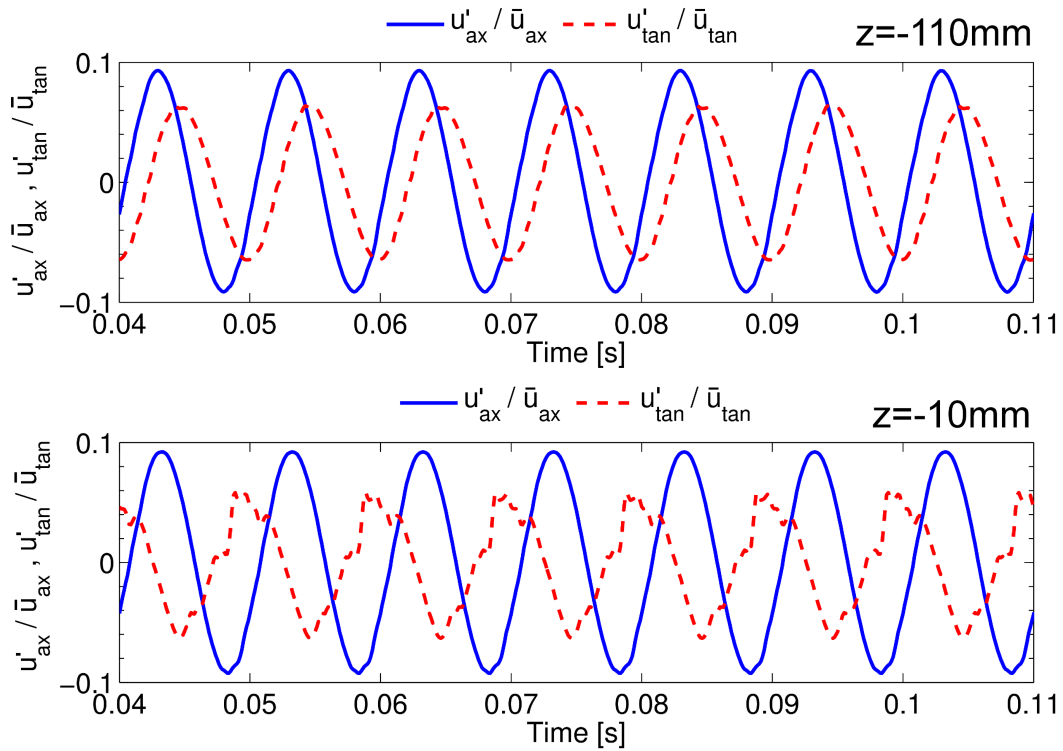


**Figure 5.31:** Normalized area averaged axial and tangential velocity fluctuations on a cross-section at  $z = -10 \text{ mm}$  and  $z = -110 \text{ mm}$  with harmonic excitation at 100 Hz.

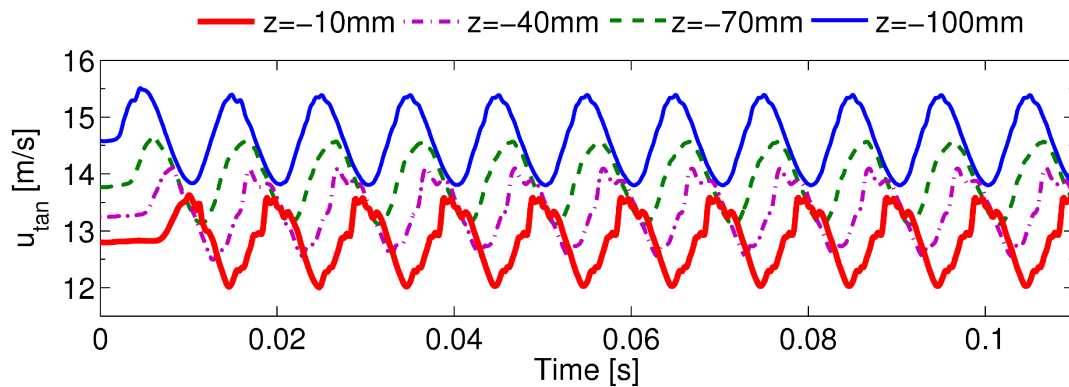


**Figure 5.32:** Area averaged tangential velocity on a cross-section at various positions with harmonic excitation at 100 Hz.

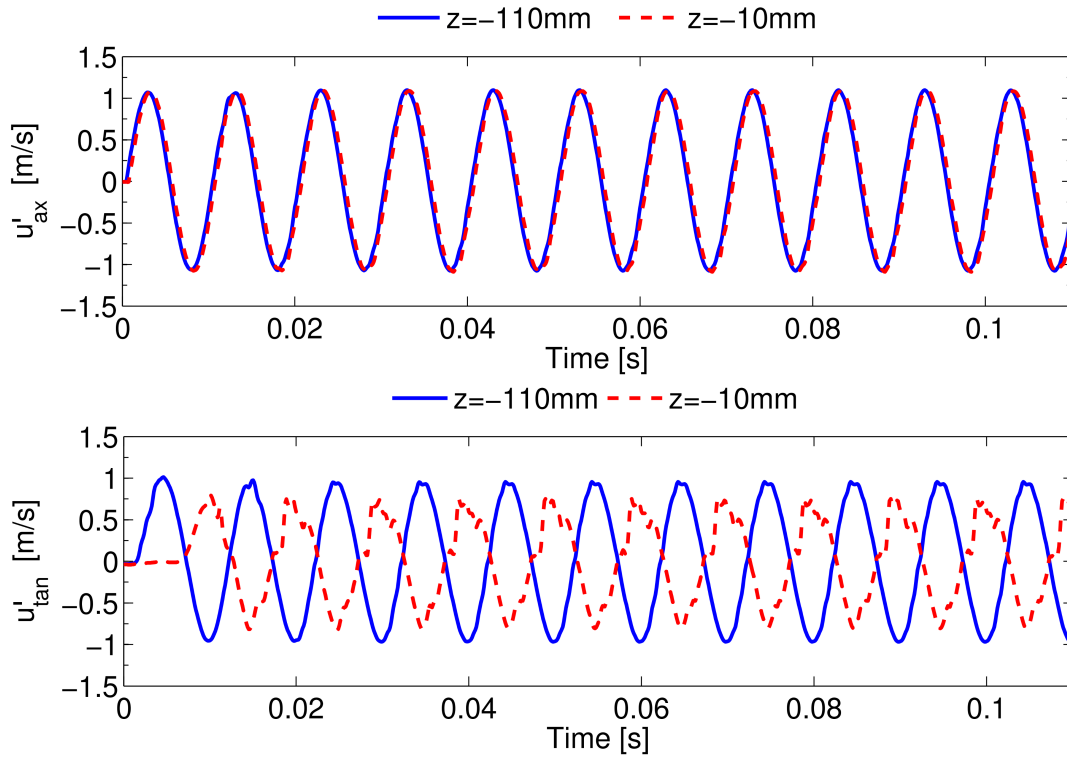


**Figure 5.33:** Area averaged axial and tangential velocity fluctuations on a cross-section at at  $z=-10$  mm and  $z=-110$  mm with harmonic excitation at 100 Hz.

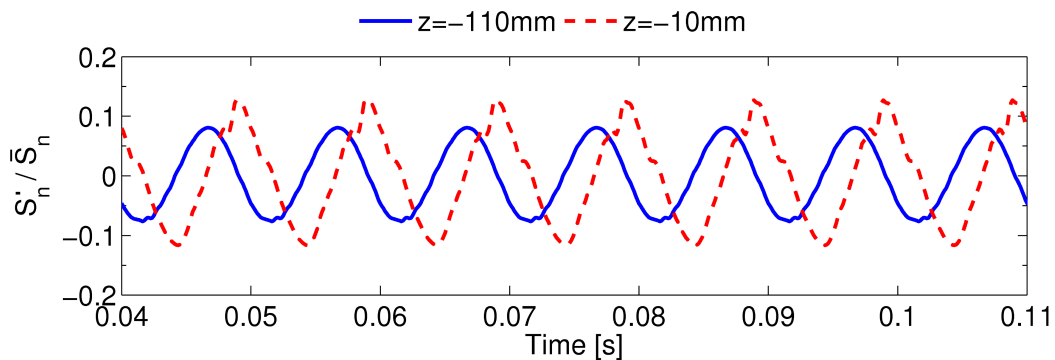


**Figure 5.34:** Area averaged swirl number fluctuations on a cross-section at  $z=-10$  mm and  $z=-110$  mm with harmonic excitation at 100 Hz.

Additionally, as the induced tangential velocity fluctuations created by the swirler have a strong impact on the flame dynamics, the swirler geometry

must be taken into account in CFD simulations in order to capture this effect. As shown by Komarek and Polifke in [103], introducing only axial velocity perturbations in a simulation without the geometrical swirler, and replacing it by 3D velocity profiles at a reference position, tangential velocity perturbations are not produced and the flame responds only to axial perturbations. Thus the constructive/destructive interaction between axial and tangential velocity fluctuations, which influence the flame response on swirling flames, does not take effect.

### **5.6 Influence of Combustor Confinement on the Flame Transfer Function**

The combustor in single burner test-rigs has in general a cross section size and shape that differ from the one in the industrial gas turbines. The change in combustor cross-section induces differences in the flow field and in the flame. Measurements of FTFs with varied combustor confinement ratio were carried out by Birbaud et al. [11] in laminar cases and by Hauser et al. [75] in a radial swirl burner, showing variations between FTFs with different confinement ratio. In the present work, the influence of combustor confinement on the flow field, flame and FTF is analyzed numerically with LES. The BRS burner is simulated using two combustors with different cross-section area. The dimensions of the cross-sections are similar to the ones used by Hauser et al.: One with 90 mm × 90 mm called high-confinement (HC) combustor (CR=0.156); and another with 160 mm × 160 mm, called low-confinement (LC) combustor (CR=0.049). Both cases use the same boundary conditions, as specified in Table 5.1. The length of the combustor is longer in the low-confinement combustor (300 mm) than in the high-confinement combustor (200 mm) to reduce the interaction of the long recirculation zone (see section 5.6.1) with the outlet. Experiments were not carried out in the low-confinement combustor. Mean flow field and mean heat release from simulations are compared initially between cases, followed by the identification of the FTFs using the different combustors.

### 5.6.1 Mean Flow Field and Heat Release

In Fig. 5.35, the mean axial velocity contours and velocity vectors for the cases with variation of combustor confinement ratio at the combustor middle cross plane are shown. The case with the low-confinement combustor shows a recirculation zone much longer than the one with high-confinement. At around 60 mm downstream of the burner exit, a “neck” is formed in the recirculation zone. Between positions 0 mm and 60 mm, the inner recirculation zone (IRZ) of the low-confinement case is narrower than the one with high-confinement; while after 60 mm, the IRZ with low-confinement becomes broader than the one with high-confinement, and extended to more downstream positions. Similar effect on the shape of the recirculation zone with the increase of confinement was found by Fu et al. [61] in isothermal cases. Additionally, the case with high-confinement shows a higher maximum negative velocity in the inner recirculation zone. The flow recirculation is mainly produced by the presence of an adverse axial pressure gradient induced by the swirling flow [72, 125, 195], which changes due to the varied expansion ratio.

The variations mentioned before are shown in more detail in Fig. 5.36 by plotting axial velocity profiles at various axial positions of the combustor middle cross plane. A grey line at zero axial velocity is introduced to indicate the position of the recirculation zone. Additionally, the jet angle from the burner exit exhibits some variations between cases. From the vector plots and the axial velocity profiles, the jet angle is slightly higher on the high-confinement case ( $\approx 30$  deg) than on the low-confinement case ( $\approx 20$  deg). The increment is produced because the recirculation zone is broader and more intense in the high-confinement case. The increment in jet angle, but to a higher degree, was observed also by Fanaca et al. [49] in the flow field comparison between a single burner rig and an annular combustor. Additionally, the maximum axial velocity with low-confinement shows a higher decay with positions more downstream to the burner exit due to the higher area expansion. A decay in the tangential velocity (Fig. 5.37) and turbulent kinetic energy (Fig. 5.38) is also observed. For the turbulent kinetic energy, a higher level of turbulence is observed with low-confinement than with high-confinement at 60 and 80 mm downstream the burner exit. This is produced by the flame, which is longer in

## 5.6 Influence of Combustor Confinement on the Flame Transfer Function

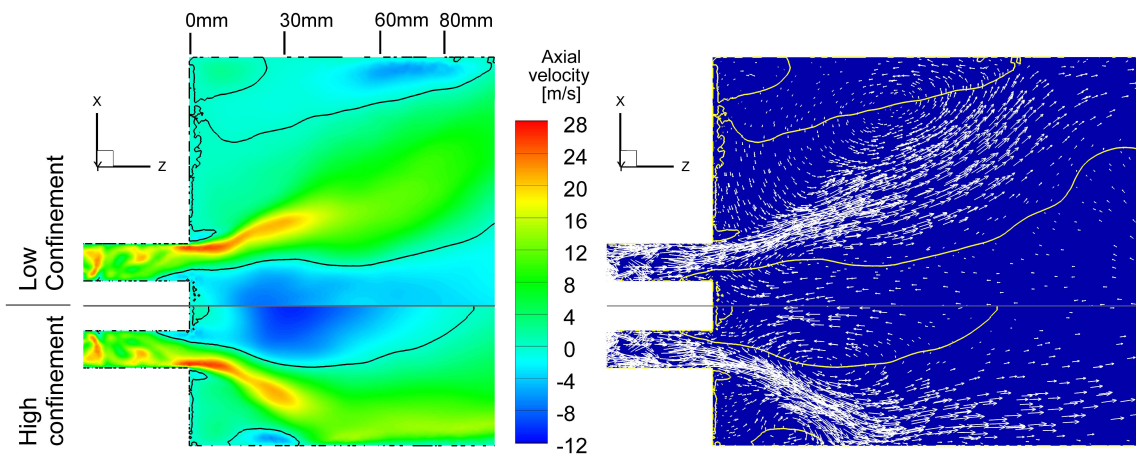


**Figure 5.35:** Contours of mean axial velocity (left) and velocity vectors (right): Combustor chamber with 160 x 160 mm of cross section (top), Combustor chamber with 90 x 90 mm of cross section (bottom). Zero-axial velocity isolines in black (left) and yellow (right)

the low-confinement case, inducing higher velocity fluctuations at these positions. Furthermore, higher turbulent kinetic energy is shown on the center line with low-confinement than with high-confinement. This is in agreement with the experimental observations by Fu et al. [61].

Comparing the profiles at 30 mm, where the shear layer and flame have not reached the wall, the cases show similar velocities and turbulent kinetic energy on the shear layers. This indicates that close to the burner exit the confinement has a low influence on the flow field in the area where the flame is present. Thus, the propagation speed of the perturbations along the flame, which is convective [78, 181], is similar at this position. Further downstream, the flow field and flame are affected by the presence of the wall in the high-confinement case, which will create a different flame response with respect to the low-confinement case.

In Fig. 5.39, the LOS integrated view of the averaged heat release from both simulations is shown. Both flames exhibit similar flame stabilization mainly in the inner shear layer (“V-flame”), but different spatial heat release distributions are observed. The low-confinement case shows a broader spatial heat

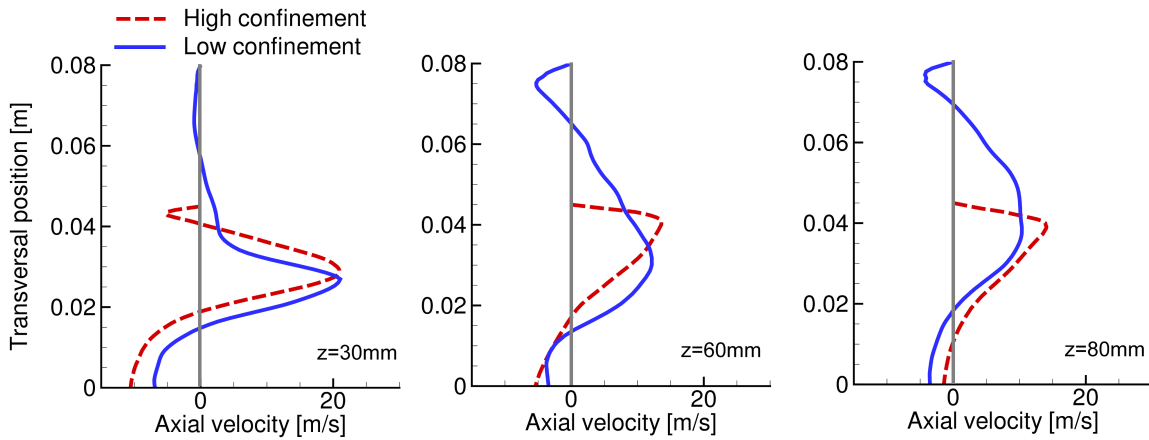


**Figure 5.36:** Mean axial velocity profiles with low and high confinement combustors at various positions of the middle cross plane shown in Fig. 5.2. Grey line to indicate zero-axial velocity.

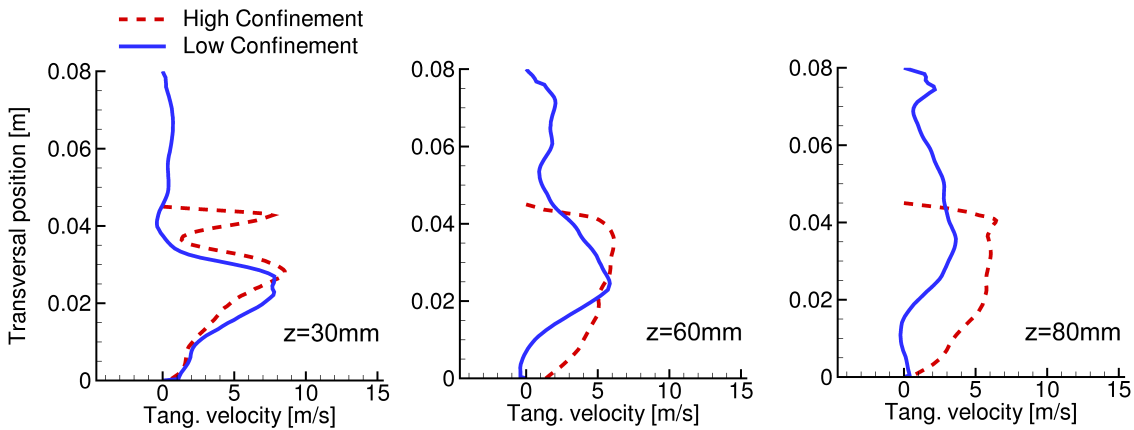


**Figure 5.37:** Mean tangential velocity profiles with low and high confinement combustors at various positions of the middle cross plane shown in Fig. 5.2.

release distribution than the high-confinement case. This is in agreement with experimental results performed by Hauser et al. [75] using a radial swirl burner in similar combustors to the ones used in this study.

In Fig. 5.40, the axial heat release distributions from simulations are shown. The values are normalized taking into account that the area of the distribution

## 5.6 Influence of Combustor Confinement on the Flame Transfer Function

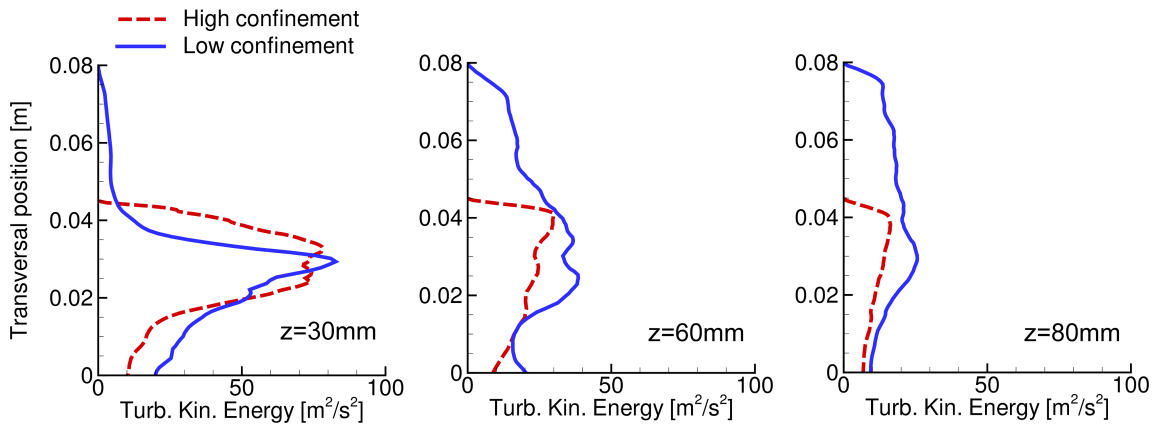


**Figure 5.38:** Turbulent kinetic energy profiles with low and high confinement combustors at various positions of the middle cross plane shown in Fig. 5.2.

should be the same between cases. Results show that the low-confinement case has a longer flame than the high-confinement case with a low level of reaction close to the burner exit. The flame lengths, computed as the position of the maximum heat release, are 45 and 75 mm, for the high- and low-confinement cases, respectively.

### 5.6.2 Comparison of Flame Transfer Functions

The low-confinement simulation is excited using the same signal indicated on section 5.4.3 with an amplitude of 9.5% of the mean inlet velocity for 350 ms in real time (2.8 million iterations). The identified FTF is compared with the one obtained with high confinement at nonadiabatic conditions and shown in Fig. 5.41. For the low confinement case, the amplitude shows similar behavior to the high-confinement, but with the maximum amplitude slightly higher and at a lower frequency. The time lag response is larger which is represented by the higher steepness in the phase. This is in agreement with the differences in flame length shown in Fig. 5.40. Comparing the dynamic behavior of the flames, the high-confinement case shows strong interaction between the flame and the wall, being elongated along the walls as shown

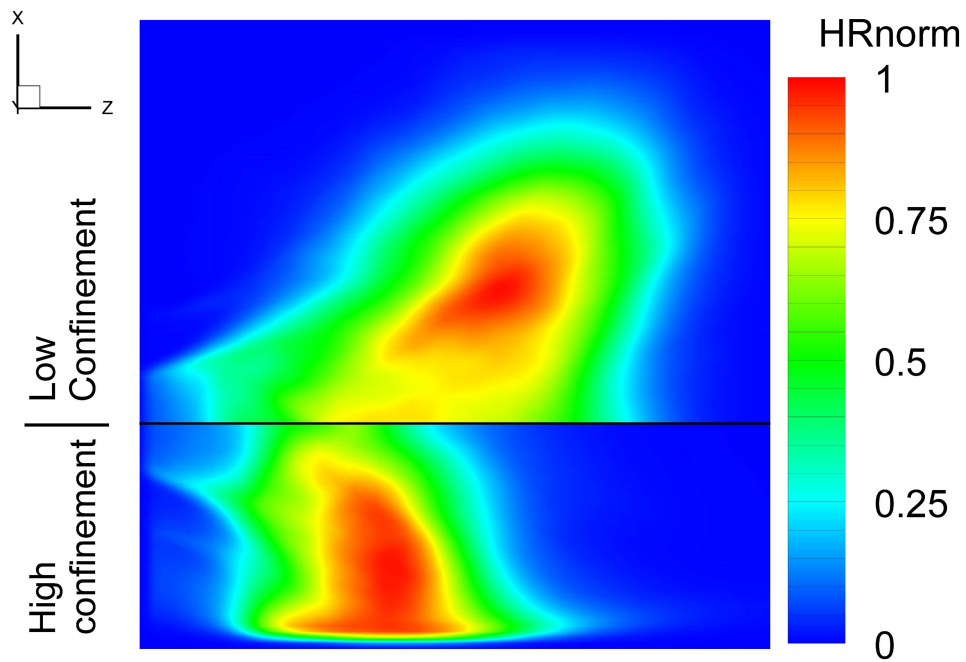


**Figure 5.39:** Normalized spatial heat release distribution for 30 kW: (Top) Combustor chamber with 160 x 160 mm of cross section (Bottom) Combustor chamber with 90 x 90 mm of cross section

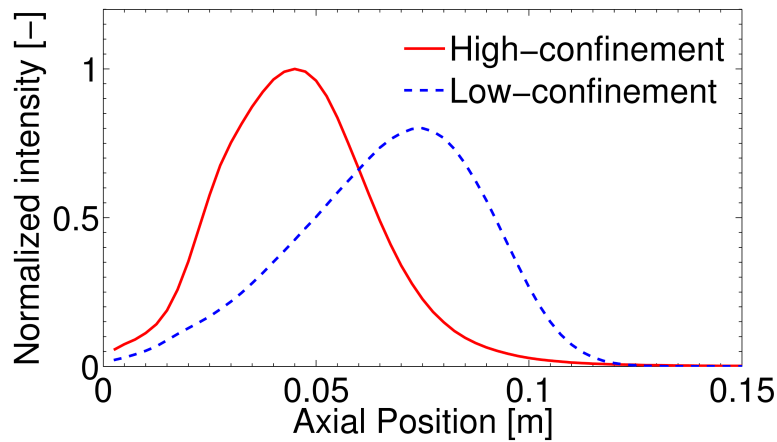


**Figure 5.40:** Area normalized axial heat release distribution with different combustor cross section.

in Fig. 5.25; while with low-confinement, the flame does not reach the wall, being elongated until all the fuel is consumed. In the experimental studies

for different confinement ratio by Birbaud et al. [11] in laminar cases, and in the one from Hauser et al. [75] in a radial swirl burner, higher differences in the amplitude of FTFs were observed. The increment in the phase steepness with lower-confinement in our study is in agreement with their studies. In Birbaud's work, the flame is laminar and stabilized on a bluff body without swirler; while in Hauser's work, the flame is turbulent and the swirler position is at a more upstream position from the burner exit (around 100 mm upstream the burner exit) than in our case. The variations in the FTF with varied confinement in both experimental studies were observed mainly at frequencies around 150 to 300 Hz; while at lower frequencies, similar behavior was observed between both confinement ratios. These experimental studies indicate that the influence in amplitude in the confinement appears at high frequencies. In our case, the flame response is low in this range of frequencies, with amplitudes around 0.5 at 200 Hz and decaying for higher frequencies. In the range from 150 to 300 Hz in the experimental studies mentioned before, the flame shows a response with amplitudes around 1 for the high-confinement case, and above 1 for the low-confinement case. Thus at these frequencies, the flame is more sensible to capture influences on the response by the different confinement, which are not observed in the simulations due to the low flame response.

From the investigations carried out, it should be taken into account that the phase shown in the FTF represents a global time lag response as from the definition of the FTF in Eq. (3.1), the flame is considered as a discontinuity. It has been seen that the flame response is a distribution of time lags from various contributions. The observed variations in the flame response between cases are discussed in relation to the unit impulse response (UIR) of the flame using the FTF model presented in section 3.4.

## 5.7 Flame Transfer Function Model

The FTF model presented in section 3.4 (see Eq. (3.13)) is used to analyze the UIRs of the HC-nonadiabatic, the HC-adiabatic and the LC-nonadiabatic cases with 30 kW to look at the impact of the different parameters on the flame

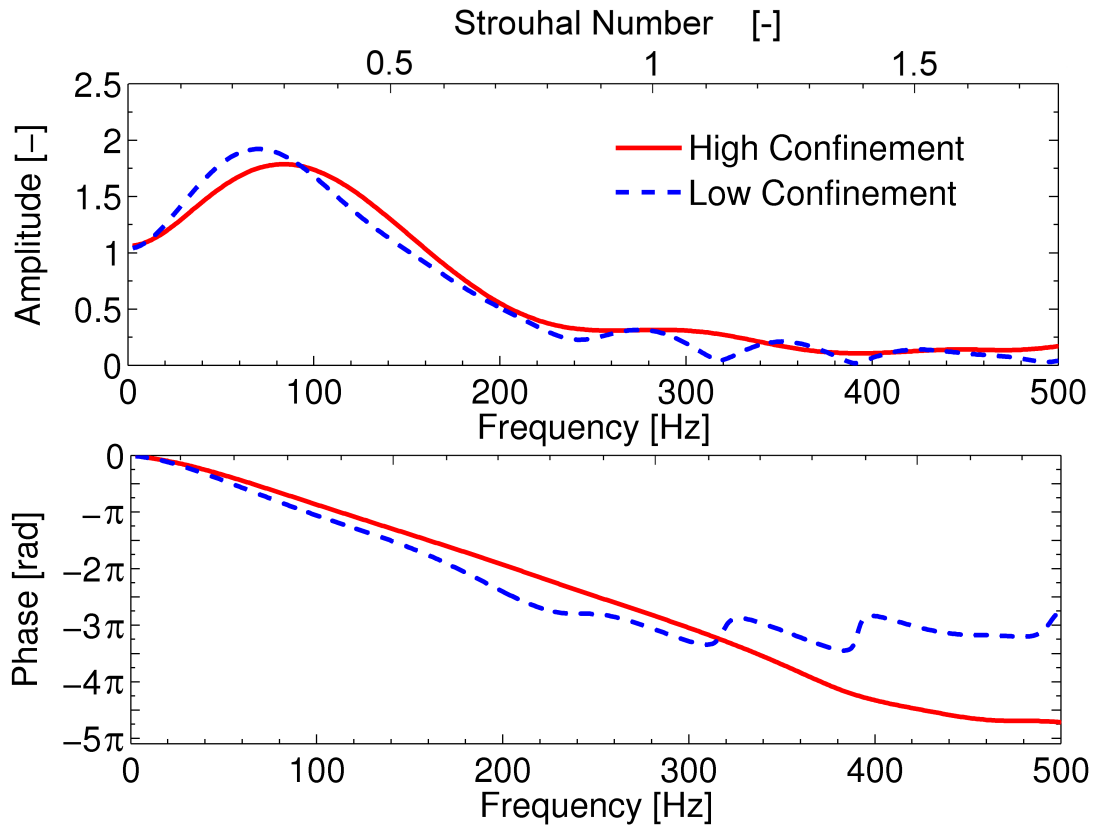


**Figure 5.41:** Flame transfer functions from LES/SI with low and high confinement combustors with 30 kW. Excitation=9.5%.

response. An analysis of the cases with varied swirler position is additionally carried out to identify the respective time lags between perturbations and the discrepancies in the amplitudes between experimental and identified FTFs shown in section 5.5.2.

### 5.7.1 Dependence of Unit Impulse Responses on Thermal Conditions, Combustor Confinement and Power Rating

The  $FTF(\omega)$  in Eq. (3.14) is fitted to the identified FTFs to obtain the time lags  $\tau_i$  and standard deviations  $\sigma_i$ ,  $i = 1, 2, 3$ . The parameter values are shown in Table 5.2. The coefficient  $a$  in Eq. (3.14) in the contribution from swirl fluctuations has been modified from the original model [103] to a value of 1.05, which

**Table 5.2:** Time lag model

$\tau, \sigma$ [ms]	$\tau_1$	$\sigma_1$	$\tau_2$	$\sigma_2$	$\tau_3$	$\sigma_3$
30 kW HC-NA-P1	3.75	1	5.29	0.75	7.8	2.5
30 kW HC-A-P1	2.25	0.64	4.13	0.35	5.5	0.5
30 kW LC-NA-P1	5.3	1.6	6.0	1.0	9.9	3.0
30 kW HC-NA-P2	3.75	1	10.42	1.4	12.93	3.2
50 kW HC-Nonadiabatic	2.8	1.0	3.6	0.65	4.83	0.8

produced a better quality.

The UIRs obtained using Eq. (3.13) and 140 coefficients with a time step of  $1.25 \times 10^{-4}$  s and with the parameters in Table 5.2 are shown in Fig. 5.42, indicating the respective time delays in the flame response to the different perturbations. The variation in time lags between cases are in agreement with the changes in flame lengths shown in Figs. 5.4 and 5.40. Also, the amplitude in the UIR of the HC-Adiabatic case is higher because the flame is shorter and reacts in the inner and outer shear layer at the same time. Thus, the standard deviations in the model are smaller than in the other cases, indicating that the response is in a narrower period of time. The identified FTF for 50 kW is fitted also with the model and its parameters are included in Table 5.2. The FTFs obtained using the model are shown in Fig. 5.43 with very good agreement with the identified FTFs. Additionally, the sum of all coefficients between cases is equal to unity, in agreement with the zero frequency limit for the amplitude of the FTF [159]. The cases with higher power rating and with adiabatic walls show a broader frequency response in the FTF than the cases with LC and HC with non-adiabatic. From the model, there is some relation between a broader frequency response and the period of time for the flame reaction. The flame response to the perturbations in both cases is in a shorter period of time as shown in Fig. 5.42 due to the stabilization in both shear layers in the adiabatic case, and the higher velocities in the higher power rating case. It is argued that the broader frequency response is produced by the consumption in a shorter period of time of the fuel introduced by the mass flow fluctuations. This can be shown using the Strouhal number. It is known that

with only the change of power rating in a combustor system, the FTF has a good scaling behavior [8, 97, 137] with the Strouhal number (see Eq. (5.3)). In Eq. (5.3), the main parameter in the scaling is the velocity  $u_{\text{bexit}}$ . Thus, an increase in  $u_{\text{bexit}}$  moves the flame response to higher frequencies. Now, using adiabatic combustor walls the flame stabilizes in both shear layers, so the additional mass flow introduced by the perturbation is consumed at the same moment, but by 2 flames. This can be represented as a consumption 2 times faster. Thus, similar to the increase in power rating, the flame response moves to higher frequencies. Indeed, Durox et al. in [44], considered a similar criterion for normalization of the FTF in a M-flame, taking as the characteristic length the half of the distance between inner and outer radius in an annular burner exit due to the presence of two flames. A M-flame does not scale with a V-flame by the Strouhal number due to the strong differences on the flame dynamics produced by the varied flame topology, but produces a broader frequency response than the V-flame, which can be understood by the shorter time necessary to consume the fuel introduced by the mass flow fluctuations.

The evaluation of the UIRs for the cases with similar position of the swirler confirms that the variations in flow field and flame shape can lead to a varied flame response and time lags.

### 5.7.2 Comparison of Unit Impulse Responses with Swirler at Varied Positions

The FTF model is used to identify the various time lags and the discrepancies in the amplitudes between experimental and identified FTF shown in section 5.5.2. To obtain the UIR from experimental data, the inverse z-transform of an experimental FTF( $\omega_{\text{real}}$ ) is applied:

$$h_k = \text{Re} \left( \frac{\Delta t}{\pi} \sum_{\omega_{\text{real}}=0}^{\pi/\Delta t} \text{FTF}(\omega_{\text{real}}) e^{i\omega_{\text{real}}k\Delta t} \right), \text{ for } k = 0, \dots, L, \quad (5.7)$$

where  $\Delta t$ ,  $\omega$ ,  $k$ ,  $L$  are the time step, angular frequency, UIR coefficient index, and the maximum index of the UIR coefficients, respectively.

The UIR from the experimental FTFs in Figs. 5.8 and 5.29 at positions 1 and 2,

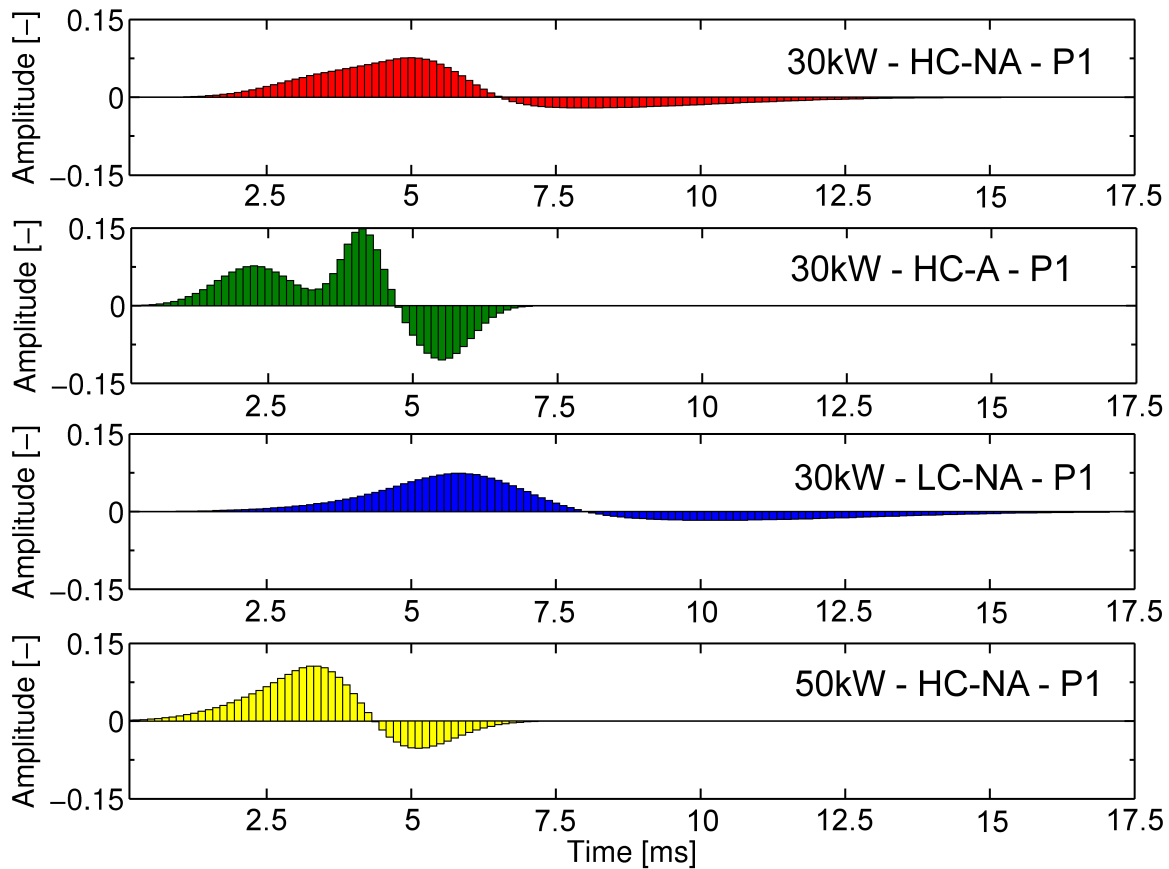


**Figure 5.42:** UIRs from time lag model.

respectively, are obtained using a time step of  $1.25 \times 10^{-4}$  s and 190 coefficients. The UIRs are shown in Fig. 5.44. The UIR from the experiments with the swirler at position 1 has a finite response until around 100 time steps, and after that time (that all fuel has been consumed), there is no additional response from the flame. The UIR with the swirler at position 2 shows a longer response in time with strong variations of the coefficients along that period of time. This is an indication of some uncertainty on the experimental data. The two responses from the axial and tangential fluctuations can be appreciated, where the one from the tangential fluctuations is at later time than in the experimental UIR at position 1. This is due to the longer time lag response to the tangential velocity fluctuations as they are induced by the swirler at a more upstream position. Similar characteristics as in the experimental UIRs

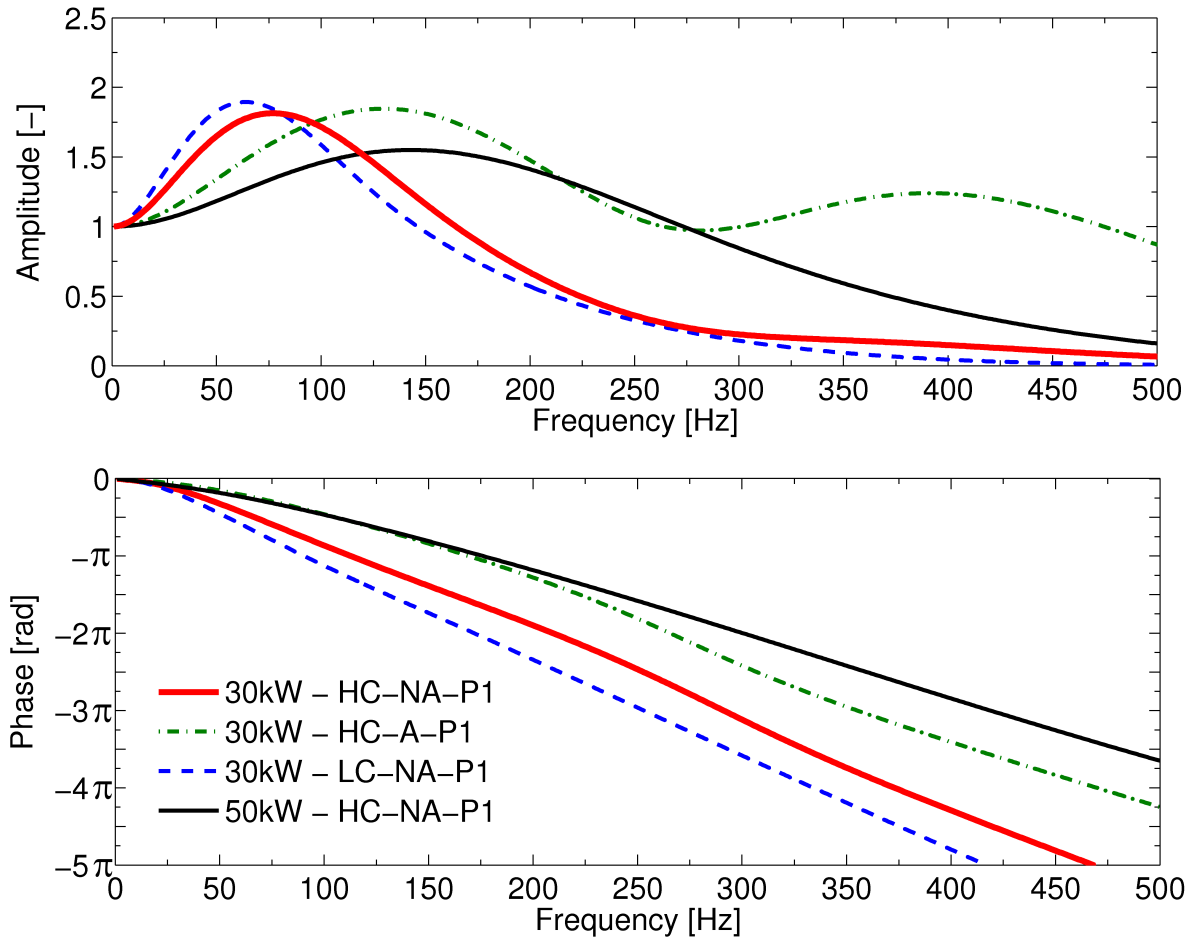


**Figure 5.43:** Flame transfer function from time lag model.

are observed on the UIRs obtained from the identified FTFs. The UIRs from LES shown in Fig. 5.44 are not the ones obtained directly from the identification using LES/SI (which usually show higher oscillations due to information from higher frequencies), but obtained using Eq. (5.7). This is done to obtain the UIR from experiments and LES/SI in the same frequency range. The identified UIRs and the ones obtained using Eq. (5.7) show the same frequency response and similar shape in the UIR but with lower oscillations.

Equation (3.14) is used to obtain a modeled FTF for the case with the swirler at position 2. This is done by modifying the parameters in Table 5.2 of the case with the swirler at position 1 according to physical variations observed in the

## 5.7 Flame Transfer Function Model

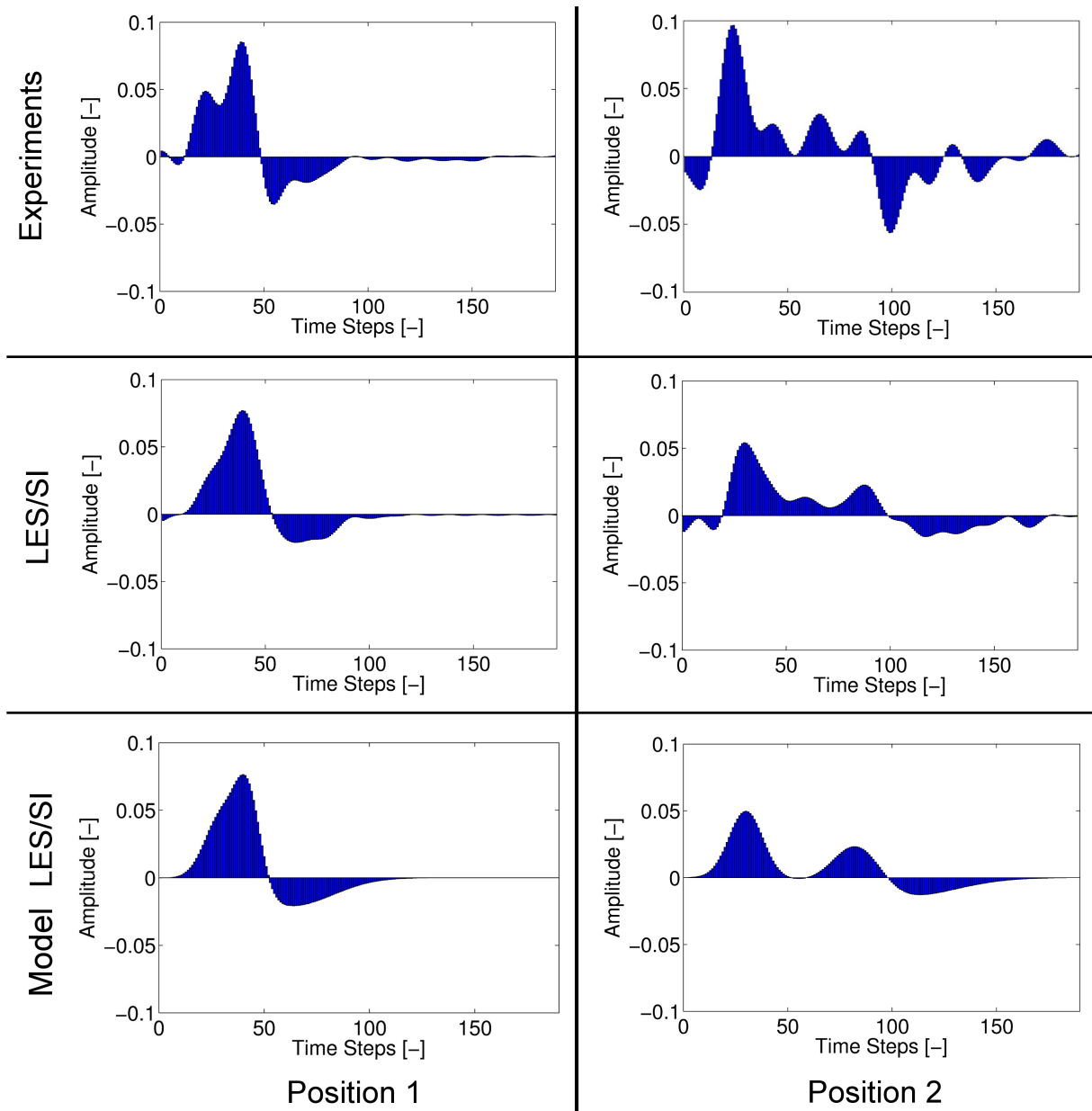


**Figure 5.44:** UIR from modelled, experimental and identified FTF with 30 kW at varied swirler positions.

case at position 2. First, the coefficient  $a$  in Eq. (3.13) is decreased from 1.05 to 0.952 to be in agreement with the decay in swirl observed in section 5.5.1. The  $\tau_1$  and  $\sigma_1$  from the mass flow fluctuations are not modified (as done by

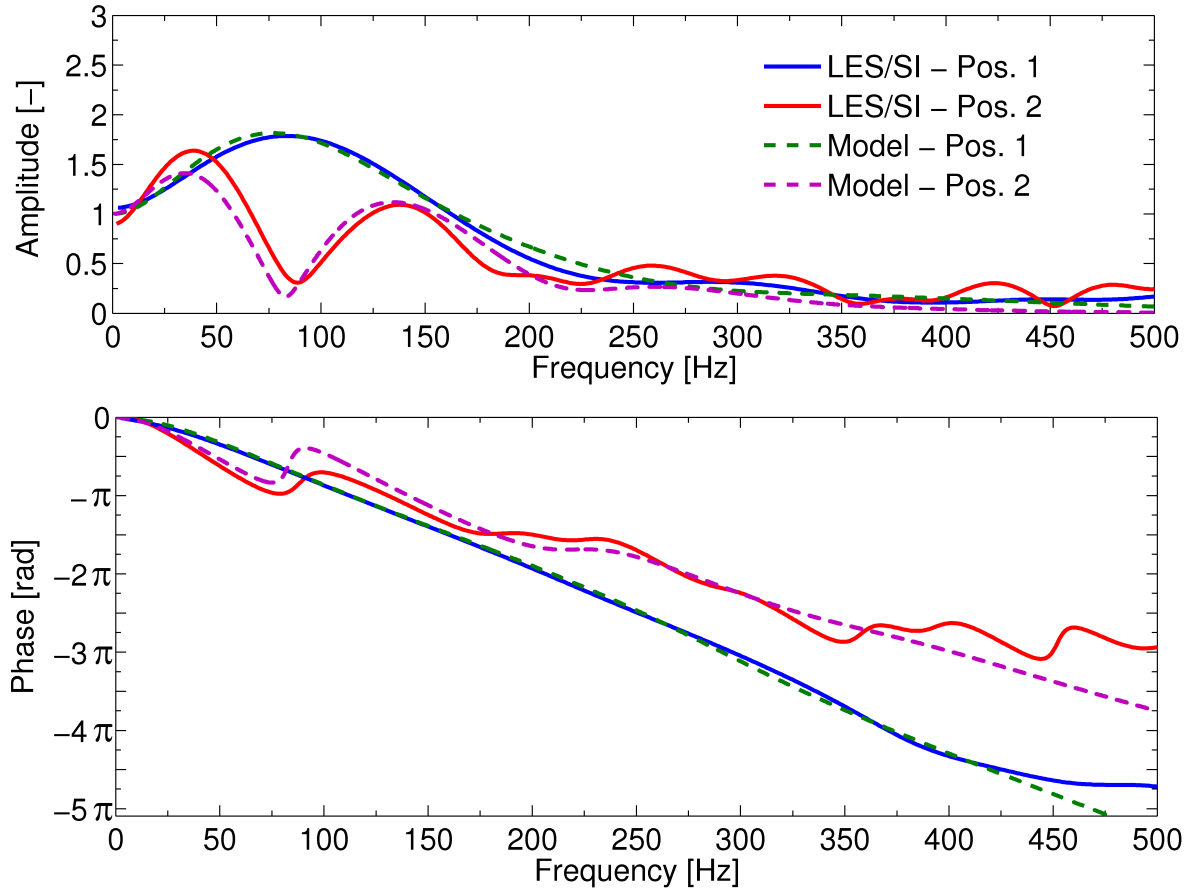


**Figure 5.45:** Flame transfer function from LES/SI and time lag model for varied swirler positions with 30kW.

Komarek in [103]), while the  $\tau_2$  is increased and defined by:

$$\tau_2 = \tau_1 + \frac{l_{s,\text{bexit}}}{u_{\text{prop}}}, \quad (5.8)$$

where  $l_{s,\text{bexit}}$  is the distance from the exit of the swirler (130 mm upstream the burner exit at position 2) to the burner exit, and  $u_{\text{prop}}$  is the propagation velocity of the tangential velocity fluctuations equal to 19.5 m/s (see section 5.5.2).  $\tau_1$  represents the propagation time of the perturbation on the flame. Indeed, good agreement with  $\tau_2$  from the case with the swirler at position 1 (30 mm upstream the burner exit) is obtained applying Eq. (5.8). Then, the time difference between  $\tau_2$  and  $\tau_3$  for the swirler at position 1 is kept. The standard deviations  $\sigma_2$  and  $\sigma_3$  are increased to create a shape of the UIR similar to the one

**Table 5.3:** Time lag model for experimental FTF at position 2

$\tau, \sigma$ [ms]	$\tau_1$	$\sigma_1$	$\tau_2$	$\sigma_2$	$\tau_3$	$\sigma_3$
30kW HC-NA-P2 Exp.	3	0.55	5.4	2.3	12.18	0.68

from the identified UIR. This increase in the standard deviations for the contribution of swirl fluctuations was also observed and identified by Komarek et al. [103]. Applying these changes, the UIR and FTF of the model for the swirler at position 2 are shown in Figs. 5.44 and 5.45, respectively. Good agreement with the identified UIRs and FTF was obtained. The model captured the two amplitude peaks and the strong decrease between the peaks, with good agreement also in the phase. The amplitudes from the experimental FTF are not reproduced by the model introducing the physical modifications mentioned before. This modifications in the model exhibit good agreement with the identified FTF. This is an indication that some inaccuracies are present in the experimental data for the case measured with 30 kW of power rating with the swirler at position 2, because good agreement between the model and experimental data for varied swirler positions was obtained before for a case with higher power rating (70 kW) [103].

An additional analysis is carried out to fit the time lag model to the experimental data to look the level of mismatch between  $\tau_i$  and  $\sigma_i$  of the identified and experimental FTFs, which can create the discrepancies shown in Fig. 5.29. To obtain the best fit of the model to the FTF from experiments, the  $\tau_i$  and  $\sigma_i$  in Table 5.3 are used. The UIR and FTF from experiments and with the model fit are shown in Figs. 5.46 and 5.47. Good agreement is obtained between the experiments and the model. However, the value of  $\tau_2$  that is necessary to obtain this agreement is unphysical as it corresponds to a propagation speed of the tangential fluctuations more than 470% higher than the mean axial velocity using Eq. (5.8), while applying physical modifications in the model from the identified FTF at position 1, the model is able to reproduce the identified FTF at position 2 with good agreement. This is another indication of inaccuracies in the experimental data.

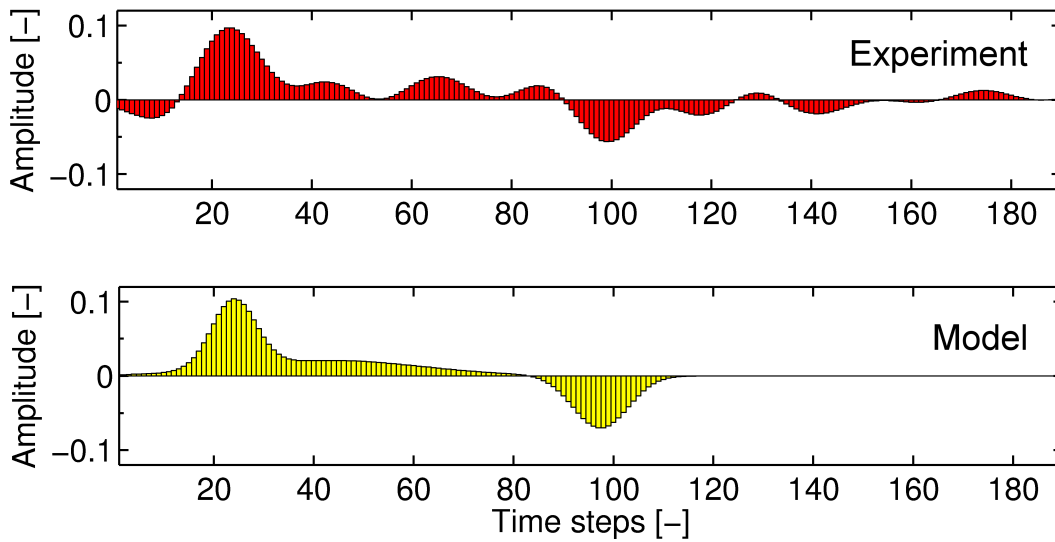


**Figure 5.46:** UIR from time lag model for the experimental FTF at position 2.

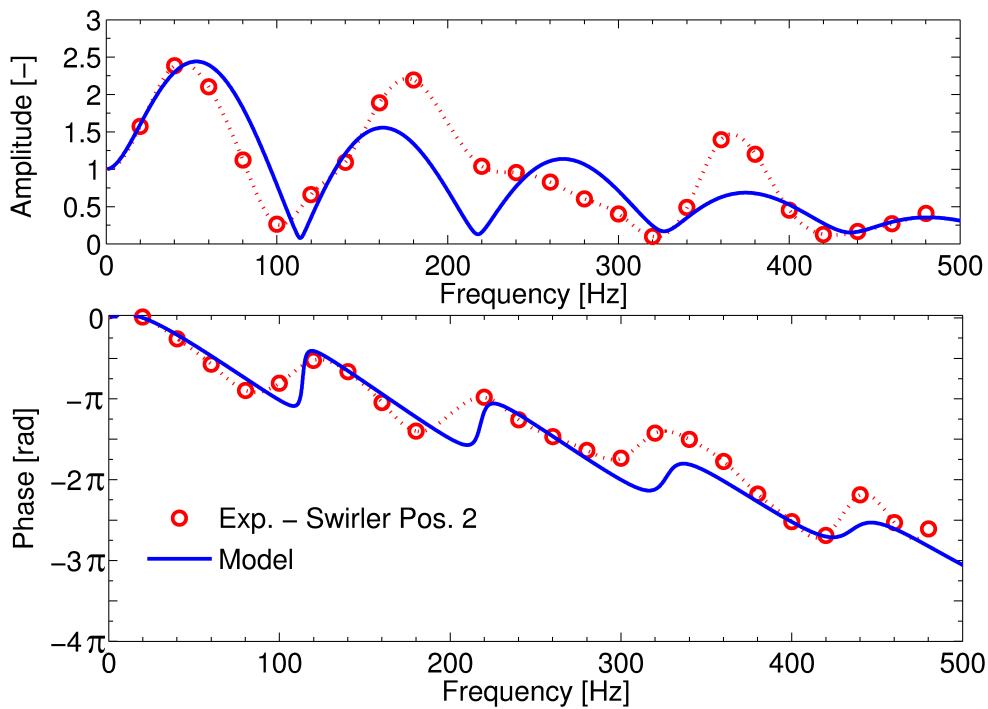


**Figure 5.47:** FTFs from experiments and from the time lag model for the experimental FTF at position 2. Experiments in (o)

## 5.7 Flame Transfer Function Model

---

Additionally, as shown in the analysis of the UIRs, the flame response is mainly produced from two contributions (which in the case of the swirler at position 2 shows much higher separation due to the longer time lags). Then the system can be analyzed as a MISO system to identify the contributions in the flame response from mass flow and swirl fluctuations separately. This kind of analysis was not extended in the present study, but will be investigated in future works.

## 6 Stability Analysis with Low-Order Network Models

A final step after the identification of the flame transfer functions is the stability analysis. The LES/SI results have confirmed that the FTF does depend not only on the burner geometry, but also on the boundary conditions that the combustor provides for the flame (combustor wall temperature, confinement, etc.) and on the position of the swirl generator. Thus, if the burner is installed in a facility with variations in the environment interacting with the flame, the flame response will be different. The stability behavior of the system should be obtained taking into account these discrepancies. Using a network model, the stability analysis is carried out to assess the impact of such discrepancies in FTFs on combustor stability limits.

In this chapter, background about 1D acoustics and network models is presented in the beginning, followed by the stability analysis of the combustion system with the varied conditions investigated on Chapter 5.

### 6.1 Linear Acoustic 1D Equations

In acoustics, the flow variables of velocity ( $u$ ), pressure ( $p$ ) and density ( $\rho$ ) can be expressed in a similar way as in the Reynolds decomposition (see section 2.1) in a stationary mean ( $\bar{\phantom{x}}$ ) and a fluctuating part ( $'$ ):

$$u(x, t) = \bar{u} + u'(x, t), \quad (6.1)$$

$$p(x, t) = \bar{p} + p'(x, t), \quad (6.2)$$

$$\rho(x, t) = \bar{\rho} + \rho'(x, t). \quad (6.3)$$

where  $x$  and  $t$  are the position and time, respectively. The fluctuating part in this section is referred to acoustic fluctuations without the presence of turbulent fluctuations.

Considering that the fluctuations are much smaller than their mean values ( $p'(x,t) \ll \bar{p}$ ), and that the flow is homentropic (homentropic refers to an isentropic ( $DS/Dt=0$ ) and uniform ( $\nabla S=0$ ) flow [83, 161, 211]) and non-viscous, the equations of mass and momentum can be linearized to obtain the linearized convective acoustic equations (see Appendix A.6 for the derivation):

$$\frac{\partial \rho'}{\partial t} + \bar{u} \frac{\partial \rho'}{\partial x} + \frac{\partial \bar{\rho} u'}{\partial x} = 0, \quad (6.4)$$

$$\bar{\rho} \left( \frac{\partial u'}{\partial t} + \bar{u} \frac{\partial u'}{\partial x} \right) + \frac{\partial p'}{\partial x} = 0. \quad (6.5)$$

Defining the density fluctuations  $\rho'$  in terms of the speed of sound  $a$  and the pressure fluctuations (see Appendix A.6):

$$\rho' = \frac{p'}{a^2}, \quad (6.6)$$

replacing Eq. (6.6) in Eq. (6.4), applying the total time derivative ( $\partial/\partial t + \bar{u}\partial/\partial x$ ) to Eq. (6.4), the divergence ( $\partial/\partial x$ ) to Eq. (6.5), and subtracting both equations in order to eliminate the terms including the acoustic velocity ( $u'$ ), the *convective wave* equation is obtained:

$$\left( \frac{\partial}{\partial t} + \bar{u} \frac{\partial}{\partial x} \right)^2 p' - a^2 \frac{\partial^2 p'}{\partial x^2} = 0. \quad (6.7)$$

The solution of Eq. (6.7) is [2, 161]:

$$\frac{p'}{\rho a} = f(x - (a + \bar{u})t) + g(x + (a - \bar{u})t), \quad (6.8)$$

which is the superposition of the traveling waves  $f$  (with a propagation speed of  $a + \bar{u}$  in downstream direction) and  $g$  (with a propagation speed of  $a - \bar{u}$  in upstream direction). A scheme of acoustic waves  $f$  and  $g$  in a fluid with mean flow is shown in Fig. 6.1. The term  $\rho a$  is introduced for normalization and it

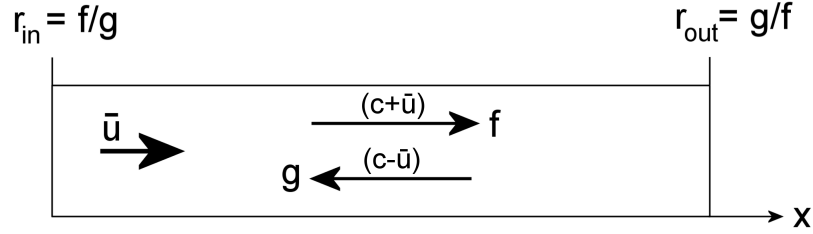


**Figure 6.1:** Acoustic wave propagation in fluid with mean flow. Adapted from [48].

is called the *characteristic impedance*.  $f$  and  $g$  are called the Riemann Invariants, which are arbitrary functions of their arguments [161].

Considering time-depending harmonic planar waves,

$$p' \sim e^{i(\omega t - k_x x)}, \quad (6.9)$$

the solution of Eq. (6.7) is:

$$\frac{p'}{\rho a} = f e^{i(\omega t - k_{x+} x)} + g e^{i(\omega t - k_{x-} x)}, \quad (6.10)$$

where  $\omega$  and  $k_{x\pm}$  are the angular frequency and acoustic wave number defined by:

$$\omega = 2\pi f, \quad (6.11)$$

$$k_{x\pm} = \pm \frac{\omega}{a \pm \bar{u}} = \pm \frac{\omega/a}{1 \pm M}, \quad (6.12)$$

where  $M = \bar{u}/a$  is the mean flow Mach number. The acoustic velocity fluctuation is defined also in terms of Riemann invariants by:

$$u' = f e^{i(\omega t - k_{x+} x)} - g e^{i(\omega t - k_{x-} x)}. \quad (6.13)$$

From Eqs. (6.10) and (6.13), the Riemann invariants are defined in terms of the acoustic fluctuations  $p'$  and  $u'$  by:

$$f = \frac{1}{2} \left( \frac{p'}{\rho a} + u' \right), \quad (6.14)$$

$$g = \frac{1}{2} \left( \frac{p'}{\rho a} - u' \right). \quad (6.15)$$

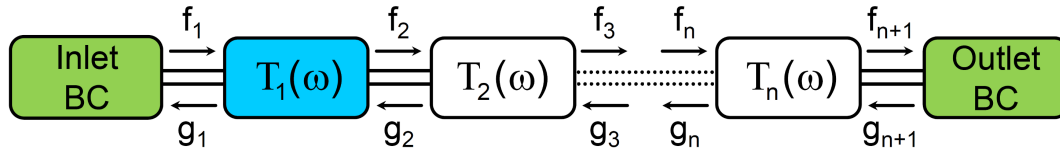


**Figure 6.2:** Scheme of a Low-order model.

## 6.2 Low-order Network Models

Low-order network models allow to quickly analyze a (thermo-)acoustic system. They are highly flexible and provide insight into the interrelations between the single components. Only a minor computational effort is required to draw conclusions regarding system stability. The analysis is based on the assumption of linear and time-harmonic acoustics, and is carried out in the frequency domain. The system is represented by a network of acoustic elements, such as ducts, area changes or a (compact) flame as well as boundary conditions. A scheme of a network model is presented in Fig. 6.2. Generally, the network topology can be arbitrarily complex including several inlet and outlet boundaries.

In low-order network models, the acoustic variables  $u'$ ,  $p'$  – or rather the acoustic waves described in terms of Riemann Invariants  $f$  and  $g$  [156] – at the upstream/input ( $u$ ) and downstream/output ports ( $d$ ) of each element are related by the frequency dependent element transfer matrix  $\mathbf{T}$ :

$$\begin{pmatrix} f_d \\ g_d \end{pmatrix} = \mathbf{T}(\omega) \begin{pmatrix} f_u \\ g_u \end{pmatrix}. \quad (6.16)$$

The output from one element is passed to the input ports of the next one. Boundary conditions are applied to terminate the system. The assembly of the individual transfer matrices yields a system of equations of the form:

$$\begin{pmatrix} \text{Matrix} \\ \text{of} \\ \text{coefficients } \mathbf{S} \end{pmatrix} \begin{pmatrix} f_m \\ g_m \\ \vdots \\ g_n \end{pmatrix} = \begin{pmatrix} 0 \\ 0 \\ \vdots \\ 0 \end{pmatrix}. \quad (6.17)$$

The characteristic equation  $\text{Det}(\mathbf{S}) = 0$  is fulfilled for complex eigenfrequencies,  $\omega = \omega_{real} + i\omega_{imag} \in \mathbb{C}$ . With harmonic time dependence  $\exp(i\omega t)$ , the imaginary part of an eigenfrequency indicates whether the corresponding eigenmode grows or decays over time. The cycle increment (CI) of a mode, i.e. the relative growth in amplitude per period of the oscillation, may be defined as [83, 156]:

$$\text{CI} = e^{-2\pi \frac{\omega_{imag}}{\omega_{real}}} - 1. \quad (6.18)$$

With this definition,  $\text{CI} = 0$  corresponds to marginal stability. The real part of the eigenfrequency determines the frequency of the eigenmode.

Transfer matrices for many elements have been derived analytically and can be found in the literature [156]. Also, for more complex elements, transfer matrices can be obtained from measurements or CFD simulations. The analytical flame transfer matrix of a compact flame is presented in this chapter. The definitions of other acoustic elements included in the network model for the stability analysis are shown in Appendix A.7.

### 6.2.1 Flame Transfer Matrix of a Compact Flame

In the case of a thermoacoustic problem, the flame must be incorporated into the system model. The flame is commonly represented by an acoustically “compact” element. That is, its spatial dimensions are assumed small compared to the acoustic wave length. Hence, it is treated as a discontinuity where heat is added. According to Chu [25], the acoustic variables at the upstream ( $u$ ) and downstream ( $d$ ) sides of the heat source then satisfy the linearized Rankine-Hugoniot relations [83, 156]:

$$\left( \frac{p'}{\rho a} \right)_d = \frac{(\rho a)_u}{(\rho a)_d} \left[ \left( \frac{p'}{\rho a} \right)_u - \left( \frac{T_d}{T_u} - 1 \right) u'_u M_u \left( 1 + \frac{\dot{Q}'/\bar{Q}}{u'_u/\bar{u}_u} \right) \right], \quad (6.19)$$

$$u'_d = u'_u \left[ 1 + \left( \frac{T_d}{T_u} - 1 \right) \frac{\dot{Q}'/\bar{Q}}{u'_u/\bar{u}_u} \right] - \left( \frac{p'}{\rho a} \right)_u M_u \gamma \left( \frac{T_d}{T_u} - 1 \right). \quad (6.20)$$

In order to obtain a closed system of equations, the heat release fluctuations  $\dot{Q}'$  in Eqs. (6.19) and (6.20) must be related to the fluctuations in the

acoustic variables  $u'$  and  $p'$ . This is achieved by introducing the FTF from Eq. (3.1) into Eqs. (6.19) and (6.20). In general, the reference location “ $r$ ”, where the input signal  $u'_r$  is recorded, is not immediately upstream of the flame at location “ $u$ ”. Thus, the flame is represented as a 6-port element in the network, linking  $f$ 's and  $g$ 's at positions “ $u$ ”, “ $d$ ” and “ $r$ ” (see Fig. 6.4)). The element is defined in terms of Riemann invariants by [83]:

$$\begin{pmatrix} \frac{\rho_d a_d}{\rho_u a_u} & \frac{\rho_d a_d}{\rho_u a_u} \\ 1 & -1 \end{pmatrix} \begin{pmatrix} f_d \\ g_d \end{pmatrix} = \begin{pmatrix} 1 - M_u \left( \frac{T_d}{T_u} - 1 \right) & 1 + M_u \left( \frac{T_d}{T_u} - 1 \right) \\ 1 - M_u \left( \frac{T_d}{T_u} - 1 \right) \gamma & -1 - M_u \left( \frac{T_d}{T_u} - 1 \right) \gamma \end{pmatrix} \begin{pmatrix} f_u \\ g_u \end{pmatrix} \quad (6.21)$$

$$+ \left[ \frac{\bar{u}_u}{\bar{u}_r} \left( \frac{T_d}{T_u} - 1 \right) \text{FTF}(\omega) \right] \begin{pmatrix} -M_u & M_u \\ 1 & -1 \end{pmatrix} \begin{pmatrix} f_r \\ g_r \end{pmatrix}. \quad (6.22)$$

The derivation of this expression is presented in Appendix A.7.2.

### 6.2.2 Use of Experimental Data in Eigenfrequency Analysis (The UIR Method)

The eigenfrequency analysis requires to evaluate coefficients of the system matrix  $\mathbf{S}(\omega)$  also for frequencies  $\omega \in \mathbb{C}$  away from the real axis. This requirement is obviously not a problem if analytical expressions for network elements are known [156]. Also, it is not a problem for a flame transfer function determined with LES/SI, because the argument  $\omega$  in the  $z$ -transform (see Eq. (4.32)) may be complex-valued, such that from the UIR  $\mathbf{h}$  the transfer function  $\text{FTF}(\omega)$  may be evaluated anywhere in the complex plane [83].

However, in experiments the flame transfer function is determined with harmonic forcing at constant amplitude, i.e. the FTF is known only for a number of purely real frequencies  $\omega_n \in \mathbb{R}$ . In such a situation the FTF at intermediate frequencies is often determined by interpolation between measured values. However, for stability analysis the FTF is needed for frequencies away from the real axis. Extrapolating the FTF from known values on the real axis into the complex plane leads that the growth or decay of oscillation amplitudes is not properly reflected in the system matrix coefficients, if the imaginary part of the frequency is not taken into account.

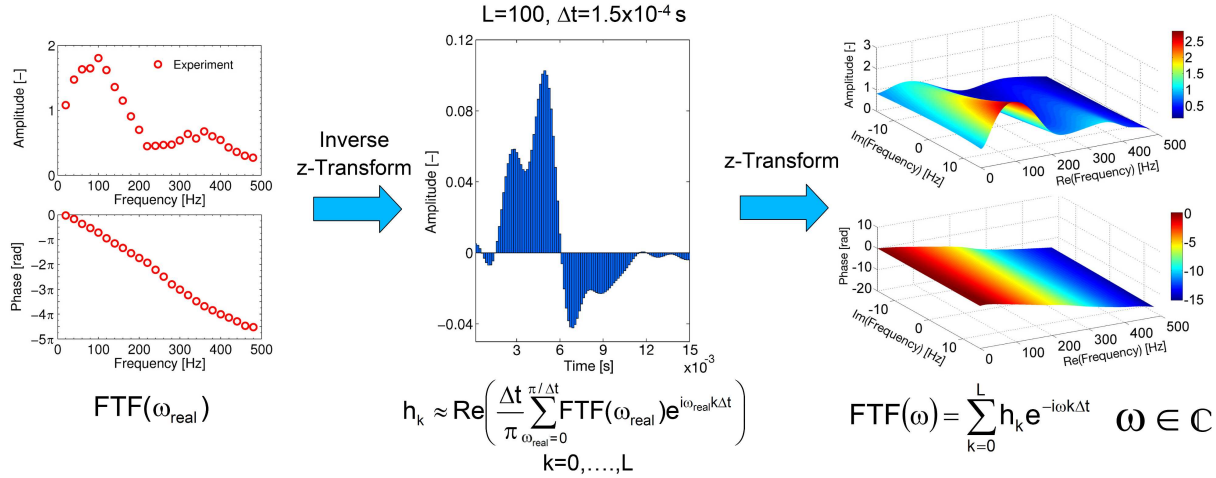


**Figure 6.3:** UIR Method

To overcome this difficulty with elements that are defined only for purely real frequencies, it is proposed to first compute the UIR of the element by the inverse  $z$ -transform using Eq. (5.7). After obtaining the different UIR coefficients, which describe the element in the time domain, a forward  $z$ -transform (see Eq. (4.32)) is applied evaluating the element with complex frequencies ( $\omega \in \mathbb{C}$ ). A similar procedure was applied by Schuermans in [177]. A scheme of the procedure is shown in Fig. 6.3.

## 6.3 Stability Analysis of the System

To look at the impact of the different conditions on predicting stability limits of a system, a stability analysis is carried out with the network model tool “taX” [117] developed at TU Munich to evaluate and compare their eigenfrequencies and cycle increments.

### 6.3.1 Network Model of the System

The low-order model of the premix burner test rig (see Fig. 5.1) is shown in Fig. 6.4. The network model consists of different elements as ducts, area

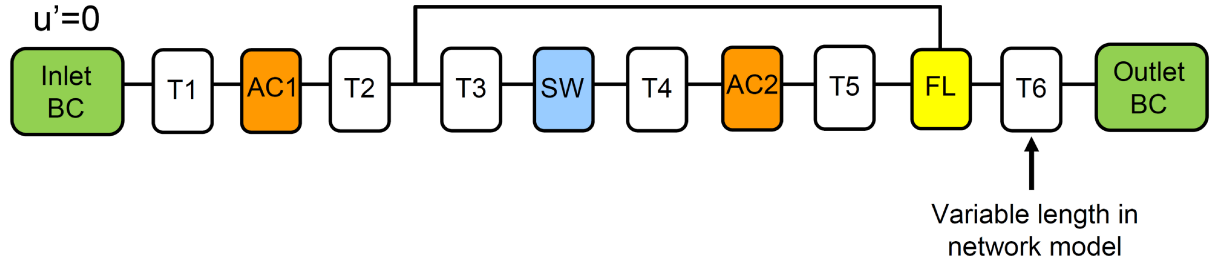


**Figure 6.4:** Low-order model of premix burner test rig.

**Table 6.1:** Network Model.

Name	Details
Closed end	$u'=0, R=1, T=293\text{ K}$
Plenum	Duct (A.7.1), $l=0.17\text{ m}, T=293\text{ K}$
Area change 1	Compact element with losses (A.7.3), $A_u=0.031416\text{ m}^2$ , $A_d=0.001056\text{ m}^2, \zeta=0.029$
Tube 1, 2 and 3	Duct (A.7.1), $l_1=0.11\text{ m}, l_2=0.025\text{ m}$ and $l_3=0.045\text{ m}$ . $T=293\text{ K}$
Swirler	Swirler Transfer Matrix identified using LES/SI
Area change 2	Compact element with losses (A.7.3), $A_u=0.001056\text{ m}^2$ , $A_{d,HC}=0.0081\text{ m}^2, A_{d,LC}=0.0256\text{ m}^2, \zeta=8.08$
Combustor 1	$l=l_f, T=293\text{ K}$
Flame	Transfer matrix model with upstream reference location (A.7.2).
Combustor 2	$l=l_{cc} - l_f, T=1930\text{ K}$
Reflective end	Reflection coefficient from Fig. 6.5. $T=1930\text{ K}$

changes, flame, swirler and boundary conditions, which are defined in Appendix A.7 and described in Table 6.1.

There is uncertainty about the boundary conditions (reflection coefficients) of the experiments. For the stability analysis, the reflection coefficients measured by Reddy Alemela (shown in [213]) in a similar cross section combustor and perforated plate, but with another swirl burner, power rating (50 kW) and equivalence ratio (0.735) are used (see Fig. 6.5).

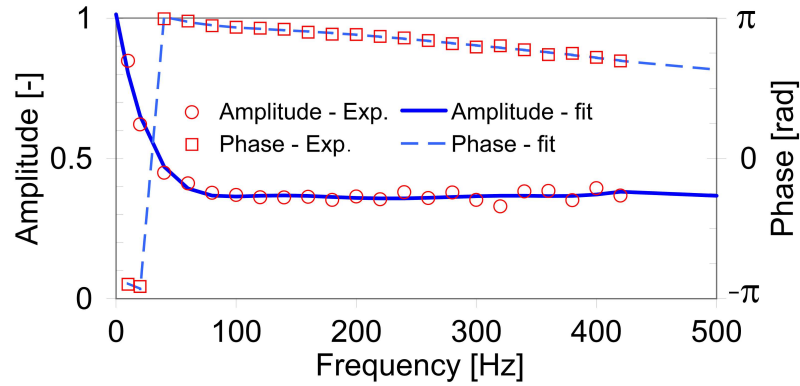


**Figure 6.5:** Downstream reflection coefficient used in network model

## 6.4 Results of the Stability Analysis

In the experiments using the swirler position at 30 mm upstream the burner exit and the high-confinement combustor (performed by T. Komarek), the system was stable with a combustor length of 300 mm. Instability developed using a combustor length of 700 mm for different power ratings. The unstable eigenfrequencies were 101.3 and 142 Hz using 30 and 50 kW of power rating, respectively. In a first step, the stability analysis is carried out introducing the experimental FTFs of both power ratings in the network model (in the element *flame* (FL) to obtain its flame transfer matrix (see section 6.2.1)). The analysis is performed for combustor lengths of 300 and 700 mm in order to validate the stability behavior obtained with the network model with the one found in the experiments. Results from experiments and the network model are shown in Table 6.2. Good agreement is found between stability conditions in the experiments and using the network model with the FTFs from experiments. The unstable eigenfrequencies found with the network model are around 10% higher than the ones from the experiments. The differences might be due to the uncertainty in the boundary conditions mentioned before, and that more precise models should be applied for the area changes and in the combustion chamber (it is considered as adiabatic, while in the experiment, temperature and speed of sound change over the length due to heat losses). Considering this, good agreement for the eigenfrequencies between experiments and network model is also obtained.

**Table 6.2:** Stability behavior from experiments and using Network Model (NM) with experimental FTF

	$l_{comb}=300$ mm				$l_{comb}=700$ mm				
	Exp.	$f$ [Hz]	NM <sub>expFTF</sub>	$f$ [Hz]	Exp.	$f$ [Hz]	NM <sub>expFTF</sub>	$f$ [Hz]	CI[-]
30 kW	Stable	-	Stable	-	Unst.	101.3	Unst.	110.2	0.22
50 kW	Stable	-	Stable	-	Unst.	142	Unst.	160.2	0.28

The next step is to introduce the identified FTFs of the 30 and 50 kW nonadiabatic cases in the network model and compare their stability behavior with the one using the experimental FTF. Results from the stability analysis are shown in Table 6.3. Using the combustor length of 300 mm, both cases are stable as in the experiments. Using the combustor with 700 mm length, good agreement is found in the stability behavior and eigenfrequency for the case with 30 kW of power rating. As it has been shown before, the identified FTF presented good agreement in amplitude and phase with the experimental one. In the other hand, for the case with 50 kW of power rating, the network model predicted a moderate stable condition of the system, while it has shown an unstable condition in experiments and using the experimental FTF in the network model. The identified FTF showed a lower amplitude with respect to the experimental one. An increase in the amplitude of the FTF represents an increase of the heat release fluctuations produced by the velocity fluctuations. Thus, if the Rayleigh criterion is fulfilled, the flame will add more acoustic energy to the system, becoming more prone to combustion instabilities. The lower amplitude of the identified FTF was discussed in section 5.3.2.

An extended evaluation on the stability analysis is carried out changing the length of the combustor on the network model ( $l_{cc}$ ) from 0.6 to 0.9 m in steps of 0.1 m, keeping the same boundary conditions for all cases. In Fig. 6.6, the eigenfrequencies and the growth rates obtained with the network model for the different combustor lengths are presented. The unstable eigenfrequency from experiments is additionally plotted. The system is unstable for all the considered combustor lengths using the experimental FTF, while it is only unstable for combustor lengths higher than 0.75 m using the identified FTF. The stability analysis indicates that the differences in the predicted FTF may have

**Table 6.3:** Stability analysis using Network Model (NM) with identified FTFs

	$l_{comb}=300$ mm		$l_{comb}=700$ mm			$l_{comb}=800$ mm		
	NM	$f$ [Hz]	NM <sub>FTF</sub>	$f$ [Hz]	CI[-]	NM <sub>FTF</sub>	$f$ [Hz]	CI[-]
30 kW	Stable	-	Unstable	103	0.385	Unstable	103.1	0.55
50 kW	Stable	-	Stable	135.2	-0.106	Unstable	134.9	0.1

a significant impact on stability prediction and cycle increments.

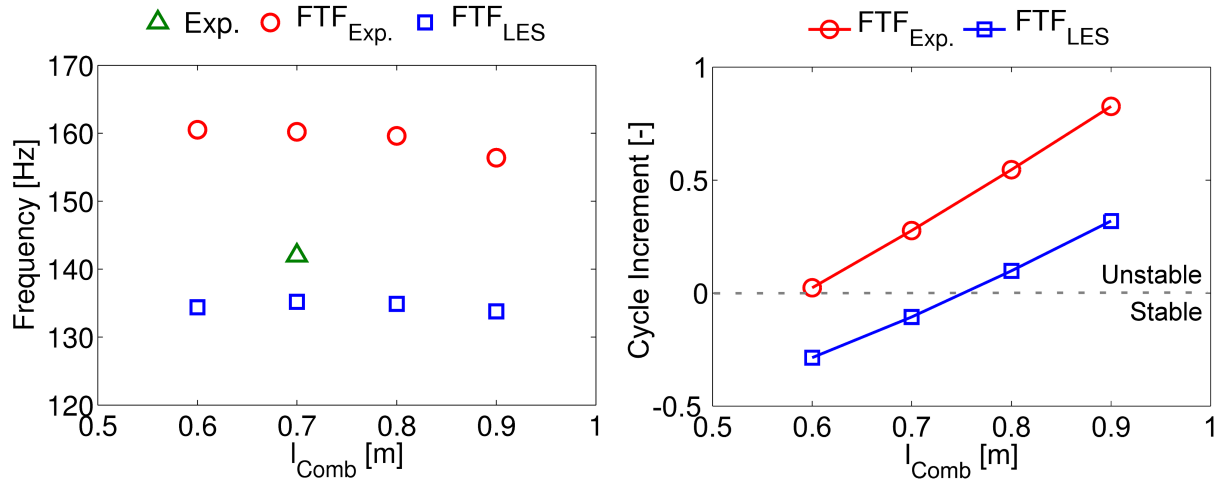


**Figure 6.6:** Eigenfrequencies and cycle increments using experimental and identified FTF in the network model at various combustor lengths with 50 kW. ( $\Delta$ ) Unstable eigenfrequency in experiments.

As shown in Chapter 5, using the same inlet conditions and swirler position, differences in the FTF with respect to the reference case are found using adiabatic combustor walls and with a varied combustor cross section. Results of the stability analysis introducing the identified FTFs and at different combustor lengths are shown in Table 6.4. Experiments were not carried out for these conditions. The case using adiabatic walls shows similar stability behavior than the reference (nonadiabatic) case for both combustor lengths, but with a higher value of the unstable eigenfrequency. The case with varied combustor confinement is unstable at both combustor lengths and with lower unstable eigenfrequencies than the reference case.

The amplitude and phase of the FTFs at the unstable eigenfrequencies for the

**Table 6.4:** Stability analysis using Network Model (NM) with identified FTFs

	$l_{comb}=300$ mm			$l_{comb}=700$ mm		
	NM	$f$ [Hz]	CI[-]	NM <sub>FTF</sub>	$f$ [Hz]	CI[-]
Adiabatic	Stable	128.9	-0.376	Unstable	138	0.302
Lower Confinement	Unstable	82.48	0.653	Unstable	87.61	1.125
Dif. Swirler Pos.	Stable	67.09	-0.255	Stable	69.69	-0.259
	Stable	-	-	Stable	120	-0.45

**Table 6.5:** Amplitude and phase at the unstable eigenfrequency with different conditions at 30 kW

	$f$ [Hz]	Amplitude [-]	Phase [°]
Reference (FTF <sub>Exp.</sub> )	110	1.714	151
Reference (FTF <sub>LES</sub> )	103	1.717	163
Adiabatic walls	138	1.863	151.2
Lower Confinement	87.61	1.831	164.7

different cases at 30 kW are shown in Table 6.5. The amplitudes are higher than 1 and close to the maximum value of the FTF's amplitude. The phases are very similar and around 160° in all cases. The instability behavior indicates that the Rayleigh criterion is fulfilled in this system for a flame with a phase of around 160° between velocity fluctuations at the reference point and the heat release fluctuation; and with amplitudes in the FTF higher than 1.

For the stability analysis using the FTF with a varied swirler position, the network model is modified and shown in Fig. 6.7. Two stable eigenfrequencies at 69.69 and 120 Hz are found with the network model. Looking at the identified FTF with the swirler at position 2, three frequencies have a phase of 160 deg: 68, 87 and 121 Hz, which are in good agreement with the ones found by the network model. Their respective amplitudes on the identified FTF are 0.946, 0.3 and 0.952. The amplitudes at those frequencies are much lower than the ones with the swirler at position 1 at the eigenfrequencies, indicating that less acoustic energy is provided to the system and showing stable conditions. An acoustic energy balance analysis was not carried out, but this stability analy-

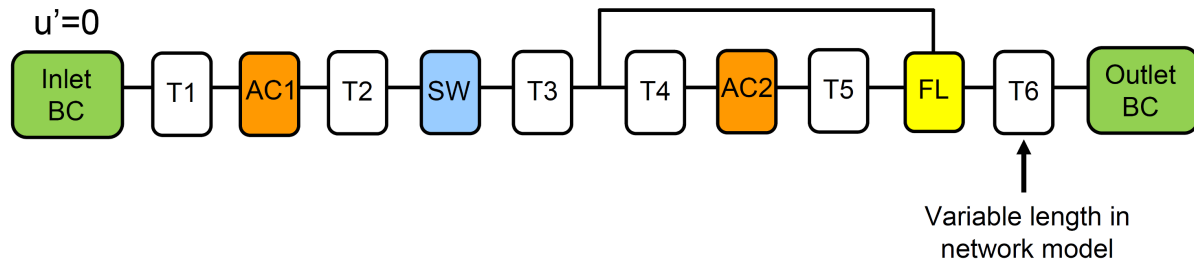


**Figure 6.7:** Low-order model of premix burner test rig with swirler at position 2.

sis indicates that in the design process, if an unstable eigenfrequency of the system is found and its phase is identified, the swirler position can be modified by looking for a flame response that exhibits a low amplitude in the FTF at this phase. The position of the swirler can be estimated using models like the one presented in section 3.4 based on the different time lags. Under such conditions, a stable behavior would be achieved. Nevertheless, there is also the potential that another unstable eigenfrequency would develop changing the position of the swirler, which is not the case in the present analysis.

Due to lack of experimental data, a 1:1 validation of these results is not possible, but the analysis confirms in a qualitative manner that combustor boundary conditions should have a significant impact on system stability.

## 7 Summary and Conclusions

The flame dynamics of a perfectly premixed axial swirl burner is investigated. The study is based on large eddy simulations of compressible reacting flow in combination with system identification based on correlation analysis. The unit impulse response and the transfer function of swirling turbulent flames at various operating conditions are determined. The advantage of using LES/SI methods in comparison with single frequency harmonic excitations (as in the determination of the experimental flame transfer function) is that it is possible to obtain the frequency flame response over a range of frequencies from a single LES simulation, reducing the computational effort.

The LES/SI approach is validated against experiments taking as reference case the swirl burner operating with 30 kW of power rating and with non-adiabatic combustor wall boundary conditions. Application of nonadiabatic boundary conditions are necessary to predict the correct flame structure and heat release distribution. The identified flame transfer function shows good agreement with experiments and with harmonic excitation carried out for a single frequency. A comparison of the flame transfer functions identified with LES/SI with varied reference positions for extracting the velocity fluctuations has shown small differences between them. Additional simulations with variation of power rating, thermal boundary conditions at the combustor walls, combustor confinement and swirler position are carried out to investigate their impact on flame dynamics.

The case with higher power rating (50 kW) exhibits a flame longer than the one with 30 kW due to the higher velocities. Comparing non-reacting and reacting simulations, strong differences on flow field and turbulence are observed. In the reacting flow simulations, a transversal eigenmode developed in the combustion chamber producing pressure oscillations in the combustor which grew in time. Two methodologies based on the combination of multiple time

series generated from several LES runs are derived to obtain a more robust identification. The FTF exhibits good qualitative agreement with the experiment and good scaling in Strouhal number with the 30 kW case.

Changing the combustor walls to adiabatic conditions, strong reaction in the outer shear layer is obtained, having the topology of a “M-flame”. Variations in the flow field, spatial and axial heat release distributions are observed between adiabatic and nonadiabatic conditions. The adiabatic flames has a shorter flame than the nonadiabatic cases due to the incorrect flame stabilization topology. The flame transfer function with adiabatic walls shows a broader frequency response (with amplitudes higher than one) and a less steeper phase (produced by the smaller time lag response to the perturbations) than the nonadiabatic case.

The work of Komarek and Polifke [103, 104] in the impact of swirler position on the FTF is extended to a LES context. Comparing the identified flame transfer functions at varied swirler positions, both show a very different flame response. The mechanism of the different propagation speeds and phase between perturbations, recognized in previous investigations [78, 103, 137] as the mechanism of the variations in the flame response, is also investigated by applying harmonic excitation only to the swirler at position 2 without the combustor. As the induced tangential velocity fluctuations created by the swirler have a strong impact on the flame dynamics, the swirler geometry must be taken into account in CFD simulations in order to capture the constructive/destructive interaction between axial and tangential velocity fluctuations.

The influence of combustor confinement on the flame transfer function is investigated numerically using two combustors with varied cross-section area. Previous experimental studies [11, 75] in other configurations have shown an impact on the FTF by the combustor confinement. Results from the carried out simulations show variations on the mean axial and tangential velocity, as well for the turbulent kinetic energy and jet angle. For the mean heat release, the flames in both combustors exhibit similar flame stabilization mainly in the inner shear layer, but with different axial and spatial heat release distributions, showing a broader spatial heat release distribution and a longer flame than the high-confinement case. This is in agreement with the observations found

---

in the experimental work of Hauser et al. [75]. For the identified flame transfer function with low-confinement, the amplitude shows similar behavior to the one with high-confinement, but with the maximum amplitude slightly higher and at a lower frequency. The time lag response is larger which is represented by the higher steepness in the phase.

The FTF model proposed by Komarek and Polifke [103] to describe the responses to perturbations of mass flow rate and swirl in the time domain by unit impulse responses is used to analyze the varied flame response for the various cases analyzed before. The analysis illustrates how differences in flow field and flame shape can influence time lags and thus the flame response in the time or frequency domain.

Using a network model, stability analysis is carried out for two different combustor lengths to assess the impact of the variations in the flame transfer functions on combustor stability limits. The stability analysis indicates that the variations in the predicted FTF may have a significant impact on stability prediction and cycle increments. Furthermore, it is shown that by changing the position of the swirler, stable conditions are predicted for the investigated combustor lengths.

The present work leads to the following conclusions and contributions to previous studies:

- The LES/SI approach for the identification of flame transfer functions is validated with a perfectly premixed axial swirl burner with good agreement with experiments.
- Heat loss effects on the boundary conditions and on the combustion model must be taken into account for the prediction of flame dynamics. Nonadiabaticity has a strong influence on flame shape and on the spatial distribution of heat release.
- The LES/SI approach is capable of detecting the impact of variations on thermal boundary conditions at the combustor wall, power rating, combustor confinement and swirler position on premixed flame transfer functions.

- The identified flame transfer functions confirm previous observations in other studies, showing that the flame transfer function does depend not only on the burner geometry, but also on the boundary conditions that the combustor provides to the flame (combustor wall temperature, confinement, etc.). Furthermore, the mean flow field just downstream of the burner outlet and the flame characteristics depend on the combustor confinement and boundary conditions.
- A model for the impact of the axial and swirl fluctuations on the flame transfer function shows the varied response and time lag distributions for the various cases considered.
- Variations in the flame transfer function produced by the different conditions have an impact on the stability behavior predicted with a thermoacoustic low-order network model.
- There is a strong influence of the swirler position on the flame response. The stability behavior of the engine can be modified by changing the position of the swirler without strong changes on the mean flow and flame.
- Results indicate that the flame transfer function obtained from single burner combustors - be it by experimental or numerical means - should only be used for stability analysis of multi-burner industrial gas turbines provided that operating and boundary conditions, as well as, combustor geometries are equivalent.

## 8 Outlook

The present study shows the potential of the LES/SI method to identify the flame response for fully premixed conditions. The following ideas are proposed as outlook to this work:

- In technical applications, as in operating gas turbines, the mixing between fuel and air is produced moments before reaction occurs. Thus, the flame reacts in most cases under the presence of mixture inhomogeneity. The impact of equivalence ratio fluctuations on the flame response was investigated previously by Huber and Polifke [85] in a RANS context as a MISO system. Application of the method on the LES context is planned in future investigations.
- Investigation of the impact of operating pressure and multi-burner configurations on the flame dynamics. These conditions are typical in industrial gas turbines, and not considered in this study.
- It is recommended to investigate the flame dynamics using the same burner with different combustion models and mesh resolution. Most industrial applications are usually simulated with a lower level of mesh resolution due the limited availability of computational resources. Investigations to quantify the impact on the flame response by the lower mesh resolution have not been carried out.
- The separation of the flame response to axial and swirl fluctuations. The system can be analyzed as a MISO system to identify the contributions in the flame response from mass flow and swirl fluctuations separately.
- For the prediction of limit cycle amplitudes from stability analysis, it is necessary to introduce the non-linear behavior of the flame with dependence of the perturbation amplitude by the flame describing func-

tion. The system identification method shown in this study to identify the flame dynamics is for linear time-invariant systems. The implementation of non-linear system identification for thermoacoustic system is still in its early stages, and should be further investigated.

- Finally, simulations should introduce damping effects on the wall boundary conditions. Real systems have a level of acoustic damping by vibration, which is not taken into account in CFD simulations. Furthermore, the development of 3D non-reflective boundary conditions to take into account transversal sources is also recommended.

# Bibliography

- [1] U.S. Energy Information Administration. Annual Energy Outlook 2011 with Projections to 2035. Technical Report DOE/EIA-0383, April 2011.
- [2] P.R. Alemela. *Measurement and Scaling of Acoustic Transfer Matrices of Premixed Swirl Flames*. PhD Thesis, Technische Universität München, 2009.
- [3] C. Angelberger, D. Veynante, and F. Egofopoulos. LES of Chemical and Acoustic Forcing of a Premixed Dump Combustor. *Flow, Turbulence and Combustion*, 65:205–222, 2000.
- [4] S.S. Archer. *Morphology of Unconfined and Confined Swirling Flows under Non-reacting and Combustion Conditions*. PhD Thesis, University of Mariland, College Park, 2005.
- [5] C.A. Armitage, R. Balachandran, E. Mastorakos, and R.S. Cant. Investigation of the nonlinear response of turbulent premixed flames to imposed inlet velocity oscillations. *Combust. Flame*, 146:419–436, 2006.
- [6] T. Ayinde. A Generalized Relationship for Swirl Decay in Laminar Pipe Flow. *Sadhana*, 35:129–137, 2010. 1.
- [7] B. O. Ayoola, R. Balachandran, J. H. Frank, E. Mastorakos, and C. F. Kaminski. Measurements of Local Heat Release Rates in a Turbulent Premixed Bluff Body Stabilised Flame with Acoustic Forcing. In *European Combustion Meeting*, 2005.

- [8] H. Büchner, C. Hirsch, and W. Leuckel. Experimental Investigation on the Dynamics of Pulsated Premixed Axial Jet Flames. *Combust. Sci. and Tech.*, 94:219–228, 1993.
- [9] B.D. Bellows, Y. Neumeier, and T. Lieuwen. Forced Response of a Swirling, Premixed Flame to Flow Disturbances. *Journal of Propulsion and Power*, 22(5):1075–1084, 2006.
- [10] S.A. Beltagui and N.R.L. Maccallum. Aerodynamics of Vane-swirled Flames in Furnaces. *Journal of the Institute of Fuel*, 49(401):183–193, 1976.
- [11] A. L. Birbaud, D. Durox, S. Ducruix, and S. Candel. Dynamics of Confined Premixed Flames Submitted to Upstream Acoustic Modulations. *Proc. Combust. Inst.*, 31(1):1257–1265, 2007.
- [12] M. Boger, D. Veynante, H. Boughanem, and A. Trouve. Direct Numerical Simulation Analysis of Flame Surface Density Concept for Large Eddy Simulation of Turbulent Premixed Combustion. *Symposium (International) on Combustion*, 27(1):917 – 925, 1998. Twenty-Seventh Symposium (International) on Combustion.
- [13] G. Borghesi, F. Biagioli, and B. Schuermans. Dynamic Response of Turbulent Swirling Flames to Acoustic Perturbations. *Combustion Theory and Modelling*, 13(3):487–512, 2009.
- [14] W. J. T. Bos, H. Touil, and J. P. Bertoglio. Reynolds Number Dependency of the Scalar Flux Spectrum in Isotropic Turbulence with a Uniform Scalar Gradient. *Physics of Fluids*, 17(12):125108, 2005.
- [15] L. Boyer and J. Quinard. On the Dynamics of Anchored Flames. *Combust. Flame*, 82:51–65, 1990.
- [16] P. Breeze. Efficiency versus Flexibility: Advances in Gas Turbine Technology. *Power Engineering International Magazine*, 19(3):30–34, 2011. <http://www.powerengineeringint.com/articles/print/volume-19/issue-3/gas-steam-turbine-directory/efficiency-versus-flexibility-advances-in-gas-turbine-technology.html>.

- [17] N. Bunce, J.G. Lee, B.D. Quay, and D.A. Santavicca. Mixture-forced Flame Transfer Function Measurements and Mechanisms in a Single-Nozzle Combustor at Elevated Pressure. Number GT2011-46744 in Proc. of ASME Turbo Expo 2011, page 10, Vancouver, Canada, June 6-10 2011. ASME.
- [18] H. Burchard and L. Umlauf. Turbulence in Natural Waters. Lecture Notes, October 2008. <http://www.io-warnemuende.de/burchard-teaching.html>.
- [19] S. Candel, D. Durox, S. Ducruix, A.L. Birbaud, N. Noiray, and T. Schuller. Flame Dynamics and Combustion Noise: Progress and Challenges. *International Journal of Aeroacoustics*, 8(1-2):1–56, 2009.
- [20] R.S. Cant and E. Mastorakos. *An Introduction to Turbulent Reacting Flows*. Imperial College Press, 2008.
- [21] CERFACS. <http://www.cerfacs.fr/4-26334-The-AVBP-code.php>.
- [22] CERFACS. *AVBP 6.0 Handbook*. 2008.
- [23] CERFACS. AVBP Help Manual, 2011.
- [24] J.H. Chen. Petascale Direct Numerical Simulation of Turbulent Combustion – Fundamental Insights towards Predictive Models. *Proc. Combust. Inst.*, 33(1):99–123, 2011.
- [25] B. T. Chu. On the Generation of Pressure Waves at a Plane Flame Front. *Fourth Symposium (International) on Combustion*, pages 603–612, 1953.
- [26] B.R. Clayton and Y.S.M. Morsi. Determination of Principal Characteristics of Turbulent Swirling Flow along Annuli: Part1: Measurement of Time Mean Parameters. *International Journal of Heat and Fluid Flow*, 5(4):195–203, 1984.
- [27] O. Colin, F. Ducros, D. Veynante, and T. Poinso. A Thickened Flame Model for Large Eddy Simulations of Turbulent Premixed Combustion. *Physics of Fluids*, 12(7):1843–1863, 2000.

- [28] P.J. Colucci, F.A. Jaber, P. Givi, and S.B. Pope. Filtered Density Function for Large Eddy Simulation of Turbulent Reacting Flows. *Physics of Fluids*, 10(2):499–515, 1998.
- [29] L. Crocco. Aspects of Combustion Stability in Liquid Propellant Rocket Motors Part1: Fundamentals. Low Frequency Instability with Monopropellants. *J. of American Rocket Society*, pages 163–178, 1951.
- [30] L Crocco and S.I. Cheng. *Theory of combustion instability in liquid propellant rocket motors*. Butterworths Science Publication, AGARDOGRAPH N 8, 1956.
- [31] B. Cuenot, Y. Sommerer, L.Y.M. Gicquel, and T. Poinot. LES of Reacting Flows. 3rd International workshop on Rocket Combustion Modeling, Paris, 2006.
- [32] A. Cuquel, D. Durox, and T. Schuller. Experimental Determination of Flame Transfer Function using Random Velocity Perturbations. Number GT2011-45881 in Proc. of ASME Turbo Expo 2011, Vancouver, Canada, page 10, Vancouver, Canada, June 6-10 2011. ASME.
- [33] Y. Danning, Y. Huang, and Y. Vigor. A Generalized Model of Acoustic Response of Turbulent Premixed Flame and its Application to Gas-Turbine Combustion Instability Analysis. *Combustion Science and Technology*, 177(5-6):1109–1150, 2005.
- [34] J. Daou and M. Matalon. Influence of Conductive Heat-losses on the Propagation of Premixed Flames in Channels. *Combust. Flame*, 128(4):321–339, 2002.
- [35] N. Darabiha, S.M. Candel, V. Giovangigli, and M.D. Smooke. Extinction of Strained Premixed Propane-Air Flames with Complex Chemistry. *Combust. Sci. Technol.*, 60:267–285, 1988.
- [36] S.R. de Parias Neto, P. Legentilhomme, and J. Legrand. Finite-element Simulation of Laminar Swirling Decaying Flow Induced by Means of a Tangential Inlet in an Annulus. *Computer Methods in Applied Mechanics and Engineering*, 165(1-4):189–213, 1998.

- [37] A.P. Dowling. The Challenges of Lean Premixed Combustion. Number IGTC2003Tokyo KS-5 in Proceedings of the International Gas Turbine Congress, Tokio, 2003.
- [38] A.P. Dowling and A.S. Morgans. Feedback Control of Combustion Oscillations. *Annu. Rev. Fluid Mech.*, 37::151–182, 2005.
- [39] A.P. Dowling and J.E.F. Williams. *Sound and Sources of Sound*. Ellis Horwood series in engineering science. E. Horwood, West Sussex, England, 1983.
- [40] F. Duchaine and T. Poinso. Sensitivity of Flame Transfer Functions of Laminar Flames. Proc. of the Summer Program CTR, Stanford, 2010.
- [41] S. Ducruix, D. Durox, and S. Candel. Theoretical and Experimental Determinations of the Flame Transfer Function of a Laminar Premixed Flame. *Proc. Combust. Inst.*, 28:765–773, 2000.
- [42] L. Durand. *Development, Implementation, and Validation of LES Models for Inhomogeneously Premixed Turbulent Combustion*. PhD thesis, Technische Universität München, 2007.
- [43] D. Durox, T. Schuller, and S. Candel. Combustion Dynamics of Inverted Conical Flames. *Proceedings of the Combustion Institute*, 30(2):1717–1724, 2005.
- [44] D. Durox, T. Schuller, N. Noiray, and S. Candel. Experimental Analysis of Nonlinear Flame Transfer Functions for Different Flame Geometries. *Proc. Combust. Inst.*, 32(1):1391–1398, 2009.
- [45] B. Efron and R. Tibshirani. *An Introduction to the Bootstrap*. Chapman & Hall, 1993.
- [46] F. El-Mahallawy and S. El-Din Habik. *Fundamentals and Technology of Combustion*. ELSEVIER, 2002.
- [47] D. Fanaca. (Private communication).

- [48] D. Fanaca. *Influence of Burner-Burner Interactions on the Flame Dynamics in an Annular Combustor*. PhD Thesis, Technische Universität München, 2010.
- [49] D. Fanaca, P.R. Alemela, C. Hirsch, T. Sattelmayer, and B. Schuermans. Comparison of the Flow Field of a Swirl Stabilized Premixed Burner in an Annular and a Single Burner Combustion Chamber. *J. Eng. Gas Turbines Power*, 132(6):071502, 2010.
- [50] A. Fischer. *Hybride, thermoakustische Charakterisierung von Drallbrennern*. PhD thesis, Technische Universität München, 2004.
- [51] A. Fleifil, A. M. Annaswamy, Z. A. Ghoneim, and A. F. Ghoniem. Response of a Laminar Premixed Flame to Flow Oscillations: A Kinematic Model and Thermoacoustic Instability Results. *Combust. Flame*, 106:487–510, 1996.
- [52] P. Flohr, C. O. Paschereit, and V. Bellucci. Steady CFD Analysis for Gas Turbine Burner Transfer Functions. Number AIAA 2003-1346 in 41st AIAA Aerospace Sciences Meeting and Exhibit, page 11, Reno, NV, Jan 6-9 2003. AIAA.
- [53] P. Flohr, C. O. Paschereit, B. van Roon, and B. Schuermans. Using CFD for Time-Delay Modeling of Premix Flames. Number 2001-GT-0376 in Proc. ASME Turbo Expo 2001, page 10, New Orleans, Louisiana, June 4-7 2001. ASME.
- [54] P. Flohr and H. Pitsch. A Turbulent Flame Speed Closure Model for LES of Industrial Burner Flows. *C. Turb. Research, Annual Research Briefs*, pages 169–179, 2000.
- [55] C.W. Foley, I. Chterevev, J. Seitzman, and T. Lieuwen. Flame Configurations in a Lean Premixed Dump Combustor with an Annular Swirling Flow. In *7th US National Combustion Meeting*, number 1D16, Atlanta, GA, March 2011. Eastern States Section of the Combustion Institute.
- [56] S. Föller, A. Gentemann, T. Komarek, and W. Polifke. Wiener-Hopf-Inverter (WHI) - A Correlation Based Signal Analysis Tool

- for Single-Input, Single-Output (SISO) and Multiple-Input, Multiple-Output (MIMO) Systems. Internal Report - Lehrstuhl für Thermodynamik - Technische Universität München, December 2009.
- [57] S. Föllner and W. Polifke. Determination of Acoustic Transfer Matrices via Large Eddy Simulation and System Identification. Number AIAA-2010-3998 in 16th AIAA/CEAS Aeroacoustics Conference, Stockholm, Sweden, June 7–9 2010. AIAA.
- [58] S. Föllner and W. Polifke. Advances in Identification Techniques for Aeroacoustic Scattering Coefficients from Large Eddy Simulation. 11th Int. Congress on Sound and Vibration, St. Petersburg, 2011.
- [59] E. Freitag. *On the Measurement and Modelling of Flame Transfer Functions at Elevated Pressure*. PhD Thesis, Technische Universität München, 2009.
- [60] E. Freitag, H. Konle, M. Lauer, C. Hirsch, and T. Sattelmayer. Pressure Influence on the Flame Transfer Function of a Premixed Swirling Flame. Number GT2006-90540 in Proc. of ASME Turbo Expo 2006, page 10, Barcelona, Spain, May 8-11 2006. ASME.
- [61] Y. Fu, J. Cai, Jeng S.M., and Mongia H. Confinement Effects on the Swirling Flow of a Counter-Rotating Swirl Cup. Number GT2005-68622 in Proc. of ASME Turbo Expo 2005, Reno. ASME, 2005.
- [62] C. Fureby and C. Löfström. Large-eddy Simulations of Bluff Body Stabilized Flames. *Symposium (International) on Combustion*, 25(1):1257 – 1264, 1994. Twenty-Fifth Symposium (International) on Combustion.
- [63] E. Garnier, N. Adams, and P. Sagaut. *Large Eddy Simulation for Compressible Flows*. Springer Science+Business Media, 2009.
- [64] A. Gentemann, C. Hirsch, K. Kunze, F. Kiesewetter, T. Sattelmayer, and W. Polifke. Validation of Flame Transfer Function Reconstruction for Perfectly Premixed Swirl Flames. Number GT2004-53776 in Proc. of ASME Turbo Expo 2004, Vienna. ASME, 2004.

- [65] M. Germano, U. Piomelli, P. Moin, and W. Carbot. A Dynamic Subgrid-scale Eddy Viscosity Model. *Phys. Fluids*, 7(A 3):1760 – 1765, July 1991.
- [66] A. Giauque. *Fonctions de Transfert de Flamme et Energies des Perturbations dans les Ecoulements Reactifs*. PhD Thesis, Institut National Polytechnique, Toulouse, 2007.
- [67] A. Giauque, T. Poinso, W. Polifke, and F. Nicoud. Validation of a Flame Transfer Function Reconstruction Method for Complex Turbulent Configurations. In *14th AIAA/CEAS Aeroacoustics Conference*, Vancouver, Canada, 2008.
- [68] A. Giauque, L. Selle, T. Poinso, H. Buechner, P. Kaufmann, and W. Krebs. System Identification of a Large-scale Swirled Partially Premixed Combustor using LES and Measurements. *Journal of Turbulence*, 6(21):1–20, 2005.
- [69] P. Givi. Filtered Density Function for Subgrid Scale Modeling of Turbulent Combustion. *AIAA Journal*, 44(1):16, 2006.
- [70] C.J. Goy, S.R. James, and S. Rea. *Monitoring of Combustion Instabilities: E.ON UK's Experience*, chapter 8, pages 163–175. *Combustion Instabilities in Gas Turbine Engines: Operational Experience, Fundamental Mechanisms and Modelling*. American Institute of Aeronautics and Astronautics, Reston, VA, 2005.
- [71] V. Granet, O. Vermorel, T. Léonard, L.Y.M. Gicquel, and T. Poinso. Comparison of Nonreflecting Outlet Boundary Conditions for Compressible Solvers on Unstructured Grids. *AIAA Journal*, 48(10):2348–2364, 2010.
- [72] A.K. Gupta, D.G. Lilley, and N. Syred. *Swirl Flows*. Energy and engineering science series. Abacus Press, 1984.
- [73] C.L. Hackert, J.L. Ellzey, and O.A. Ezekoye. Effects of Thermal Boundary Conditions on Flame Shape and Quenching in Ducts. *Combust. Flame*, 112(1-2):73–84, 1998.

- [74] W. L. H. Hallett and C.-Y. Ding. A Momentum Integral Model for Central Recirculation in Swirling Flow in a Sudden Expansion. *The Canadian Journal of Chemical Engineering*, 73(3):284–291, 1995.
- [75] M. Hauser, C. Hirsch, and T. Sattelmayer. Influence of the Confinement on the Flame Transfer Function. 18th International Congress on Sound and Vibration, Rio de Janeiro, Brazil, July 10–14 2011.
- [76] E. R. Hawkes and R. S. Cant. Implications of a Flame Surface Density Approach to Large Eddy Simulation of Premixed Turbulent Combustion. *Combust. Flame*, 126(3):1617 – 1629, 2001.
- [77] M. Hettel, P. Habisreuther, H. Büchner, H. Bockhorn, and N. Zarzalis. URANS-Modelling of Flame Transfer Functions of Turbulent Premixed Jet Flames. Number GT2004-53831 in Proc. of ASME Turbo Expo 2004, Vienna. ASME, 2004.
- [78] C. Hirsch, D. Fanaca, P. Reddy, W. Polifke, and T. Sattelmayer. Influence of the Swirler Design on the Flame Transfer Function of Premixed Flames. Number GT2005-68195 in Proc. of ASME Turbo Expo 2005, Reno. ASME, 2005.
- [79] C. Hirsch, J. Wäsle, A. Winkler, and T. Sattelmayer. A Spectral Model for the Sound Pressure from Turbulent Premixed Combustion. *Proceedings of the Combustion Institute*, 31(1):1435 – 1441, 2007.
- [80] Y. Huang, J. Benesty, and J. Chen. *Acoustic MIMO Signal Processing. Signals and Communication Technology*. Springer-Verlag Berlin Heidelberg, Germany, 2006.
- [81] Y. Huang and V. Yang. Bifurcation of Flame Structure in a Lean-premixed Swirl-stabilized Combustor: Transition from Stable to Unstable Flame. *Combust. Flame*, 136(3):383–389, 2004.
- [82] Y. Huang and V. Yang. Dynamics and Stability of Lean-premixed Swirl-stabilized Combustion. *Progress in Energy and Combustion Science*, 35:293–364, 2009.

- [83] A. Huber. *Impact of Fuel Supply Impedance and Fuel Staging on Gas Turbine Combustion Stability*. PhD Thesis, Technische Universität München, 2009.
- [84] A. Huber and W. Polifke. Dynamics of Practical Premixed Flames, Part I: Model Structure and Identification. *International Journal of Spray and Combustion Dynamics*, 1(2):199–228, 2009.
- [85] A. Huber and W. Polifke. Dynamics of Practical Premixed Flames, Part II: Identification and Interpretation of CFD Data. *International Journal of Spray and Combustion Dynamics*, 1(2):229–250, 2009.
- [86] A. Huber, P. Romann, and W. Polifke. Filter-based Time-Domain Impedance Boundary Conditions for CFD Applications. Number GT2008-51195 in Proceedings of ASME Turbo Expo, Berlin, Berlin, Germany, June 9-13 2008. ASME.
- [87] B. Jones, J.G. Lee, Quay B.D., and D.A. Santavicca. Flame Response Mechanisms Due to Velocity Perturbations in a Lean Premixed Gas Turbine Combustor. *Journal of Engineering for Gas Turbines and Power*, 133(2):021503, 2011.
- [88] W.P. Jones and B.E. Launder. The Prediction of Laminarization with a Two-Equation Model of Turbulence. *International Journal of Heat and Mass Transfer*, 15(2):301 – 314, 1972.
- [89] R. Kaess, A. Huber, and W. Polifke. Time-domain Impedance Boundary Condition for Compressible Turbulent Flows. Number AIAA 2008-2921 in 14th AIAA/CEAS Aeroacoustics Conference, Vancouver. AIAA, 2008.
- [90] R. Kaess, T. Poinso, and W. Polifke. Determination of the Stability Map of a Premix Burner based on Flame Transfer Functions computed with Transient CFD. Number 810304 in Proc. of European Combustion Meeting, Vienna. Combustion Institute, 2009.
- [91] R. Kaess, W. Polifke, T. Poinso, N. Noiray, D. Durox, T. Schuller, and S. Candel. CFD-based Mapping of the Thermo-acoustic Stability of a Laminar Premix Burner. Proc. of the Summer Program CTR, Stanford, 2008.

- [92] S. Kaplan. Power Plants: Characteristics and Costs. Technical Report Order Code RL34746, Congressional Research Service, USA, November 2008. <http://www.fas.org/sgp/crs/misc/RL34746.pdf>.
- [93] A. Kaufmann, F. Nicoud, and T. Poinsot. Flow Forcing Techniques for Numerical Simulation of Combustion Instabilities. *Combustion and Flame*, 131(4):371–385, 2002.
- [94] A. Kaw. *Introduction to Matrix Algebra*. Autarkaw, 1st edition, 2008.
- [95] J. Keller. Thermoacoustic Oscillations in Combustion Chambers of Gas Turbines. *AIAA Journal*, 33(12):2280–2287, 1995.
- [96] K.T. Kim, H.J. Lee, J.G. Lee, B.D. Quay, and D. Santavicca. Flame Transfer Function Measurement and Instability Frequency Prediction Using a Thermoacoustic Model. Number GT2009-60026 in Proc. of ASME Turbo Expo 2009, Orlando. ASME, 2009.
- [97] K.T. Kim, J.G. Lee, H.J. Lee, B.D. Quay, and D. Santavicca. Characterization of Forced Flame Response of Swirl-stabilized Turbulent Premixed Flames. Number GT2009-60031 in Proc. of ASME Turbo Expo 2009, Orlando. ASME, 2009.
- [98] K.T. Kim, J.G. Lee, B.D. Quay, and Santavicca D.A. Spatially Distributed Flame Transfer Functions for Predicting Combustion Dynamics in Lean Premixed Gas Turbine Combustors. *Combust. Flame*, 157(9):1718–1730, 2010.
- [99] W.W. Kim and S. Menon. Numerical Modeling of Turbulent Premixed Flames in the Thin-Reaction-Zones Regime. *Combustion Science and Technology*, 160(1):119–150, 2000.
- [100] O. Kitoh. Experimental Study of Turbulent Swirling Flow in a Straight Pipe. *Journal of Fluid Mechanics*, 225:445–479, 1991.
- [101] A.N. Kolgomorov. The Local Structure of Turbulence in Incompressible Viscous Fluid for Very Large Reynolds Numbers. *Dokl. Akad.Nauk SSSR*, 30:299–303, 1941.

- [102] T. Komarek. Private communication.
- [103] T. Komarek and W. Polifke. Impact of Swirl Fluctuations on the Flame Response of a Perfectly Premixed Swirl Burner. *J. Eng. Gas Turbines Power*, 132:061503, 2010.
- [104] T. Komarek, L. Tay Wo Chong, and W. Polifke. GV6: Dynamik von Vormischflammen. In *Abschlussbericht Forschungsinitiative*, pages 704–723. Kraftwerke des 21. Jahrhunderts (KW21), 2008.
- [105] J. Kopitz, E. Bröcker, and W. Polifke. Characteristics-based Filter for Identification of Planar Acoustic Waves in Numerical Simulation of Turbulent Compressible Flow. 12th Int. Congress on Sound and Vibration, Lisbon, 2005.
- [106] J. Kopitz and W. Polifke. CFD-based Application of the Nyquist Criterion to Thermo-acoustic Instabilities. *Journal of Computational Physics*, 227(14):6754–6778, 2008.
- [107] V.N. Kornilov, M. Manohar, and L.P.H. de Goey. Thermo-acoustic Behaviour of Multiple Flame Burner Decks: Transfer Function (de)composition. *Proceedings of the Combustion Institute*, 32(1):1383–1390, 2009.
- [108] V.N. Kornilov, K.R.A.M. Schreel, and L.P.H. de Goey. Experimental Assessment of the Acoustic Response of Laminar Premixed Bunsen Flames. *Proceedings of the Combustion Institute*, 31(1):1239–1246, 2007.
- [109] W. Krebs, S. Hoffmann, B. Prade, M. Lohrmann, and H. Büchner. Thermoacoustic Flame Response of Swirl Flames. Number GT-2002-30065 in Proc. ASME Turbo Expo 2002, page 12, Amsterdam, NL, June 3-6 2002. ASME.
- [110] W. Krebs, B. Prade, P. Flohr, and S. Hoffmann. Thermoacoustic Stability Chart for High-Intensity Gas Turbine Combustion Systems. *Combustion Science and Technology*, 174(7):99–128, 2002.
- [111] C. Külsheimer and H. Büchner. Combustion Dynamics of Turbulent Swirling Flames. *Combust. Flame*, 131:70–84, 2002.

## BIBLIOGRAPHY

---

- [112] L. Langston. The "Elephant in the Room: Gas Turbine Power". *Mechanical Engineering Magazine*, 132(12):57, December 2010. <http://files.asme.org/IGTI/News/27361.pdf>.
- [113] L. Langston. Powering Ahead. *Mechanical Engineering Magazine*, 133(5):31–33, May 2011. [http://memagazine.asme.org/Articles/2011/May/Powering\\_Ahead.cfm](http://memagazine.asme.org/Articles/2011/May/Powering_Ahead.cfm).
- [114] B. E. Launder, G. J. Reece, and W. Rodi. Progress in the Development of a Reynolds-stress Turbulence Closure. *Journal of Fluid Mechanics*, 68:537–566, 1975.
- [115] C. K. Law. *Combustion Physics*. Cambridge University Press, New York, 2006.
- [116] C. J. Lawn and W. Polifke. A Model for the Thermo-acoustic Response of a Premixed Swirl burner: Part II: The Flame Response. *Combust. Sci. Technol.*, 176(8):1359–1390, 2004.
- [117] R. Leandro, A. Huber, and W. Polifke. taX - a Low-Order Modeling Tool for Thermo- and Aero-Acoustic Instabilities. Technical report, TU München, 2010. [www.td.mw.tum.de/tum-td/en/forschung/infrastruktur/scientific\\_comp](http://www.td.mw.tum.de/tum-td/en/forschung/infrastruktur/scientific_comp).
- [118] A. Lefebvre. *Gas Turbine Combustion*. Taylor & Francis, 2nd edition, 1998.
- [119] J.P. Legier, T. Poinso, and D. Veynante. Large Eddy Simulation Model for Premixed and Non-premixed Turbulent Combustion. Proc. 2000 Summer Program, Center for Turbulence Research, Stanford, USA, pages 157–168, 2000.
- [120] T. Lieuwen and K. McManus. That Elusive Hum. *Mechanical Engineering Magazine*, 124(6):53–55, June 2002.
- [121] T. Lieuwen and B.T. Zinn. The Role of Equivalence Ratio Oscillations in Driving Combustion Instabilities in Low NO<sub>x</sub> Gas Turbines. *Proceedings of the 27th Symposium (International) on Combustion*, pages 1809–1816, 1998.

- [122] L. Ljung. *System Identification: Theory for the User*. Prentice Hall PTR, 2nd edition, 1999.
- [123] L. Ljung. Perspectives on System Identification. *Annual Reviews in Control*, 34(1):1–12, 2010.
- [124] M. Lohrmann and H. Büchner. Scaling of Stability Limits in Lean-Premixed Gas Turbine Combustors. Number GT2004-53710 in Proc. of ASME Turbo Expo 2004 Power for Land, Sea and Air, page 11, Vienna, Austria, June 14-17 2004. ASME.
- [125] O. Lucca-Negro and T. O’Doherty. Vortex Breakdown: A Review. *Progress in Energy and Combustion Science*, 27:431–481, 2001.
- [126] Ch. Martin, L. Benoit, Y. Sommerer, F. Nicoud, and T. Poinso. LES and Acoustic Analysis of Combustion Instability in a Staged Turbulent Swirled Combustor. *AIAA Journal*, 44(4):741–750, 2006.
- [127] E. Mastorakos, A.M.K.P. Taylor, and J.H. Whitelaw. Extinction of Turbulent Counterflow Flames with Reactants Diluted by Hot Products. *Combust. Flame*, 102:101–114, 1995.
- [128] E.R. Menter, M. Kuntz, and R. Langtry. Ten Years of Industrial Experience with the SST Turbulence Model. In K. Hanjalic, Y. Nagano, and M. Tummers, editors, *Turbulence, Heat and Mass Transfer 4*, pages 625–632. Begell House, Inc., 2003.
- [129] H.J. Merk. An Analysis of Unstable Combustion of Premixed Gases. *Symposium (International) on Combustion*, 6(1):500–512, 1957.
- [130] P. Moin and J. Kim. Tackling Turbulence with Supercomputers. *Scientific American*, 276(1):62–68, 1997.
- [131] Y. S. M. Morsi, P. G. Holland, and B. R. Clayton. Prediction of Turbulent Swirling Flows in Axisymmetric Annuli. *Applied Mathematical Modelling*, 19(10):613–620, 1995.

- [132] V. Moureau, G. Lartigue, Y. Sommerer, C. Angelberger, O. Colin, and Poinsot T. Numerical Methods for Unsteady Compressible Multi-component Reacting Flows on Fixed and Moving Grids. *J. Comput. Phys.*, 202:710–736, 2005.
- [133] F. Nicoud and F. Ducros. Subgrid-scale Stress Modeling Based on the Square of the Velocity Gradient Tensor. *Flow Turb. Combust.*, 62:183–200, 1999.
- [134] N. Noiray, D. Durox, T. Schuller, and S. Candel. A Unified Framework for Nonlinear Combustion Instability Analysis based on the Flame Describing Function. *Journal of Fluid Mechanics*, 615:139–167, 2008.
- [135] C. C. Paige and M. A. Saunders. LSQR: An Algorithm for Sparse Linear Equations and Sparse Least Squares. *ACM Trans. Math. Softw.*, 8(1):43–71, 1982.
- [136] P. Palies. *Dynamique et Instabilités de Combustion des Flamme Swirlées*. PhD thesis, Ecole Centrale Paris, 2010.
- [137] P. Palies, D. Durox, T. Schuller, and S. Candel. The Combined Dynamics of Swirler and Turbulent Premixed Swirling Flames. *Combust. Flame*, 157:1698–1717, 2010.
- [138] P. Palies, D. Durox, T. Schuller, and S. Candel. Swirling Flame Instability Analysis Based on the Flame Describing Function Methodology. Number GT2010-22294 in Proc. of ASME Turbo Expo 2010, Glasgow, UK, page 10, Glasgow, UK, June 14-18 2010. ASME.
- [139] P. Palies, D. Durox, T. Schuller, and S. Candel. Acoustic-convective Mode Conversion in an Aerofoil Cascade. *Journal of Fluid Mechanics*, 672:545–569, 2011.
- [140] P. Palies, D. Durox, T. Schuller, and S. Candel. Experimental Study on the Effect of Swirler Geometry and Swirl Number on Flame Describing Functions. *Combustion Science and Technology*, 183(7):704–717, 2011.

- [141] P. Palies, T. Schuller, D. Durox, L. Y. M. Gicquel, and S. Candel. Acoustically Perturbed Turbulent Premixed Swirling Flames. *Physics of Fluids*, 23(3):037101, 2011.
- [142] R. Palm, S. Grundmann, M. Weismüller, S. Saric, S. Jakirlic, and C. Tropea. Experimental Characterization and Modelling of Inflow Conditions for a Gas Turbine Swirl Combustor. *International Journal of Heat and Fluid Flow*, 27(5):924–936, 2006. Special issue of the 6th International Symposium on Engineering Turbulence Modelling and Measurements.
- [143] N. Peters. *Turbulent Combustion*. Cambridge University Press, 2000. ISBN 0-521-66082-3.
- [144] N. Peters. Multiscale Combustion and Turbulence. *Proc. Combust. Inst.*, 32(1):1–25, 2009.
- [145] U. Piomelli. Large Eddy Simulation: Achievements and Challenges. *Progress in Aerospace Science*, 35:335–362, 1999.
- [146] H. Pitsch. A G-equation Formulation for Large-Eddy Simulation of Premixed Turbulent Combustion. *Annual Research Briefs*, pages 3–14, 2002.
- [147] H. Pitsch. A Consistent Level Set Formulation for Large-Eddy Simulation of Premixed Turbulent Combustion. *Combust. Flame*, 143(4):587 – 598, 2005. Special Issue to Honor Professor Robert W. Bilger on the Occasion of His Seventieth Birthday.
- [148] H. Pitsch. Large-Eddy Simulation of Turbulent Combustion. *Annu. Rev. Fluid Mech.*, 38:453–482, 2006.
- [149] T. Poinso and SK.. Lele. Boundary Conditions for Direct Simulation of Compressible Viscous Flows. *J. Comput. Phys.*, 101:104–129, 1992.
- [150] T. Poinso, A. Trounev, D. Veynante, S. Candel, and E. Esposito. Vortex-driven acoustically coupled combustion instabilities. *Journal of Fluid Mechanics*, (vol. 177), 1987. vorhanden.
- [151] T. Poinso and D. Veynante. *Theoretical and Numerical Combustion*. R T Edwards, Philadelphia, 1st edition, 2001.

- [152] T. Poinso and D. Veynante. *Theoretical and Numerical Combustion*. R T Edwards, Philadelphia, 2nd edition, 2005.
- [153] W. Polifke. Combustion Instabilities. In *Advances in Aeroacoustics and applications, VKI lecture series, Brussels*, 2004.
- [154] W. Polifke. Divide et Impera - Combining CFD, System Sdentification and System Modelling to Analyse Combustion Instabilities. *NAFEMS Seminar*, May 2006.
- [155] W. Polifke. System Modelling and Stability Analysis. In Von Karman Institute, editor, *Basics of Aero-acoustics and Thermo-acoustics, VKI lecture series, Brussels*, 2007.
- [156] W. Polifke. Low-order Analysis Tools for Aero- and Thermo-Acoustic Instabilities. In C. Schram, editor, *Advances in Aero-Acoustics and Thermo-Acoustics*. Van Karman Inst for Fluid Dynamics., Brussels, 2010.
- [157] W. Polifke. Non-normality and Non-linearity in Aero- and Thermo-acoustic Systems. In C. Schram, editor, *Advances in Aero-Acoustics and Thermo-Acoustics*. Van Karman Inst for Fluid Dynamics., Brussels, 2010.
- [158] W. Polifke. System Identification for Aero- and Thermo-Acoustic Applications. In C. Schram, editor, *Advances in Aero-Acoustics and Thermo-Acoustics*. Van Karman Inst for Fluid Dynamics., Brussels, 2010.
- [159] W. Polifke and C. Lawn. On the Low-frequency Limit of Flame Transfer Functions. *Combust. Flame*, 151(3):437–451, 2007.
- [160] W. Polifke, A. Poncet, C. O. Paschereit, and K. Döbbeling. Reconstruction of Acoustic Transfer Matrices by Instationary Computational Fluid Dynamics. *J. of Sound and Vibration*, 245(3):483–510, 2001.
- [161] W. Polifke, J. van der Hoek, and B. Verhaar. Everything You Always Wanted to Know about f and g. Technical report, ABB Corporate Research, Baden, Switzerland, 1997.
- [162] W. Polifke, C. Wall, and P. Moin. Partially Reflecting and Non-reflecting Boundary Conditions for Simulation of Compressible Viscous Flow. *J. Comput. Phys.*, 213:437–449, 2006.

- [163] S.B. Pope. Computations of Turbulent Combustion: Progress and Challenges. *Symposium (International) on Combustion*, 23(1):591 – 612, 1991. Twenty-Third Symposium (International) on Combustion.
- [164] S.B. Pope. *Turbulent Flows*. Cambridge University Press, 2000.
- [165] Preetham, H. Santosh, and T. Lieuwen. Dynamics of Laminar Premixed Flames Forced by Harmonic Velocity Disturbances. *Journal of Propulsion and Power*, 24(6):1390–1402, 2008.
- [166] J.G. Proakis and D.G. Manolakis. *Digital Signal Processing*. Pearson Prentice Hall, 3rd edition, 2007.
- [167] A. N. Rao, V. Ganesan, K. V. Gopalakrishnan, and R. Natarajan. Experimental and Theoretical Investigations of Vane Generated Swirling Flows in a Circular Chamber. *J. Inst. Energy*, 56:137–144, 1983.
- [168] L. Rayleigh. The Explanation of Certain Acoustical Phenomena. *Nature*, 18:319–321, 1878.
- [169] O. Reynolds. An Experimental Investigation of the Circumstances Which Determine Whether the Motion of Water Shall Be Direct or Sinuous, and of the Law of Resistance in Parallel Channels. *Phil. Trans. R. Soc. Lond.*, 174:935–982, January 1883.
- [170] L. F. Richardson. *Weather Prediction by Numerical Process*. Cambridge University Press, 1922.
- [171] S. Roux, G. Lartigue, T. Poinsot, U. Meier, and C. Berat. Studies of Mean and Unsteady Flow in a Swirled Combustor Using Experiments, Acoustic Analysis, and Large Eddy Simulations. *Combust. Flame*, 141:40–54, 2005.
- [172] P. Sagaut, D. Deck, and M. Terracol. *Multiscale and Multiresolution Approaches in Turbulence*. Imperial College Press, 2006.
- [173] T. Sattelmayer. Influence of the Combustor Aerodynamics on Combustion Instabilities from Equivalence Ratio Fluctuations. Number 2000-GT-0082 in Proc. ASME Turbo Expo 2000, Munich, Germany, May 8-11 2000. ASME.

- [174] P. Schmitt. *Simulation aux grandes échelles de la combustion étagée dans les turbines à gaz et son interaction stabilité - polluants-thermique*. PhD thesis, Institut National Polytechnique de Toulouse, France, 2005.
- [175] P. Schmitt, T. Poinso, B. Schuermans, and K. P. Geigle. Large-eddy Simulation and Experimental Study of Heat Transfer, Nitric Oxide Emissions and Combustion Instability in a Swirled Turbulent High-pressure Burner. *J. Fluid Mech.*, 570:17–46, 2007.
- [176] P. Schmitt, B. Schuermans, K. Geigle, and T. Poinso. Effects of Radiation, Wall Heat Loss and Effusion Cooling on Flame Stabilisation and Pollutant Prediction in LES of Gas Turbine Combustion. ECCOMAS Thematic Conference on Computational Combustion, Lisbon, 2005.
- [177] B. Schuermans. *Modeling and Control of Thermoacoustic Instabilities*. PhD Thesis, Ecole Polytechnique Federale de Lausanne, 2003.
- [178] B. Schuermans, V. Bellucci, F. Guethe, F. Meili, P. Flohr, and O. Paschereit. A Detailed Analysis of Thermoacoustic Interaction Mechanisms in a Turbulent Premixed Flame. Number GT2004-53831 in Proc. of ASME Turbo Expo 2004, Vienna. ASME, 2004.
- [179] B. Schuermans, H. Luebcke, D. Bajusz, and P. Flohr. Thermoacoustic Analysis of Gas Turbine Combustion Systems Using Unsteady CFD. volume 2005 of *Proc. of ASME Turbo Expo 2005, USA*. ASME, June 6-9 2005.
- [180] T. Schuller, D. Durox, and S. Candel. Self-Induced Combustion Oscillations of Laminar Premixed Flames Stabilized on Annular Burners. *Combust. Flame*, 135:525–537, 2003.
- [181] T. Schuller, D. Durox, and S. Candel. A Unified Model for the Prediction of Laminar Flame Transfer Functions: Comparisons between Conical and V-Flame Dynamics. *Combust. Flame*, 134:21–34, 2003.
- [182] F. Selimefendigil, R.I. Sujith, and W. Polifke. A Frequency Domain System Model with Coupled Modes for Limit Cycle Prediction of Thermoacoustic Systems. *Int. J. Spray Comb. Dynamics*, 3(4):303–330, 2011.

- [183] F. Selimefendigil, R.I. Sujith, and W. Polifke. Identification of Heat Transfer Dynamics for Non-modal Analysis of Thermoacoustic Stability. *Applied Mathematics and Computation*, 217(11):5134–5150, 2011. Special issue on Fluid Flow and Heat Transfer.
- [184] L. Selle, G. Lartigue, T. Poinso, R. Koch, K.U. Schilmacher, W. Krebs, B. Prade, P. Kaufmann, and D. Veynante. Compressible Large Eddy Simulation of Turbulent Combustion in Complex Geometry on Unstructured Meshes. *Combust. Flame*, 137:489–505, 2004.
- [185] J.B. Sewell and P.A. Sobieski. *Monitoring of Combustion Instabilities: Calpine's Experience*, chapter 7, pages 147–162. Combustion Instabilities in Gas Turbine Engines: Operational Experience, Fundamental Mechanisms and Modelling. American Institute of Aeronautics and Astronautics, Reston, VA, 2005.
- [186] J. Smagorinsky. General Circulation Experiments with the Primitive Equations, I. The Basic Experiment. *Monthly Weather Review*, 91(3), March 1963.
- [187] M.D. Smooke, J. Crump, K. Seshadri, and V. Giovangigli. Comparison between Experimental Measurements and Numerical Calculations of the Structure of Counterflow, Diluted, Methane-air, Premixed Flames. *Symposium (International) on Combustion*, 23:463–470, 1991.
- [188] Y. Sommerer, D. Galley, T. Poinso, S. Ducruix, F. Lacas, and D. Veynante. Large Eddy Simulation and Experimental Study of Flashback and Blow-off in a Lean Partially Premixed Swirled Burner. *Journal of Turbulence*, 5:037, 2004.
- [189] Z. B. Song, L. J. Wei, and Z. Z. Wu. Effects of Heat Losses on Flame Shape and Quenching of Premixed Flames in Narrow Channels. *Combustion Science and Technology*, 180(2):264–278, 2008.
- [190] C. G. Speziale, S. Sarkar, and T. B. Gatski. Modelling the Pressure-Strain Correlation of Turbulence: An Invariant Dynamical System Approach. *Journal of Fluid Mechanics*, pages 245–272, 1991.

- [191] G. Staffelbach, L. Y. M. Gicquel, and T. Poinso. Highly Parallel Large Eddy Simulations of Multiburner Configurations in Industrial Gas Turbines. In S. C. Kassinos, C. A. Langer, G. Laccarino, and P. Moin, editors, *Complex Effects in Large Eddy Simulations*, volume 56 of *Lecture Notes in Computational Science and Engineering*, pages 325–336. Springer Berlin Heidelberg, 2007.
- [192] W. Steenbergen and J. Voskamp. The Rate of Decay of Swirl in Turbulent Pipe Flow. *Flow Measurement and Instrumentation*, 9(2):67–78, 1998.
- [193] J. Stein. *Digital Signal Processing - A Computer Science Perspective*. John Wiley & Sons, Inc., New York, USA, 2000.
- [194] D. L. Straub and G. A. Richards. Effect of Axial Swirl Vane Location on Combustion Dynamics. Number 99-GT-109 in Int. Gas Turbine & Aero-engine Congress & Exhibition, Indianapolis, Indiana, 1999. ASME.
- [195] N. Syred. A Review of Oscillation Mechanisms and the Role of the Precessing Vortex Core (PVC) in Swirl Combustion Systems. *Progress in Energy and Combustion Science*, 32(2):93–161, 2006.
- [196] G. Tabor and H.G. Weller. Large Eddy Simulation of Premixed Turbulent Combustion Using  $\Xi$  Flame Surface Wrinkling Model. *Flow, Turbulence and Combustion*, 72:1–27, 2004.
- [197] E. Tangermann, R. Keppeler, and M. Pfitzner. Premixed Turbulent Combustion Models for Large Eddy and RANS Simulations. Number GT2010-22298 in Proc. of ASME Turbo Expo 2010, Glasgow, UK, Glasgow, UK, June 14-18 2010. ASME.
- [198] L. Tay-Wo-Chong, S. Bomberg, A. Ulhaq, T. Komarek, and W. Polifke. Comparative Validation Study on Identification of Premixed Flame Transfer Function. *Journal of Engineering for Gas Turbines and Power*, 134(2):021502, 2012.
- [199] L. Tay Wo Chong, T. Komarek, R. Kaess, S. Föllner, and W. Polifke. Identification of Flame Transfer Functions from LES of a Premixed Swirl Burner. Number GT2010-22769 in Proc. of ASME Turbo Expo 2010, Glasgow, UK, page 13, Glasgow, UK, June 14-18 2010. ASME.

- [200] L. Tay Wo Chong, T. Komarek, M. Zellhuber, J. Lenz, C. Hirsch, and W. Polifke. Influence of Strain and Heat Loss on Flame Stabilization in a Non-adiabatic Combustor. Number 810366 in Proceedings of European Combustion Meeting, Vienna. Combustion Institute, 2009.
- [201] H. Tennekes and J. L. Lumley. *A First Course in Turbulence*. The MIT Press, 11th printing edition, 1972. ISBN 0-262-200198.
- [202] S. A. Thorpe. *An Introduction to Ocean Turbulence*. Cambridge University Press, 2007.
- [203] C. Tong and Z. Warhaft. Passive Scalar Dispersion and Mixing in a Turbulent Jet. *J. Fluid Mech.*, 292:1–38, 1995.
- [204] S. R. Turns. *An Introduction to Combustion*. McGraw-Hill, Boston, 2000.
- [205] E. R. Van Driest. On Turbulent Flow near a Wall. *J. Aerospace Sci.*, 23:1007–1011, 1956.
- [206] J. van Kampen. *Acoustic Pressure Oscillations Induced by Confined Turbulent Premixed Natural Gas Flames*. PhD Thesis, University of Twente, Enschede, The Netherlands, 2006.
- [207] S.V. Vaseghi. *Advanced Digital Signal Processing and Noise Reduction*. John Wiley & Sons, Ltd., 3rd edition, 2006.
- [208] H. K. Versteeg and W. Malalasekera. *Introduction to Computational Fluid Dynamics : The Finite Volume Method* . Longman Scientific & Technical, 1995.
- [209] D. Veynante and T. Poinso. Large Eddy Simulation of Combustion Instabilities in Turbulent Combustion. Annual Reserach Briefs, pages 253–274, CTR Stanford, USA, 1997.
- [210] D. Veynante and L. Vervisch. Turbulent Combustion Modeling. *Progress in Energy and Combustion Science*, 28(3):193 – 266, 2002.
- [211] C. Wagner, T. Huettl, and P. Sagaut. *Large-Eddy Simulation for Acoustics*. Cambridge University Press, 2007.

- [212] S. Wang and V. Yang. Unsteady Flow Evolution in Swirl Injectors with Radial Entry. II. External Excitations. *Physics of Fluids*, 17(4):045107, 2005.
- [213] E. Wanke. *FE-Verfahren zur Analyse der Thermoakustischen Stabilität nichtisentropischer Strömungen*. PhD Thesis, Technische Universität München, 2010.
- [214] J. Warnatz, U. Maas, and R.W. Dibble. *Combustion: Physical and Chemical Fundamentals, Modeling and Simulation, Experiments, Pollutant Formation*. Springer-Verlag, Berlin/Heidelberg, 4th edition, 2006.
- [215] J. Wäsle, A. Winkler, E. Rössle, and T. Sattelmayer. Development of an Annular Porous Burner for the Investigation of Adiabatic Unconfined Flames. 13th Int Symp on Applications of Laser Techniques to Fluid Mechanics, Lisbon, Portugal, June 26-29 2006.
- [216] K. Wieczorek and F. Nicoud. Prediction of Thermoacoustic Instabilities: Numerical Study of Mach Number Effects. In *16th AIAA/CEAS Aeroacoustics Conference*, Stockholm, Sweden, 2010.
- [217] N. Wiener. *Extrapolation, Interpolation, and Smoothing of Stationary Time Series*. The MIT Press, 1964.
- [218] D.C. Wilcox. *Turbulence Modelling for CFD*. DCW Industries, 1993.
- [219] F. A. Williams. *Combustion Theory*. Benjamin/Cummings, Menlo Park, CA, 1985.
- [220] S. Xiao and V. Martling. Reducing Gas Turbine NO<sub>x</sub> and CO Emissions Through Improved Combustor Design. Technical report, Power Systems Manufacturing, Florida, USA, 2003. <http://www.psm.com/PDF/Combustor.pdf>.
- [221] S. W. Yuen, A. Gentemann, and W. Polifke. Influence of Boundary Reflection Coefficient on the System Identifiability of Acoustic Two-Ports. 11th Int. Congress on Sound and Vibration, St. Petersburg, 2004.
- [222] V. Zimont and V. Battaglia. Joint RANS/LES Approach to Premixed Flame Modelling in the Context of the TFC Combustion Model. *Flow, Turbulence and Combustion*, 77:305–331, 2006.

- [223] B.T. Zinn and T. Lieuwen. *Combustion Instabilities: Basic Concepts*, chapter 1, pages 3–26. *Combustion Instabilities in Gas Turbine Engines: Operational Experience, Fundamental Mechanisms and Modelling*. American Institute of Aeronautics and Astronautics, Reston, VA, 2005.

# A Appendices

## A.1 The Rayleigh Criterion

Lord Rayleigh [168] proposed a criterion, the so-called Rayleigh criterion, to describe the mechanism that a periodic heat-addition process adds energy to acoustic oscillations [223]. In his words [168]:

*“If heat be periodically communicated to, and abstracted from, a mass of air vibrating (for example) in a cylinder bounded by a piston, the effect produced will depend upon the phase of the vibration at which the transfer of heat takes place. If the heat is given to the air at the moment of greatest condensation, or be taken from it at the moment of greatest rarefaction, the vibration is encouraged. On the other hand, if heat be given at the moment of greatest rarefaction, or abstracted at the moment of greatest condensation, the vibration is discouraged.”*

This indicates that an oscillation can be enhanced or damped depending of the phase between pressure ( $p'$ ) and heat (release) ( $\dot{Q}'$ ) oscillations, and prone to instability if heat is added at moment of maximum pressure. The Rayleigh criterion is formulated mathematically by [83, 156]:

$$R = \oint_T \int_V p' \dot{Q}' dV dt, \quad (\text{A.1})$$

where  $T$  is the period of the oscillation and  $V$  is the volume of the domain.  $R$  is known as the Rayleigh Index. Then, if the absolute phase between the pressure and heat (release) oscillations is lower/higher than 90 degrees, the Rayleigh Index is positive/negative and the heat-addition process adds/damps energy to/from the acoustic field [223]. This is shown graphically in Fig. A.1.

Having a positive Rayleigh Index is not the only condition for an instability to develop. The other condition is that the energy added by the flame is higher

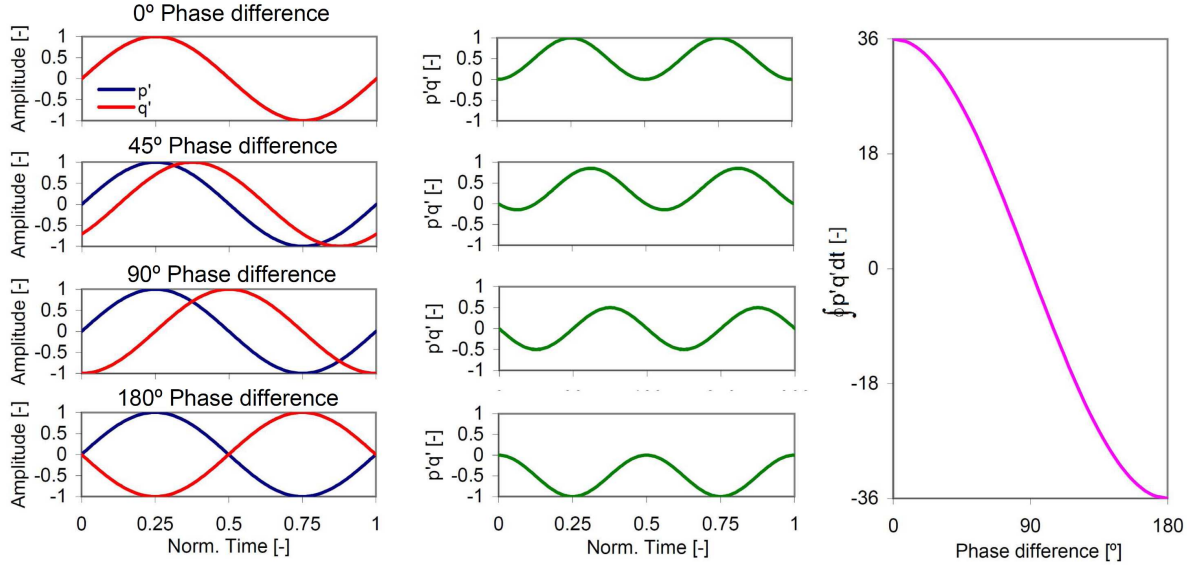


**Figure A.1:** Evaluation of Rayleigh Criterion with different absolute phase between pressure and heat fluctuations.

than the energy losses by the damping mechanisms. Further details about the Rayleigh Criterion and energy balances can be found in [38, 156, 223].

## A.2 Laminar Flame Reaction Kinetics

For laminar flames, the transport equations for conservation of species and energy are defined by:

- Species mass fraction

$$\frac{\partial \rho Y_k}{\partial t} + \frac{\partial \rho u_j Y_k}{\partial x_j} = \frac{\partial J_{j,k}}{\partial x_j} + \dot{\omega}_k, \quad (\text{A.2})$$

- Conservation of energy

$$\frac{\partial \rho E}{\partial t} + \frac{\partial \rho u_j E}{\partial x_j} = - \frac{\partial [u_i (p \delta_{ij} - \tau_{ij}) + q_j]}{\partial x_j} + \dot{\omega}_T. \quad (\text{A.3})$$

where  $\dot{\omega}_T$  and  $\dot{\omega}_k$  are the heat release and the reaction rate of the  $k^{th}$  species, respectively. These source terms are closed using the Arrhenius law. For a system with  $N$  number of species  $\mathcal{Y}_k$  and  $M$  reactions [22, 152]:

$$\sum_{k=1}^N v'_{kj} \mathcal{Y}_k \rightleftharpoons \sum_{k=1}^N v''_{kj} \mathcal{Y}_k \text{ for } j = 1, \dots, M. \quad (\text{A.4})$$

where  $\mathcal{Y}_k$  represents the different species  $k$  on the reaction,  $v'_{kj}$  and  $v''_{kj}$  are the molar stoichiometric coefficients of species  $k$  in reaction  $j$  [152].

The reaction rate  $\dot{\omega}_k$  is defined by the sum of the rates from all reactions:

$$\dot{\omega}_k = \sum_{j=1}^M \dot{\omega}_{kj} = W_k \sum_{j=1}^M v_{kj} \mathcal{R}_j, \quad (\text{A.5})$$

where  $W_k$  is the molecular weight of species  $k$ ,  $v_{kj}$  is defined by [152]:

$$v_{kj} = v''_{kj} - v'_{kj}, \quad (\text{A.6})$$

and  $\mathcal{R}_j$  is the rate of progress of reaction  $j$ . Considering a only forward reactions,  $\mathcal{R}_j$  is defined by:

$$\mathcal{R}_j = K_{fj} \prod_{k=1}^N \left( \frac{\rho Y_k}{W_k} \right)^{v'_{kj}}, \quad (\text{A.7})$$

where  $K_{fj}$  is the forward rate of reaction  $j$ .  $K_{fj}$  is modeled using Arrhenius law by:

$$K_{fj} = A_{fj} T^{\beta_j} \exp\left(-\frac{E_{a,j}}{RT}\right), \quad (\text{A.8})$$

where  $A_{fj}$  is the pre-exponential factor of the reaction,  $\beta_j$  is the temperature exponent and  $E_{a,j}$  is the activation energy of reaction  $j$ .

Due to the high number of reactions and species involved in the reacting process, reduced chemical mechanisms with smaller number of species and reactions are usually used. The idea is to represent the detailed reaction mechanism by a few reaction steps including some important species and with the chemical kinetic constants empirically determined [115]. Thus, Eq. (A.7) is modified by:

$$\mathcal{R}_j = K_{fj} \prod_{k=1}^N \left( \frac{\rho Y_k}{W_k} \right)^{n_k}, \quad (\text{A.9})$$

**Table A.1: One Step Reaction Mechanism**

Description	Value
$E_a$ [cal/mol]	20000
A [cgs]	$1.1 \times 10^{10}$
$\beta$	0
$n_{CH_4}$	1
$n_{O_2}$	0.5

where  $n_k$  is the reaction order with respect to the  $k_{th}$  species, which can be different to  $\nu'_{kj}$ . The reaction mechanism provides information of the pre-exponential factor, the temperature exponent, the activation energy and the reaction order for each involved reaction.

The heat release  $\dot{\omega}_T$  is obtained by:

$$\dot{\omega}_T = - \sum_{k=1}^N \dot{\omega}_k \Delta h_{f,k}^0, \quad (\text{A.10})$$

where  $\Delta h_{f,k}^0$  is the enthalpy of formation of species k at temperature  $T_0 = 0$  K, which is provided in AVBP from a database.

### A.3 One Step Reaction Mechanism for Methane-air Mixtures

A one step global reaction mechanism was provided by CERFACS for methane-air mixtures. The global reaction is defined by:



The coefficients of the mechanism and the Schmid number of the different species are indicated in Table A.1 and Table A.2, respectively.

**Table A.2: Schmid Number**

Species	Value
$CH_4$	0.677
$O_2$	0.739
$CO_2$	0.945
$H_2O$	0.544
$N_2$	0.726

## A.4 Derivation of the Turbulent Kinetic Energy Spectrum

The turbulent kinetic energy can be defined by its spectrum in wave number space  $E(\kappa)$ . To illustrate the definition of wave number, let's consider a fixed measuring point through which the different eddies are transported at a mean velocity  $\bar{u}$ , and that the time taken for an eddy of size  $l_{eddie}$  to pass this point is  $T=l_{eddie}/\bar{u}$ . Then the small eddies will create fluctuations in the flow with higher frequency than the ones created by the large eddies [202]. The corresponding angular frequency of this process can be defined as  $\omega_{eddie}=2\pi/T$ , and is related to an eddy wave number ( $\kappa$ ) by:

$$\kappa = \frac{\omega_{eddie}}{\bar{u}} = \frac{2\pi}{l_{eddie}}. \quad (A.12)$$

The turbulent kinetic energy spectrum represents the density of kinetic energy per unit wave number. It can be obtained (considering that the flow is spatially homogeneous) by the Fourier transform of the two-point correlation function of the velocity fluctuations ( $R_{ii}$ ) [18, 164]:

$$R_{ii}(\mathbf{x}, t) = \langle u'_i(\mathbf{x}_0, t) u'_i(\mathbf{x}_0 + \mathbf{x}, t) \rangle. \quad (A.13)$$

$$S_{ii}(\boldsymbol{\kappa}) = \frac{1}{(2\pi)^3} \iiint_{-\infty}^{\infty} e^{i\boldsymbol{\kappa}\cdot\mathbf{x}} R_{ii}(\mathbf{x}, t) d\mathbf{x}, \quad (A.14)$$

$$\langle k \rangle = \frac{1}{2} \overline{u'^2} = \frac{1}{2} R_{ii}(0) = \iiint_{-\infty}^{\infty} \frac{1}{2} S_{ii}(\boldsymbol{\kappa}) d\boldsymbol{\kappa}. \quad (A.15)$$

where  $\mathbf{x}_0$ ,  $\mathbf{x}$ ,  $\boldsymbol{\kappa}$ ,  $S_{ii}(\boldsymbol{\kappa})$  is the reference position (x,y,z), the vector between the two points, the wave number vector ( $\kappa_x$ ,  $\kappa_y$ ,  $\kappa_z$ ) and the velocity-spectrum tensor, respectively. Considering the turbulence as homogeneous

and isotropic, the energy spectrum  $E(\kappa)$ , is obtained from  $S_{ii}(\boldsymbol{\kappa})$  by removing all directional information considering the length of the wave number vector as  $|\boldsymbol{\kappa}|=\kappa$  instead of the vector itself [18, 164]. Considering a sphere in wave number space with radius  $\kappa$ , and integrating over the surfaces of the sphere ( $A(\kappa)$ ), the energy spectrum and the turbulent kinetic energy are obtained by:

$$\langle k \rangle = \frac{1}{2} \langle u' \rangle^2 = \int_0^\infty \oint \frac{1}{2} [S_{ii}(\boldsymbol{\kappa}) dA(\kappa)] d\kappa, \quad (\text{A.16})$$

$$E(\kappa) = \oint \frac{1}{2} S_{ii}(\boldsymbol{\kappa}) dA(\kappa), \quad (\text{A.17})$$

$$\langle k \rangle = \frac{1}{2} \langle u' \rangle^2 = \int_0^\infty E(\kappa) d\kappa. \quad (\text{A.18})$$

## A.5 Generation of Signals for LES/SI

To perform the excitation, broadband perturbations are introduced in the boundary condition. The signal used in this study is a Discrete Random Binary Signal. To create this kind of signal, a routine is available in the WHI code. The discrete random binary signal is defined by:

$$u_{\text{fluc},n}^o = u_{\text{amp}} \{ \text{sign} [(\text{rand}(n) - 0.5)] \}, \text{ if } n = 1, 2, \dots, N. \quad (\text{A.19})$$

where  $N$  is the number of elements of the signal,  $\text{rand}()$  is a random generator of numbers between 0 and 1, and  $\text{sign}$  is the sign function.

The signal defined in Eq. (A.19) has a frequency content until the Nyquist frequency ( $f_{\text{nyq}}=1/(2\Delta t)$ , where  $\Delta t$  is the time step). Considering the time steps mentioned before for LES, the Nyquist frequency is around 1 MHz. As mentioned before, it is desirable to maximize the low-frequency content of the signal (in this case, lower than 1000 Hz), but keeping the characteristic of the DRBS. A “filtered” discrete random binary signal can be created using a *clocking period* [122]. The idea is to create a new signal based on an original signal obtained using  $u_{\text{fluc},n}^o$  from Eq. (A.19). This is done by selecting a sample of the original random signal and keeping it constant over a number of samples (*clocking period*), then selecting the next sample of the original random signal

and repeating the procedure. The clocking period is defined by:

$$P_{\text{clock}} = \text{floor}\left(\frac{f_{\text{nyq}}}{f_c}\right), \quad (\text{A.20})$$

where  $f_c$  is the desired maximum frequency of the signal and  $\text{floor}(x)$  is a function that rounds the content inside the parentheses to the largest integer not greater than  $x$ . The “filtered” discrete random binary signal is defined by:

$$u_{\text{fluc},n}^{\text{flt}} = \begin{cases} u_{\text{fluc},1}^o, & \text{if } n = 1 \\ u_{\text{fluc},m}^o, & \text{if } n = mP_{\text{clock}} \\ u_{\text{fluc},(n-1)}, & \text{if } n \neq mP_{\text{clock}}, \end{cases} \quad (\text{A.21})$$

for  $m=1,2,3,\dots,\text{floor}(N/P_{\text{clock}})$ . Using Eq. (A.21),  $u_{\text{fluc},n}^{\text{flt}}$  will take a new random value every multiple of  $P_{\text{clock}}$ , creating a high power spectrum content for frequencies lower than  $f_c$  and taking only values of  $\pm u_{\text{amp}}$  at any time. This filter does not have a sharp cut-off behavior because the shape of the signal is kept with sharp corners, where high frequency content is always present. To remove the high frequency content, an additional low-pass filter is applied, which “smooth” the sharp corners of the signal.

With a frequency limited signal, its autocorrelation does not keep all the properties of a white noise signal, becoming less decorrelated with itself (shown by a level of autocorrelation for a number of time steps). In Fig. A.2, signals generated using a time step of  $1.25 \times 10^{-5}$  s with different frequency content are shown. One signal was created using Fig. A.19 without frequency limit ( $P_{\text{clock}}=1$ , Nyquist frequency =40000 Hz), and the other using Eq. (A.21) with  $f_c=600$  Hz followed by a rectangular low pass filter with a cut-off frequency of 1000 Hz. Both signals have the same maximum amplitude  $u_{\text{fluc}}$  in time. Comparing the power spectrum of the signal shown in Fig. A.4, the signal with lower frequency limit presents a much stronger signal on the frequency range of interest. This will improve the identification process, as the signal-to-noise ratio using the low frequency limit signal is much higher than using the one with high frequency content. The auto-correlation matrices of both signals are shown in Fig. A.5. It would be optimal to use a signal with high decorrelation characteristics in a limited frequency range as shown by Foeller and

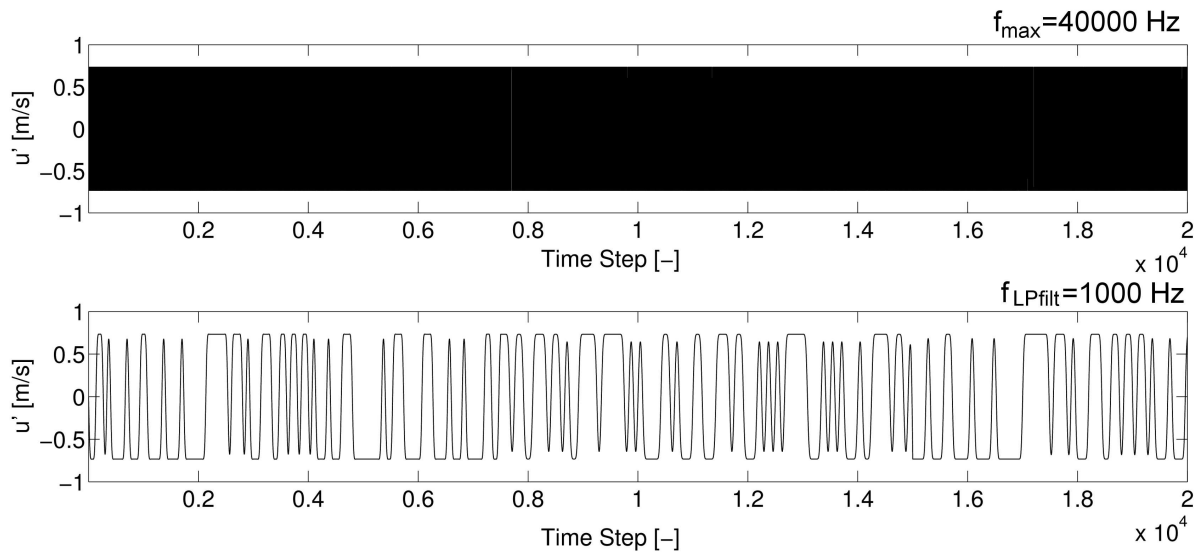


**Figure A.2:** DRBS Input signals in time with different frequency limit. Range: 1 to 20000 iterations

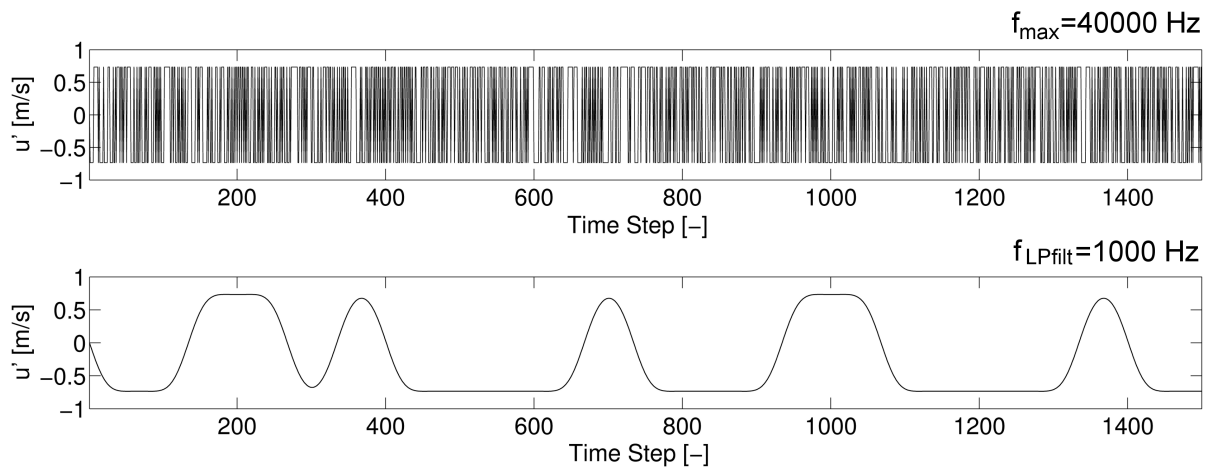


**Figure A.3:** DRBS Input signals in time with different frequency limit. Range: 1 to 2000 iterations

Polifke [58], where it has been seen that using this kind of signals, the number of time steps required to perform the identification can be reduced. This investigation was not carried out in the present work.

## A.6 Derivation of the Linearized Acoustic Equations

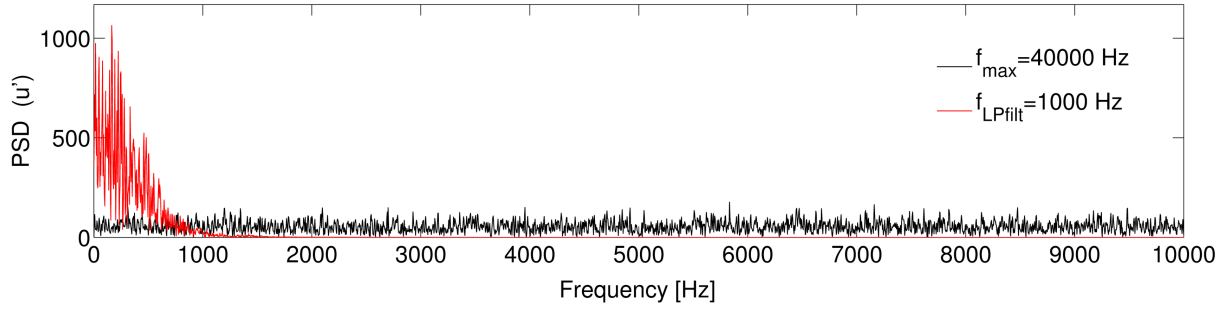


**Figure A.4:** Power spectrum of DRBS Input signals with different frequency limit.

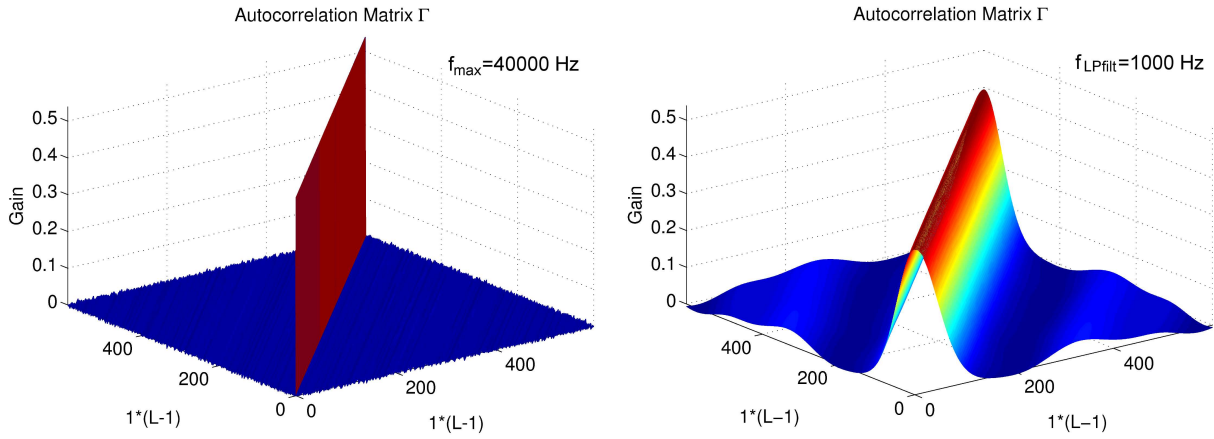


**Figure A.5:** Autocorrelation matrix of DRBS Input signals with different frequency limit.

## A.6 Derivation of the Linearized Acoustic Equations

The 1D linearized acoustic equations are derived using the decomposition presented in section 6.1:

$$u(x, t) = \bar{u} + u'(x, t), \quad (\text{A.22})$$

$$p(x, t) = \bar{p} + p'(x, t), \quad (\text{A.23})$$

$$\rho(x, t) = \bar{\rho} + \rho'(x, t). \quad (\text{A.24})$$

Considering that:

- (a) The flow is homentropic,  
 (b) mean terms are uniform at different positions,  
 (c) the terms containing only mean quantities are part of the stationary solution [48],  
 (d) only terms of first order in the fluctuations are considered (neglecting higher order terms, e.g.  $\rho' u'$ ),

the following equations are obtained:

- Conservation of mass

$$\frac{\partial \rho}{\partial t} + \frac{\partial \rho u}{\partial x} = 0, \quad (\text{A.25})$$

$$\frac{\partial (\bar{\rho} + \rho')}{\partial t} + \frac{\partial (\bar{\rho} + \rho') (\bar{u} + u')}{\partial x} = 0, \quad (\text{A.26})$$

$$\frac{\partial \bar{\rho}}{\partial t} + \frac{\partial \rho'}{\partial t} + \frac{\partial (\bar{\rho} \bar{u} + \bar{\rho} u' + \rho' \bar{u} + \rho' u')}{\partial x} = 0, \quad (\text{A.27})$$

$$\frac{\partial \rho'}{\partial t} + \bar{u} \frac{\partial \rho'}{\partial x} + \frac{\partial \bar{\rho} u'}{\partial x} = 0. \quad (\text{A.28})$$

- Conservation of momentum

$$\frac{\partial \rho u}{\partial t} + \frac{\partial \rho u u}{\partial x} + \frac{\partial p}{\partial x} = 0, \quad (\text{A.29})$$

$$\frac{\partial (\bar{\rho} + \rho') (\bar{u} + u')}{\partial t} + \frac{\partial (\bar{\rho} + \rho') (\bar{u} + u') (\bar{u} + u')}{\partial x} + \frac{\partial (\bar{p} + p')}{\partial x} = 0, \quad (\text{A.30})$$

$$\underbrace{\left[ \frac{\partial \bar{\rho} \bar{u}}{\partial t} + \frac{\partial \bar{\rho} \bar{u} \bar{u}}{\partial x} + \frac{\partial \bar{p}}{\partial x} \right]}_{=0 \text{ from stationary solution}} + \underbrace{\left[ \frac{\partial \rho' \bar{u}}{\partial t} + \frac{\partial \rho' \bar{u} \bar{u}}{\partial x} + \frac{\partial \bar{\rho} u' \bar{u}}{\partial x} \right]}_{=0 \text{ from Conservation of mass}} + \quad (\text{A.31})$$

$$\underbrace{\left[ \frac{\partial \rho' u'}{\partial t} + \frac{\partial 2(\rho' u' \bar{u} + \rho' u' u')}{\partial x} \right]}_{=0 \text{ from neglecting high order terms}} + \frac{\partial \bar{\rho} u'}{\partial t} + \frac{\partial \bar{\rho} \bar{u} u'}{\partial x} + \frac{\partial p'}{\partial x} = 0, \quad (\text{A.32})$$

$$\bar{\rho} \left( \frac{\partial u'}{\partial t} + \bar{u} \frac{\partial u'}{\partial x} \right) + \frac{\partial p'}{\partial x} = 0. \quad (\text{A.33})$$

In a homentropic flow, the pressure is only function of the density as:

$$\frac{p}{\rho^\gamma} = \text{constant}. \quad (\text{A.34})$$

Then, applying a Taylor expansion of the pressure ( $p$ ) around its mean value ( $\bar{p}$ ) with respect to the density ( $\rho$ ) [39, 161] with a first order approximation, the following expression is obtained:

$$p = \bar{p} + \left( \frac{\partial p}{\partial \rho} \right)_s \rho', \quad (\text{A.35})$$

and from the definition of speed of sound ( $a$ ):

$$a^2 = \frac{\partial p}{\partial \rho} = \frac{p'}{\rho'} = \gamma \bar{R}T. \quad (\text{A.36})$$

## A.7 Description of Elements in the Network Model

The definitions of the different elements used in the network model (Fig. 6.4) in terms of Riemann invariants are presented. First, the transfer matrix of a constant section duct is presented, followed by the transfer matrices of the acoustically “compact” elements, as the flame and the area change. An acoustically “compact” element is an element without physical dimensions (e.g., a discontinuity) or that its spatial dimensions are small compared to the acoustic wave length. For the Flame Transfer Matrix, the derivation has been done for a case with a different reference location. At the end of this section, the acoustic relations for the inlet and outlet boundary conditions are presented.

### A.7.1 Constant Section Duct

In a constant section duct with length  $l$ , without acoustic losses and in the presence of mean flow, the acoustic waves between two different positions propagate undisturbed. Only a phase shift is observed on the wave between both positions [83, 161]. Evaluating at the upstream ( $u$ ) and downstream ( $d$ )

ends of the duct, the following equations are obtained [117, 161]:

$$f_d = e^{-ik_{x+}l} f_u, \quad (\text{A.37})$$

$$g_d = e^{-ik_x l} g_u. \quad (\text{A.38})$$

where  $k_{x\pm}$  is defined in Eq. (6.12). In matrix notation as in *taX*:

$$\begin{bmatrix} -e^{-ik_{x+}l} & 0 \\ 0 & -e^{-ik_x l} \end{bmatrix} \begin{bmatrix} f_u \\ g_u \end{bmatrix} + \begin{bmatrix} 1 & 0 \\ 0 & 1 \end{bmatrix} \begin{bmatrix} f_d \\ g_d \end{bmatrix} = \begin{bmatrix} 0 \\ 0 \end{bmatrix}. \quad (\text{A.39})$$

### A.7.2 Flame Transfer Matrix of a Compact Flame with a Different Reference Location

The flame transfer matrix defined in Eqs. (6.19) and (6.20) was extended (in terms of the Riemann invariants) to consider the different reference position of velocity fluctuations in the FTF [83, 117]. This element will become a 6-port instead of a 4-port element. The heat release fluctuations in Eq. (6.19) and (6.20) are defined by:

$$\frac{\dot{Q}'(\omega)}{\bar{Q}} = \text{FTF}(\omega) \frac{u'_r(\omega)}{\bar{u}_r}, \quad (\text{A.40})$$

where  $r$  indicates the reference position for velocity fluctuations (see Fig. A.6). Introducing Eq. (A.40) on Eqs. (6.19) and (6.20), and by replacing the acoustic variables  $u'$  and  $p'$  to their definitions in Riemann Invariants  $f$  and  $g$  [156]:

$$u' = f - g, \quad (\text{A.41})$$

$$\frac{p'}{\rho a} = f + g, \quad (\text{A.42})$$

the following relations are derived:

- From Eq. (6.19):

$$\frac{p'}{\rho_d a_d} = \frac{\rho_u a_u}{\rho_d a_d} \left[ \frac{p'}{\rho_u a_u} - n u'_u M_u \left( 1 + \frac{\dot{Q}'/\bar{Q}}{u'_r/\bar{u}_r} \frac{u'_r/\bar{u}_r}{u'_u/\bar{u}_u} \right) \right] \quad (\text{A.43})$$

$$\frac{\rho_d a_d}{\rho_u a_u} \left( \frac{p'}{\rho_d a_d} \right) = \frac{p'}{\rho_u a_u} - n u'_u M_u \left( 1 + \frac{\dot{Q}'/\bar{Q}}{u'_r/\bar{u}_r} \frac{u'_r/\bar{u}_r}{u'_u/\bar{u}_u} \right) \quad (\text{A.44})$$

$$\frac{\rho_d a_d}{\rho_u a_u} \left( \frac{p'}{\rho_d a_d} \right) = \frac{p'}{\rho_u a_u} - n u'_u M_u - n M_u \frac{u'_r \bar{u}_u}{\bar{u}_r} \text{FTF}(\omega) \quad (\text{A.45})$$

$$\frac{\rho_d a_d}{\rho_u a_u} (f_d + g_d) = f_u + g_u - n (f_u + g_u) M_u - n M_u \frac{(f_r + g_r) \bar{u}_u}{\bar{u}_r} \text{FTF}(\omega) \quad (\text{A.46})$$

$$\frac{\rho_d a_d}{\rho_u a_u} (f_d + g_d) = (1 - n M_u) (f_u + g_u) - n M_u \frac{\bar{u}_u}{\bar{u}_r} \text{FTF}(\omega) (f_r + g_r). \quad (\text{A.47})$$

- From Eq. (6.20):

$$u'_d = u'_u \left[ 1 + n \frac{\dot{Q}'/\bar{Q}}{u'_r/\bar{u}_r} \frac{u'_r/\bar{u}_r}{u'_u/\bar{u}_u} \right] - n M_u \gamma \frac{p'}{\rho_u a_u} \quad (\text{A.48})$$

$$u'_d = u'_u + n \frac{u'_r \bar{u}_u}{\bar{u}_r} \text{FTF}(\omega) - n M_u \gamma \frac{p'}{\rho_u a_u} \quad (\text{A.49})$$

$$f_d - g_d = f_u - g_u + n \frac{(f_r - g_r) \bar{u}_u}{\bar{u}_r} \text{FTF}(\omega) - n M_u \gamma (f_u + g_u) \quad (\text{A.50})$$

$$f_d - g_d = (1 - n M_u \gamma) f_u - (1 - n M_u \gamma) g_u + n \frac{\bar{u}_u}{\bar{u}_r} \text{FTF}(\omega) (f_r - g_r). \quad (\text{A.51})$$

where the index  $u$  and  $d$  are for the unburnt and burnt sides of the heat source, respectively (see Fig. A.6). The interaction coefficient  $n$  is defined as:

$$n = \left( \frac{T_d}{T_u} - 1 \right). \quad (\text{A.52})$$

In matrix form, the equations are arranged as:

$$\begin{pmatrix} \frac{\rho_d a_d}{\rho_u a_u} & \frac{\rho_d a_d}{\rho_u a_u} \\ 1 & -1 \end{pmatrix} \begin{pmatrix} f_d \\ g_d \end{pmatrix} = \begin{pmatrix} 1 - n M_u & 1 + n M_u \\ 1 - n M_u \gamma & -1 - n M_u \gamma \end{pmatrix} \begin{pmatrix} f_u \\ g_u \end{pmatrix} \quad (\text{A.53})$$

$$+ \begin{bmatrix} n \frac{\bar{u}_u}{\bar{u}_r} \text{FTF}(\omega) \\ 0 \end{bmatrix} \begin{pmatrix} -M_u & M_u \\ 1 & -1 \end{pmatrix} \begin{pmatrix} f_r \\ g_r \end{pmatrix}. \quad (\text{A.54})$$

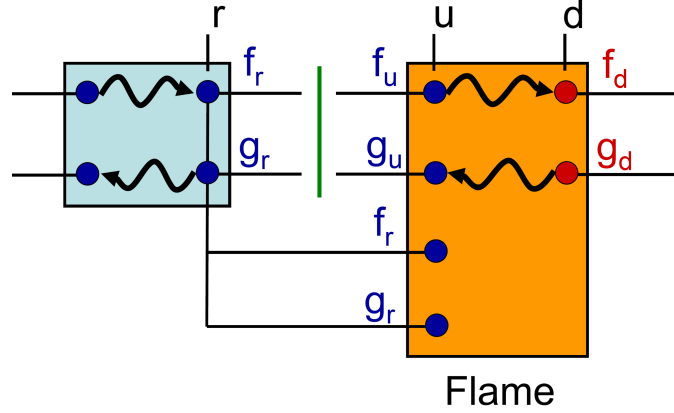


**Figure A.6:** Scheme for flame transfer matrix with a different velocity reference position for the FTE. Adapted from [83].

### A.7.3 Area change

The area change is considered as a compact element with losses and without physical dimensions (for simplification). From the conservation of mass equation for a quasi-1D flow (variation only in one direction):

$$\frac{\partial}{\partial t} \int_V \rho dV + \int_A \rho u dA = 0, \quad (\text{A.55})$$

$$\frac{\partial}{\partial t} \int_{x_u}^{x_d} \rho A dx + [\rho u A]_u^d = 0. \quad (\text{A.56})$$

Replacing the acoustic variables from Eqs. (A.22) and (A.24) in Eq. (A.56); and after linearization, the following relation is obtained:

$$\frac{\partial}{\partial t} \int_{x_u}^{x_d} \rho' A dx + [(\rho' \bar{u} + u' \bar{\rho}) A]_u^d = 0. \quad (\text{A.57})$$

Replacing Eq. (6.6) in Eq. (A.57), assuming constant speed of sound, and for time-dependent harmonic waves, the following relation is obtained [161]:

$$\frac{i\omega}{a} \int_{x_u}^{x_d} \frac{p'}{a} A dx + \left[ \left( \frac{p'}{a} M + u' \bar{\rho} \right) A \right]_u^d = 0. \quad (\text{A.58})$$

Considering the area change as a discontinuity, the first term in the left hand side of Eq. (A.58) is neglected, obtaining:

$$\left[ \left( \frac{p'}{a} M + u' \bar{\rho} \right) A \right]_u^d = 0. \quad (\text{A.59})$$

From the Bernoulli equation for unsteady compressible flow [155]:

$$\frac{\partial}{\partial x} \left( \frac{\partial \Phi}{\partial t} + \frac{1}{2} u^2 + \frac{\gamma}{\gamma - 1} \frac{p}{\rho} \right) = 0, \quad (\text{A.60})$$

where  $\gamma$  is the ratio of specific heats and  $\Phi$  is the velocity potential defined by:

$$\nabla \Phi = u, \quad (\text{A.61})$$

$$\Phi = \int_{x_u}^{x_d} u dx, \quad (\text{A.62})$$

the following relation is obtained including the effects of pressure losses:

$$\frac{\partial}{\partial t} \int_{x_u}^{x_d} u dx + \left[ \frac{1}{2} u^2 + \frac{\gamma}{\gamma - 1} \frac{p}{\rho} \right]_u^d + \frac{1}{2} \zeta u_d^2 = 0. \quad (\text{A.63})$$

An approximation of  $\zeta$  can be obtained by:

$$\zeta = \frac{2\Delta \bar{p}_t}{\bar{\rho}_2 \bar{u}_d^2}. \quad (\text{A.64})$$

taking into account that for low Mach number flows, the steady incompressible and compressible Bernoulli equations are equivalent up to second order in Mach number [83, 161]. This information was obtained using non-reacting RANS of the full geometry (including plenum).

For a discontinuity, the first term in the left hand side of Eq. (A.63) is neglected, and by linearizing Eq. (A.63) through a series expansion:

$$\left[ \bar{u} u' + \frac{\gamma}{\gamma - 1} \frac{p'}{\bar{\rho}} - \frac{\gamma}{\gamma - 1} \frac{\bar{p} \rho'}{\bar{\rho}^2} \right]_u^d + \zeta \bar{u}_d u' = 0. \quad (\text{A.65})$$

Using the relation for  $\rho'$  and the definition of speed of sound from Eq. (6.6) in Eq. (A.65); and dividing by the speed of sound, the following relation is obtained:

$$\left[ M u' + \frac{p'}{\bar{\rho} \bar{a}} \right]_u^d + \zeta M_d u' = 0. \quad (\text{A.66})$$

Expressing Eqs. (A.59) and (A.65) in terms of Riemann invariants, the transfer matrix is defined by:

$$\begin{bmatrix} 1 + M_u & 1 - M_u \\ A_u(1 + M_u) & A_u(-1 + M_u) \end{bmatrix} \begin{bmatrix} f_u \\ g_u \end{bmatrix} \quad (\text{A.67})$$

$$+ \begin{bmatrix} -(1 + M_d(1 + \zeta)) & -(1 - M_d(1 + \zeta)) \\ -A_d(1 + M_d) & -A_d(-1 + M_d) \end{bmatrix} \begin{bmatrix} f_d \\ g_d \end{bmatrix} = \begin{bmatrix} 0 \\ 0 \end{bmatrix}. \quad (\text{A.68})$$

#### A.7.4 Inlet

The inlet is considered as a fully reflective inlet, the acoustic velocity fluctuation to zero, i.e.  $u' = 0$ . Due to the presence of mean flow, the inlet is defined by a condition of no acoustic mass flow fluctuation [117]. The acoustic mass flow fluctuation disappears at a closed end:

$$(\rho u)' = 0. \quad (\text{A.69})$$

Then:

$$u' + M \frac{p'_i}{\bar{\rho}_i \bar{c}_i} = 0. \quad (\text{A.70})$$

This leads to:

$$[1 + M \quad -1 + M] \begin{bmatrix} f_i \\ g_i \end{bmatrix} = 0 \quad (\text{A.71})$$

#### A.7.5 Outlet

For the outlet, the reflection coefficient  $R(\omega)$  in Fig. 6.5 was obtained using the definition:

$$R(\omega) = \frac{g(\omega)}{f(\omega)}. \quad (\text{A.72})$$

In the network model, the reflective outlet is defined by:

$$[R \quad -1] \begin{bmatrix} f_i \\ g_i \end{bmatrix} = 0. \quad (\text{A.73})$$

### A.7.6 Swirler

The transfer matrix of the swirler was identified using LES/SI using only the swirler and connecting tube without the combustion chamber as shown in Fig. 5.30. The identification was carried out with 30 kW of power rating. Perturbations on the characteristic ingoing waves were imposed at the inlet and outlet using broadband excitation with a frequency limit to 6000 Hz and an amplitude of 5% of the mean velocity. The transfer matrix was identified as a MIMO system. Further details on MIMO identification for transfer matrices are shown in [57, 160].

The transfer matrix of the swirler is shown in Fig. A.7 using the Scattering Matrix representation. The scattering matrix is defined by:

$$\begin{pmatrix} f_d \\ g_u \end{pmatrix} = \mathbf{S}(\omega) \begin{pmatrix} f_u \\ g_d \end{pmatrix}. \quad (\text{A.74})$$

where  $f$  and  $g$  are the Riemann invariants defined in Eq. (6.14). The elements  $S_{11}$  and  $S_{22}$  of the scattering matrix represent the transmission of the acoustic waves from upstream and downstream direction through the swirler, respectively; while the elements  $S_{12}$  and  $S_{21}$  represent the reflection of the acoustic waves by the presence of the swirler. A length correction between the reference planes and the center of the swirler is included [83]. The element is introduced in the network model using the identified UIRs together with the UIR method specified in section 6.3 for evaluation of complex eigenfrequencies. The transformation of the scattering matrix in terms of Riemann Invariants  $f$  and  $g$  can be found in [50, 83].

## A.8 FTF at Different Velocity Reference Position with 30 kW and 9.5% of Excitation Amplitude

In Fig. A.8, the identified flame transfer function of the BRS burner with 30 kW with acoustic velocity ( $u'_r$ ) fluctuations measured at different reference position is shown. The excitation amplitude is 9.5% of the mean inlet velocity. The simulations were run for 2800000 iterations (0.35 s), considering the first

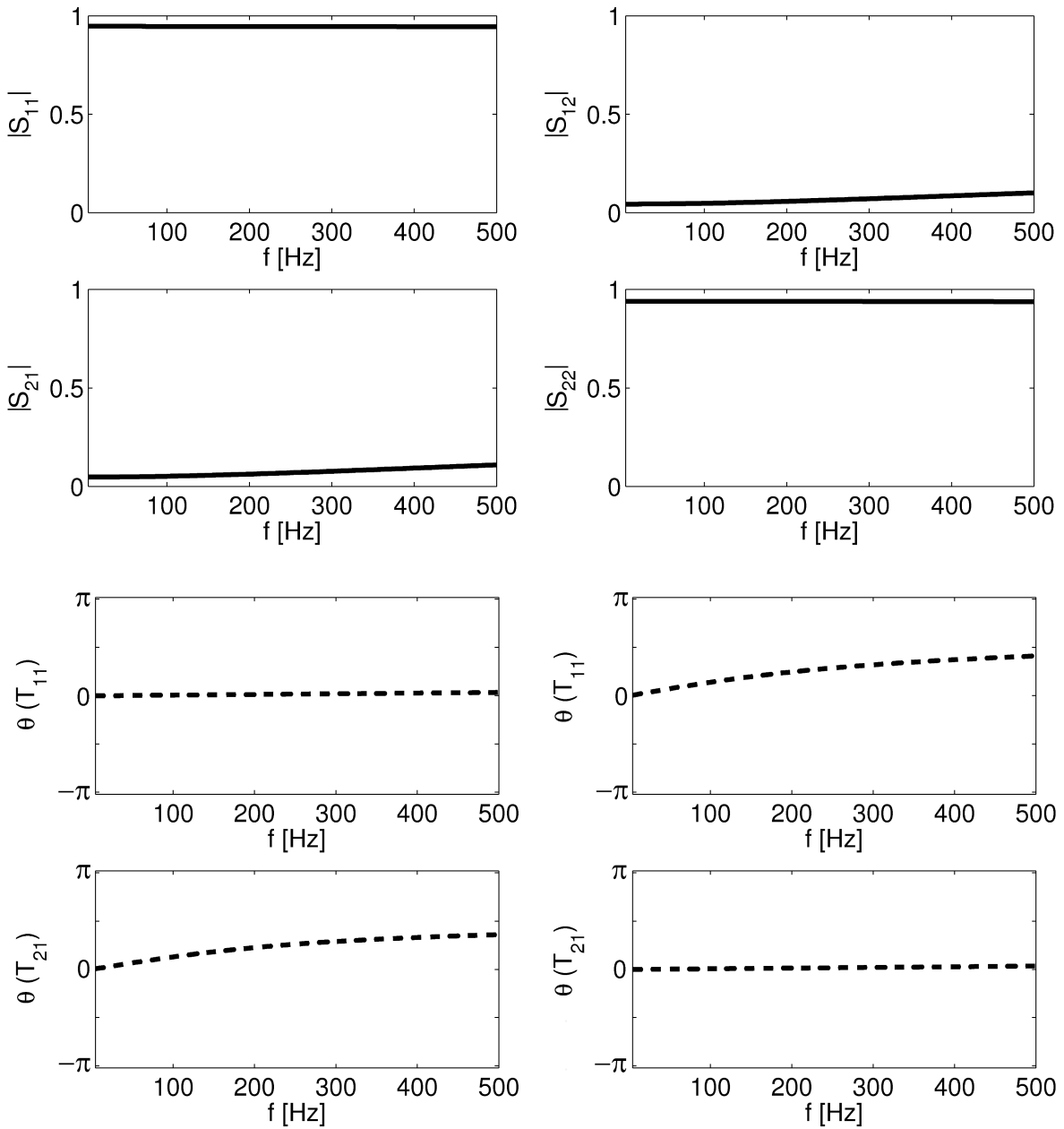


**Figure A.7:** Scattering Matrix of the swirler including length correction.

190000 iterations as a transition period and not taken into account for the identification. Similar to the case shown in Fig. 5.7 using 6.5% of excitation amplitude, the influence in the FTF by having the reference position at 70 mm was small.

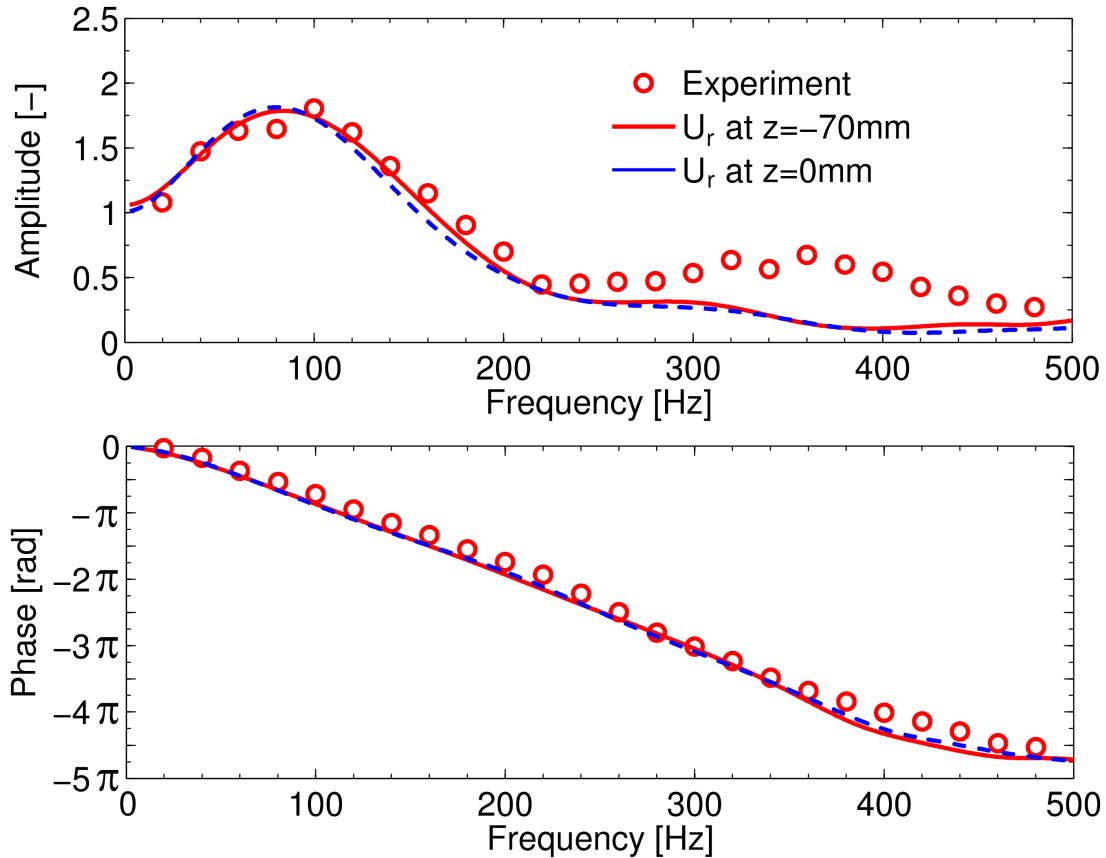


**Figure A.8:** Flame transfer functions for case with 30 kW with acoustic velocity ( $u_r'$ ) fluctuations measured at 0 and 70 mm upstream of the burner exit (Dump plane of combustor at  $z=0$  mm). Excitation amplitude=9.5%. Experiments for  $u_r$  at 70 mm upstream of the burner exit in circles.

## A.9 Confidence Analysis of Flame Transfer Function

The quantitative determination of measurement error for the FTF is complicated, because a long sequence of post-processing steps stands between the raw data and the final result. This is also true for LES/SI based error estimates. Nevertheless, two methods are developed to analyze the statistics of the acquired data from simulations and experiments and determine associated standard deviations. For the simulations, a method based on bootstrap-

ping [45] is used. The idea is to create artificial new data by randomly drawing elements from the original data set. Some elements will be chosen more than once. The procedure is repeated around 1000 times and statistical distributions of amplitude and phase are obtained. Standard deviations are computed from the distributions, indicating a measure of the deviation of the FTF identification by different levels of noise in the signal. In our case, this random process must be done to the correlation pairs obtained from Eqs. (4.28) and (4.27), because they keep the correlation information between our original signals and responses. This procedure gives us a level of confidence that if the identification would have been repeated with another signal, the results would be between this range. This method was applied for the reference case with 30 kW and with 9.5% of excitation amplitude. For the experiments, the data was taken with a frequency of 10 kHz for a total time of 40 s for each single frequency. Then, multiple sequences of 15 s from this data (e.g., the first interval from 0 to 15 s, the next from 0.05 to 15.05 s, until 40 s) are created, and by a Fast Fourier Transform (FFT), statistical distributions of amplitude and phase are computed for each frequency. The standard deviation indicates possible deviations created by noise included in the acquired data. The deviation percentage as the standard deviation over the mean of the amplitude of the FTF is shown in the top of Fig. A.9. Deviations lower than 2% are mostly found in the data. The FTF from LES/SI presents increased deviations for frequencies higher than 300 Hz, indicating a higher influence of noise at those frequencies.

## **A.10 Post-processing Tool for Line-of-sight Heat Release Integration in Tecplot**

This Macro was created to integrate the heat release from a CFD simulation with the Z coordinate as the axial axis. If the axial axis is in other coordinate, it needs to be adapted.

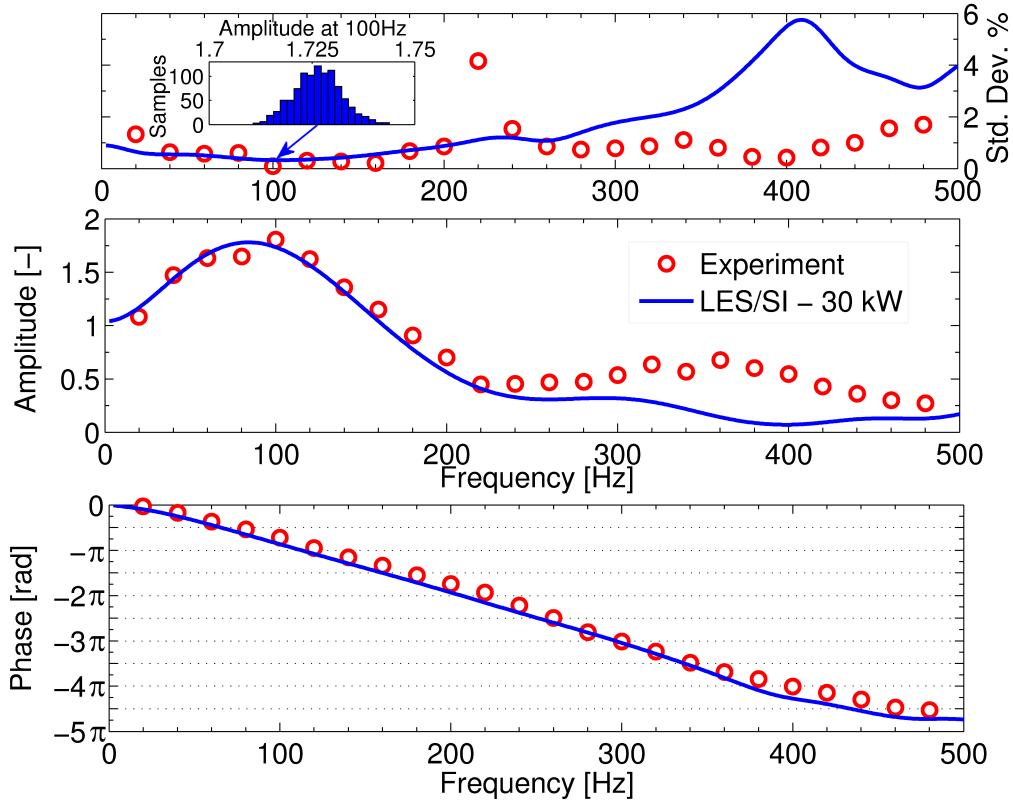


**Figure A.9:** Flame Transfer Function from experiments and LES/SI for 30 kW.  
 Top: Confidence analysis including a histogram of amplitudes from LES/SI at 100 Hz for 1000 sequences

### A.10.1 Steps before running the Macro

1. In the domain (Zone A), create a rectangular zone (Zone B) covering the volume that one wants to integrate (for example, for a selected volume of 90x90x140 mm, 80x80x100 zone was used). To create the rectangular zone, the dimensions I, J and K in TECPLOT represent the number of cells in X, Y and Z coordinates, respectively.
2. Interpolate only the variable corresponding the Reaction rate or heat release from Zone A into Zone B.
3. Save the interpolated Zone. Save only the variable of the reaction rate or heat release and the coordinates (X, Y and Z).

4. Load in TECPLOT only the saved interpolated zone (use the replace data set option, if you have something loaded before). It must contain only 4 variables. The heat release must be the fourth variable.
5. Create a plane (define J=1) with a similar number of cells I and K as in the interpolated zone.
6. Run the macro.
7. The macro will create a variable called V5, which is the Line-of-Sight Integrated heat release.

Check the `!GETFIELDVALUE` and `!SETFIELDVALUE` macro commands in the Tecplot Script Manual for the index notation to identify the corresponding cells for the integration.

### A.10.2 Macro

```
# Set the zone and variable:
!VarSet |indexI| = 1
!VarSet |indexJ| = 1
!VarSet |indexK| = 1
!VarSet |RootZone| = 1
# The heat release is the variable number 4:
!VarSet |Variable| = 4
# The destination zone is the plane (Zone 2)
!VarSet |DestZone| = 2
# The destination variable containing the integration is the fifth variable,
which is created by the macro.
!VarSet |Integ|=0
!AlterData
Equation = "v5 = 0"
!VarSet |DestVar| = 5
# Extract the data point:
!ActiveFieldZones = [|RootZone|]
```

```

$!Loop |MaxK|
$!VarSet |indexK| = |loop|
$!Loop |MaxI|
$!VarSet |indexI| = |loop|
$!VarSet |Integ|=0
$!Loop |MaxJ|
$!VarSet |indexJ| = |loop|
# Index notation for the cells:
$!VarSet |nodevalue| = ((|indexK|-1)*|MaxI|*|MaxJ| + (|indexJ|-1)*|MaxI| + |indexI|)
# Index notation for the plane:
$!VarSet |nodeplane| = ((|indexK|-1)*|MaxI|*1 + (1-1)*|MaxI| + |indexI|)
# Extract integrated variable:
$!GetFieldValue |variab|
Zone = |RootZone|
Var = |Variable|
Index = |nodevalue|
$!VarSet |Integ|+=|variab|
# Introduce integrated variable in the plane:
$!SetFieldValue
Zone = |DestZone|
Var = |DestVar|
Index = |nodeplane|
FieldValue = |Integ|
$!EndLoop
$!EndLoop
$!EndLoop

```